Physical Properties and Design of Light-Emitting Devices Based on Organic Materials and Nanoparticles

by

Polina Olegovna Anikeeva

Submitted to the Department of Materials Science and Engineering
in partial fulfillment of the requirements for the degree of

Doctor of Philosophy in Materials Science and Engineering

at the

MASSACHUSETTS INSTITUTE OF TECHNOLOGY

February 2009

Author .....
Department of Materials Science and Engineering
February 2009

Certified by..
Vladimir Bulović
Associate Professor of Electrical Engineering and Computer Science
Thesis Supervisor

Certified by..
Yoel Fink
Associate Professor of Materials Science
Thesis Reader

Accepted by..
Christine Ortiz
Chairman, Department Committee on Graduate Students

Physical Properties and Design of Light-Emitting Devices Based on Organic Materials and Nanoparticles

by

Polina Olegovna Anikeeva

Submitted to the Department of Materials Science and Engineering
on February 2009, in partial fulfillment of the
requirements for the degree of
Doctor of Philosophy in Materials Science and Engineering

Abstract

This thesis presents the detailed experimental and theoretical characterization of light-emitting devices (LEDs) based on organic semiconductors and colloidal quantum dots (QDs). This hybrid material system has several advantages over crystalline semiconductor technology; first, it is compatible with inexpensive fabrication methods such as solution processing and roll-to-roll deposition; second, hybrid devices can be fabricated on flexible plastic substrates and glass, avoiding expensive crystalline wafers; third, this technology is compatible with patterning methods, allowing multicolor light sources to be fabricated on the same substrate by simply changing the emissive colloidal QD layer. While the fabrication methods for QD-LEDs have been extensively investigated, the basic physical processes governing the performance of QD-LEDs remained unclear. In this thesis we use electronic and optical measurements combined with morphological analysis to understand the origins of QD-LED operation. We investigate charge transport and exciton energy transfer between organic materials and colloidal QDs and use our findings as guidlines for the device design and material choices. We fabricate hybrid QD-LEDs with efficiencies exceeding those of previously reported devices by 50-300%. Novel deposition methods allow us to fabricate QD-LEDs of controlled and tunable color by simply changing the emissive QD layer without altering the structure of organic charge transport layers. For example, we fabricate white light sources with tunable color temperature and color rendering index close to that of sunlight, inaccessible by crystalline semiconductor based lighting or fluorescent sources. Our physical modeling of hybrid QD-LEDs provides insights on carrier transport and exciton generation in hybrid organic-QD devices that are in agreement with our experimental data. The general nature of our experimental and theoretical findings makes them applicable to a variety of hybrid organic-QD optoelectronic devices such as LEDs, solar cells, photodetectors and chemical sensors.

Thesis Supervisor: Vladimir Bulović
Title: Associate Professor of Electrical Engineering and Computer Science

Acknowledgments

First of all I would like to thank my advisor Prof. Vladimir Bulović for his inspiration, criticism and support. He makes me a better scientist and a better person. He is a true teacher, the most critical judge and the most avid supporter of this work.

My co-advisor Prof. Yoel Fink who brings an entire new prospective in my research and career paths. Thank you for always willing to share your valuable time.

I'm infinitely grateful to my thesis committee members Prof. Millie Dresselhaus and Prof. Ned Thomas. Meetings with each of you helped me develop my direction in science and life. Your insatiable curiosity always reminds me that there is so much more that I need to learn.

Prof. Moungi Bawendi for being an inexhaustible source of knowledge of quantum dot physics and chemistry.

My collaborator Jon Halpert for his incredible talent in synthetic chemistry, sense of humor and adventurous spirit. This work would have been simply impossible without you.

Thank you everyone in LOOE group. Especially LeeAnn Kim, Jen Yu and Vanessa Wood who are always there to help and inspire; Conor Madigan for being a teacher and a friend; Alexi Arango and Jon Ho for being patient and always helping with equipment; Matt Panzer for supporting even questionable efforts; Yasu Shirasaki for always asking hard questions; Ian Rousseau for writing a beautiful user interface to my initially user-unfriendly model.

I can never be grateful enough to my parents and my brother who allowed me to leave them for such long time. Your unquestioning love and support made it all possible. Thank you for letting me grow.

Everyone from MIT Outing Club, especially Dan Walker and Kate D'Epagnier, who showed me life outside the lab, and hence made me more productive and complete human.

Finally, The Hoburgs, an american family that essentially adopted me and fed me through most of the writing process. Woody Hoburg for teaching me how to use

MATLab and for being himself.

Contents

List of Figures

Chapter 1

Introduction

1.1 Thesis Summary

Since their first successfull synthesis in 1993 [1], colloidal quantum dots (QDs) of inorganic semiconductors have demonstrated exceptional optical properties that initiated their application in a variety of opto-electronic devices. Their high absorption crossection proved to be usefull in photovoltaic cells and photodetectors [2]. Narrow photoluminescence spectra tunable across the visible and infrared parts of spectrum led to colloidal QD applications in light-emitting devices (LEDs) [3]. Organic ligands that passivate the surface of QDs and provide their solubility in various organic solvents and water allow for their solution processing, and consequently, the development of inexpensive QD deposition techniques such as spin-coating and roll-to-roll deposition.

Despite the superior QD processibility and spectral characteristics, the development of QD-based opto-electronic devices is impeded by the insulating nature of organic ligands that obstruct the charge transport through QD films. Consequently, it is beneficial to use QDs in hybrid opto-electronic devices that take advantage of QD unique optical properties combining them with a material set tuned to shuttle charges towards (LEDs) or away (solar cells) from QD layers.

In this thesis we focus on the design and physical properties of efficient LEDs based on colloidal QDs and organic semiconductors. Organic LEDs (OLEDs) are

extensively studied and have been recently introduced into commercial information display applications. Hybrid organic-QD LEDs (QD-LEDs) benefit from reliable and controlled charge transport through amorphous organic thin films and narrow QD emission, yielding efficiencies approaching those of OLEDs and saturated electroluminescense (EL) spectra solely due to QD luminescence. The latter property of QD-LEDs allows for the universal design of multicolor QD-LEDs by simply changing the QD emission layer without altering the transport layers.

While the fabrication methods for QD-LEDs received wide interest, the fundamental physical processes that govern the behavior of these devices remained unclear. This thesis is dedicated to understanding of interactions between organic semiconductors and colloidal QDs through the development of QD-LED test-beds. Combining electronic and optical measurements with morphological analysis, we find the physical origins of the operation of QD-LEDs, which provide us with guidelines to QD-LED design and material choices. We are able to improve upon existing hybrid LED technology increasing the efficiency of QD-LEDs operating throughout the visible part of spectrum by 50-300%. The development of novel deposition methods allows for controlled tuning of QD-LED colors without changing the structure of charge transport layers, leading us to fabrication of white light sources with tunable color temperature and color rendering close to that of sunlight, inaccessible by crystalline semiconductor based lighting or fluorescent light sources.

We supplement our experimental investigation of physical properties of QD-LEDs with theoretical studies by building a model based on fundamental physical processes such as carrier drift, diffusion and recombination that provides an insight into carrier distribution and exciton formation in QD-LEDs. The results of our numerical simulations are consistent with our experimental data.

The design guidelines and theoretical insights obtained from our optical, electronic and morphological studies of QD-LEDs and the numerical model are equally applicable in fabrication and characterization of a variety of hybrid optoelectronic devices, such as LEDs, solar cells, photodetectors and chemical sensors.

This chapter reviews the history and development of QD-LEDs and OLEDs, fo-

cusing on the properties of both organic semiconductors and colloidal QDs. Chapter 2 details the experimental techniques used in QD-LED fabrication and characterization. Chapter 3 is dedicated to the development and fabrication of mixed color QD-LEDs and the concominant design of blue QD-LEDs. Chapter 4 discusses the exciton energy transfer from organic phosphorescent and fluorescent donors to colloidal QDs and exciton diffusion in thin organic films. Chapter 5 discusses the carrier transport and exciton generation in QD-LEDs from the experimental prospective. Chapter 6 is dedicated to the modeling of QD-LED structures discussed throughout this manuscript. QD-LED design guidelines obtained from the analysis in Chapters 5 and 6 are implemented in Chapter 7 to create multicolor QD-LEDs with record high efficiencies and spectral purity. Chapter 8 contains the conclusions.

1.2 Evolution of Solid State Lighting

Despite its invention in 1879, the incandescent light bulb [4] still occupies a large share of the entire lighting market. In particular, 90% of the residential sector in the US is still lighted up by incandescent bulbs. While incandescent bulbs provide light color temperature close to that of sunlight and excellent color rendering, their luminous efficiency is comparatively low < 20 lm/W. Today, the general lighting constitutes $\sim 15\%$ of US energy consumption. Consequently, improving the efficiency of light sources will significantly reduce energy consumption and minimize their environmental impact.

Compact fluorescent lamps [5], invented approximately at the same time as incandescent bulbs, provide a more efficient lighting alternative $\sim$ 50-60 lm/W. Fluorescent light bulbs rely on inelastic collisions of electrons with mercury atoms that lead to the emission of ultra violet photons that are subsequently absorbed by the lamp's fluorescent coating and converted into visible light. Commercial fluorescent lamps can be as efficient as 100 lm/W but their penetration into the residential market is inhibited by their poor color rendering and color temperature.

Inorganic light emitting diodes (ILEDs) that consist of a p-n junction of two doped

semiconductor crystals, were invented in 1920s and significantly improved upon in 1962 [6]. In ILEDs electrons supplied from a cathode and holes supplied from an anode meet at the junction and recombine producing photons with an energy close to the lowest band gap of the two semiconductors. These devices have comparatively long lifetimes and efficiencies up to 90 lm/W. Despite that, they are primarily used in indicator lights due to their high cost and size limitations. Semiconductor crystals have to be grown via epitaxy which requires high vacuum, which makes the process costly and confines it to small substrate sizes. As ILEDs emit light characteristic of a constituent semiconductor band gap, their spectra are narrow and not suitable for lighting applications. The use of combination of red, green and blue emitting ILEDs is complicated by different efficiencies and lifetimes of different color devices. Solid state lighting sources are usually based on a blue ILED [7] backlight painted in a yellow phosphor (for example cerium-doped yttrium aluminum garnet (Ce^{3+}:YAG)). Akin to fluorescent lamps, these devices also suffer from poor color rendering and color temperature.

Organic light emitting devices (OLEDs) discovered in 1987 by Kodak [8, 9] make use of small aromatic organic molecules, that are capable of transporting holes or electrons that meet within the structure forming bound pairs that can recombine producing photons with energy corresponding to the emission spectrum of the organic compound. Since their original invention, OLEDs have been significantly improved upon. The use of phosphorescent organic materials, which we will discuss in detail in Chapter 4, led to the development of OLEDs with efficiencies up to 100 lm/W. Using multiple organic dopants allows for fabrication of white OLEDs with good color rendering and color temperature [10]. Alternatively, different color OLEDs can be stacked within a single structure to produce a broad white light spectrum [11].

OLED low power consumption, high brightness and very small device thickness (~200 nm) originally suggested their use in flat panel display technology that is currently dominated by liquid crystal displays (LCDs) [12]. LCDs consist of a layer of liquid crystals embedded between two orthogonal polarizer plates. Liquid crystals are birefringent, i.e. they rotate the polarization of the incoming light depending on

their orientation. In the most common twisted nematic devices, molecules deposited between the polarizer plates align themselves in a helical structure. Such alignment rotates the light that passes through the first polarizer by 90 degees so that it can pass through the second orthogonal polarizer. When a voltage is applied to the electrodes the resulting torque forces the molecules to align themselves parallel to the electric field, which distorts the helical orientation and decreases the amount of light that can pass through the second polarizer. At sufficiently high voltages, liquid crystals become completely aligned with the field and do not alter the initial polarization of light, which then cannot pass through the second polarizer, and the pixels appear black. In color displays red, green and blue filters are placed on top of LCD pixels. LCD displays suffer from a narrow angle of viewing and low power efficiency caused by the losses in absorptive color filters.

In contrast, OLEDs rely on light emission rather than on transmission, which eliminates efficiency losses in color filters and polarizer plates. Since OLEDs are omnidirectional emitters, OLED displays have wide viewing angle. One of the major challenges of the OLED technology is the lack of reliable and inexpensive patterning methods for different color pixels. Since OLEDs consist of small molecule organics, they are not compatible with traditional lithographical patterning techniques, which require exposure to solvents that simply degrade OLED structures. Therefore patterning methods for OLEDs are limited to shadow-masking of different color pixels during physical vapor deposition resulting in expensive and wasteful OLED fabrication processes.

Hybrid organic - colloidal quantum dot LEDs (QD-LEDs) [3] make use of highly emissive nanocrystals ($\sim$ 2-20 nm in diameter) of inorganic semiconductors fabricated by organo-metallic chemical synthesis [1]. As a consequence of the synthetic procedure, crystalline QDs are surrounded by the organic ligands that ensure their solubility in a variety of organic solvents and water. Quantum confinement effects dominate the electronic structure of colloidal QDs, yielding QD size dependent absorption and photoluminescence spectra, hence allowing for spectral tunability across the visible (for CdSe, CdS and ZnSe) and IR (PbSe and PbS) parts of the spec-

trum [13]. QDs were first used in LEDs within a polymer-QD composite, which did not exhibit high luminescence efficiencies [14]. The first successful demonstration of efficient QD-LEDs came in 2002 [3]. In this device a single layer of QDs was embedded into a conventional OLED structure, which resulted in the external quantum efficiency of 0.5% and electroluminescence spectra dominated by the narrow QD emission. Compatibility with solution processing allowed for the development of effective and inexpensive QD patterning methods such as microcontact printing [15, 16] and its extention to the roll-to-roll deposition. These methods allow for inexpensive pixelation of QD-LEDs by simply patterning each QD color inside the structure, while keeping the organic charge transporting layers the same [16, 17], i.e. patterning can be done in a single inexpensive step. Narrow QD spectra yield superior color purity of QD-LEDs as compared to the wide organic emission of OLEDs making QD-LEDs an attractive alternative for flat panel display applications. Simultaneous electroluminescence of multiple color QDs allows for the development of tunable LED colors such as white QD-LEDs [17]. Since the number of QD colors that can be used in a single device is virtually unlimited, it is possible to achieve superior color rendering and mimic the solar color temperature using QD-LEDs.

The main challenges of QD-LED technology are the device longevity and efficiency. Organic materials that constitute the charge transport layers in QD-LEDs are prone to photooxidation from self-emitting light and electrochemical degradation [18, 19]. They are also susceptible to chemical and morphological changes caused by atmospheric oxygen and water vapor [18, 19]. A variety of packaging methods have been developed, that extend OLED and consequently QD-LED lifetimes making them viable for commercial applications. Recent experiments demonstrate the possibility of replacement of the organic charge transporting layers with chemically stable semiconducting metal oxides [20, 21, 22]. While these devices are robust with respect to operation in ambient conditions, their efficiencies are 10-20 times lower then those of hybrid organic-QD LEDs. Currently, the efficiencies of organic-QD LEDs are 10 times lower than those of state-of-the-art OLEDs, which impedes QD-LED introduction into commercial display technologies. In this thesis we investigate

the fundamental processes that govern QD-LED operation, which allows us to understand the origins of QD-LED electroluminescence and degradation. Our analysis leads to the design guidelines that yield more efficient and potentially more stable QD-LEDs.

1.3 Colloidal Nanocrystals

Semiconductor nanocrystals are nanometer scale particles, for which the energy level structure is determined by quantum confinement effects rather than by the inherent properties of the corresponding bulk material [13]. Quantum confinement effects become important when the nanocrystal size, a, is smaller than the bulk exciton Bohr radius, $a_B = \kappa\hbar^2/\mu e^2$, where κ is the dielectric constant of the material and μ is a bulk exciton reduced mass [13]. An exciton is an excited electron-hole pair bound in a hydrogen atom-like arrangement, that occurs when the electron is excited onto a higher energy level leaving a hole behind.

1.3.1 Nanocrystal fabrication

There are two common types of nanoparticles: colloidal [23] and epitaxial [24, 25]. Colloidal nanocrystals are nanoparticles that are grown by an organo-metallic chemical synthesis (Figure (1-1)) or a so-called three-neck flask synthesis developed by Murray et al. [1]. Organo-metallic precursors (such as dimethyl cadmium and trioctylphosphine selenium) are injected into the hot (~250° C) mixture of organic molecules (such as trioctylphosphine oxide or oleic acid) acting as a high temperature solvent. Metallic and non-metallic ions react in solution to form nuclei that then uniformly grow to become nanocrystals. The nanocrystal growth can be stopped by taking the particles out of the growth solution and cooling them down to room temperature. Thus, the nanocrystal size and consequently the emission wavelength are determined by growth time and temperature.

This process allows for a very narrow particle size distribution as well as for the overcoating of particles with a monolayer of organic surface ligands. These or-

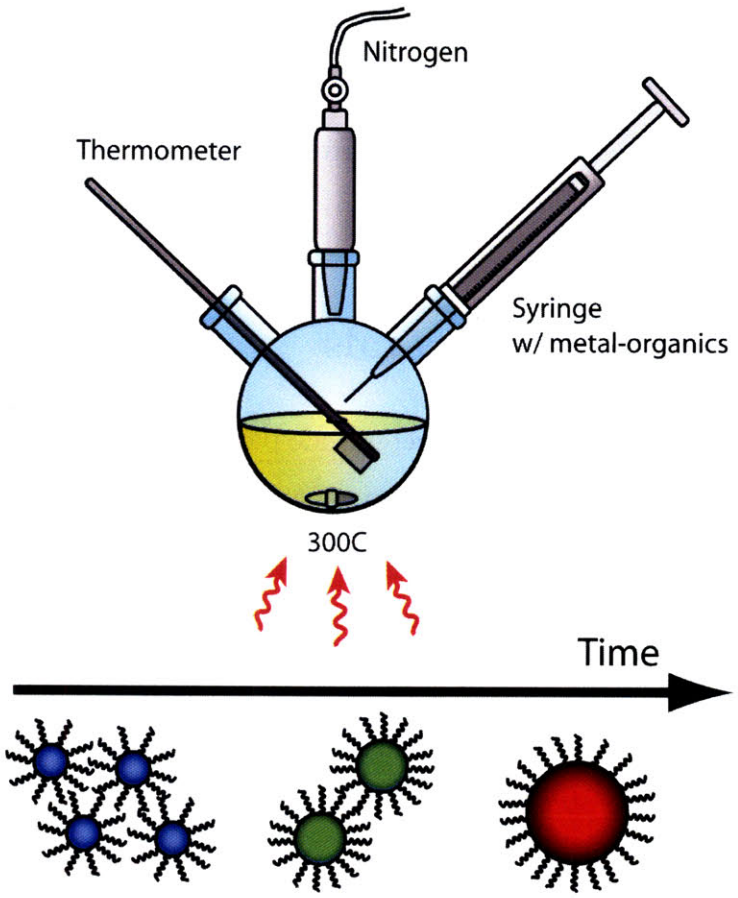

Figure 1-1: The schematic shows the QD synthesis in the three-neck flask. Organometallic precursors are injected into a boiling solution of organic molecules, that will eventually become QD ligands. The time scale indicates the growth progress. Courtesy of Timothy Osedach.

ganic molecules act as solvents during the high temperature synthesis and after the growth they allow nanocrystals to be soluble in a wide range of organic solvents or water. Their narrow size distribution and solubility in solvents make colloidal nanoparticles fundamentally different from epitaxial nanoparticles that are grown via molecular beam epitaxy on a substrate that is chosen such that interfacial energy between the substrate and a film is high enough to lead to de-wetting and islanding (Stranski-Krastanow growth) [24]. Since this process relies on stress relief in an unstable system, it poses significant challenges to the shape and size control of epitaxial nanocrystals. It is particularly difficult to achieve very small epitaxial quantum dot sizes, in which quantum effects become particularly strong and spectra are tunable across wider spectral range. In this thesis we focus on colloidal QDs because they

exhibit higher photoluminescence efficiencies, a narrower size distribution, superior control of nanocrystal shape and size, and possibility of their integration into a variety of different devices with different host materials.

1.3.2 Nanocrystal Types and Applications

The most commonly known colloidal nanoparticles are spherical colloidal quantum dots (QDs) of CdSe. CdSe QDs have been extensively studied over the last several years and their properties are fairly well understood. A wide variety of synthetic procedures have been developed leading to particles with different surface ligands and consequently soluble in different organic solvents or water [1, 26]. Unfortunately, the defects on the surface of QDs give rise to deep trap states within the energy gap decreasing QD PL quantum yield (QY) [27]. One possible solution to this problem is to engineer core-shell QDs by overcoating the CdSe core with a higher bandgap material (such as CdS, ZnS or ZnSe) and thus confine the exciton to the QD core and eliminate the deep traps within the bandgap [28, 29]. Core-shell nanocrystals exhibit superior PL QYs and have been successfully used in hybrid organic-quantum-dot LEDs (QD-LEDs) with external quantum efficiencies exceeding 2% [30, 31, 32]. These QDs also provide excellent fluorescent tags for biological imaging applications due to their photostability [26]. Using CdSe as a core material allows tuning of the emission wavelength between 500-650 nm [1]. With a CdS core, it is possible to achieve emission wavelengths between 470 and 480 nm but at the expense of PL QY [33]. Novel synthetic procedures alloy CdS and CdSe with higher bandgap materials of similar crystal structure (such as ZnS or ZnSe) leading to highly luminescent colloidal QDs with PL wavelength as low as 415 nm [17, 34, 35].

Highly luminescent core-shell QDs are not particularly suitable for photovoltaic applications, since the charge extraction out of these nanocrystals is obstructed by the energy barrier provided by the shell. Oblong particles, i.e. colloidal quantum rods (QRs), provide better charge transport desirable for efficient solar cells [2]. Recent synthetic procedures took advantage of site-specific nucleation [36] and thus enabled even more complex geometries of the colloidal nanoparticles, such as tetrapod-shape

[37] particles and hyper-branched structures [38]. For quantum tetrapods, excitons preferentially separate such that one of the charges stays in the core while the other charge migrates into one of the branches [37, 39]. Recent experiments show that photovoltaic cells based on conducting-polymer-quantum-tetrapod blends exhibit external quantum efficiencies (number of electrons per incident photon) of 45% and power conversion efficiencies of 2.8% [40].

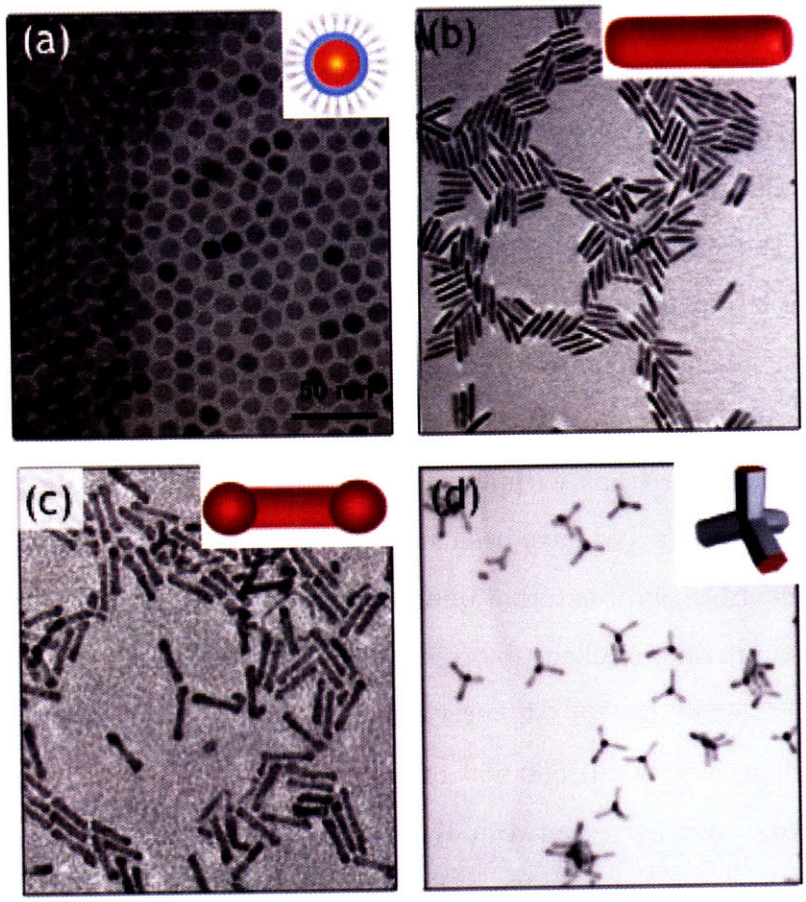

Figure 1-2: TEM micrographs of core-shell quantum dots (a), quantum rods (b), nano-barbells (c), quantum tetrapods (d).

1.3.3 Quantum Dots Optical Absorption Spectra

In the most naive approach, one can use a particle in a three-dimensional box approximation to model QD energy levels (Figure (1-3)). This model successfully explains why the gap between neighboring energy levels increases with a decreasing particle

diameter and enables bandgap engineering by changing the particle size [1].

In a strong confinement regime, when $a \ll a_B$, the QD absorption spectra are essentially determined by the optical transitions between electron and hole quantum size levels (QSLs) with a minor correction due to Coulomb attraction between the opposite charges [13]:

$$\hbar\omega_\nu = E_g + E_\nu^h(a) + E_\nu^e(a) - 1.8\frac{e^2}{\kappa a} \tag{1.1}$$

where E_g is the energy gap of the bulk material and E_ν^e and E_ν^h are electron and hole QSLs. The Coulomb correction is calculated in first order perturbation theory, as in the strong confinement regime it appears small compared to QSL energies.

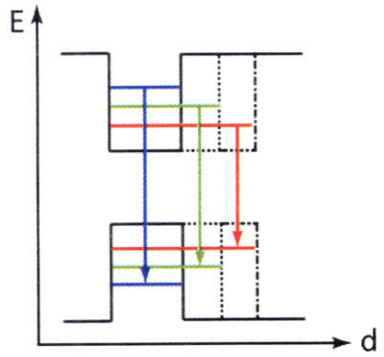

Figure 1-3: Schematic of quantum confinement, showing the dependence of the energy levels on the size of a potential well.

For a spherical nanocrystal surrounded by an infinite potential barrier, QSLs are obtained by solving a particle in a 3D box problem:

$$E_{l,n}^{e,h} = \frac{\hbar^2\phi_{l,n}^2}{2m_{e,h}a^2} \tag{1.2}$$

where $m_{e,h}$ is an electron or hole effective mass, and $\phi_{l,n}$ is the nth root of the spherical Bessel function of order l, $j_l(\phi_{l,n}) = 0$. The energy of the lowest electron and hole QSLs increases with decreasing nanocrystal size, leading to a total increase of the band edge optical transition energy.

While Equation (1.1) provides a simplistic qualitative understanding of QD band gap engineering, a realistic energy structure of crystalline semiconductors is rarely

described by a parabolic approximation. In fact, for zinc blende crystals such as CdSe, ZnSe, CdTe etc., the conduction band is parabolic only at the bottom, and the valence band consists of a 4-fold degenerate sub-band Γ_8, describing light and heavy holes, and a spin-orbit split-off sub-band Γ_7 as shown in Figure (1-4). Realistic calculation of QSLs should include the complexity of the electronic structure defined by lattice symmetry.

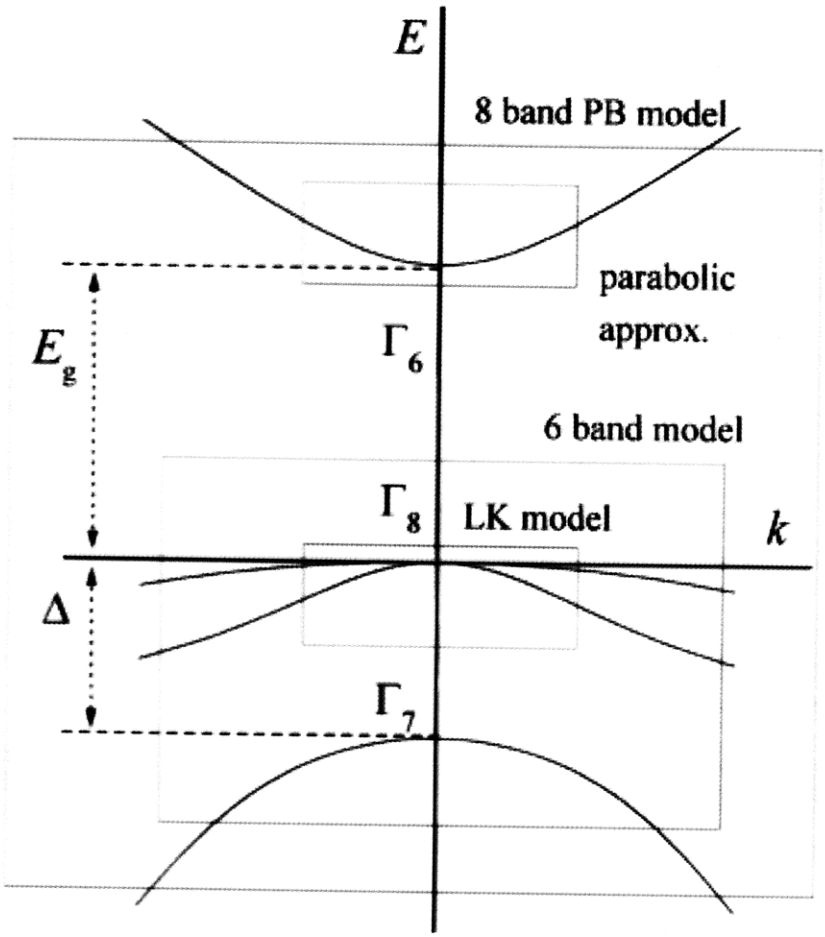

Figure 1-4: The bulk band structure of a typical direct gap semiconductor with cubic or zinc blende lattice and band edge at the Γ-point of the Brillouin zone. The boxes show the region of applicability of the various models used for the calculation of electron and hole QSLs.

Calculations within a multi-band effective mass approximation (Pidgeon-Brown model) [41] using an 8-band Luttinger-Kohn Hamiltonian [42] allow one to predict the energies of QSLs and the allowed transitions between them. While the electron QSLs

are rather simple and can be described by $1S_e$, $1P_e$, $1D_e$ orbitals, where S, P, D etc. correspond to the associated angular momentum values (0, 1, 2 etc.), the structure of hole QSLs is more complicated. The hole ground state is an even state that has a total angular momentum $j = 3/2$ and consists of a linear combination of wavefunctions with orbital momenta 0 and 2; it is usually referred to as a $1S_{3/2}$ state. The next state is an odd state with a total value of angular momentum $j = 3/2$ and corresponding values of orbital momenta 1 and 3; usually referred to as $1P_{3/2}$. There are no selection rules associated with the orbital quantum number and consequently transitions to the $1S_e$ level are allowed from any hole QSLs with $s - d$ symmetry. Similarly, transitions to the $1P_e$ levels are allowed from any hole QSLs with $p - f$ symmetry. These theoretical predictions are in impressive agreement with the experimental absorption spectra of CdSe QDs as shown in Figure (1-5) [13, 43].

1.3.4 Band Edge Photoluminescence

Unlike QD optical absorption spectra, QD photoluminescence (PL) remained controversial for a long time. PL spectra of high quality QD samples are red shifted with respect to the first absorption peak and excitation energy. QDs also exhibit an unusually long radiative relaxation time $\tau_R \sim 10 - 50$ ns at room temperature and $\tau_R \sim 1$ μs at 10 K, while the bulk relaxation time is $\tau_R \sim 1$ ns [44]. A simple parabolic band approximation fails to explain these effects through the internal band states, and initially QD PL was explained through the weakly overlapping electron and hole localized surface states [44].

However more detailed calculations using multi-band effective mass approximation demonstrate the existence of internal Dark Exciton states, that are responsible for QD PL. The existence of Dark Exciton was further confirmed experimentally in CdSe and other semiconductors [45]. A Dark Exciton is simply a ground state of an exciton (i.e. the excited state of a QD with the lowest associated energy), that in QDs corresponds to an angular momentum projection of ± 2. Since the projection of angular momentum in a non-excited state of a QD is 0, a Dark Exciton cannot be directly excited by a photon or radiatively recombine because the absorbed or emitted photons can only

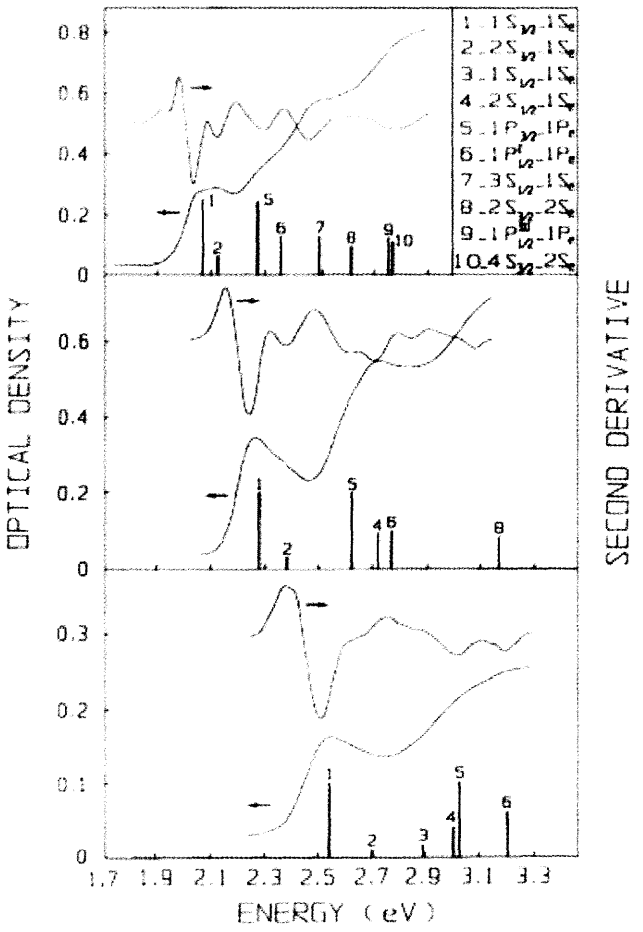

Figure 1-5: Comparison between the absorption spectra of 38, 26 and 21 $\AA$ radius CdSe QDs and their second derivatives with the results of theoretical 6-band calculations. The calculated positions of the transitions are indicated by vertical bars whose height indicates the relative transition strength. The inset shows the assignments of these transitions [43].

have angular momentum projection of ± 1. In order to create a Dark Exciton, the system has to be first excited into the lowest energy Bright Exciton, which can then thermalize via interactions with phonons to the lower energy Dark State. The energy difference between the first absorption peak and the PL peak, or Stokes shift, in QDs corresponds to the energy difference between first Bright Exciton and the Dark Exciton [13].

The difference between the Dark Exciton and the first Bright Exciton has to be on the order of the thermal energy of lattice phonons to allow transitions between these states. The origin of the splitting between these states lies in a combination of

an intrinsic crystal field, a slight asymmetry of colloidal QDs (i.e particles are slightly prolate rather than perfectly spherical) and an electron-hole exchange interaction that breaks up the degeneracy of the spherical band edge exciton.

The electron-hole exchange interaction becomes particularly important in small nanocrystals where quantum confinement is strong. The exchange interaction Hamiltonian has the following form:

$$\hat{H}_{exch} = -(2/3)\varepsilon_{exch}(a_0)^3\delta(\mathbf{r}_e - \mathbf{r}_h)\sigma\mathbf{J} \tag{1.3}$$

where the σ are the electron spin-1/2 Pauli matrices, $\mathbf{J}$ are the hole spin-3/2 matrices, a_0 is the lattice constant and ε_{exch} is the exchange strength constant. In nanocrystals with a cubic lattice, the exchange interaction splits the degenerate ground exciton state into an optically passive state with a total angular momentum 2 (triplet state) and an optically active state with the total angular momentum 1 (singlet state) and the splitting energy depends on the nanocryctal radius a:

$$\hbar\omega_{ST} = (8/3\pi)(a_0/a)^3\varepsilon_{exch} \tag{1.4}$$

In hexagonal nanocrystals, such as wurtzite CdSe, the splitting is described by:

$$\hbar\omega_{ST} = (2/\pi)(a_0/a)^3\varepsilon_{exch} \tag{1.5}$$

From the Equations (1.4) and (1.5) we can see that the splitting increases dramatically with decreasing nanocrystal radius reaching 10-20 meV in small nanocrystals ($a \sim 60\mathring{A}$). Figure (1-6) shows the experimental values of the Stokes shift (the splitting between the first absorption peak and PL maximum) and the calculated values of the splitting between the First Bright and Dark Exciton states [45]. While theory and experiment are in a good agreement for larger nanocrystal sizes, for small nanoparticles, theory underestimates the Stokes shift. It is thought that the acoustic phonons contribute to the splitting in small nanocrystals.

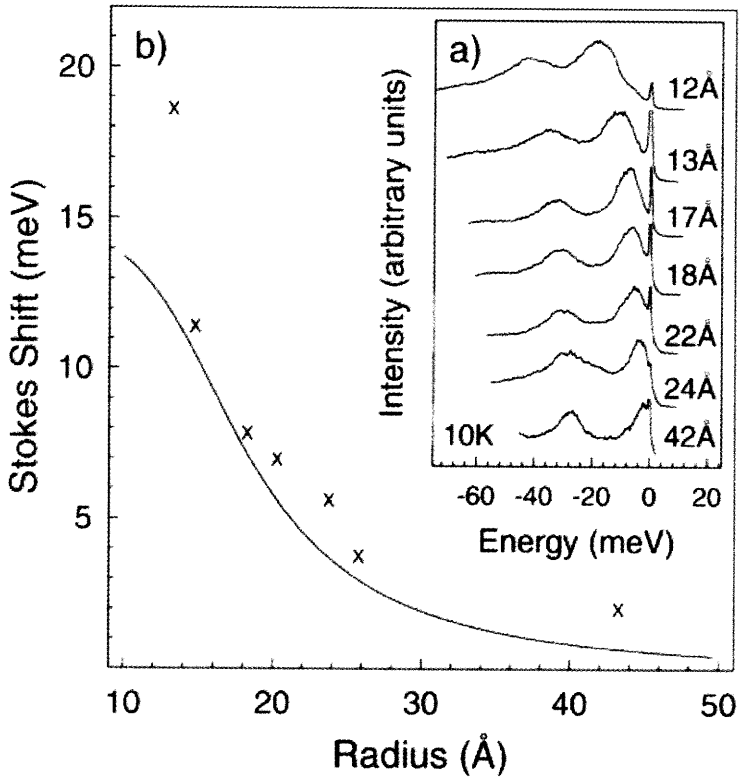

Figure 1-6: (a) Normalized fluorescence line narrowing spectra for CdSe nanocrystals between 12 and 42 $\AA$ in radius. (b) The size dependence of the resonant Stokes shift. The points labeled X are the experimental values. The solid line is the theoretical size-dependent splitting between the $\pm 1^L$ state and the ± 2 exciton ground state [45].

1.4 Organic Semiconductors

1.4.1 Material properties

Organic semiconductors are thin films of conjugated small organic molecules or polymers. Conjugated compounds are aromatic compounds where the presence of alternating single σ and double π bonds in cyclic molecular units results in sharing of p-orbitals of carbon atoms constructing the molecular backbone. The molecular orbital structure of the simplest aromatic compound benzene is shown in Figure 1-7. Sharing of atomic p-orbitals creates a molecular orbital referred to as a π-system that spans the entire backbone of an aromatic molecule. As a result, the electrons are delocalized and, consequently, mobile within the π-system [46].

Unlike in inorganic crystalline semiconductors, organic molecules in thin films are

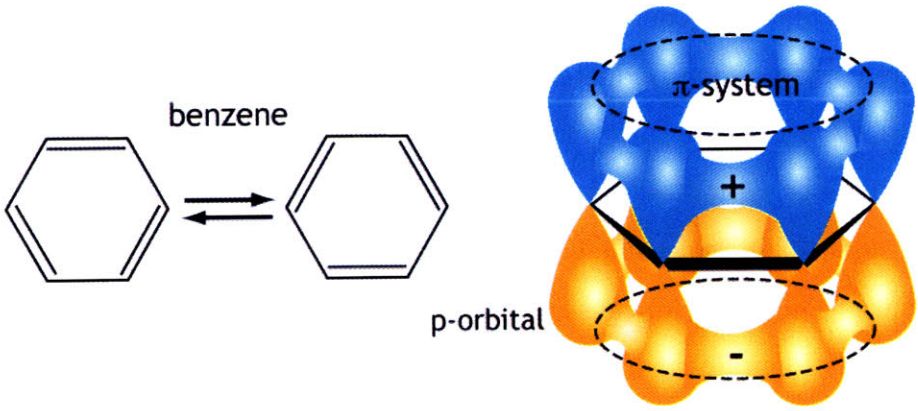

Figure 1-7: Chemical structure of a resonant molecule of benzene. p-orbitals overlap forming a π-system. Different colors correspond to different signs of the wavefunctions.

not bound by covalent or ionic bonds but rather by weak van der Waals bonds. Weak inter-molecular bonding in organic thin films is primarily a consequence of lowering the energy of neighboring molecules through their respective induced polarization on each other. The intrinsic dipoles of the neighboring molecules align relative to each other minimizing the energy, while the total dipole moment/polarization in the film remains equal to zero. Even in neutral molecules with a zero static dipole the charge distributions are susceptible to quantum fluctuations that essentially produce fluctuating dipoles. In organic solids that we will continue to discuss in this thesis the dipole-dipole interactions act as a main cohesive force.

As a result of weak van der Waals bonding between the molecules, organic solids have lower cohesive strength and are more penetrable than inorganic solids. Consequently, organic thin films are mechanically soft and fragile as well as more susceptible to degradation upon exposure to water and/or oxygen. On the other hand, organic solids are less brittle and thus can be deposited onto inexpensive flexible plastic substrates [47].

In a thin film π-system orbitals of neighboring conjugated organic molecules can slightly overlap allowing electrons to hop from one molecule to another. Higher degree of charge delocalization in aromatic thin films leads to better charge conduction in these materials as compared to aliphatic (linear) organic molecules. Electrical con-

ductivity in organic semiconductors depends on the relative molecular orientation. In crystalline organic semiconductors, molecules form close-packed planes stacked on top of each other so that their molecular orbitals overlap yielding superior charge transport in plane as well as in the direction of stacking [46]. In amorphous thin films with no specific molecular ordering the overlap between orbitals of neighboring molecules is smaller and, consequently, the charge mobility is lower. Amorphous films are mostly found in small molecule OLEDs and photovoltaic cells produced via standard deposition methods described in Chapter 2. Crystalline organic semiconductors are primarily used in organic field-effect transistors (OFETs), which require high carrier mobilities for faster switching speeds [48].

The band structure of crystalline inorganic semiconductors is determined by the crystal lattice, and periodicity results in continuous delocalized bands. The band structure of organic thin film semiconductors is determined by the molecular orbitals of the molecules composing the film. Electrons can hop between lowest unoccupied molecular orbital (LUMO) levels of neighboring molecules, and analogously holes can hop between highest occupied molecular orbital (HOMO) levels of neighboring molecules. Organic solids are disordered and the positions of HOMO and LUMO orbitals for each molecule in a solid are influenced by the local environment. Consequently, hopping of an electron from a molecule with a relatively low position of the LUMO or hopping of a hole from a molecule with a relatively high position of the HOMO is impeded by the energy barrier. Such molecules then form trap sites, where charges can rest over extended periods of time unless they are excited by external perturbation such as an electric field or a lattice vibration.

1.4.2 Electronic Excitations

The behavior of organic opto-electronic devices is governed by electrons, holes and excitons. In contrast to inorganic crystalline semiconductors, where electrons and holes are delocalized and move freely within bands, in organic thin film semiconductors, electrons and holes are localized and are more appropriately referred to as positive and negative polarons. A polaron is a charge carrier localized to a particular molecule

and that initiates a polarization of the surrounding environment (Figure 1-8).

In organic semiconductors, polarons can be either formed spontaneously when a neutral molecule transfers an electron to a neighboring neutral molecule, or by charge injection from a reservoir, such as a metal electrode. Polarons move through an organic solid by hopping as described in the section above. If two polarons of opposite charge reside on neighboring molecules they may combine on a single molecule, either annihilating with each other and releasing the excess energy as heat (or a photon) or forming an exciton. Figure 1-9 illustrates polaronic transitions [49].

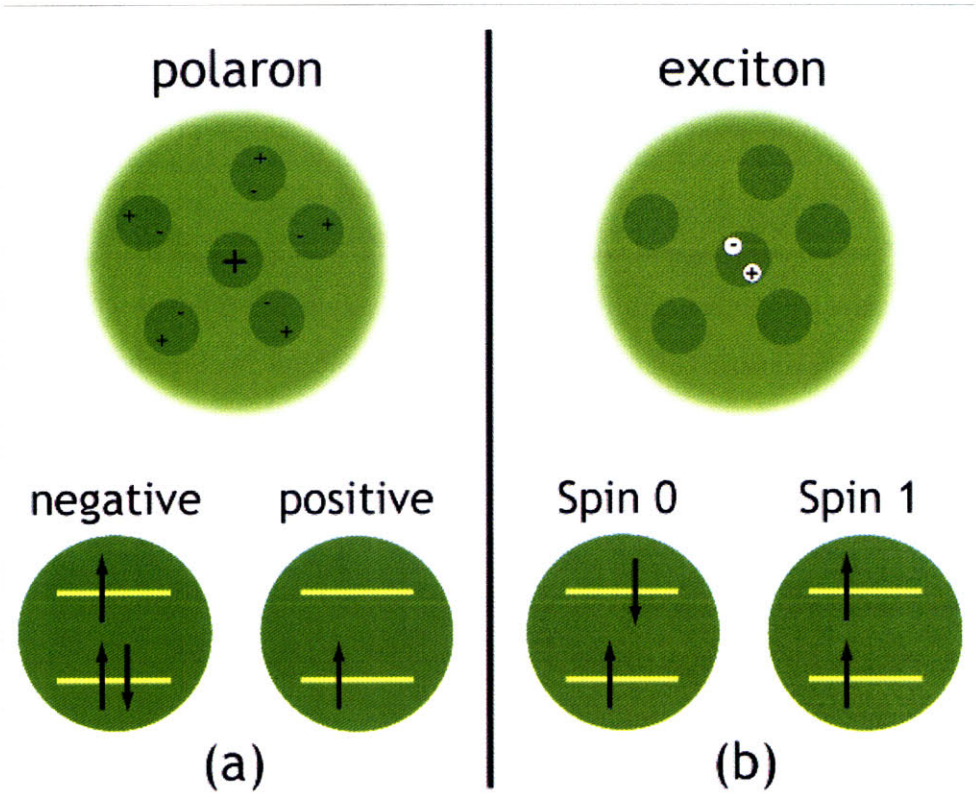

Figure 1-8: Diagrams of a polaron (a) and an exciton (b). The arrows represent electrons with the direction referring to positive or negative spin. The horizontal lines represent energy levels associated with molecular orbitals, with higher lines reflecting higher energies. Courtesy of Dr. Conor Madigan.

An exciton is a bound electron-hole pair, where a hole is a vacated electronic ground state. In contrast to the large Bohr radii and low binding energies of excitons in inorganic crystalline semiconductors, binding energy of an electron-hole pair confined to a particular molecule (Frenkel exciton) can be as high as 1 eV. Excitons

can also form when an electron and a hole reside on the neighboring molecules. In this case the exciton Bohr radius is larger and binding energy is lower, this type of excitons is often present in photovoltaic devices and is referred to as charge-transfer (CT) excitons. In this thesis we will primarily focus on Frenkel excitons, as they are the sources of emission in organic light emitting devices. The type of an exciton also depends on the total spin of the electron-hole pair comprising it. If the total spin is 0 the exciton is referred to as a "singlet", if the total spin is 1 then the exciton is referred to as a "triplet" (Figure 1-8). More detailed discussion of triplet and singlet excitons can be found in Chapter 4.

Excitons can be formed upon absorption of a photon with energy no less than the HOMO-LUMO gap or upon the meeting of two opposite charge polarons on the same molecule as described above. Excitons can recombine radiatively releasing a photon or non-radiatively releasing its energy as heat. Excitons can also dissociate when one polaron transfers to a neighboring molecule leaving an opposite charge polaron behind. Finally, excitons can transfer from one molecule to another by means of Förster or Dexter transfer. Förster energy transfer is a resonant process resulting from dipole-dipole interaction between donor and acceptor molecules, and during this process the energy released from the recombination of the donor exciton is non-radiatively transfered and used to create an exciton on the acceptor molecule. Förster energy transfer is a long range transfer, during which the donor molecule and acceptor molecule do not have to be immediate neighbors. The critical distance at which Förster transfer can take place is referred to as Förster radius, and it is determined by the overlap of donor and acceptor molecular orbitals. Dexter energy transfer is a direct electron exchange between the donor and acceptor molecules, during which excited electron hops from the donor molecule onto the acceptor molecule and the ground state electron hops onto the donor molecule from the acceptor molecule. Dexter transfer is a short range process, with the characteristic distance of $\sim$ 1 nm, which essentially requires donor and acceptor to be in immediate proximity of each other. Figure 1-10 shows excitonic transitions [49].

Another type of excitation present in organics are molecular, atomic or lattice

vibrations or phonons. These excitations are present in any solid at non-zero temperatures, but in organic semiconductors phonons play a more significant role as they facilitate electronic transitions by adding or absorbing energy into phonon modes. The ubiquitous presence of phonons is often referred to as a "thermal bath", that supplies or absorbs "heat" as needed [46].

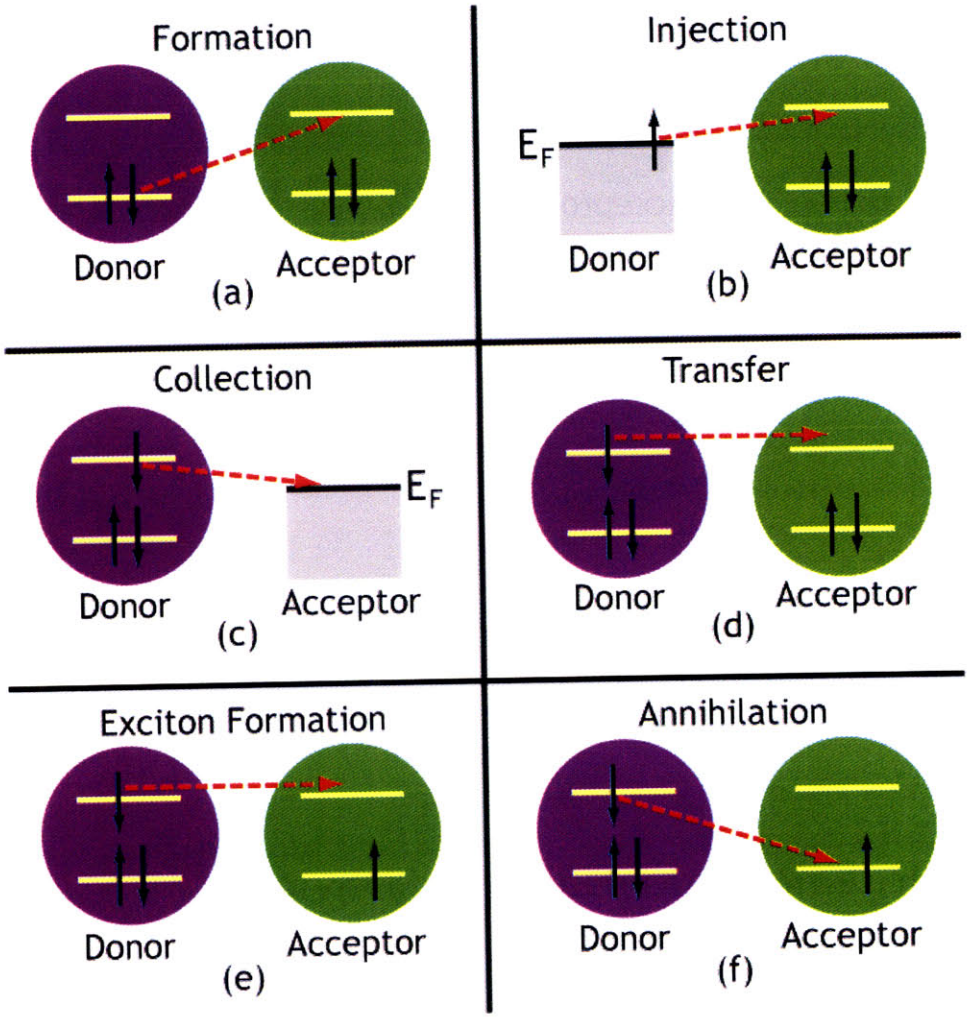

Figure 1-9: Cartoon diagrams of relevant polaron processes. (a) Spontaneous formation. (b) Injection from a charge reservoir (negative polaron injection shown). (c) Collection by a charge reservoir (negative polaron collection shown). (d) polaron transfer (negative polaron transfer shown). (e) Exciton formation. (f) Polaron annihilation. Courtesy of Dr. Conor Madigan.

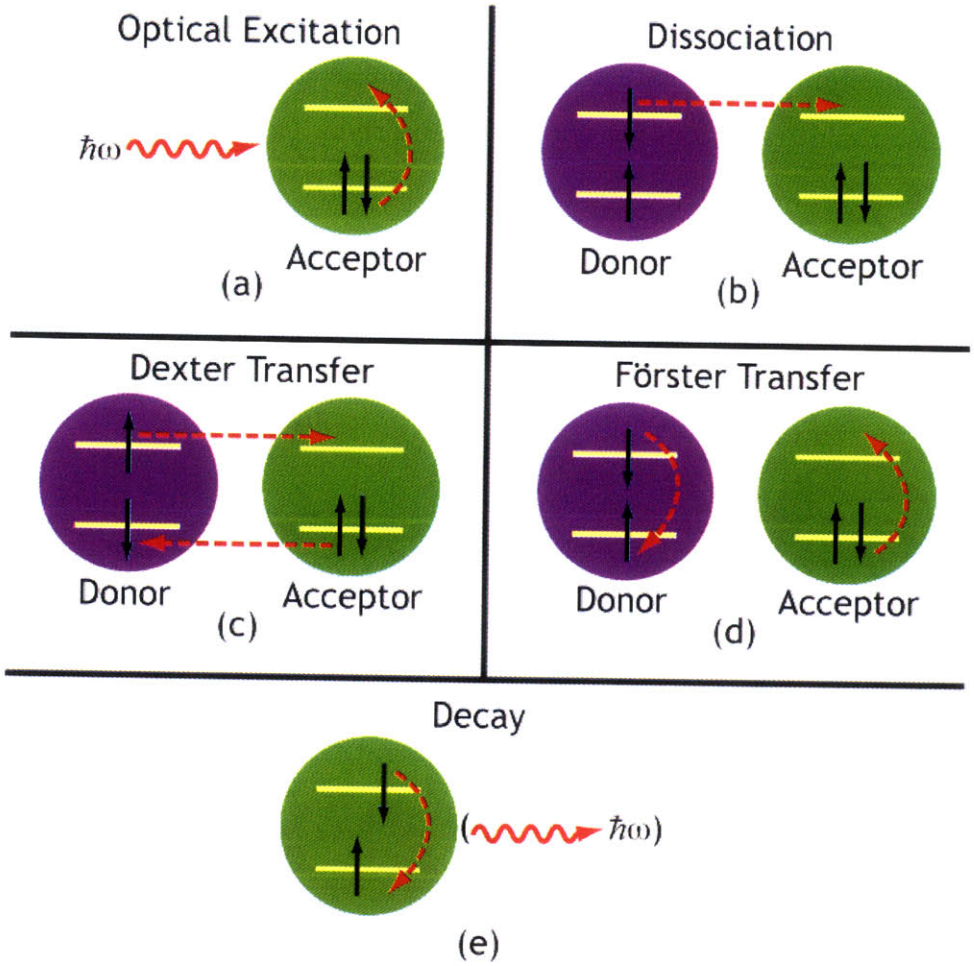

Figure 1-10: Cartoon diagrams of relevant exciton processes. (a) Optical formation (by photon absorption) (b) Dissociation into two polarons. (c) Dexter transfer (comprising two simultaneous electron transfers). (d)Förster transfer (comprising long range energy transfer by dipole-dipole coupling). (e) Decay (either emissive or non-emissive). Courtesy of Dr. Conor Madigan.

1.5 Organic Light Emitting Devices

The idea to use fluorescent organic molecules in electroluminescent structures appeared in 1960s [50]. However these devices, which consisted of a single fluorescent material placed between two electrodes exhibited extremely high turn-on voltages ~ 100 V and low power efficiencies $< 0.01\%$. The first successful demonstration of organic EL came in 1980s from Kodak [8, 9]. This OLED consisted of a transparent indium-tin oxide (ITO) anode, a layer of a hole transporting material originally an aromatic diamine (later replaced by N,N'-bis(3-methylphenyl)-N,N'-

bis(phenyl)benzidine (TPD)), a layer of emissive electron transporting material tris-(8-hydroxyquinoline) aluminum (Alq_3), and finally Mg:Ag electrode (Figure 1-11). This device had an external quantum efficiency, i.e. number of emitted photons per injected electron, of 0.8% and operating voltages in the range of 2.5-10V. The two design keys to a dramatically higher efficiency and lower operating voltage were: (1) using a double-layer device, where each of the layers preferentially transports a single carrier type, as it allowed to decrease the device resistance; (2) using a Mg:Ag alloy cathode instead of conventional Ag or Al, as the higher work function of Mg improved the electron injection into the device.

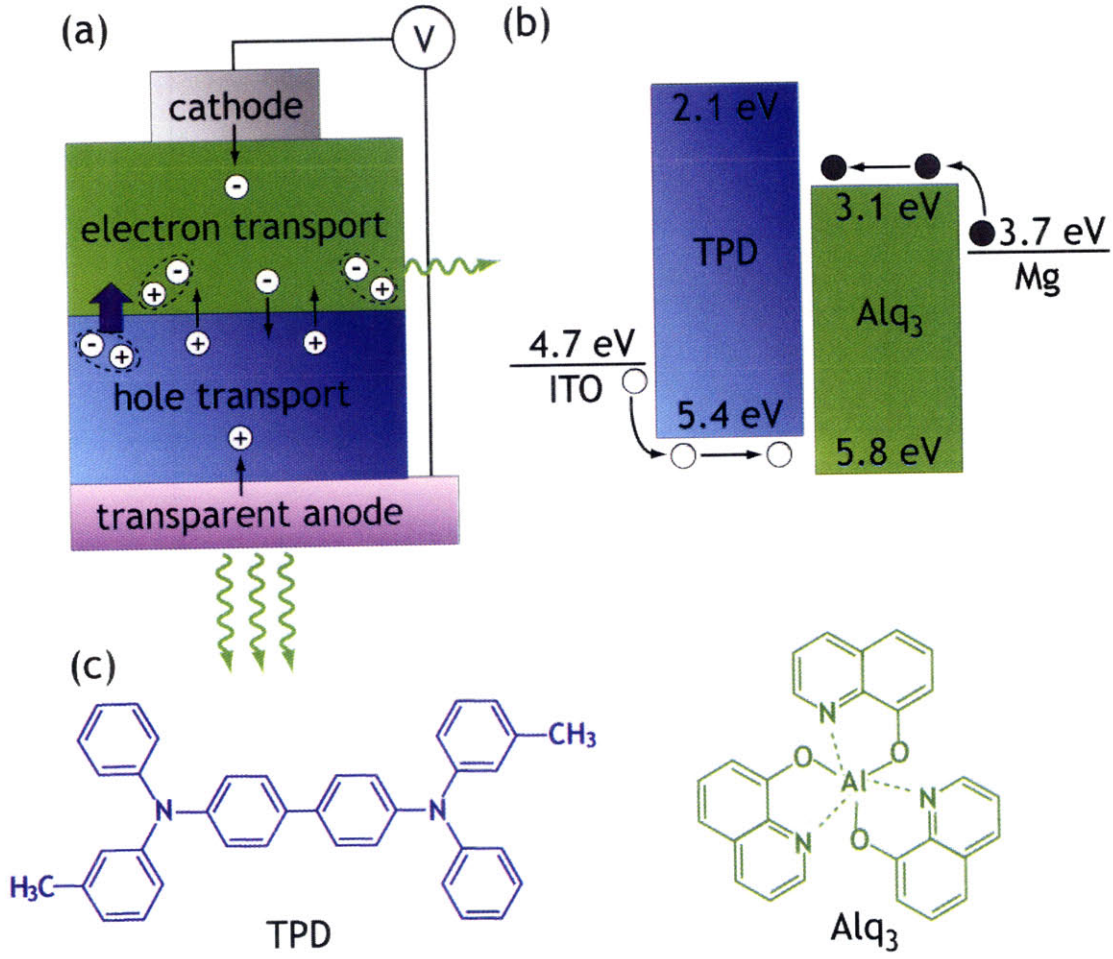

Figure 1-11: (a) Cartoon diagram of an archetypical OLED. (b) Band diagram of a Kodak OLED. (c) Chemical formulas of TPD and ALq_3

In TPD/Alq_3 OLED holes are injected from the ITO anode into TPD and then transported to the TPD/Alq_3 interface. Analogously, electrons are injected from

the Mg:Ag cathode into Alq_3 and then transported to the material interface (Figure 1-11(a)). It is evident from the band diagram in Figure 1-11(b) that the barrier for the hole injection into Alq_3 is lower than that for electron injection into TPD, consequently most excitons form in Alq_3 close to the material interface. Additionally the excitons formed in TPD are higher in energy as compared to those of Alq_3 and can transfer non-radiatively to Alq_3 molecules via a Förster or Dexter mechanism. As a result of these two processes OLED EL is solely due to Alq_3 emission as shown in Figure 1-12 .

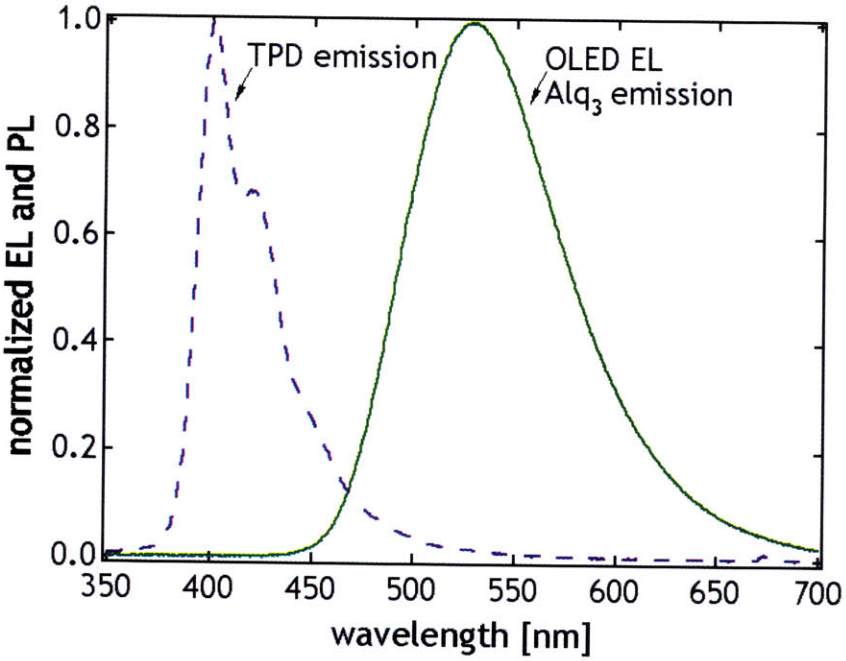

Figure 1-12: OLED EL spectrum resulting from ALq_3 emission is shown together with TPD emission spectrum.

1.6 Hybrid Organic/QD Light Emitting Devices

A hybrid organic/QD LED is essentially an extension of an OLED. The first demonstration of hybrid organic-QD LEDs employed polymer-QD blends as emissive layers embedded between the ITO anode and metallic cathode [51]. These devices, as well as their extensions that employed QD multilayers deposited on top of hole transport-

ing layers between the electrodes [14], were inefficient because of the poor QD-to-QD charge transport due to insulating organic ligands surrounding colloidal QDs. Efficient QD emission in an electrically driven structure was first observed in a device that incorporated a single close-packed colloidal QD monolayer between the TPD hole transporting layer (HTL) and Alq_3 electron transporting layer (ETL) as shown in Figure 1-13 [3]. This device exhibited EQE of 0.5% and EL spectra dominated by narrow QD emission. This QD-LED design takes advantage of efficient carrier transport through the organic semiconductor films and minimizes the QD-to-QD transport contribution.

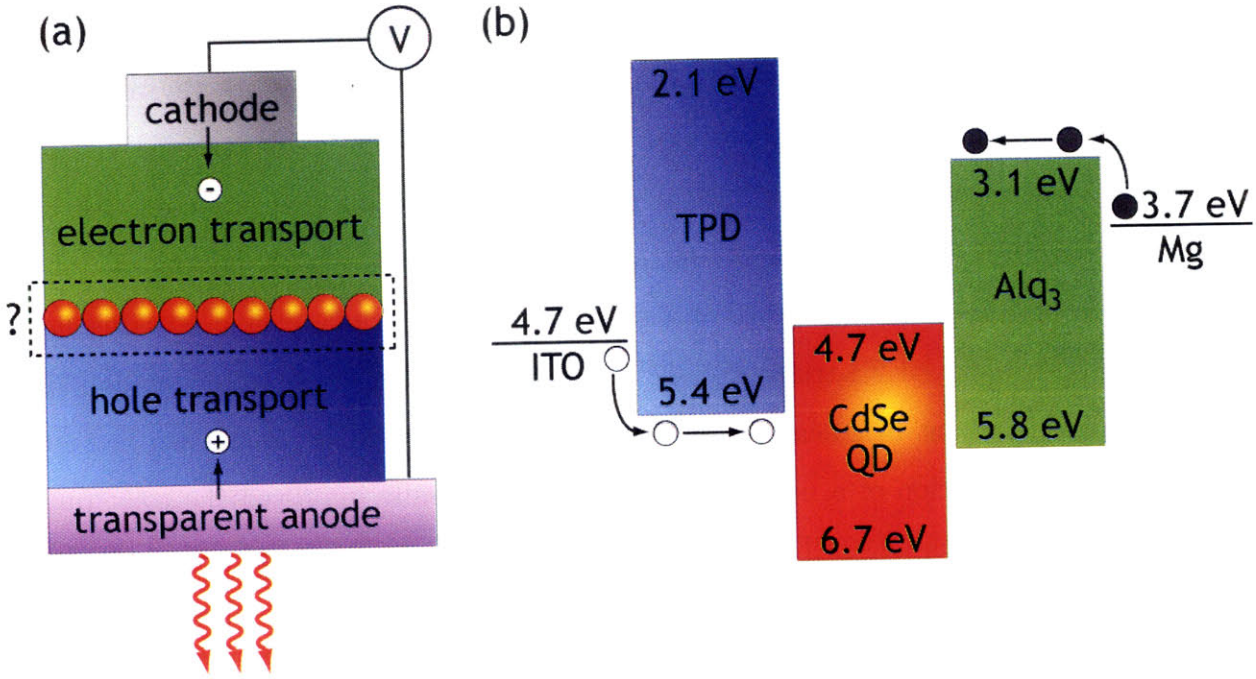

Figure 1-13: (a) Cartoon diagram of an archetypical QD-LED. (b) Band diagram of a QD-LED. QD bands are determined using the model described by Efros et al.

Analogous to the Kodak OLED described above, in this device holes are injected into TPD HTL from the ITO anode and electrons are injected into Alq_3 from the Mg:Ag cathode. Electrons and holes are then transported to the TPD/Alq_3 interface, where QDs are deposited. Several possible processes may take place in the vicinity of the QD monolayer: (1) electrons and holes can be injected into QDs to form excitons, which can recombine radiatively producing narrow QD emission; (2) electrons and holes can meet in TPD and Alq_3 films and form excitons on organic molecules; (3)

excitons formed in TPD and Alq_3 have higher energies (as evident from the band diagram in Figure 1-13) than the band gap of red QDs, so these excitons can transfer to QDs and recombine there.

Because of their narrow EL spectra (manifested in pure saturated colors) QD-LEDs are an attractive alternative for electroluminescent display applications. While the first demonstrations of efficient QD-LEDs used red and yellow emitting ZnS over-coated CdSe core-shell QDs, the display applications demand true red-green-blue color resolution. It became apparent that design of green and blue QD-LEDs presented a significant scientific challenge. While EQE values for red QD-LEDs reached 2% [30, 31], the efficiencies of green QD-LEDs seamed to reach the maximum of 0.5% [52] and EQE of blue QD-LEDs arrived at 0.2% [33] despite the novel synthetic procedures developed to create highly emissive ZnSe/CdSe/ZnS [53, 52] core double-shell green QDs and CdS/ZnS core-shell QDs [33] (as conventional CdSe/ZnS core-shell QDs are less efficient emitters in the range between 400 nm and 550 nm). Moreover, the device structure of a QD-LED had to include a hole blocking layer of 3,4,5-triphenyl-1,2,4-triazole (TAZ) on top of QDs to avoid Alq_3 emission that became dominant in green and blue QD-LEDs with the structure shown in Figure 1-13. The addition of a hole blocking layer dramatically improved the color purity of blue and green QD-LEDs but decreased the efficiency of red and yellow QD-LED to 1% [54, 15]. Some research groups resorted to deposition of multiple QD layers in a QD-LED structure in order to achieve color purity in green and blue QD-LEDs [31, 32]. While these efforts sometimes produced devices of high brightness, they suffered of high operating voltages and, consequently, low power efficiencies as well as poor utilization of valuable QD material.

The development of novel solvent-free QD deposition techniques allowed an increased flexibility in material choices [15, 16, 54]. The use of wider band-gap hole transporting material 4,4-N,N-dicarbazole-byphenyl (CBP) yielded improved efficiency and color purity of blue QD-LEDs. Despite the advances in fabrication techniques and device design, the gap between EQE values of red QD-LEDs and green and blue QD-LEDs persisted in the QD-LED literature. Figure 1-14 shows the EQEs and

spectra of red-green-blue QD-LEDs preceding current work.

Understanding the origins of QD emission is essential to designing QD-LEDs of superior performance. While fabrication methods for QD-LEDs have been extensively studied (as discussed in detail in Chapter 2), the basic mechanisms of QD-LED operation remain poorly understood [54]. For example, it is essential to find the origins of the dramatic differences in performance of QD-LEDs of different colors, since the adoption of this technology for display applications demands similar efficiencies of red, green and blue pixels.

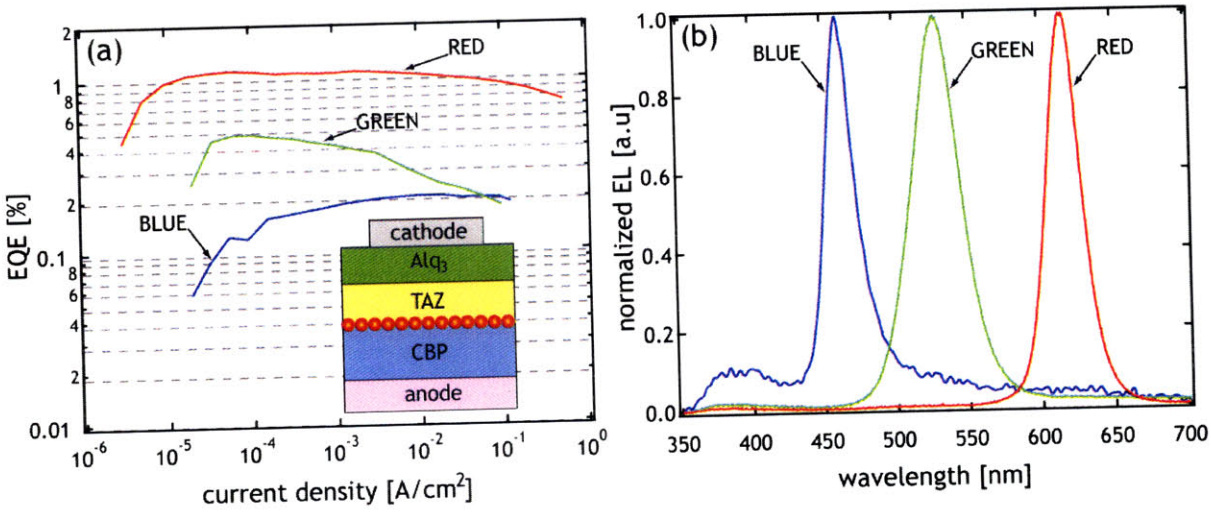

Figure 1-14: (a) EQE curves for the red, green and blue QD-LEDs with the device structure shown in the inset. (b) Normalized EL spectra for red, green and blue QD-LEDs

The narrow QD-LED EL spectra characteristic of QD emission suggest that essentially all of the excitons formed inside the device recombine on QD sites. The location of exciton generation regions in QD-LEDs remains controversial [54]. The two main mechanisms have been proposed to explain narrow QD-LED spectra: (1) excitons are generated on QD sites via direct charge injection from the organic charge transporting layers; (2) excitons are generated in organic films an then non-radiatively transferred to QDs. In this thesis I use electronic and optical measurements in conjunction with morphological analysis to resolve the questions associated with the QD-LED operation mechanism. I also built a numerical modeling tool to further confirm the design guidelines originating from my experimental measurements. The advances in

understanding the operating mechanisms of QD-LEDs allow me to design devices of superior performance.

Chapter 2

Experimental Methods

2.1 Fabrication Techniques

In this section I detail the techniques used in the fabrication of hybrid organic/QD LEDs. As organics and colloidal QDs belong to vastly different classes of materials, naturally they require different deposition methods. Consequently, this section is broken into two subsections: first describing the deposition methods for organic thin films and second describing the deposition of colloidal QDs. In these subsections I address the issues relevant to the deposition of each material type as well as their compatibility with the other QD-LED components.

2.1.1 Deposition of Organic Thin Films

The methods of deposition of small molecule organic materials can be divided into two groups [47]: (1) thermal evaporation and (2) solution processing.

Thermal evaporation, also referred to as physical vapor deposition (PVD), is a traditional method for deposition of high purity and controlled thickness organic films. During evaporation a boat containing an organic material is heated up to the material boiling or sublimation temperature; organic molecules then travel ballistically towards the rotating substrate (substrate rotation insures uniform coverage), which is usually kept at room temperature or below. The material then sublimates on the

substrate forming a thin film. The deposition rate is controlled by the boat temperature. The ballistic transport of organic molecules towards the substrate requires high vacuum of $\sim 10^{-6} - 10^{-7}$ Torr in the evaporation chamber to prevent collisions of organic molecules with the molecules of air. The high vacuum can be achieved in air-tight (usually) stainless steel chambers that are first brought to low vacuum of $\sim 10^{-2} - 10^{-3}$ Torr with a simple scroll or oil pump. The chamber is then further evacuated with a turbo pump. For precise control over film thickness during the deposition process, evaporation systems are usually equipped with source and substrate shutters as well as a thickness monitor mounted next to the substrate holder. The substrate shutter allows us to start deposition when the evaporation rate reaches a desired value, and the source shutter allows to stop the deposition when the organic film reaches a desired thickness as indicated by thickness monitor. This method allows fast deposition of organic and metallic films up to 1000 nm thick with a precision of 0.1 nm. The schematic diagram of a thermal evaporator and a corresponding photograph of the evaporator in the Lab of Organic Optics and Electronics at MIT are shown in Figure 2-1.

While PVD allows us to fabricate thin films with superior thickness control and purity, its requirement for high vacuum results in high fabrication costs. Additionally PVD is wasteful as the material that evaporates from the heated boat travels omnidirectionally in the chamber, consequently, depositing on the walls of the chamber as well as on the substrate. The material emission profile depends on the type of the carrier source, i.e. point source approximation results in a spherical profile, while a finite small source leads to a Lambertian profile. The deposition of large quantities of organic materials on the walls of the chamber can reduce the quality of the vacuum and result in contamination of films deposited in the chamber.

Solution processing methods are widely used in the industrial setting due to their low cost and high throughput. Spin-casting is the most ubiquitous method for depositing thin films for electronic applications. During spin-casting a solution of an organic material is dropped onto the substrate, which is placed onto the rotating stage and held down by low vacuum. When a substrate is spun at speeds of $\sim 500 - 4000$

rpm the solution is pushed to the edges of the substrate, forming a thin uniform film, the solvent usually evaporates after 30 sec (for low boiling point solvents, e.g. chloroform, hexane) to 120 sec (for high boiling point solvents, e.g. water, toluene) of spinning. The schematic diagram describing spin-casting is shown in Figure 2-2. Akin to evaporative deposition, spin-casting is wasteful as most of the solution escapes the substrate during the spinning process.

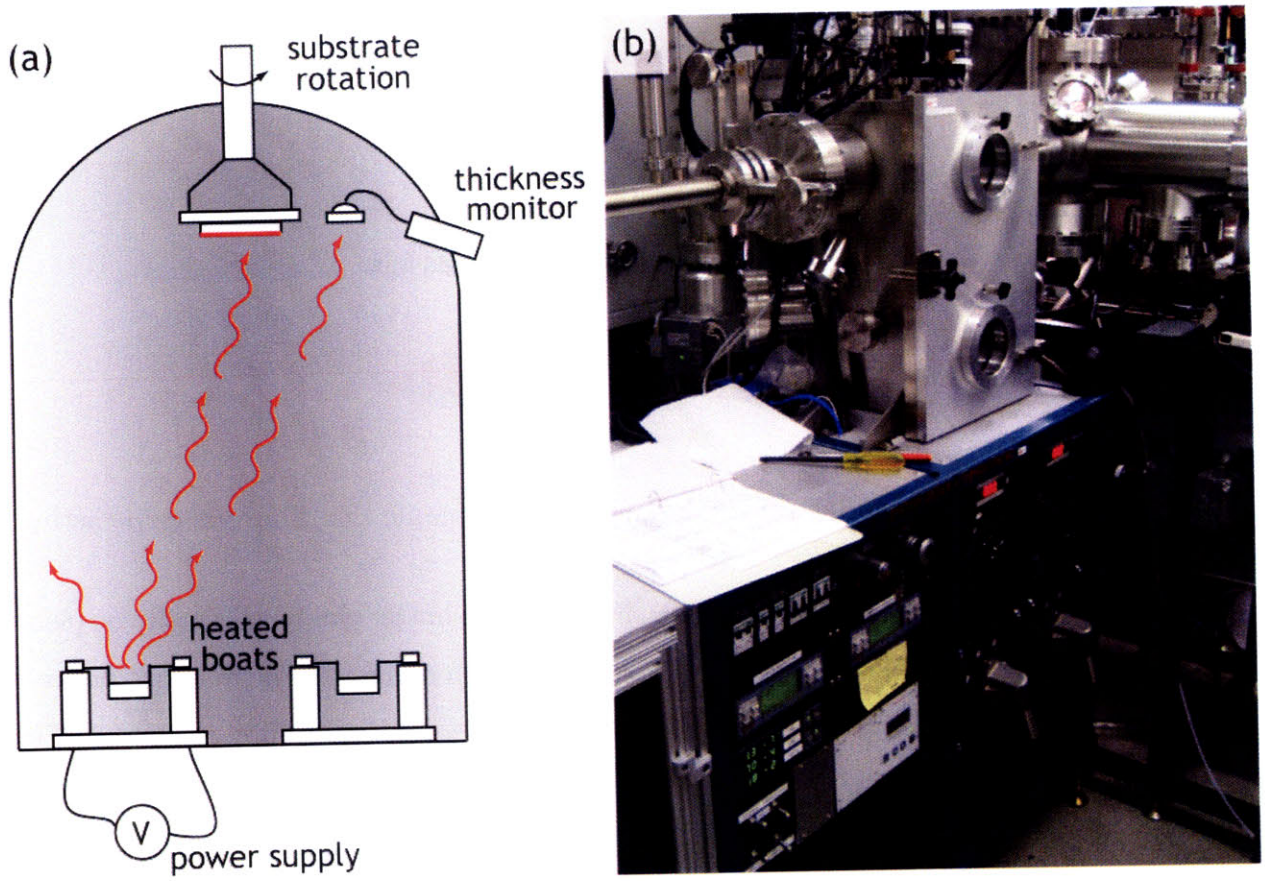

Figure 2-1: (a) Schematic diagram illustrates the basic structure of a thermal evaporator. (b) Photograph (courtesy of Timothy Osedach) of the thermal evaporator in the Lab of Organic Optics and Electronics, which was used for deposition of all thin films of small molecule organics and metals in this thesis.

Another important method of deposition of organic thin films is ink-jet printing. The ink-jet technology has been rapidly advancing over the past decade, pushed by the manufacturers of commercially available desk-top printers. While design details are different for every advanced printhead, the basic principles of operation remain the same. The solution of organic material (the "ink") is loaded into a cartridge

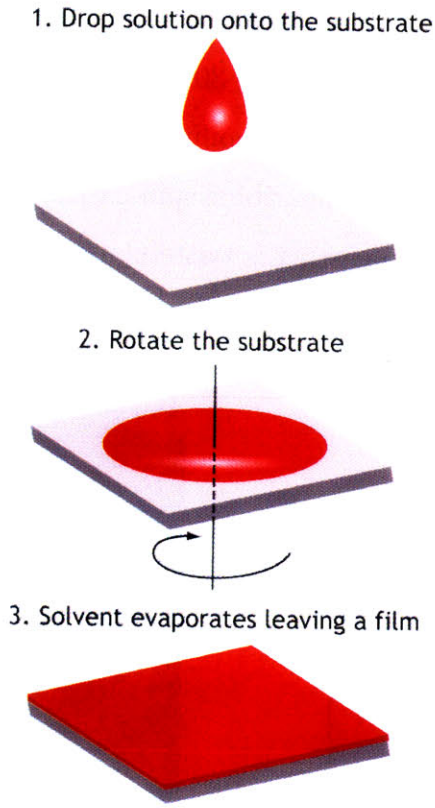

Figure 2-2: Cartoon illustrates the deposition of organic thin films via spin-casting.

which is connected to a nozzle with a shutter. The shutter can be thermally or piezoelectrically driven to release a drop of a material on demand. The distance between the drops can be controlled by a computer, so that a continuous film is formed. This method uses material more efficiently than spin-casting or evaporative deposition, but is highly dependent on the compatibility of the substrate and solvent carrying the organic material. Films deposited by ink-jet are generally significantly less uniform than those deposited by spin-casting or evaporation and often exhibit a "coffee-ring" pattern when material escapes to the edges of the drop upon drying of the solvent.

Recently developed molecular jet (MoJet) printing combines the film quality of evaporative deposition and the high material utilization efficiency of ink-jet printing [55]. In this method, organic material is loaded into a crucible surrounded by a heating coil, and a MEMS shutter mounted on top of the crucible allows the micron-size aperture to be opened and closed by applying a voltage. The flux of organic vapor is then directed through the aperture to form circular pixels upon opening of the

micro-shutter. This method provides the solution for the patterning of organic thin films. Patterning of OLEDs presents a major technological challenge and traditionally is accomplished by shadow-masking, which is a wasteful process and does not yield reproducible micron-size features from one deposition to another.

2.1.2 Deposition of Colloidal QDs

As a consequence of organo-metallic synthesis, colloidal QDs are passivated by organic ligands that provide QD solubility in organic solvents. Consequently, QDs are compatible with solution processing methods, such as spin-casting and ink-jet printing. There are three main challenges associated with QD deposition inside QD-LED structures: (1) material compatibility between QD-carrying organic solvents and fragile organic charge transporting films, easily damaged by solvents; (2) controlled deposition of close-packed QD monolayers, as it has been shown that QD monolayers rather than thick QD films or organic-QD blends result in superior QD-LED performance characteristics; (3) patterning of QD films in QD-LEDs to produce R-G-B pixels desirable for display applications.

The simplest QD deposition method is spin-casting (Figure 2-2) from a solvent compatible with a substrate, i.e. that does not dissolve the underlying organic thin film. It has been previously shown that QDs produce large-scale close-packed monolayers when spin-casted from chloroform, chlorobenzene or their mixtures [30]. These solvents also dissolve the majority of small molecule organic materials used for charge transport in QD-LEDs and OLEDs. Consequently, spin-casting QDs out of these solvents onto the small molecule organic charge transport layers is not appropriate. However, it is possible to use polymer charge transporting layers in QD-LEDs, but such materials are limited and often result in inferior QD-LED performance.

Despite an obvious materials incompatibility, spin-casting can be applied to the deposition of QD monolayers on top of small molecule organic films using the process of phase-segregation [30, 54]. This method takes advantage of chemical incompatibility between aliphatic ligands surrounding QDs and aromatic organic molecules used in QD-LEDs. Some organic materials used in QD-LEDs have similar solubility in

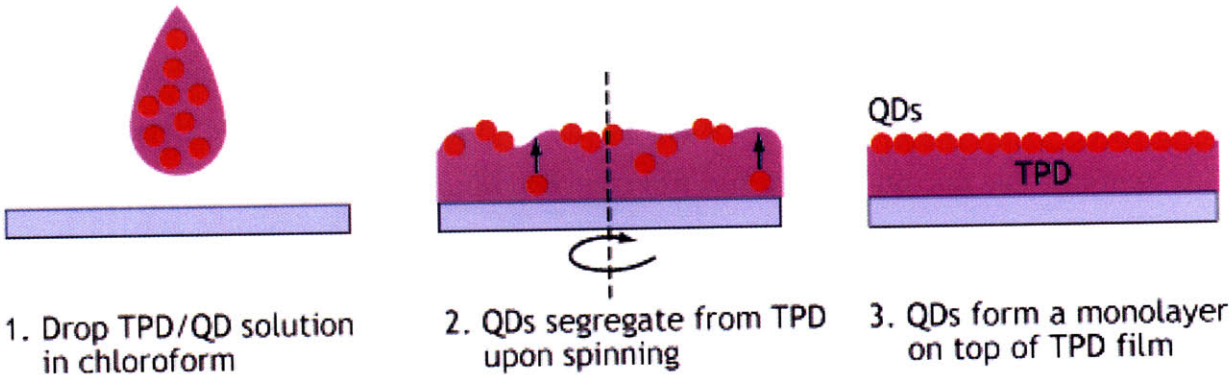

Figure 2-3: Cartoon illustrates the deposition of QD monolayers on top of organic thin films via phase segregation upon spin-casting. Courtesy of Dr. Seth Coe-Sullivan

chloroform and chlorobenzene to that of colloidal QDs surrounded by hydrophobic organic ligands. For example TPD (material used for the hole transport in QD-LEDs and OLEDs) can be mixed with QDs in solution. The resulting heterogeneous solution is then casted onto the substrate. In the processes of spinning the solvent escapes and QDs segregate from the TPD molecules and float to the top of the forming film. As a result QDs form full or partial close-packed layers on top of TPD (Figure 2-3). The relative concentrations of QDs and TPD and spin-speed can be tuned to adjust the TPD film thickness and QD coverage. Atomic force microscopy (AFM) is used to examine QD/TPD film morphology (Figure 2-4).

While the phase-segregation method successfully addresses the first two challenges associated with QD deposition, it cannot be applied to the patterning of QD monolayers. Additionally, it requires high solubility of organic charge transport layers in QD-carrying solvents, which restricts the choice of organic materials compromising the design of efficient QD-LEDs.

In order to address all the issues associated with QD deposition in our group we developed a microcontact printing technique [56, 57], which allows us to deposit patterned close-packed monolayers inside any organic structure solvent free [15, 16, 54].

The QD printing process follows a schematic shown in Figure 2-5: (1) polydimethylsiloxane (PDMS) is molded using a silicon master; (2) resulting PDMS stamp

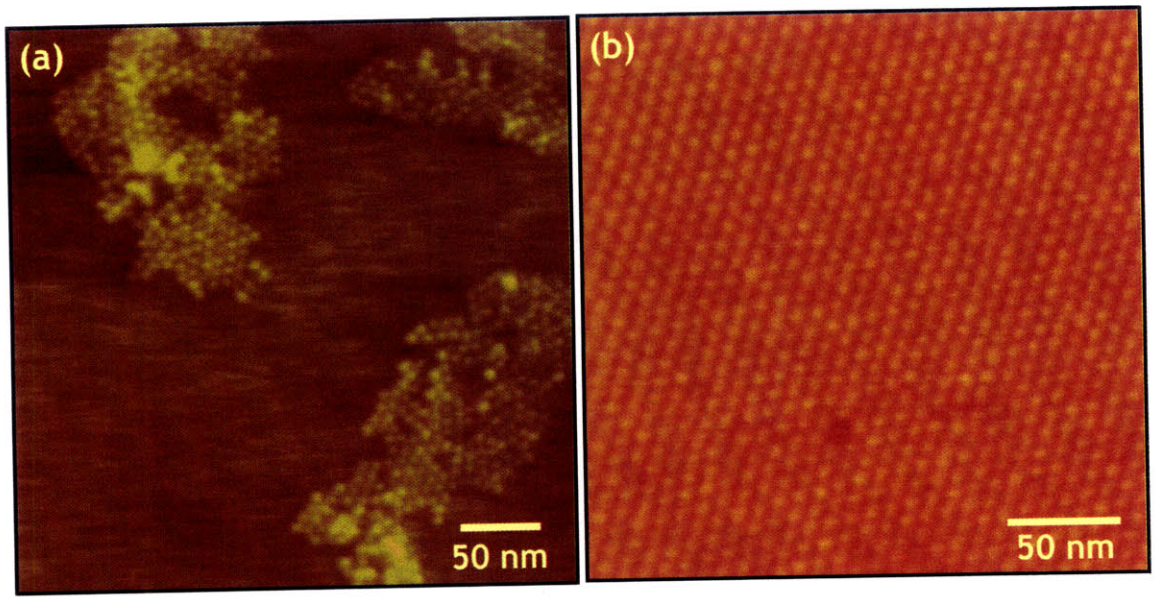

Figure 2-4: AFM images of a partial (a) and a close-packed (b) QD monolayers on top of TPD films formed by phase-segregation. Courtesy of Dr. Seth Coe-Sullivan

is conformally coated with a thin film of parylene-C, a chemical-vapor deposited (CVD) aromatic organic polymer (chemical structure is shown in the inset of Figure 2-6); (3) parylene-C coated stamp is inked via spin-casting of a solution of colloidal QDs suspended in an organic solvent; (4) after the solvent evaporates, the formed QD monolayer is transferred onto the substrate (e.g. on top of the first few layers of a multilayer device) by contact printing.

We prepare PDMS elastomer stamps by mixing PDMS base with a curing agent (Dow Corning Sylgard®184 silicone elastomer) at the ratio of 10:2. The mixture is then poured into a petri dish that may contain silicon masters with relief patterns if patterned films are desired. The dish is then placed under low vacuum at room temperature to eliminate air pockets generated by mixing process. After air pockets have collapsed, the mixture is brought to atmospheric pressure and cured at room temperature for ~7-10 days. The curing process can be accelerated by baking the mixture at 60 °C for ~5 hrs. The cured PDMS block is then released from the petri dish and silicon masters and cut into ~1 cm^3 cubes.

Chemical compatibility between organic solvents used in QD processing and elastomer stamp is crucial for the QD film morphology and, consequently, QD-LED

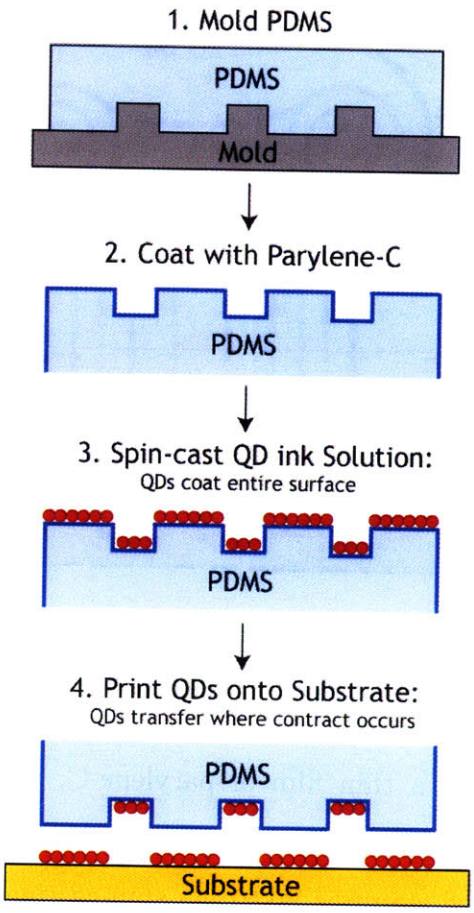

Figure 2-5: Cartoon representation of 4-step microcontact printing technique.

performance. Since QDs form continuous close-packed monolayers upon spin-casting (phase segregation) from chloroform or chlorobenzene solutions, we choose to use chloroform as a primary solvent for QD processing and deposition. We find that the plain PDMS surface is chemically incompatible with chloroform solutions of QDs, which is manifested in non-uniform QD films, due to chloroform dewetting from PDMS during spin-casting. Figure 2-6(a) shows an AFM image of a QD film printed onto a TPD underlayer using a plain PDMS stamp. The film is discontinuous and exhibits morphology characteristic of spinodal dewetting [36]. The peak-to-peak roughness of QD films in this case is >160 nm and RMS is >20 nm, which makes these films impractical for device fabrication as the characteristic organic charge transporting layer thickness is ~50 nm. Consequently, rough QD layers yield electrically shorted devices.

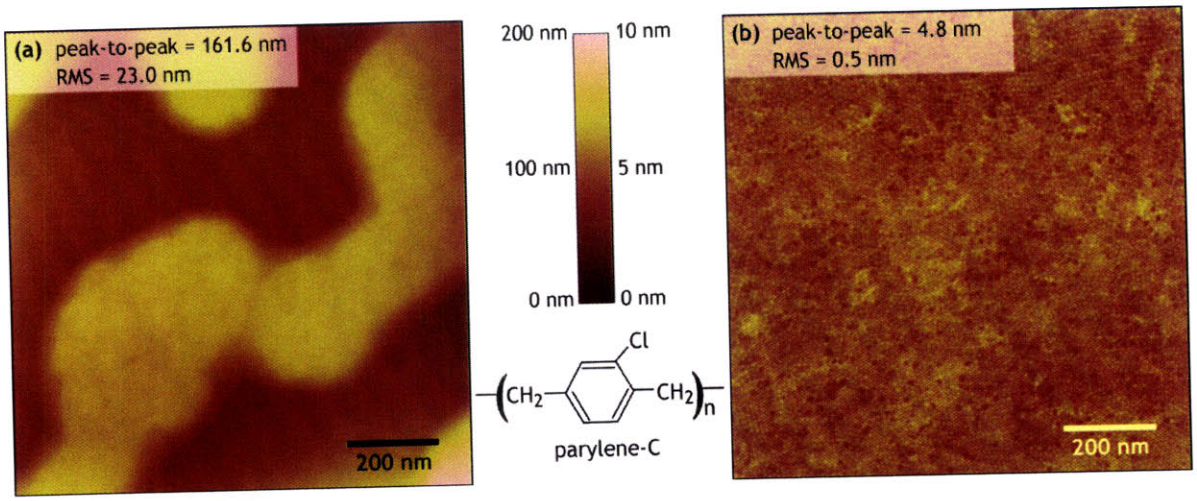

Figure 2-6: AFM images show QD films deposited on top of TPD layer using (a) a plain PDMS stamp and (b) a parylene-C-coated PDMS stamp. QD films on plain PDMS exhibit a spinoidal decomposition pattern with high surface roughness (RMS=23.0 nm), while on parylene-overcoated PDMS QDs form smooth hexagonally close-packed monolayers (RMS=0.5 nm). The chemical formula of parylene-C is shown in the inset.

Coating the stamp with parylene-C results in a chemical surface, which is compatible with the spreading of colloidal QDs solvated in chloroform. The contact angle measurements show that chloroform wets the parylene-C surface more efficiently than it does with plain PDMS, which is indicated by a decrease in contact angle from $28°\pm1°$ to $6°\pm1°$. Parylene-C also acts as a release layer for QDs during the printing process. Organic ligands surrounding colloidal QDs are generally aliphatic (e.g., trioctylphosphine, oleic acid etc.) while most of the organic charge transporting materials are conjugated aromatic compounds. Being an aromatic polymer parylene-C provides a sub-optimal surface for aliphatic-passivated QDs and facilitates their release from the stamp. Using an aliphatic surfactant may result in stronger interaction between QDs and a stamp surface than between QDs and an aromatic organic film on the substrate and, hence, may impede the QD release. The AFM image in Figure 2-6(b) shows a close-packed monolayer of QDs printed onto a TPD film using a parylene-C overcoated PDMS stamp. Peak-to-peak roughness of $\sim$5 nm indicates a controlled deposition of a single QD layer, and low RMS$\approx$0.5 nm allows these films to be used in thin (<100 nm) hybrid opto-electronic devices.

Figure 2-7 demonstrates patterning of close-packed monochrome and multicolor

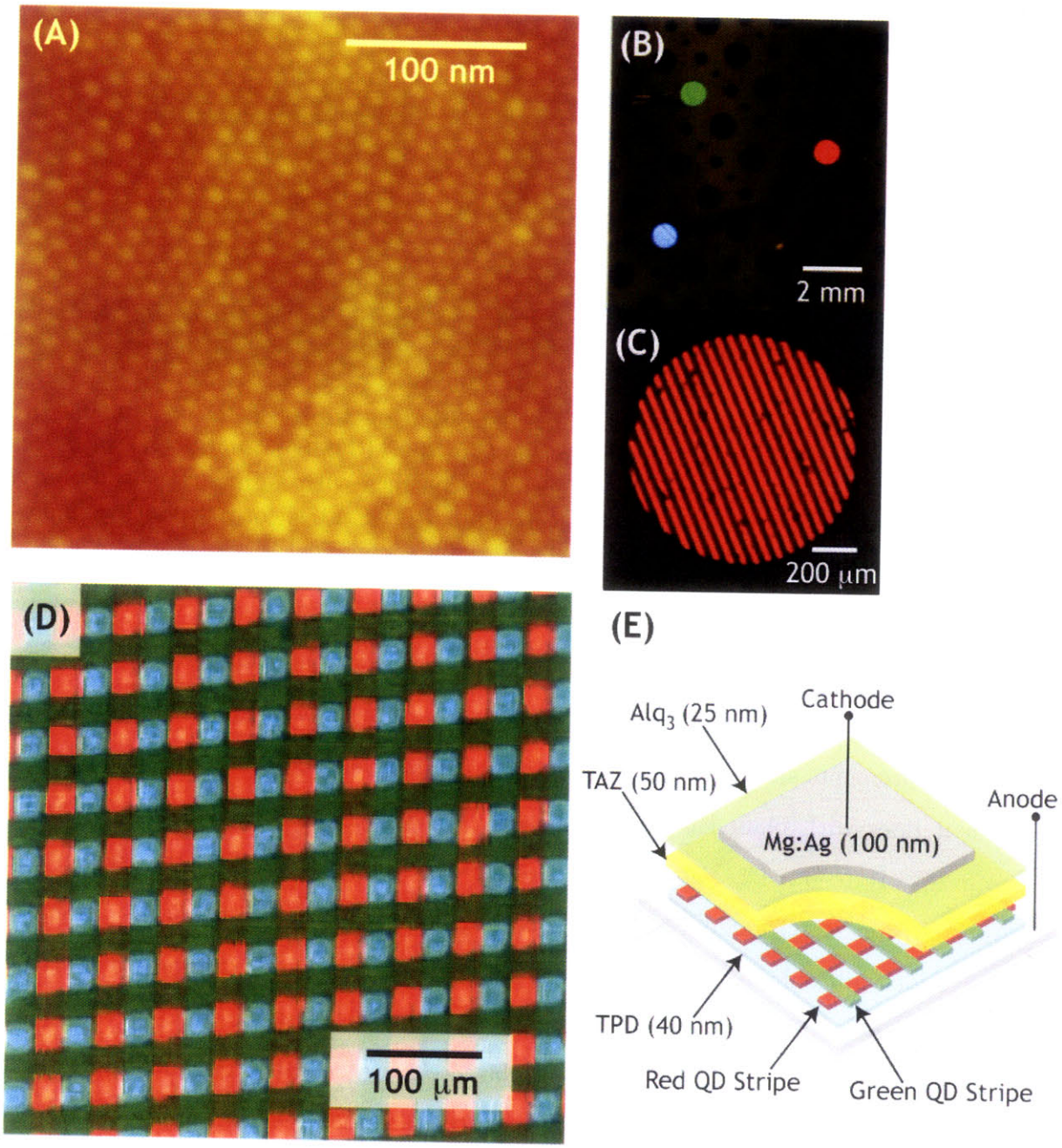

Figure 2-7: (a) A high resolution AFM micrograph shows a close-packed monolayer of QDs deposited on top of a CBP hole transporting layer prior to deposition of hole blocking and electron transporting layers. (b) Electroluminescent red and green QD-LED pixels are fabricated on the same substrate. Blue pixel is the result of TPD emission in the area where QDs were not deposited. (c) An electroluminescent QD-LED pixel is patterned with 25 μm lines. (d) Electroluminescence from 25 μm green and red QD monolayer lines deposited inside the structure shown in (e). Blue emission is due to the TPD hole transporting underlayer.

QD-LED pixels with a resolution as small as 25 μm (1000 dpi). Here, the QD-LED structure consists of a transparent Indium Tin oxide (ITO) anode coated with a hole injecting polymer poly(3, 4-ethylenedioxythiophene):poly(styrenesulfonate) PEDOT:PSS, followed by a 40 nm thick TPD hole transporting layer (HTL), a printed QD monolayer, a 15 nm thick 3,4,5-triphenyl-1,2,4-triazole (TAZ) hole blocking layer, a 25 nm thick Alq_3 electron transporting layer (ETL), and a 100 nm thick Mg:Ag cathode with a 20 nm thick Ag protective overlayer. In Figure 2-7(b) red, green and blue pixels are fabricated on the same substrate. Red (CdSe/ZnS core-shell [29]) and green (ZnSe/CdSe/ZnS core-double-shell [52]) QDs are separately printed onto a blanket TPD film and the structure is completed by a blanket deposition of the remaining charge transport layers. The red and green pixels exhibit electroluminescence (EL) solely due to QD emission, while the blue pixel is the result of TPD EL in the absence of QDs. For the multicolor pixels the 25 μm wide intersecting stripes of red and green QD monolayers are printed over each other in a QD-LED structure shown in Figure 2-7 (d), (e). EL of red and green QDs and blue TPD is simultaneously observed when the QD-LED is biased at 5V.

The contact printing method, described in this section, presents a critical step towards the realization of pixelated, full color, high resolution QD-LED displays.

2.2 Surface Analysis Tools

Often analyzing the surface of a hybrid structure can lead to understanding of the interactions between various components of the structure. For example, one can obtain information about the interface strains in a binary system from analyzing a spinodal decomposition characteristic wavelength [36]. Wetting or de-wetting of one component of the system by the other yields information about their chemical or structural compatibility. In the previous section, surface analysis has been shown to be a critical step in the development of a powerful deposition method, providing information about chemical compatibility between chloroform and PDMS.

A variety of techniques such as atomic force microscopy (AFM), transmission

electron microscopy (TEM), and scanning electron microscopy (SEM) have been developed to allow visualization of surfaces on the nanoscale. In this section we will discuss the applicability of these methods to various aspects of the morphological analysis during the QD-LED fabrication and testing.

2.2.1 Atomic Force Microscopy

During atomic force microscopy (AFM) measurements, the substrate surface is scanned with a mechanical cantilever, which is usually made of silicon or silicon nitride. The cantilever tip has a radius of curvature of ~10 nm. Depending on the cantilever design and AFM operation mode, one can use this form of microscopy to probe mechanical contact, van-der-Waals, capillary, chemical bonding, electrostatic or magnetic forces [58]. In contact mode (or static mode) AFM, the cantilever and the sample surface interact, causing deflection of the cantilever, which is measured with a laser beam that is focused onto a cantilever tip and then reflected into the detector. Close to the substrate surface, where interactions between the surface and the cantilever become very strong, this mode is prone to noise and drift, and often low stiffness cantilevers must be used in order to boost the deflection. In the dynamic (or tapping) mode AFM, the cantilever oscillates at a frequency close to its resonant frequency. The surface-cantilever interaction causes amplitude and frequency changes in cantilever oscillation, which are detected in a similar fashion as in the contact mode. In the tapping mode, the cantilever tip can be brought sufficiently close to the surface for interaction forces to be detected, but sticking of the cantilever tip to the surface is avoided [58]. Figure 2-8 shows the Veeco Dimension 3000 atomic force microscope used in tapping mode to obtain all the AFM images presented in this thesis.

AFM is an attractive surface analysis tool due to the simplicity of its use and no special requirements on sample preparation. The latter is particularly important in fabrication of active opto-electronic devices. The morphology of every layer in a multi-layer QD-LED structure is crucial for the device performance; hence the surface has to be analyzed at every step of QD-LED fabrication. This requires a tool that can be operated on real substrates used during the QD-LED fabrication. Since conventional

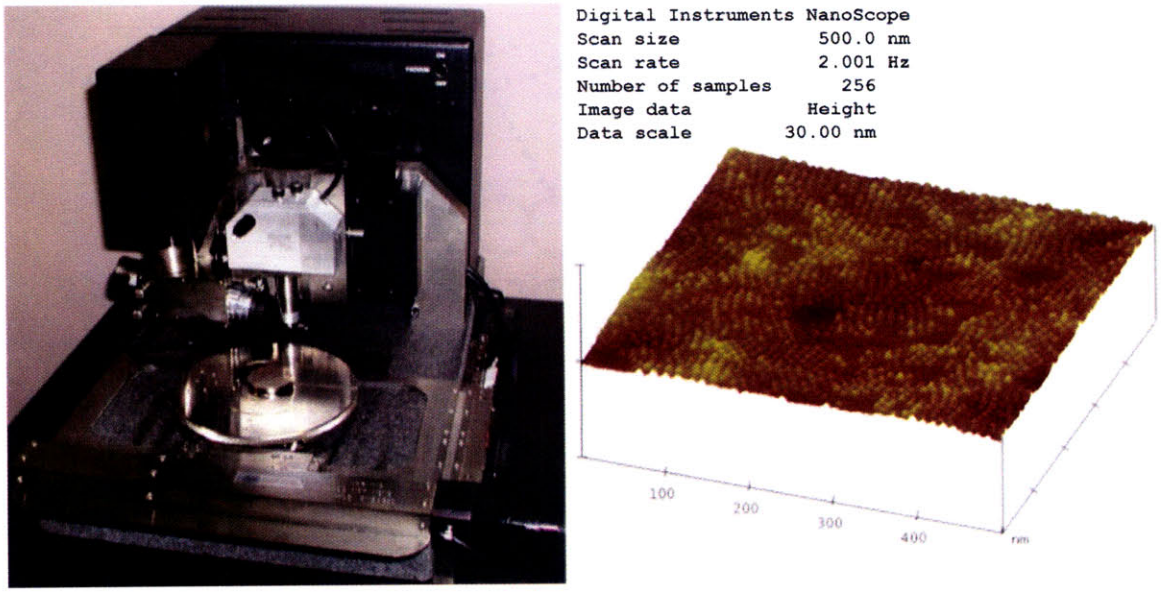

Figure 2-8: A photograph of the atomic force microscope Veeco Dimension 3000 and a surface plot of the colloidal QDs on top of a thin organic film on a glass substrate.

AFM solely relies on mechanical forces between the surface and the tip, it is possible to image the landscape of essentially any planar substrate. Consequently, we can use AFM to image each layer during the QD-LED fabrication process.

The tapping mode AFM height (vertical) resolution is limited by the error in detection of the amplitude and frequency of the tip oscillation when the forces between the tip and the substrate become strong and is usually ~1 nm. The lateral resolution of AFM is limited by the tip diameter and the aspect ratio, i.e. the ratio of tip length to tip diameter. The average lateral resolution of conventional silicon tips that were primarily used in this study is ~10 nm. In this work, though, we were interested in imaging not only organic thin films but also QD films with a lateral resolution of individual QDs. The sizes of QDs employed in QD-LEDs vary between 4-12 nm. Consequently, here we attempt to use AFM in a regime beyond its lateral resolution. This can be achieved when imaging relatively smooth surfaces such as QD monolayers. In this case only the top most point of the tip is used for scanning, which pushes the lateral resolution beyond the tip diameter (Figure 2-9 (a)). In contrast, when imaging rough surfaces the entire tip may be approaching the surface and consequently resolution is limited by the tip size (Figure 2-9 (b)).

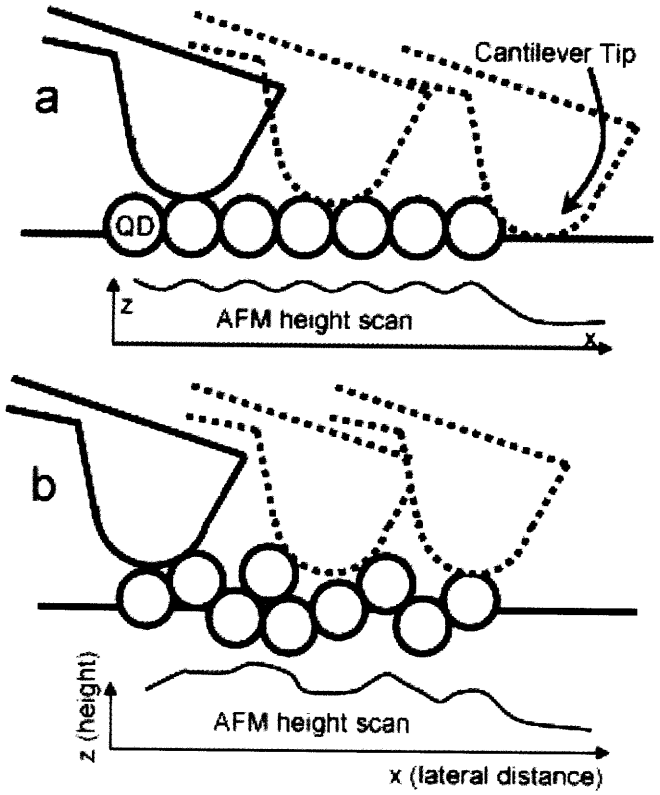

Figure 2-9: Cartoon shows the resolution of AFM when imaging (a) close-packed QD monolayers and (b) rough QD films. Courtesy of Dr. Seth Coe-Sullivan.

While conventional AFM probes mechanical forces and provides information about the surface landscape, electrostatic force microscopy (EFM) or magnetic force microscopy (MFM) use conductive (or magnetic) cantilevers that can be electrically biased with respect to the surface of interest to study charged (or magnetic) surfaces and the interaction between components of the system in their non-equilibrium state.

2.2.2 Electron Microscopy

Operation of a transmission electron microscope (TEM) is analogous to conventional (fluorescent) microscopy, but instead of a beam of light, a focused electron beam is transmitted through the specimen, causing an enlarged image to appear on a fluorescent screen [59]. Due to the extremely short wavelength of electrons ~2-15 pm, this technique provides resolution on the sub-angstrom scale. However, this short electron wavelength demands a total sample thickness < 1 μm, and consequently, samples

have to be prepared on special TEM grids. Additionally, samples have to withstand the vacuum inside the TEM chamber. TEM has proven to be an extremely powerful characterization tool for nanoparticles and their blends, providing detailed information on shape, size and even crystal structure structure. However, restrictions on the specimen design make TEM less attractive for characterization of hybrid structures. Particularly, optoelectronic devices cannot always be prepared on special TEM grids. In addition, TEM cannot be used for the imaging of organic thin films and molecules due to their high transmissivity resulting in poor image contrast.

In scanning electron microscopy (SEM) measurements, a beam of accelerated electrons is focused to a fine spot approximately ~1-5 nm in diameter, which is then rastered across the sample [59]. When the electron beam strikes a sample, the incoming electrons get scattered over the teardrop shape volume known as an interaction volume extending from <100 nm to 5 μm into the substrate surface. An interaction of scattered primary electrons with the substrate causes emission of secondary electrons that are then detected to produce an image. Resolution of an SEM is limited by the initial size of the electron beam (depending on the magnetic electro-optical system, it varies between <1 nm to 20 nm) and thus is about an order of magnitude lower than that of a TEM, but since the SEM technique relies on surface interactions rather than on transmission, it allows imaging of the bulk of the sample and provides detailed information about 3D structure. Akin to TEM, SEM requires samples to be placed under high vacuum to avoid the electron beam scattering by the molecules of air. Using SEM on insulating samples poses additional challenges as these samples are prone to charging when exposed to the scanning electron beam, which yields poor image contrast and consequently complicates the focusing process. Imaging of QDs and organic thin films requires speed and precision in the electron beam focusing, in order to be able to take high resolution images prior to charging the sample.

While AFM provides a powerful tool for imaging of smooth QD monolayers on top organic thin films, its resolution is insufficient for imaging rougher QD multilayers or material interfaces within QD-LEDs. In contrast, SEM can provide information about the number of QD layers within a film or be used for the imaging of QD-LED

cross-sections (Figure 2-10).

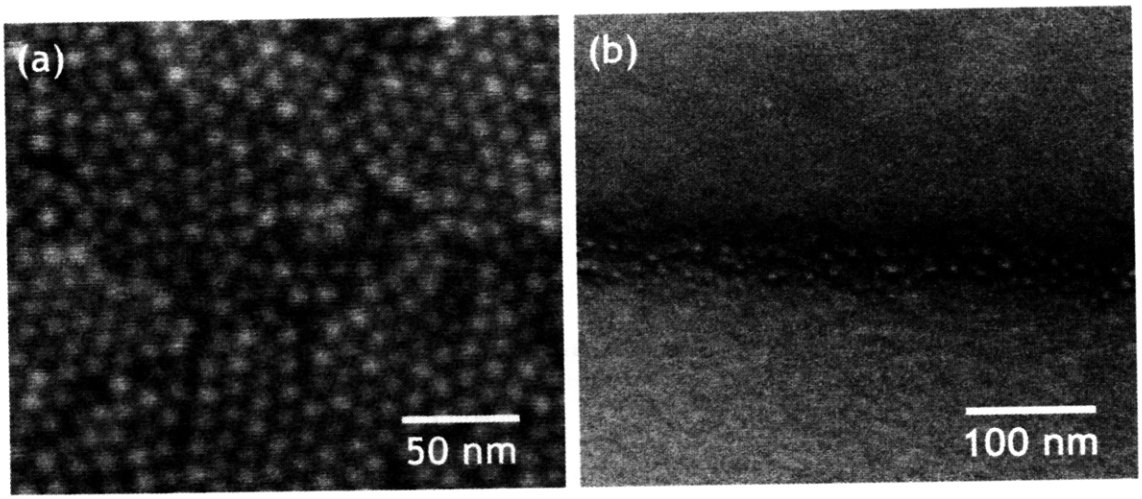

Figure 2-10: SEM images show (a) a multilayer of colloidal QDs on a silicon substrate and (b) a cross-section of a hybrid metal-oxide/QD LED, that distinguishes the QDs

2.3 Optical Spectroscopy

2.3.1 Absorption and Transmission Measurements

Optical absorption and transmission are important characteristics of the material since they provide information about molecular or crystal structure. In these measurements, light from a source (typically a tungsten or mercury lamp) passes through a monochromator producing a set of wavelengths that are used to excite the sample. The amount of light transmitted through the sample at each wavelength is then detected with a CCD array or a grating to produce a transmission spectrum. The transmission spectrum can be then converted into absorbance by Beers law:

$$A = -\log_{10} T = -\log_{10} \frac{I_1}{I_0} \tag{2.1}$$

where, A is absorbance, T is transmission, I_0 is the intensity of the incident light and I_1 is the intensity of the transmitted light.

For semiconductors, optical absorption provides a direct measurement of the elec-

tronic bandgap, i.e. the material begins to absorb when the energy of the optical excitation is sufficient for an electron to get excited onto the next available energy level. In molecules where a complex superposition of atomic orbitals determines the electronic structure of the molecular orbitals, optical absorption can give information about the different types of bonds involved and even their geometrical orientation with respect to each other [46]. Often for a hybrid system the interactions between different system components can lead to mixed energy states that are not present for any of the components separately. For example transition metals (such as Cd) promote spin-orbit coupling in organic materials leading to the mixing of spin-singlet and spin-triplet states [60]. As a result normally forbidden excitation into a triplet state becomes allowed in a presence of a transition metal, which changes the absorption spectrum.

In addition to the energy associated with optical transitions, absorption measurements can be used to measure the probability of these transitions manifested in the value of a transition dipole strength or an absorption cross-section σ. Using the Lambert-Beer law, one can find the value of absorption cross-section by measuring the absorbance (or transmission) in a system with known geometrical parameters:

$$A = \sigma l N \tag{2.2}$$

where σ is the absorption cross section, l the absorption path length (thickness of the sample), and N is the number density of absorbers ($1/\text{cm}^3$).

2.3.2 Steady State and Time-Resolved Photoluminescence Spectroscopy

In photoluminescence (PL) spectroscopy, a sample is generally excited with a single wavelength within the absorption range of a material, which leads to the promotion of an electron to higher energy levels from where it then relaxes back to the ground state with a simultaneous emission of the photon [61] (see Figure 1-8). The PL spectrum of a material rarely replicates its absorption spectrum, since a part of the

absorbed energy is usually lost for example due to interactions between the excited electron and phonons, or bond vibrations and rotations in molecules [46, 60]. Room temperature measurements generally do not allow for the resolution of PL peaks that correspond to interactions of excited electrons with different fields, since thermal energy is comparable to the energy of the corresponding interactions. One can extract information about the fine structure of a PL spectrum at low temperatures, where thermal mixing is not significant.

Time-resolved PL measurements not only provide information of PL spectral shape, but also allow the determination of an average lifetime of an excited state within a given material [61]. In these measurements, a sample is excited by a short laser pulse and the resulting PL is detected for every time increment. Modern instruments such as streak cameras allow simultaneous capture of the PL in both temporal and photonic domains.

After the initial excitation the population of electron-hole pairs starts to deplete due to radiative and non-radiative processes, which is detected as the PL decay with time:

$$\tau = \frac{1}{k_r + k_{nr}} \tag{2.3}$$

where k_r and k_{nr} are radiative and non-radiative decay rates, respectively. The PL lifetime is determined by the processes contributing to the depletion of the electron-hole pairs for a given material and may drastically change due to interaction with a different material. For example, in the case where one material acts as a donor of an excited electron-hole pair to a neighboring acceptor material, the PL lifetime of the first material decreases due to the presence of an additional mechanism for electron-hole pair depletion in the system [46].

Time-resolved PL measurements are an essential part of this thesis, due to their applicability to measuring exciton energy transfer between the different components of a hybrid organic-QD system. Figure 2-11 shows the schematic diagram of a time-resolved optical set-up used in Chapter 4. In this set-up a titanium sapphire

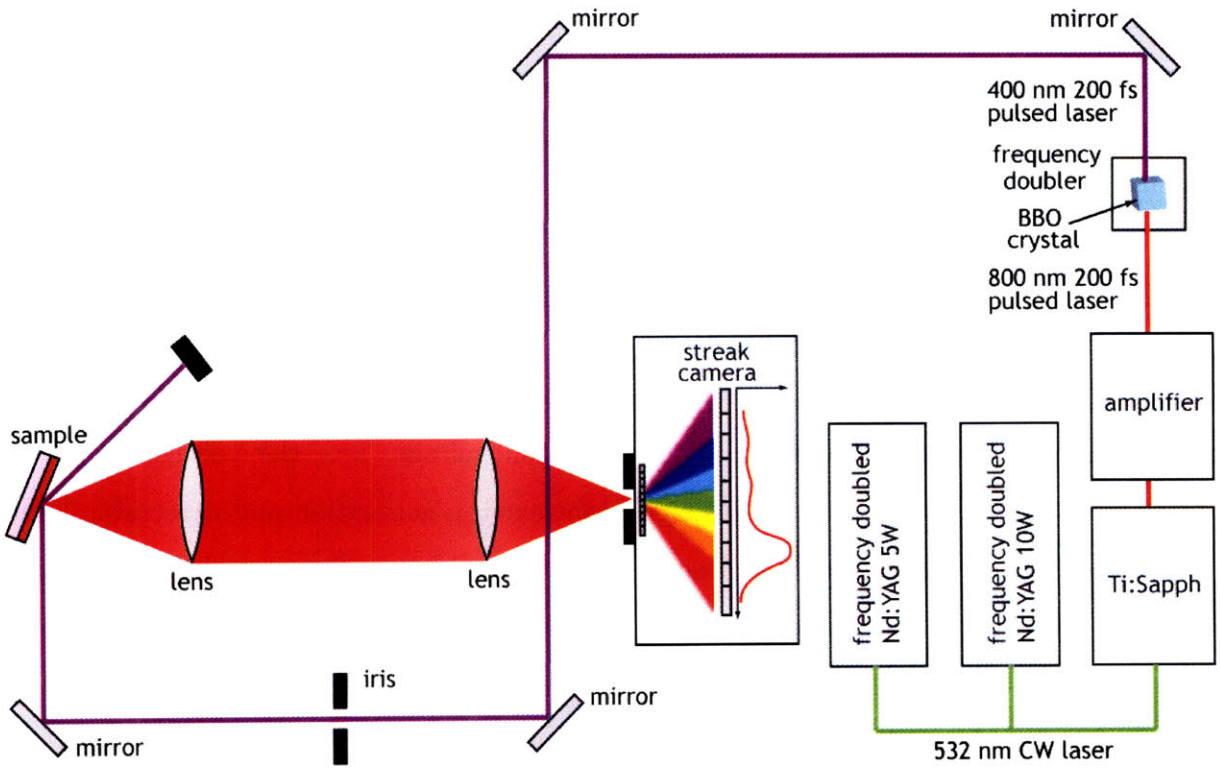

Figure 2-11: A schematic diagram shows a time resolved PL set-up used for the energy transfer measurements in Chapter 4.

(Ti:Sapph) pulsed laser (Mira Optima 900, Coherent Inc.) is pumped by two frequency doubled neodymium yttrium aluminum garnet (Nd:YAG) continuos wave (CW) lasers with intensities of 5 and 10 W (Verdi V5 and Verdi V10, Coherent Inc.). The pulsed laser light with wavelength of ~800 nm is then amplified (RegA 9000, Coherent Inc.) and frequency doubled with a β-barium borate (BBO) crystal to produce ~400 nm light; this beam is then used to excite our samples. PL is collected with two collecting lenses into a Hamamatsu C4780 picosecond fluorescence lifetime system consisting of a C5094 spectrograph and a C4334 streak camera triggered onto the laser repetition rate. Our system allows us to tune the output of the Ti:Sapph laser between 700-900 nm (consequently, the frequency doubled beam has a wavelength between 350-450 nm); average pulse width of the Ti:Sapph is ~ 200 fs and repetition rate (i.e. number of pulses per second) can be tuned between 10-250 kHz. The repetition rate is chosen depending on the PL relaxation time of the materials used in a particular sample. For example, for materials with short relaxation times

< 100 ns, high repetition rates can be used, while materials with long PL relaxation times ~ 1 μs require slow repetition rates in order to prevent the overlap of PL signal initiated by the previous laser pulse with the signal initiated by current laser pulse.

2.4 Electronic Measurements

In this section I discuss the core measurements of QD-LED testing. The important characteristics of a QD-LED are: (1) Turn-on voltage, i.e. the voltage at which current through the device yields significant exciton generation and detectable light output (this voltage is usually close or coincides with the voltage at which the device switches from ohmic to space-charge limited conduction). (2) External quantum efficiency (EQE), i.e. the number of photons emitted per injected electron. (3) Power efficiency, i.e. amount of light (measured in lumens) output per Watt of input power. (4) Electroluminescence (EL) spectrum, i.e. wavelength (photon energy) dependent light output of an LED resulting from electrical excitation (applied bias voltage).

While it is convenient to describe various regimes of QD-LED operation in terms of applied bias voltage, it is crucial to understand that these devices are driven by current rather then voltage. Since intrinsic carrier densities in organic materials are negligible comparing to those of inorganic semiconductors, EL is produced by radiative recombination of excitons generated from injected carriers.

2.4.1 Current-Voltage Characteristics and External Quantum Efficiency

Current-voltage (IV) characteristics are an essential part of QD-LED characterization as they provide information about the turn-on voltage, as well as device resistance and different conduction mechanisms that dominate the device operation at different applied bias voltages. To obtain an IV characteristic of a device, one should simply sweep the applied voltage between the values of interest and measure the current passing through the device at every value of applied voltage. The conventional way

to display an IV characteristic is on the log-log scale (i.e. $\log I$ is displayed vs. $\log V$), since such plot visualizes a power law dependence between current and voltage.

$$I \sim V^n \Rightarrow \log I \sim n \log V \tag{2.4}$$

where n is characteristic of a particular type of conduction. For example, $n = 1$ indicates ohmic conduction and $n = 2$ is characteristic of space-charge (trap limited) conduction in organic materials [62]. On a IV characteristic plotted on a log-log scale n is simply the slope of a curve; consequently, a change in slope indicates a change in conduction mechanism.

External quantum efficiency (EQE) is a precise measure of how efficiently a particular QD-LED converts carriers into photons. EQE is usually measured in conjunction with an IV characteristic. At every value of applied bias voltage, one can measure current and light output of the device. Light output is usually measured with a calibrated photodetector as a photocurrent reading I_{photo}, which is then converted into power P in Watts using a detectivity constant R_{photo} for a particular detector at a wavelength of LED emission.

$$P = \frac{I_{photo}}{R_{photo}} \tag{2.5}$$

Then knowing the photon energy ($E_{phot} = 2\hbar\pi c/\lambda$) one can calculate the number of photons per second:

$$N_{phot} = \frac{P}{E_{phot}} \tag{2.6}$$

Finally EQE is the ratio of the number of photons per second (N_{phot}) to the number of electrons per second (current normalized by the charge of single electron):

$$EQE = \frac{N_{phot}}{(I/1.6 \times 10^{-19})} \times 100\% \tag{2.7}$$

While power efficiency is an important characteristic for industrial applications of LEDs, it is dependent on visual perception, and consequently on the sensitivity of a

human eye to a particular wavelength, hence QD-LEDs with the same EQE emitting at different wavelength may have drastically different values of power efficiency values. Figure 2-12 shows the standard luminosity function used in calculations of light output or device luminance and luminous flux.

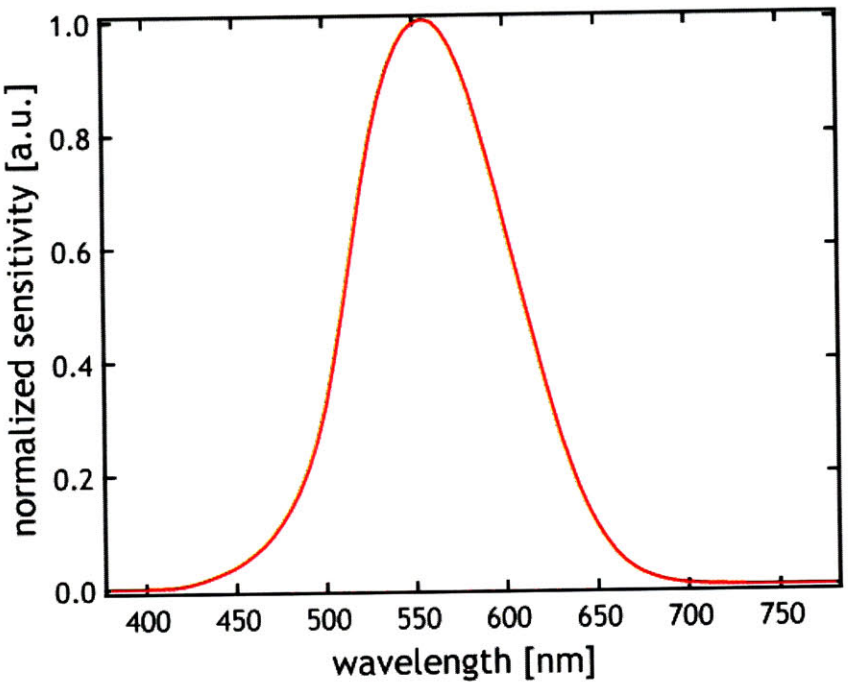

Figure 2-12: Standard luminosity function $\bar{y}(\lambda)$.

The luminance is measured in $\mathrm{Cd/m^2}$ and is a measure of a luminous flux perceived by the eye looking at a surface from a particular angle. Luminance L_v scales as an overlap of a normalized LED EL spectrum (notice that normalization has to be performed with respect to the area under the spectrum rather than to the EL peak as it is simply a measure of a total number of emitted photons) and a standard luminosity function and is calculated using a following equation:

$$L_v = \frac{683}{2\pi} \times \frac{EQE}{100} I \int_{380}^{780} I(\lambda)\bar{y}(\lambda)E_{phot}(\lambda)d\lambda \tag{2.8}$$

here, $I(\lambda)$ is the EL spectrum of an LED (or the so called spectral power distribution), $\bar{y}(\lambda)$ is the standard luminosity function, E_{phot} is the photon energy corresponding to the wavelength λ, I is the current through the device.

The power efficiency (or luminous efficacy) in lumens/Watt (lm/W) F_w is then

determined as following:

$$F_w = \frac{L_v 2\pi}{IV} \tag{2.9}$$

here $L_v 2\pi$ is the luminous flux, and $IV = W$ is the power input into the device. Consequently, high operating voltages are undesirable for industrial applications as they increase device power consumption. While the EQEs of resistive LEDs operating at high voltages can be as high as those of less resistive devices, their power efficiency is significantly lower.

All the metrics discussed above set the criteria on LED performance. An ideal light source should have high EQE and operate at low voltages in order to meet industry standards.

For the QD-LED testing in this thesis we use a HP 2154 parameter analyzer as a voltage source and a current measuring unit as well as for light output measurements in combination with Newport calibrated photodiode. Alternatively we used Keithley 2600 electrometer for IV characteristics and Newport 1835C powermeter with a photodetector for light output measurements.

2.4.2 Electroluminescence Spectra

Electroluminescence (EL) spectra provide information about the exciton formation and recombination regions in the device. By examining EL spectra and comparing them with spectral signatures of the materials constituting the layers of a hybrid structure we can find which materials contribute the most to the LED emission. Consequently, EL measurements provide an extremely important device design tool.

Analogous to PL measurements, emission is collected into a spectrometer but the excitation of the emission in this case is electrical rather than optical. During the EL measurements a voltage source is connected to a QD-LED which results in current passing through the device and, hence, exciton formation and recombination.

It is apparent from the previous section that the overlap of a LED EL spectrum with the standard luminosity function largely determines the perceived luminous ef-

ficacy or power efficiency. The position and shape of an EL spectrum also determine the color purity of a LED emission. According to the International 1931 Convention on Illumination (Commission Internationale de l'Eclairage (CIE)) all the colors can be plotted on the CIE color space defined by the CIE standard observer color matching functions (Figure 2-13). Using the color matching functions shown in Figure 2-13, it is possible to calculate the color coordinates (X, Y, Z) of any light source:

$$X = \int I(\lambda)\bar{x}(\lambda)d\lambda \tag{2.10}$$

$$Y = \int I(\lambda)\bar{y}(\lambda)d\lambda \tag{2.11}$$

$$Z = \int I(\lambda)\bar{z}(\lambda)d\lambda \tag{2.12}$$

here $I(\lambda)$ is a spectral power distribution (i.e. EL spectrum). While the color space is three-dimentional, in order to facilitate the visualization, it is possible to display the color coordinates on a two-dimentional CIE diagram (Figure 2-14).

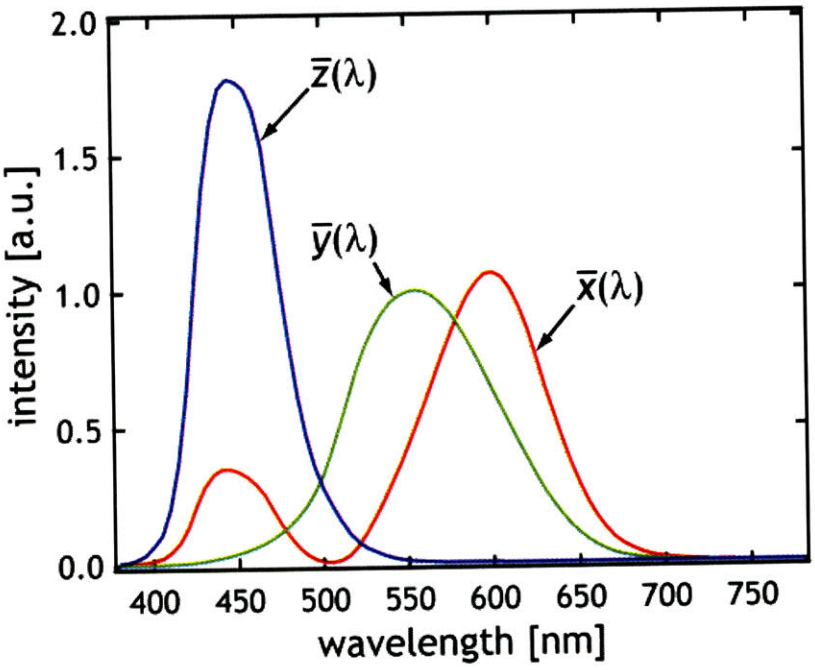

Figure 2-13: The CIE standard observer matching functions $\bar{x}(\lambda)$, $\bar{y}(\lambda)$ and $\bar{z}(\lambda)$.

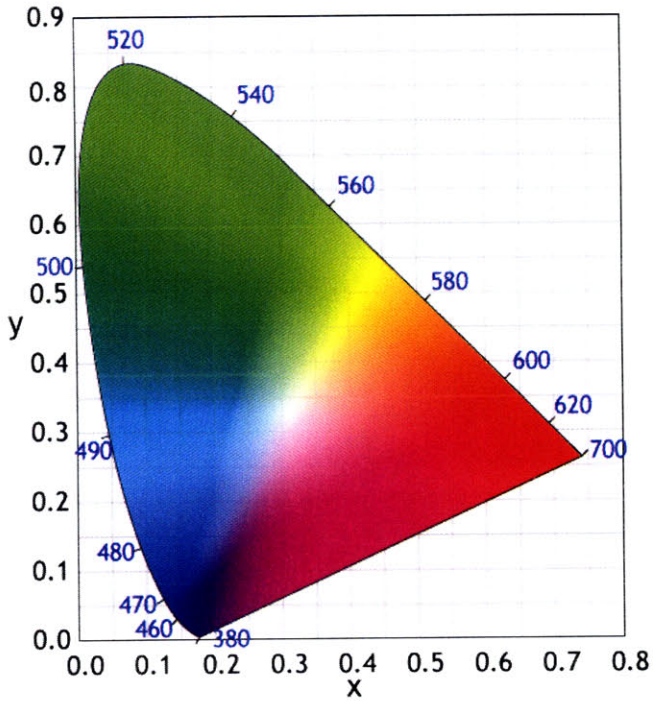

Figure 2-14: CIE chromaticity diagram

$$x = \frac{X}{X+Y+Z} \tag{2.13}$$

$$y = \frac{Y}{X+Y+Z} \tag{2.14}$$

The outer curve of a CIE color space is defined by the monochromatic sources at different wavelengths. For every light source we can now find a corresponding point on the CIE diagram. The corners of the color space correspond to the pure red, pure green and pure blue colors. It is possible to obtain any color with an arbitrary color coordinates by simply mixing the light from the pure sources. Consequently, when designing LEDs for display applications it is desirable to create colors with CIE (x, y) coordinates close to the corners of chromaticity diagram.

Chapter 3

Electroluminescence from Mixed Quantum Dot Monolayers

3.1 Motivation

This part of my thesis is motivated by the creation of essentially unlimited number of QD-LED colors through the mixing of different QD types within an emissive monolayer in a hybrid organic-QD structure. One of the most interesting applications of mixed color emission is fabrication of white-light sources. It is apparent from the CIE chromaticity diagram in Figure 2-14 that white light can be created by the mixing of red, green and blue color emission. However, there is another important metric to consider when fabricating white light sources - the color rendering index (CRI), which defines how well colors can be resolved when illuminated by the light source of interest as compared to sunlight. The ideal while-light source has to have a color temperature, i.e. the CIE color coordinates are close to those of sunlight (0.33, 0.35), and have a high CRI (the CRI of sunlight is 100).

With greater efficiency, better color tunability and fewer restrictions on shape, size or mounting, white light LED panels could someday replace incandescent or fluorescent light bulbs in many lighting applications. Several types of solid state devices have already achieved efficient white light luminescence (in the range of 15-30 lm/W), including single-chip InGaN white LEDs (WLEDs) [63], multi-chip WLEDs

[64], ZnSe-based WLEDs [65], and white organic LEDs (OLEDs), which can be further divided into single unit white OLEDs (WOLEDs) [10], stacked white OLEDs (SOLEDs) [11], and white LEDs that use blue OLED-pumped inorganic phosphors to generate a broad white spectrum [66]. Single-chip InGaN WLEDs [63] provide low cost, high luminance efficiency devices for general lighting, but they suffer from poor CRI, because their emission profiles consist of a blue InGaN component and a yellow phosphor emission (typically yttrium aluminum garnet YAG). Multi-chip WLEDs consist of red, green, and blue-emitting sub-units that lead to a high CRI, but they are relatively expensive and require a complex feedback system due to different degradation rates of their sub-units [64]. In ZnSe-based WLEDs white emission is achieved by mixing the blue emission of ZnS and yellow emission of a ZnSe substrate [65]; these devices have lower efficiency and shorter lifetimes as compared to the InGaN-based LEDs. Finally WOLEDs and SOLEDs combine the electroluminescence (EL) from three types of organic phosphors to achieve white luminescence with high electrophosphorescent efficiencies (up to 10% for WOLEDs and 30% for SOLEDs). However, the organic dyes that generate white electroluminescence are generally less photostable than inorganic materials, a quality, which does not limit their use in consumer electronics displays, but which challenges their use in high brightness applications such as room lighting.

QD lumophores were utilized as a replacement for red [67, 68] or green [69] color components in white-light LEDs employing organic emitters. A broad spectral emission using a mixture of QDs has also been demonstrated using red, green and blue emitting QDs embedded in polylaurylmethacrylate [70] with a blue GaN or Hg vapor lamp for excitation. White light photoluminescence from QDs was also obtained by Bowers, et al. [71] and Chen, et al. [72]. In these devices broad deep trap QD luminescence was photoexcited by an external ultra-violet LED. However, deep trap emission, which generally originates from defective CdS or ZnSe QDs, is inefficient, and the defect trap states of QD lumophores are poorly characterized and not easily reproducible from one synthesis to the next.

Hybrid organic-QD LEDs benefit from a virtually unlimited number of available

QD colors and simplicity of fabrication. Unlike WOLEDs that require complicated co-evaporation techniques for simultaneous deposition of multiple phosphorescent emitters into a wide band-gap host, or SOLEDs that require multiple evaporation steps to deposit different emissive layers, in QD-LEDs emissive layer can be potentially deposited in one simple contact printing step as discussed in Chapter 2. Using multiple QD colors in a QD-LED allows us to essentially reproduce the solar spectrum in the visible range without wasting energy in the UV and IR parts of spectrum. Figure 3-1 shows the EL spectrum of a hypothetical QD-LED fabricated with 5 QD colors. The hypothetical QD-LED spectrum closely traces the spectrum of a black-body radiator at 5500 K (temperature of the sun), consequently it has CIE coordinates of sunlight (0.33, 0.35) and CRI = 98.

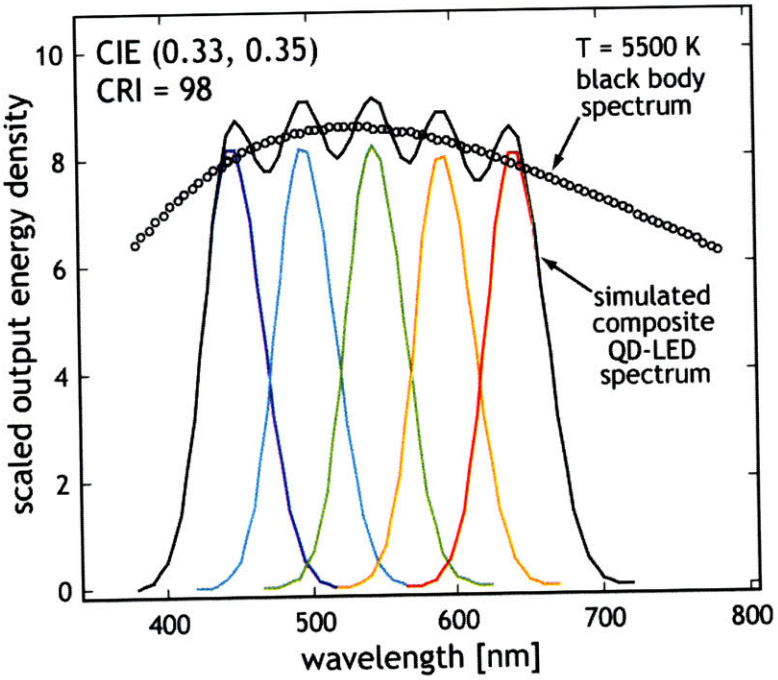

Figure 3-1: Simulated QD-LED EL spectrum is shown in comparison with a spectrum of a black body radiator at 5500 K

There are two possible approaches to fabrication of a white-light QD-LED: (1) an emissive QD monolayer can be patterned on a microscale with multiple QD colors (akin to the pattern in Figure 2-7), which from a distance will appear white; (2) QDs of different colors can be mixed in solution in a proportion that yields white-light emission from a QD monolayer. The advantage of the first approach is in the

separate deposition of different QD materials, since different color QDs have different sizes and potentially different passivating ligands. The disadvantages of this approach include multiple QD deposition steps, and consequently longer and costlier process; complicated pattern alignment step; difficult prediction of the resulting apparent color of QD-LED emission. The advantages of the second approach include simplicity of deposition in a single printing step and fairly simple prediction of a correct QD color proportion facilitated by visual examination of the QD solution PL. These factors make the second approach more appealing from the industrial point of view, additionally this approach will allow us to explore the interactions of different QD types inside a thin film contributing to our understanding of QD-LED operation mechanism.

3.2 Challenges of Mixed QD-LED Design

An ideal white-emitting QD-LED should fit the following requirements: (1) color temperature close to that of sunlight, i.e. CIE coordinates close to ideal (0.33, 0.35); (2) high CRI >80; (3) high EQE; (4) low operating voltage; (5) simple and inexpensive fabrication.

3.2.1 Material Compatibility

Our approach to QD-LED fabrication automatically addresses the fifth requirement, as we choose to deposit mixed QD monolayers in one simple printing step to achieve a mixed QD-LED EL. There are several challenges associated with this approach: (1) interactions between QDs of different type; (2) simultaneous deposition of QDs with different sizes and different organic ligands.

As the initial proof of concept, we design a white-emitting QD-LED that incorporates a mixed monolayer of red, green and blue QDs [17]. Using three types of QDs as emitters in an electrically driven structure has been previously reported as preliminary work in our group [73], and as a parallel effort by Li et al. [74], but with efficiencies of more than a factor of 4 lower.

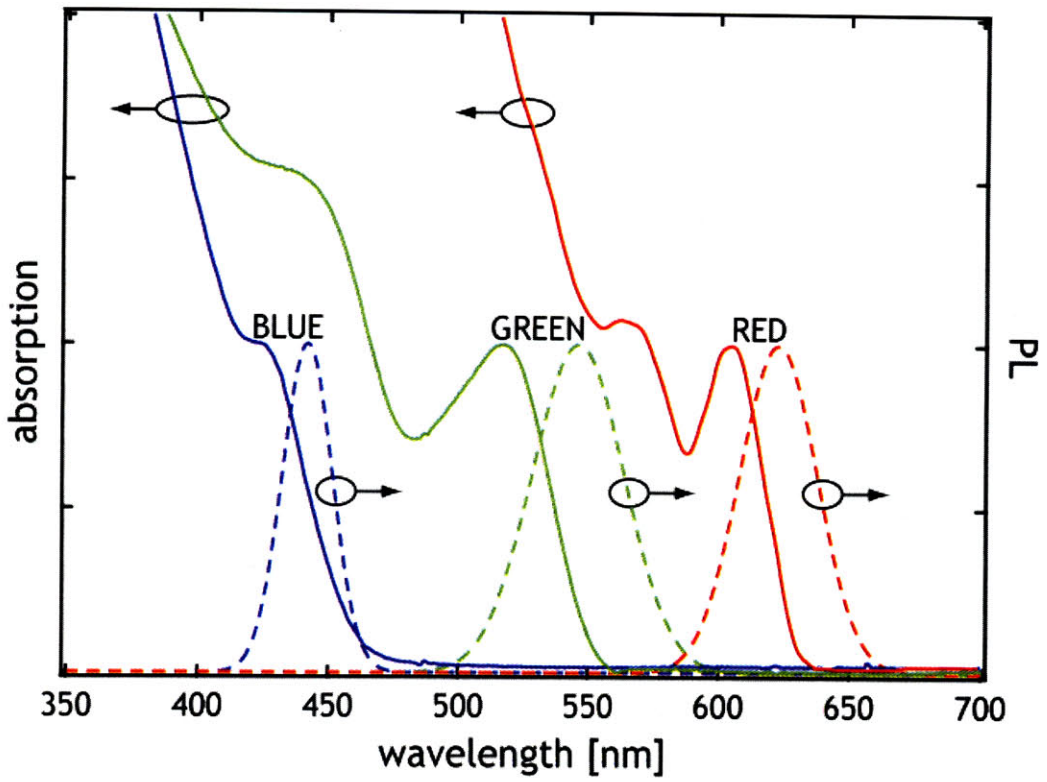

Figure 3-2: Absorption (solid lines) and PL (dashed lines) spectra of red, green and blue QDs.

It has been previously observed that the contribution of different QD colors in a mixture to PL spectrum differs from solution to thin film, i.e. the contribution of shorter wavelength (higher energy) emitters decreases from solution to thin film while the contribution of longer wavelength (lower energy) emitters increases [75, 76]. If we examine the absorption and PL spectra of blue, green and red QDs, we find that the absorption spectra of green and red QDs overlap with the emission spectrum of blue QDs (Figure 3-2). The absorption spectrum of red QDs also overlaps with the emission spectrum of green QDs.

The overlap between the emission spectrum of one material (donor) and the absorption spectrum of another material (acceptor) indicates that there may be exciton energy transfer from the first material to the second material via dipole-dipole interaction, i.e. Förster energy transfer [77, 78]. Förster energy transfer is characterized by the Förster radius R_F, the distance, at which a donor exciton is as likely to transfer its energy to an acceptor as it is to recombine on a donor. The Förster radius

for the energy transfer process between two materials is defined by the strength of the dipole-dipole interaction between the materials, and can be calculated from the overlap between the donor emission and acceptor absorption spectra [77]:

$$R_F^6 = \frac{3}{4\pi}\frac{c^4}{n^4}\int \frac{F_D(\omega)\sigma_A(\omega)}{\omega^4}d\omega \tag{3.1}$$

where c is the speed of light in vacuum, n is the material index of refraction, ω is the radial frequency of light, $F_D(\omega)$ is the normalized donor emission and $\sigma_A(\omega)$ is the acceptor absorption cross section.

The Förster energy transfer rate k_{ET} scales with the distance R between the donor and the acceptor cites:

$$k_{ET} = \frac{1}{\tau}\left(\frac{R_F}{R}\right)^6 \tag{3.2}$$

where τ is the donor PL relaxation time (i.e. an exciton lifetime).

This strong dependence of the energy transfer rate on the distance between a donor and an acceptor implies that the interactions between different QD types in solution are negligible. In contrast, in a thin film the QD-to-QD energy transfer becomes efficient. The Förster radii for the energy transfer from blue QDs to green and red QDs are on the order of ~5 nm and ~7 nm, respectively, and the Förster radius for the energy transfer from green to red QDs is on the order of ~5 nm [75, 76]. Taking into account fairly large QD size on the order of 5-10 nm, these values of Förster radius indicate that essentially any exciton formed on a blue QD that has a neighboring red (or green) QD will be transfered, and an exciton formed on a green QD can be efficiently transferred to a neighboring red QD. Consequently, the white-light emitting film needs to contain a majority of blue QDs, less green QDs, and the least amount of red QDs. Hence, the efficiency of the white-light QD-LED is expected to be similar to that of blue QD-LEDs, as blue QDs dominate the area of the mixed emissive QD monolayer.

In order to maximize the efficiency of the device, we need to use QDs with the highest possible PL efficiencies (especially for blue QDs,) and consequently, we choose the materials synthesized via novel procedures optimized to produce highly lumines-

cent particles in a particular wavelength range.

Previous reports of blue QD-LEDs quote EQE values of 0.2% using CdS/ZnS core-shell QDs [33]. While it is possible to fabricate active QD-LEDs using this material, the synthetic procedures are not robust with respect to the impurities present in metalo-organic precursors, often yielding QDs with trap states on the surface manifested in broad deep-trap emission at a wavelength longer than the main QD PL peak. The quantum yield of CdS/ZnS QDs in solution is on the order of 20% [33], while the efficiencies of CdSe/ZnS QDs used as red emitters can be as high as 80-90% [29]. Low solution PL quantum yield is an indication of potential poor performance of these QDs upon incorporating them into opto-electronic devices, as their quantum yield (QY) is usually lower in a thin film due to energy transfer from bright (emissive) to dark (non-emissive) QDs.

Consequently, we see a need for the development of new materials for blue QD-LEDs with high PL QY, narrow spectra without deep trap emission, and surface ligands compatible with QD-LED fabrication. To satisfy these requirements, my collaborator synthetic chemist, Dr. Jonathan Halpert, developed novel ZnCdS alloy QDs passivated with oleylamine and oleic acid using a synthetic procedure similar to [34]. For this type of particle the band gap is controlled by both quantum confinement effects and the ratio of Cd atoms to Zn atoms, i.e. the band gap becomes wider upon addition of increasing amounts of Zn to CdS. These QDs exhibit PL QYs $\sim$ 50% and narrow PL spectra tunable between 415-500 nm, for particles of 7-9 nm in diameter. The simplicity and robustness of the synthesis procedure allows for preparation of a wide variety of blue QDs with different PL peak wavelengths that can be tested inside the QD-LED structures.

For green emission we also use a novel type of QDs - ZnSe/CdSe/ZnS core double-shell particles synthesized via recently developed procedures [53, 52]. Despite their complex structure, these QDs, passivated with trioctylphosphine oxide (TOPO) and hexylphosphonic acid (HPA), are $\sim$4-5nm in diameter. These QDs exhibit high solution PL QYs ($\sim$ 60-70%) and have been previously used to fabricate QD-LEDs with EQE of 0.5%.

Finally red emitters are conventional CdSe/ZnS QDs overcoated with trioctylphosphine (TOP) and TOPO, produced via well established synthetic routes [28, 29]. We choose nanoparticles with a particularly thick ZnS shell ($\sim$ 2nm) that insures a high solution PL QY of $\sim$ 90% and yields large QDs $\sim$9 nm in diameter. These QDs are routinely used in QD-LED structures with EQEs up to 2%.

It is evident from the different QD descriptions above that three different types of QDs have different sizes and different passivating organic ligands. All the materials are soluble in chloroform and, consequently, can potentially be processed simultaneously from solution. However, we expect some challenges associated with simultaneous transfer of different QD types from an elastomer stamp onto an organic thin film since the affinities of different ligands can be different towards organic charge transporting materials and the parylene-C coating of a PDMS stamp. Another concern is a potential phase segregation of different QD types into clusters upon spin-casting onto a stamp.

In order to test the compatibility of different QD types with parylene-C and aromatic organic films, we first prepare films of red, green and blue QDs by contact printing onto the TPD (hole transporting material). Figure 3-3 shows AFM images of separately prepared red, green and blue QD layers. We find that all of the materials used as ligands for different QD types are compatible with both parylene-C and TPD surfaces, which is manifested in the formation of complete (when the starting solution is sufficiently concentrated) or incomplete (when the starting solution is too dilute) close-packed QD monolayers (Figure 3-3).

This encouraging discovery leads us to proceed with the preparation of mixed QD monolayers. Based on the ideal white-light source CIE coordinates, corrected for the different QD QYs and Förster energy transfer within a thin film, we find the proportion of the blue, green and red emitters in solution to be 1:2:10 (red: green: blue QDs by the monolayer area). A detailed calculation is presented in a white QD-LED design subsection. This solution is then spin-casted out of chloroform onto a parylene-C coated PDMS stamp, and a resulting layer is printed onto TPD. The film is dominated by blue QDs and it hence appears almost identical to the one in

Figure 3-3(c).

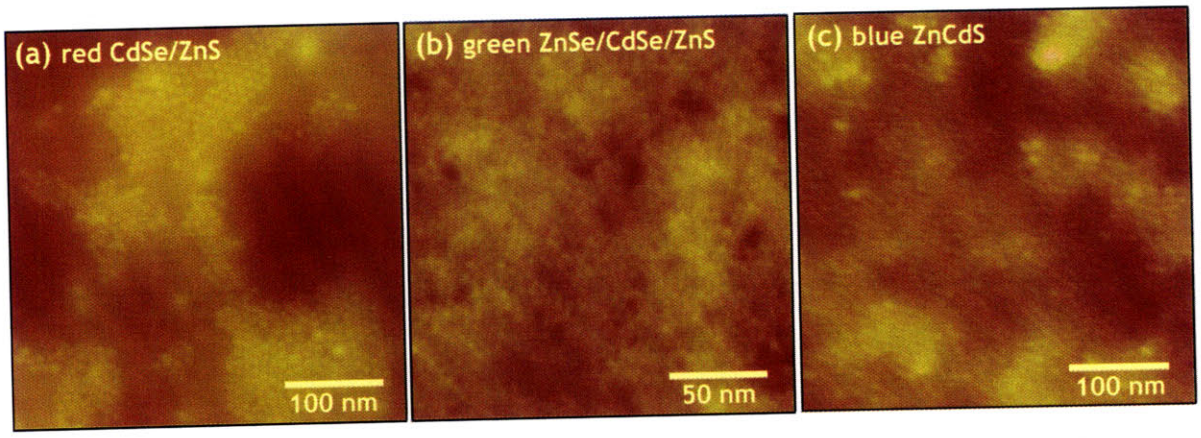

Figure 3-3: AFM height images of (a) red CdSe/ZnSe TOPO/TOP overcoated QDs, (b) green ZnSe/CdSe/ZnS TOPO/HPA overcoated QDs, (c) blue ZnCdS oleylamine/oleic acid overcoated QDs on 40 nm thick TPD films on glass substrates.

3.2.2 Designing Efficient Blue QD-LEDs

As we mentioned above, the efficiency of a white-light QD-LED is limited primarily by the EQE of blue QD-LEDs due to the Förster energy transfer from blue QDs to both green and red QDs. Consequently, the design of blue QD-LEDs is particularly important as we can use identical structures for white-light devices.

In our introductory discussion of QD-LED operation we pointed out two main processes contributing to QD EL: (1) direct charge injection from the charge transporting materials into QDs; (2) energy transfer from organic materials to QDs. Blue QD-LEDs present a design challenge with respect to both of these processes.

First, quantum confinement effects push the valence band of blue QDs lower in energy, hence increasing the barrier for hole injection into these materials from organic hole transporting layers (HTL). The position of the valence band of the CdSe QDs is approximately between ~-6.7-6.8 eV [13], for ZnCdS alloys we expect it to be below 6.8 eV, and the positions of the HOMO levels for available organic hole transporting materials vary between -5.4-6.1 eV [79]. While hole injection into QDs is obstructed by a $\sim$ 1 eV energy barrier, there is no apparent barrier for the electron injection into QD conduction band beside the thin organic passivating layer ($\sim$ 0.5 nm) that carriers

can tunnel through. The position on the CdSe QD conduction band is between -4.5-4.8 eV [13], so we expect it to be pushed up for blue ZnCdS QDs, and the position of the LUMO band of available electron transporting materials varies between -2.0-3.1 eV [79]. The difference in barrier height for the electron and hole injection into blue QDs leads to charge imbalance at QD sites, which yields to frequent formation of exciton-electron pairs that can recombine via a non-radiative Auger process [80].

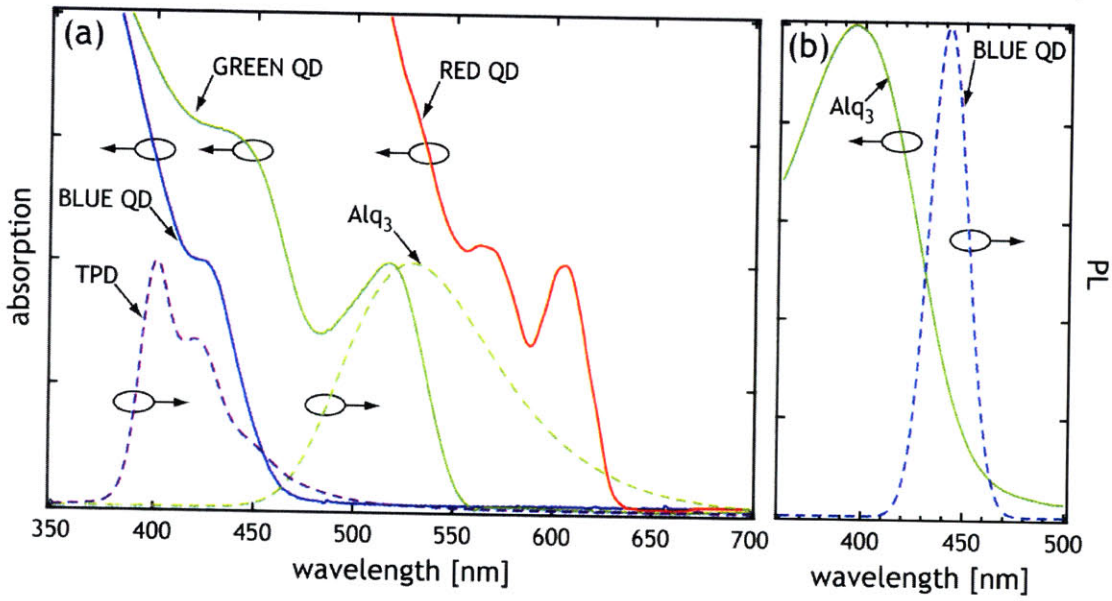

Figure 3-4: (a) Absorption spectra of red, green and blue QDs are shown with respect to the ALq$_3$ and TPD PL spectra. (b) The Alq$_3$ absorption spectrum is shown with respect to the blue QD PL spectrum.

Second, in order to be able to accept excitons formed in neighboring organic thin films, QDs should have an absorption spectrum that overlaps with the emission spectra of the relevant organic materials. Figure 3-4(a) shows a spectral overlap of red, green and blue QD absorption and emission spectra of commonly used organic materials TPD (HTL) and Alq$_3$ (ETL). It is clear that the red QDs can efficiently accept excitons from both TPD and Alq$_3$, green QDs can only accept excitons from TPD, and finally blue QDs can only poorly accept TPD excitons. Moreover, the overlap of the Alq$_3$ absorption and blue QD emission in Figure 3-4(b) suggests of a possible energy transfer from the blue QDs to the Alq$_3$ molecules, which will result in a decreased blue QD-LED EQE and the presence of an Alq$_3$ signal in the QD-LED EL spectra.

Since Alq_3 only acts as a sink for blue QD excitons, it is beneficial to introduce a spacer layer between the Alq_3 film and a QD monolayer. It is also important to impede exciton formation in the Alq_3 film as these excitons cannot be transferred to the blue QD cites, and hence, they recombine on Alq_3 molecules leading to undesirable Alq_3 contribution to the QD-LED EL spectra. Consequently, we introduce a hole-blocking layer (HBL) of 3,4,5-triphenyl-1,2,4-triazole (TAZ) that solves both problems discussed above, acting as a spacer layer that impedes both energy transfer from QDs to Alq_3 and the exciton formation in Alq_3 film.

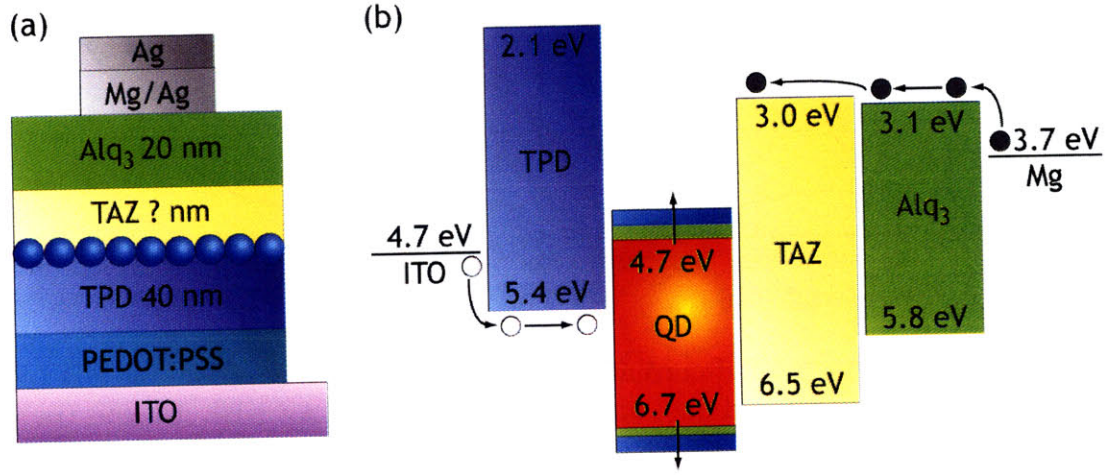

Figure 3-5: (a) Schematic cross section of a blue QD-LED. (b) Corresponding band diagram of a QD-LED. Different band gap widths are colored red, green and blue for red, green and blue QDs, respectively

Figure 3-5 illustrates the design of a blue QD-LED and a corresponding band diagram. It is evident from the band diagram that the direct charge injection into blue QDs is the primary mechanism leading to QD EL. The exciton formation is impeded in TPD by the electron accumulation at QD sites, and the energy transfer from TPD to blue QDs is not as efficient as it is to red or green QDs; exciton formation in Alq_3 is impeded by a TAZ HBL, and thus the majority of excitons are forming directly on QDs.

The HBL thickness critically influences the EL spectra of blue QD-LEDs. Figure 3-6(a) shows the EL spectra of our blue QD-LEDs fabricated with identical TPD HTL (40 nm) and Alq_3 ETL (20 nm), but with different thicknesses of TAZ HBL (20

and 27 nm). We find that the Alq_3 contribution to the QD-LED EL spectra decreases with increasing HBL thickness, since wider spacing between blue QDs and Alq_3 film impedes the Förster transfer of QD excitons to Alq_3 molecules. TPD has a minor contribution to the blue QD-LED EL spectra due to exciton formation in the TPD layer and incomplete energy transfer to blue QDs.

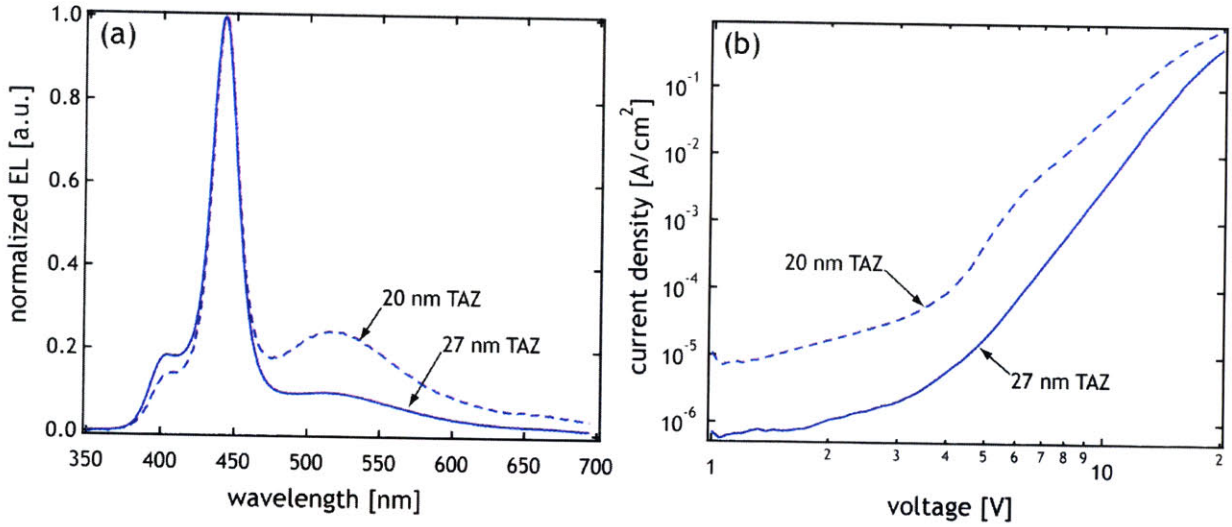

Figure 3-6: EL spectra (a) and current-voltage characteristics (b) of a blue QD-LED fabricated with 20 nm (dashed line) and 27 nm (solid line) TAZ HBL. EL spectra are shown at a current density of 10 mA/cm^2.

The device resistance also increases proportionally to the TAZ layer thickness since TAZ is essentially an insulator (Figure 3-6(b)), which implies that we cannot increase the thickness of HBL indefinitely till we fully suppress the Alq_3 emission, as the driving voltage increases dramatically and hence the power efficiency of the device decreases. Consequently, we choose a TAZ layer of 27 nm, since it provides a spectrum dominated by narrow QD emission and is sufficiently thin for the current to pass through the device.

3.3 White QD-LEDs

We adopt the structure of blue QD-LEDs developed in the previous section for our white QD-LEDs, i.e. our design consists of a transparent ITO anode, a layer of hole injecting polymer poly(3, 4-ethylenedioxythiophene):poly(styrenesulfonate) (PE-

DOT:PSS) deposited via spin-casting, 40 nm thick TPD HTL, a mixed QD monolayer micro-contact printed onto TPD, 27 nm thick TAZ HBL, 20 nm thick Alq_3 ETL, 100 nm thick Mg:Ag cathode with 20 nm Ag protective overlayer. In this device all the organic charge transporting films and a metallic cathode are deposited via evaporation (i.e. PVD).

The first step in the fabrication of a white QD-LED is finding the correct proportion of QDs in an emissive monolayer. We have to take into account the following factors: (1) desired QD-LED color coordinates; (2) EL efficiency of different QD types in a device; (3) energy transfer from blue QDs to red and green QDs and energy transfer from green QDs to red QDs.

We are interested in fabricating a white QD-LED with CIE coordinates close to (0.33, 0.35) and CRI as close to 100 as possible. Figure 3-7(b) demonstrates the EL spectra of red, green and blue QD-LEDs fabricated in the device structure described above. The EL spectra of red and green and QD-LEDs do not show any organic emission contribution, since both red and green QDs can efficiently accept TPD excitons and do not transfer the exciton energy to Alq_3 molecules. The potential white QD-LED spectrum is a linear combination of red, green and blue QD-LED EL spectra. By iterating the proportions of green and red QD-LED EL components with respect to the blue QD-LED EL, we find that the best white source that can be fabricated with these three QD types would have CIE coordinates of (0.34, 0.36) and CRI=95. The calculated white QD-LED spectrum is shown in Figure 3-7(b). These spectrum is a linear combination of red, green and blue QD-LED spectra in a proportion 1(R): 1(G): 1.2(B), assuming the same emission efficiency of different QD types.

To determine the contribution of a particular QD type to a mixed QD-LED EL we use the QD EL efficiency in a QD-LED instead of the more obvious PL QY of QDs in solution, since QDs differ not only by the starting solution PL QY but also by the efficiency with which they accept or generate excitons in an electrically driven structure. The EQE of a QD-LED provides a direct measurement of the QD EL efficiency as the majority of excitons generated in QD-LEDs recombine at QD sites

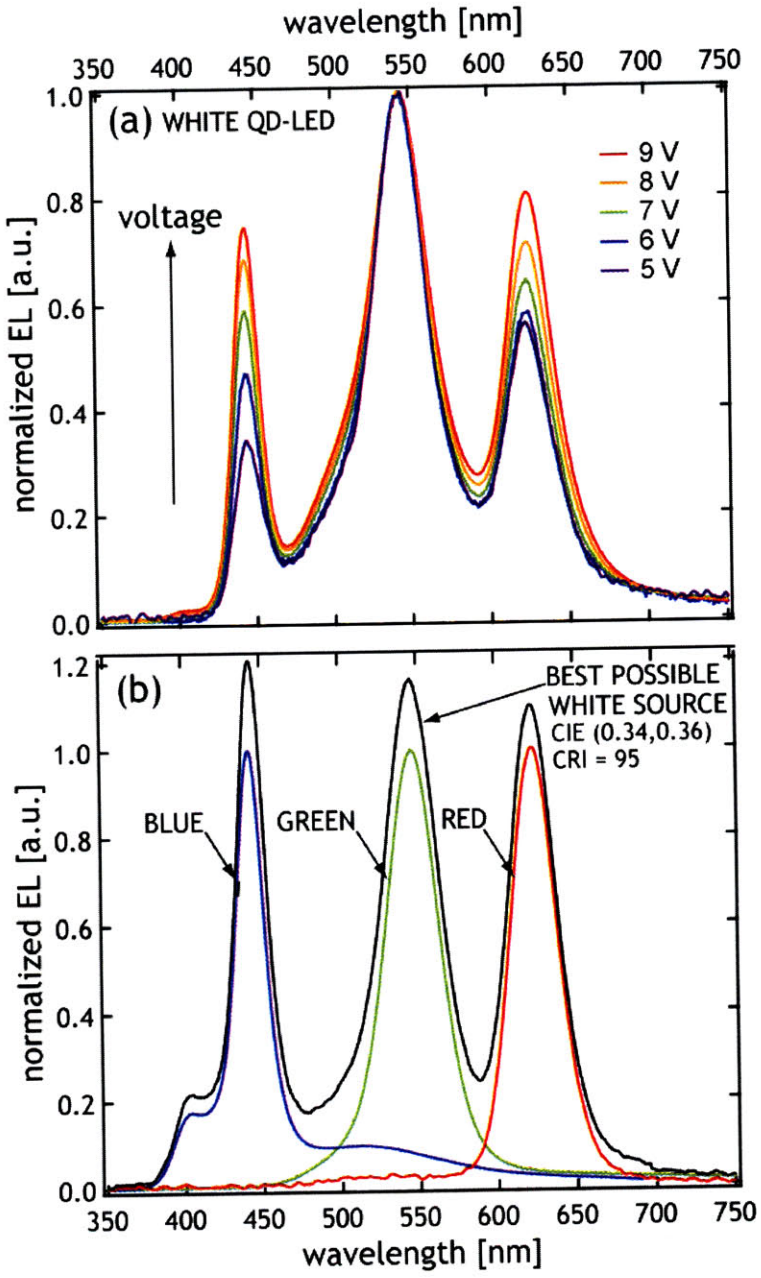

Figure 3-7: (a) EL spectra of our white QD-LED are shown at different bias voltages. An arrow indicates the direction of increasing bias voltage. (b) EL spectra of red, green and blue QD-LEDs shown at 5 V, 7 V and 10 V, respectively.

as indicated by the narrow monochromatic QD-LED EL spectra.

Figure 3-8 shows the EQE curves for red, green and blue QD-LEDs plotted vs. the current density through the devices. The peak EQE of our blue QD-LEDs is 0.35%, which is 75% higher than previously reported values [33]. The peak EQEs for red and green QD-LEDs are 1.5% and 0.65%, respectively, which is on the same order of magnitude or slightly higher than previously reported values for QD-LEDs based on similar QD materials [30, 52].

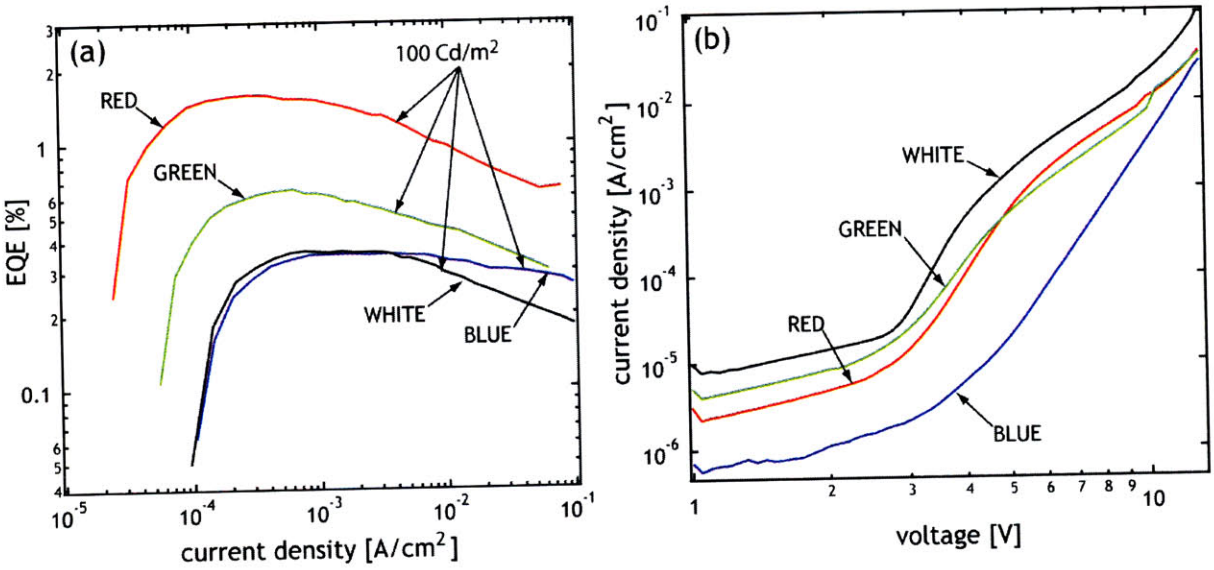

Figure 3-8: EQE (a) and IV characteristics (b) of red, green, blue and white QD-LEDs.

Based on the EQEs of the different color QD-LEDs we find that the ratio of QDs in a monolayer should be 1(R): 2.3(G): 4.3(B), i.e., inversely proportional to the QD-LED peak EQE values. Combining this data with the proportion that we obtained from the best possible white light source calculation, we find that the mixture should contain 1(R): 2.3(G): 5(B).

Finally we have to take into account Förster energy transfer from blue QDs to red and green QDs. In a mixed monolayer fabricated with a QD ratio calculated above, there are 3.3 red/green QD exciton acceptors for every 5 blue QD exciton donors, which implies that 3.3 out of 5 blue excitons will be contributing to red/green emission instead of blue emission.

We also note that blue QD-LEDs operate at higher voltages than green and red

QD-LEDs as manifested in the current-voltage characteristics in Figure 3-8. This is consistent with the suggested band diagram in Figure 3-5(b), which indicates the higher barrier for hole injection into blue QDs as compared to red and green QDs. Consequently, at any given bias past the "turn-on" voltage, a higher proportion of green and red QDs are luminescent as compared to the number of blue QDs.

To account for the energy transfer from blue QDs to red and green QDs as well as for the higher operating voltage of blue QD-LEDs, our final mixed QD monolayer contains the following ratio of QD colors: 1(R): 2(G): 10(B) (based on an area occupied by each QD type).

Figure 3-9: Photograph of our white QD-LED biased at 10 V.

The emission spectrum of the mixed-monolayer QD-LED (Figure 3-7(a)) shows a pronounced contribution of red, green and blue QD EL components. The TPD EL signal is largely quenched as compared to blue QD-LEDs due to efficient energy transfer to the red and green QDs. Alq_3 still appears to exhibit a weak spectral feature in the white QD-LED spectrum analogous to the blue QD-LEDs. The mixed-monolayer QD-LED pixels appear to be uniformly luminescent, look white to the eye (Figure 3-9), with CIE coordinates (0.35,0.41) at a 9 V applied bias and CRI of 86, when compared to a 5500K black body reference. Such a high CRI compares favorably to conventional white light sources such as cool white fluorescent (CRI = 62), incandescent (CRI = 100), and dye enhanced InGaN/GaN solid state LEDs (CRI > 80) [81].

The peak EQE of white QD-LEDs is 0.36% at 5.0 V (1.51 mA/cm^2) (Figure 3-

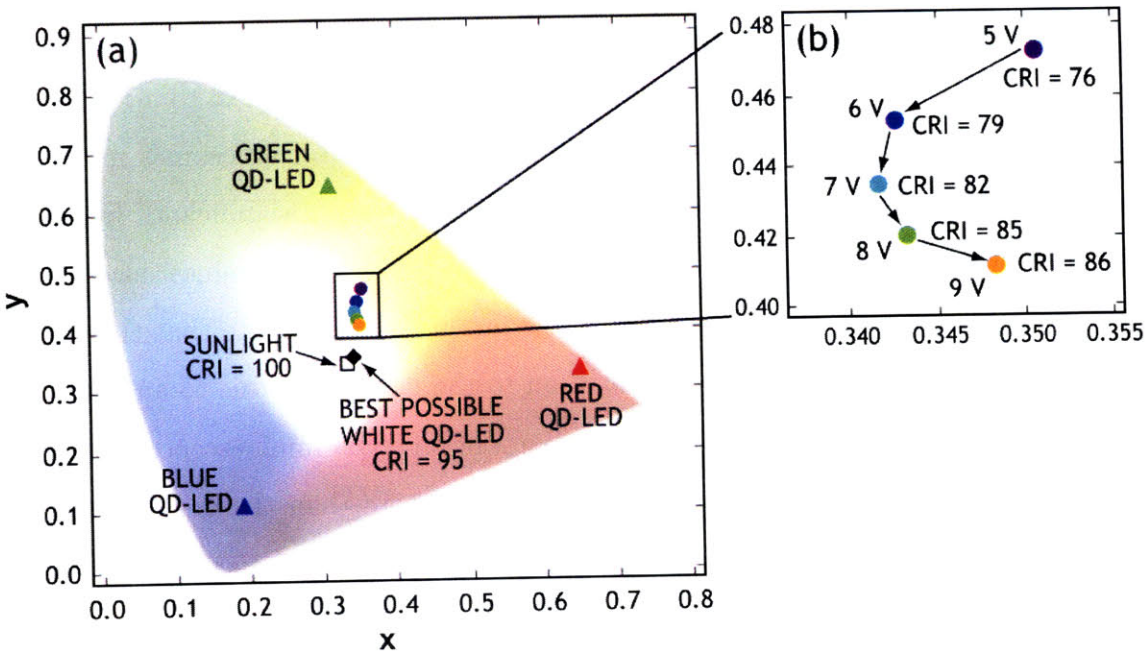

Figure 3-10: (a) CIE coordinates of red, green and white QD-LEDs are shown on a chromaticity diagram. CIE coordinates of a desired (best possible) white QD-LED source and sunlight are shown for comparison. (b) Evolution of CIE coordinates with increasing applied bias voltage.

8(a)), which corresponds to 0.9 cd/A and 0.57 lm/W, at a brightness of 13.5 cd/m^2. At 9 V applied bias, and optimal CIE position, the brightness was 92 cd/m^2, with efficiencies of 0.28% EQE, 0.7 cd/A, and 0.24 lm/W at 13 mA/cm^2 current. Maximum brightness topped 830 cd/m^2 at 14 V and 230 mA/cm^2.

The mixed-monolayer QD-LED contains three types of QDs with different responses to charge injection, leading to a change in the EL spectrum at different driving conditions. Figure 3-7(a) shows the EL spectrum color shift in a mixed-monolayer QD-LED as the applied bias increases from 5 V to 9 V, resulting in a small change of the CIE coordinates and CRI (see Figure 3-10(b)). With increasing voltage we observe an increase of the red and blue QD spectral components in the EL spectrum relative to the initially dominant green QD spectral component. This evolution of spectral features with increasing bias is consistent with the reduced efficacy of hole injection into blue QDs. At low applied bias (5V) charge injection into the mixed QD film of the white QD-LED is dominated by injection into the green and red QDs. Resonant energy transfer from green QDs to red QDs is inhibited by the relatively

small number of both red and green QDs as compared to blue QDs in the mixed QD monolayer, so that the probability of locating a green QD next to a red QD is small. At higher applied biases charge injection into blue QDs becomes more efficient, and the EL component of the blue QDs becomes more significant. Increased exciton formation on blue QDs also benefits red and green QD luminescence due to exciton energy transfer from blue QDs to red and green QDs. Note that the energy transfer to the red QDs is more efficient than to the green QDs due to an increased spectral overlap. Consequently, with an increase of blue QD luminescence (at higher operating voltages), the red QD luminescence rises more than the green QD luminescence. Exciton formation on the more numerous blue QDs governs the overall efficiency of white QD-LEDs, which closely tracks the efficiency of the monochrome blue QD-LEDs (Figure 3-8(a)).

3.4 Summary

The operation of the mixed-monolayer QD-LED is enabled by the use of identical electron transporting, hole blocking, and hole transporting layers in all of our monochrome QD-LEDs, which also imparts simplicity to color tuning the mixed-monolayer QD-LED sources. Colloidal QDs demonstrate exceptional PL stability exceeding 10^9 turnovers in the most stable QD structures [82]. Consequently, concern over differential aging of different-color QD samples is minimal, assuring the stability of spectral emission, as long as the remaining films that comprise the QD-LED stay unchanged.

Akin to mixing colors in a paint shop, the present work demonstrates that QD solutions can be precisely mixed to achieve a desired QD-LED spectrum at a desired driving condition.

Chapter 4

Energy Transfer from Organic Donors to Colloidal QDs

In Chapter 3 we discussed the interactions between different QD types. In particular we introduced Förster energy transfer (ET) as an important mechanism influencing the performance of QD-LEDs. In this chapter we will extend this discussion by studying ET between organic materials and QDs. Although we will primarily focus on ET from phosphorescent organic donors to QDs, the ET between fluorescent organic materials and QDs will be also discussed in the end of this Chapter.

4.1 Fluorescent and Phosphorescent Organic Materials

Excitons in organic materials can be classified by their total spin: singlets have total spin 0 and triplets have total spin 1. The spin of an exciton is simply defined by the sum of the electron and hole spins. Hence due to the Pauli exclusion principle, the ground state of an organic molecule is a singlet. When a molecule is excited optically (i.e. absorbs a photon), an electron is promoted onto a higher energy level leaving a hole behind, and since photons have spin 0, the total spin of a newly created exciton is also 0. This implies that all optically generated excitons are singlets. Analogously,

only singlet excitons can relax to the ground state emitting a photon.

Based on allowed optical transitions, organic materials can be divided into 2 groups: fluorescent and phosphorescent. In fluorescent materials optical transitions between singlet and triplet states are forbidden due to the spin conservation. Consequently, in these materials the triplet excitons, if generated, can theoretically exist infinitely long, i.e. triplet exciton relaxation time is ∞. In phosphorescent materials the presence of spin-orbit coupling breaks the spin conservation resulting in a mixing of different spin states, since only the total angular momentum is conserved. Consequently, in phosphorescent materials triplet excitons can potentially relax to the ground state within a finite time.

While optical excitation only produces singlet excitons, electrical excitation yields a statistical formation of electron-hole pairs with uncorrelated spins, and hence 3 out of 4 electrically formed excitons are triplets that cannot recombine radiatively in fluorescent materials [83]. Consequently, the maximum internal quantum efficiency (IQE) that can be obtained in an electrically excited fluorescent film is 25%. In contrast, in phosphorescent organic films all generated excitons can potentially recombine radiatively and IQE of a phosphorescent OLED can be as high as 100% [84, 83].

In organo-metallic materials containing heavy metal or transition metal atoms (Pt, Ir), the presence of heavy ions enhances the spin-orbit coupling, which results in decrease of a triplet exciton relaxation time (from ∞ for fluorescent materials to 0.5-10 μs for phosphorescent materials). In these materials the triplet states are split-off from the singlet state by the spin-orbit coupling energy, with triplet states generally having lower energy. Since the transitions between the singlets and triplets (inner system crossing (ISC)) are allowed in these materials, the higher energy singlet rapidly relaxes to the triplet state, which then recombines radiatively [46].

The efficiency of OLEDs is greatly improved by introducing emissive layers containing highly luminescent materials between the hole and electron transport layers (HTL and ETL). The emissive layers consist of fluorescent host materials doped with small amounts of phosphorescent (or fluorescent) emitter. Using a phosphorescent emitter in a hybrid film allows for the extraction of the otherwise nonemissive triplet

excitons generated in a fluorescent host (exciton generating layer). Figure 4-1 shows the possible scenarios of ET from fluorescent hosts. The advantage of using phosphorescent guests is evident from this diagram as all the excitons recombine radiatively in this case.

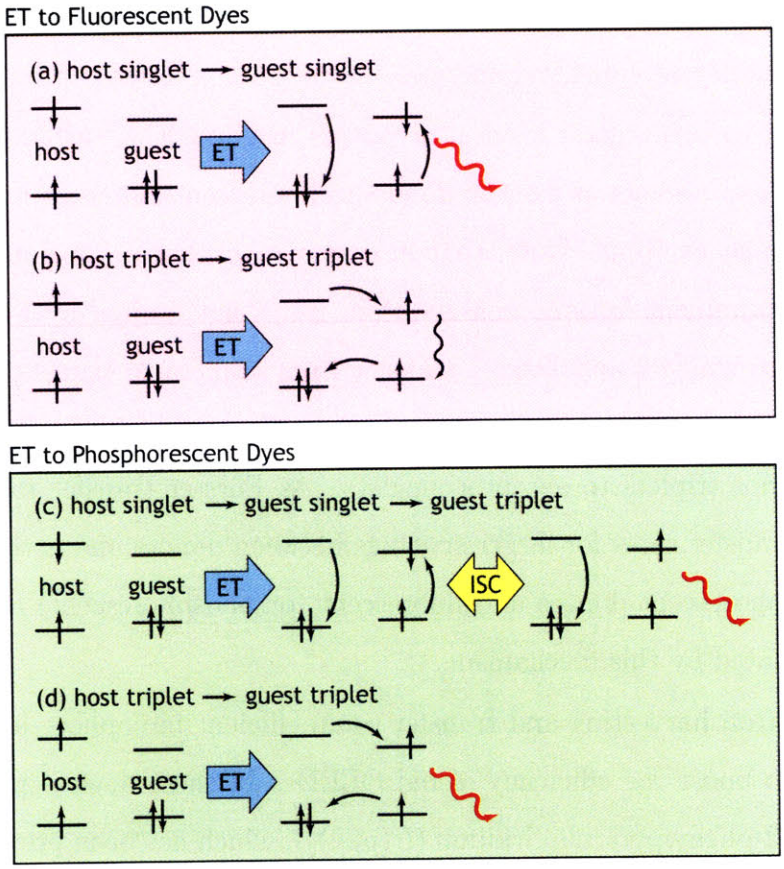

Figure 4-1: (a) ET from a singlet host to a fluorescent singlet guest. (b) ET from a triplet host to a fluorescent triplet guest. (c) ET from a singlet host to a phosphorescent singlet guest. (d) ET from a triplet host to a phosphorescent triplet guest.

There are two different mechanisms that participate in ET from fluorescent hosts: Förster and Dexter. As we discussed in previous Chapters, Förster ET is a long-range resonant process governed by the dipole-dipole coupling between the donor exciton and the future acceptor exciton (as the acceptor is originally in its ground state), which strength is determined by the overlap between the donor and acceptor exciton wave functions (in both energy and space domains). This process involves the recombination of a donor exciton and non-radiative transfer of its energy to the acceptor. Consequently, in case of fluorescent donors there can only be Förster transfer

from donor singlets to acceptor singlets. Dexter transfer is a direct electron exchange between the two neighboring molecules, and hence, only requires the total spin conservation rather than spin conservation within both donor and acceptor independently. Consequently, a triplet exciton generated on a fluorescent donor can be transfered to the triplet state of an acceptor, as shown in Figure 4-1(b) and (d), by exchanging electrons with different spins and energies.

In addition to being good exciton acceptors in guest-host systems, phosphorescent materials can also act as exciton donors to fluorescent materials harvesting both singlet and triplet excitons. Note, that in case of phosphorescent donors, for which there is no requirement for spin conservation, ET is not limited by Förster transfer from singlets to singlets and Dexter transfer from triplets to triplets. Since triplet excitons can recombine to the ground state, the Förster transfer is allowed for phosphorescent donor triplets to acceptor singlets. As Förster transfer rates are higher than Dexter transfer rates for larger spacings between donors and acceptors, the ET between phosphorescent donors and fluorescent (or phosphorescent) acceptors is on average dominated by this mechanism.

Triplet exciton harvesting and transfer to an efficient lumophore has been previously shown to boost the efficiency of red OLEDs. In these devices phosphorescent donor fac tris(2-phenylpyridine) iridium ($Ir(ppy)_3$), which has been previously used as an efficient green emitter in OLEDs with EQE = 12% [84], was used to pump a fluorescent laser dye 4-(Dicyanomethylene)-2-methyl-6-julolidyl-9-enyl-4H-pyran (DCM2), producing red OLEDs with EQE = 9% [85].

4.2 QDs as Exciton Acceptors

The energy structure of QD excited states is complex (as discussed in detail in Chapter 1) and is illustrated in Figure 4-2. Electron-hole exchange interaction in QDs results in the splitting between the bright (total angular momentum $N = 1$) and dark (total angular momentum $N = 2$) exciton states, and since the dark exciton has a lower energy than the bright exciton state, theoretically QD excitons should not recombine

radiatively. However, analogous to phosphorescent materials, transition metal ions in QDs (such as Cd) promote spin-orbit coupling, which results in allowed radiative relaxation of the "Dark Exciton".

At room temperature the thermal energy associated with phonons in QD crystal lattice is comparable to the splitting between the $N = 1$ and $N = 2$ states, and hence the excited states of QDs are most likely mixed. Consequently it is advantageous to use a phosphorescent material donor to be able to transfer energy into any of QD excitons.

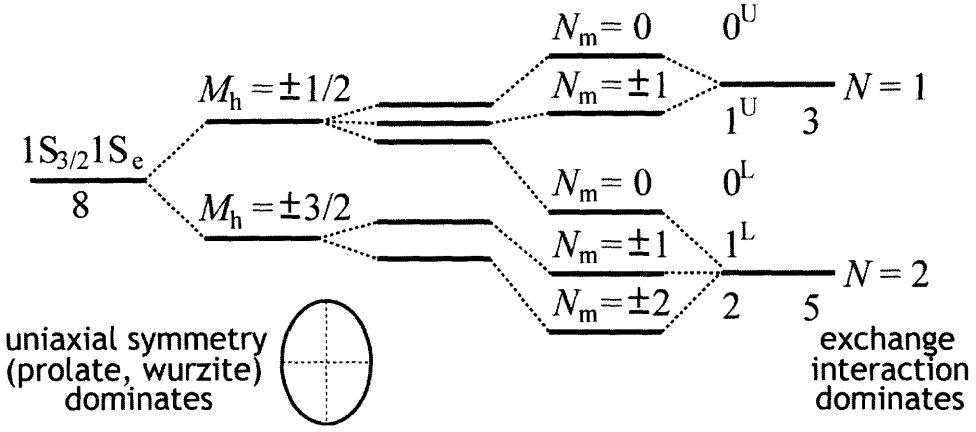

Figure 4-2: The schematic diagram shows the fine structure of excited QD states.

QDs have proven themselves as efficient exciton donors in ET experiments with various organic dyes and bioorganic molecules [86, 87]; however, there remained a debate in the literature over the demonstration of ET from an organic donor to CdSe/ZnS core-shell QD (see e.g. [88]). ET to QDs has been studied from organic fluorescent polymers [89] as well as from crystalline inorganic quantum wells [90].

The main challenge associated with demonstrating the ET from fluorescent organic materials to QDs is the long QD relaxation time on the order of >10 ns [91] as compared to short fluorescent organic exciton lifetimes of ~1 ns [46]. The standard technique used for confirming the ET between two materials is time-resolved PL spectroscopy, described in detail in Chapter 2. These measurements allow us to find the PL relaxation times for different materials and hence, one can use them to detect the differences between the relaxation times of one material in the absence or presence

of another material.

In the simplest case when the all the processes contributing to the depletion of exciton population in a material are active simultaneously, the time dependent PL intensity $I(t)$ can be described by:

$$I_{D,A}(t) \sim I_0 e^{-t/\tau} \tag{4.1}$$

where I_0 is the initial PL intensity at the moment of excitation, t is time and τ is the PL relaxation time defined as:

$$\tau = \frac{1}{k_r + k_{nr}} \tag{4.2}$$

where k_r and k_{nr} are radiative and non-radiative exciton relaxation rates, respectively. In a presence of ET the donor PL relaxation decreases due to the additional non-radiative pathway for exciton relaxation:

$$\tau_D = \frac{1}{k_r + k_{nr} + k_{ET}} \tag{4.3}$$

where k_{ET} is the energy transfer rate.

For an acceptor the dependence is slightly more complicated as ET from a donor effectively creates an additional source of excitons that are supplied to the acceptor and recombine at the rate characteristic of a donor (with the ET correction present), i.e., the time-dependent acceptor PL intensity in the presence of a donor is described by:

$$I_A(t) \sim I_0 e^{-t/\tau_A} + I' e^{-t/\tau_D} \tag{4.4}$$

and here I' is the initial correction to PL intensity due to the ET from the donor.

When the ET rate is low compared to the donor radiative decay rate, the donor PL relaxation time does not experience significant changes and hence ET is difficult to detect. Additionally, when the donor relaxation time is short compared to that of an acceptor (which is true for ET from fluorescent organics to QDs) and $I' \leq I_0$,

the additional decay component in acceptor PL intensity is overwhelmed by the PL decay due to direct acceptor excitation. Consequently, the data analysis becomes cumbersome and no definitive conclusions can be made about the ET in the potential donor-acceptor system [88].

Since we are interested in using organic donors to increase the PL intensity of colloidal QDs we have to take into account the long QD PL relaxation times >10 ns. However, we note that the PL relaxation times of phosphorescent organic materials are on the order of 0.5-10 μs, which is significantly longer than the QD relaxation time. Hence, time-resolved PL spectroscopy will allow us to draw clear conclusions about the QD properties as exciton acceptors [92].

4.3 Material Choices and Specimen Design

For the Förster ET to take place, the donor PL spectrum has to overlap with the acceptor absorption spectrum. Since the goal of this experiment is to determine whether triplet excitons can be transfered from a phosphorescent organic donor to colloidal QDs, and hence potentially benefit the performance of QD-LEDs, we choose materials and specimen geometries that are routinely used in OLED and QD-LED fabrication.

Colloidal CdSe/ZnS core-shell QDs with their PL peak at 640 nm are used as exciton acceptors. $Ir(ppy)_3$ doped into a wide band gap host 4,4-N,N-dicarbazole-byphenyl (CBP) is used as a donor, since it was previously shown to transfer excitons to red-emitting laser dyes benefitting OLED performance [85]. The overlap of the $Ir(ppy)_3$ emission with the QD absorption in Figure 4-3 indicates the potential for Förster ET.

Our specimens resemble thin film geometry of QD-LEDs (Figure 4-4). We fabricated three thin film structures: Sample I is a 40 nm thick film of 10% $Ir(ppy)_3$ doped into CBP thermally evaporated onto a glass substrate. Sample II is a monolayer of CdSe/ZnS QDs (7 nm QD diameter) contact printed onto a glass substrate. Finally, sample III is a hybrid structure consisting of a monolayer of CdSe/ZnS QDs printed

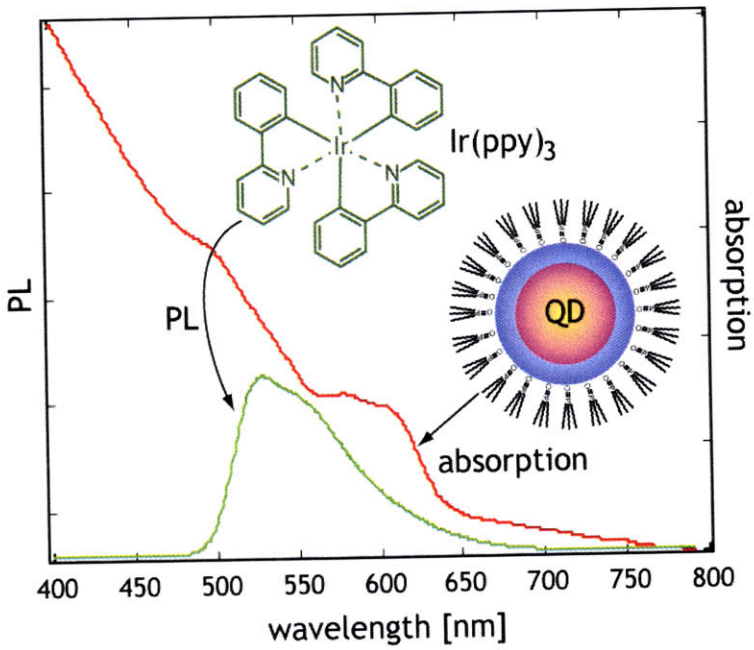

Figure 4-3: Overlap between the CdSe/ZnS QD absorption and $Ir(ppy)_3$ emission spectra suggests energy transfer from $Ir(ppy)_3$ to QDs. (Note: the QD absorption spectrum was obtained by the direct measurement in a thin film. Consequently, it exhibits a red tail due to the scattering of the organic ligands in a solid film.) Inset: Schematic drawing of a ZnS overcoated CdSe QD and the $Ir(ppy)_3$ structural formula.

onto a 40 nm thick film of 10% $Ir(ppy)_3$ in CBP on glass.

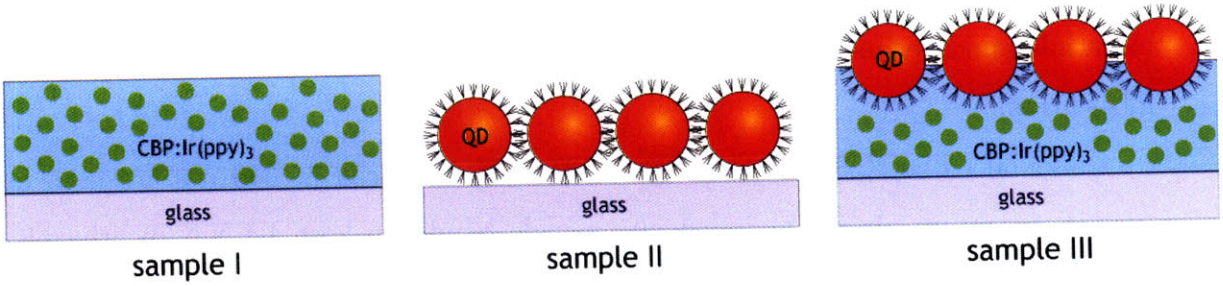

Figure 4-4: Schematic diagrams of Samples I, II and III fabricated for the ET study between a green phosphorescent donor $Ir(ppy)_3$ and QD acceptors.

4.4 Experimental Observations

Comparing the PL signatures of the three samples described in Figure 4-4 we observe a $21\% \pm 4\%$ decrease of the $Ir(ppy)_3$ time-integrated PL intensity in sample III as compared to sample I and a concomitant $55\% \pm 5\%$ increase in CdSe/ZnS QD film

PL intensity in sample III as compared to sample II (see Figure 4-5). The change in PL is calculated by numerically decomposing the sample III spectrum into CdSe/ZnS QD and $Ir(ppy)_3$ components. The PL change suggests ET from the $Ir(ppy)_3$ film to the QD monolayer. We note that simple reabsorption of $Ir(ppy)_3$ luminescence by the QD film does not account for the observed PL change since the 7 nm thick QD monolayer has very weak absorption (<1.5 %) over the $Ir(ppy)_3$ PL spectrum. Assuming a QD PL efficiency on the order of 10% (typical of QD films), we find that reabsorption of $Ir(ppy)_3$ photons by the QD layer can lead to a small QD PL flux increase of at most 0.0015 times the $Ir(ppy)_3$ photon flux, or a roughly 3 orders of magnitude smaller than the observed QD intensity. (To provide an upper limit on the reabsorption effect, we assume that all of the $Ir(ppy)_3$ flux is directed through the QD film.) Consequently, reabsorption does not significantly contribute to the observed increase in QD PL in Sample III. (Note that because the film thicknesses are much less than the wavelengths of the emitted light, and the refractive index contrasts between the layers are small, optical cavity effects are not expected to be significant.)

Data from time-resolved PL measurements are shown in Figure 4-6. The PL of CdSe/ZnS QDs in Sample II (data set E) exhibits two time constants with a shorter time constant of τ_1^{QD} =10 ns and a longer time constant of τ_2^{QD} =40 ns. The $Ir(ppy)_3$ PL decay also exhibits a bi-exponential behavior, with a dominant time constant of $\tau^{Ir(ppy)_3}$ =610 ns (as obtained from data set A). In sample III, however, the QD PL decay (data set D) is substantially elongated, leading to a longer time constant of $\tau_{2,sIII}^{QD}$= 500 ns, which is identical to the dominant time constant of the $Ir(ppy)_3$ PL from the same sample (data set B), strongly suggesting that this delayed QD PL is due to the transfer of $Ir(ppy)_3$ excitons to the QD film.

An investigation of the first 200ns of QD PL (Figure 4-6) reveals a slight increase in the initial PL intensity and a small increase of the short time constant, yielding τ_1^{QD} =12 ns. Note that in Figure 4-6, the data are obtained by integrating the PL spectra over the wavelength ranges specified in the figure caption. Furthermore, the QD PL decay for Sample III (data set D) is obtained by subtracting the $Ir(ppy)_3$

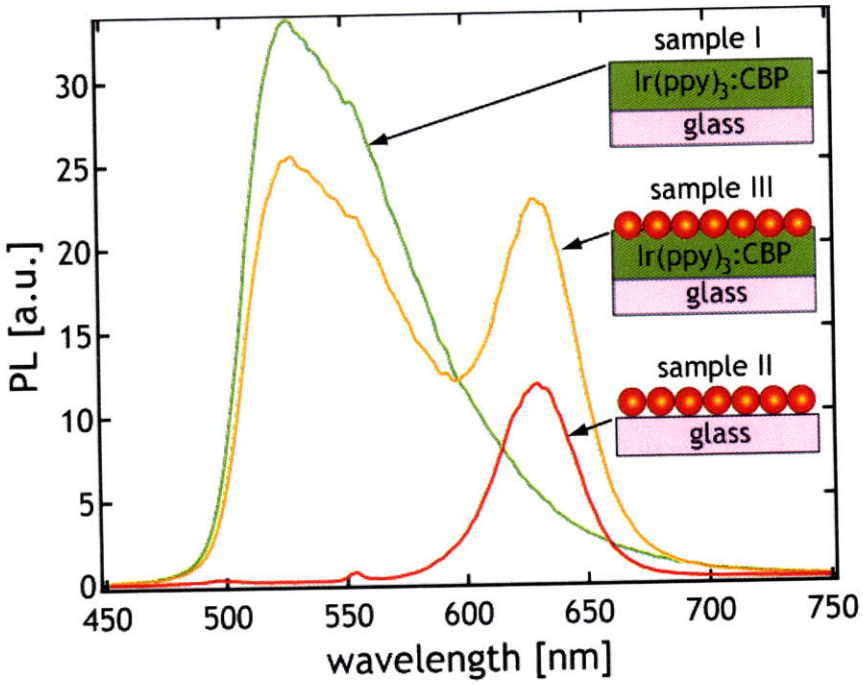

Figure 4-5: Time-integrated PL spectra of samples I, II, III. All measurements were obtained at the same excitation source power of λ =395 nm light. The PL spectrum of sample III can be constructed from a linear superposition of the PL spectra of samples I and II.

PL spectrum from the total signal, as illustrated in Figure 4-7, and then integrating the difference signal over the specified wavelength range. We again note that the time-dependent contribution of reabsorption to the QD PL is at most 0.0015 times the $Ir(ppy)_3$ flux intensity (obtained from Sample I). Therefore, for all times, the reabsorption contribution is at most 3% of the observed QD PL signal.

4.5 Numerical Analysis

Since reabsorption does not contribute significantly to the QD PL intensity in Sample III, the observed QD PL enhancement and elongation of QD PL lifetime can be attributed to exciton energy transfer from $Ir(ppy)_3$ molecules to the QD monolayer. For quantitative analysis of the data, we note that the observed PL time dependence (Figures 4-6 and 4-7) is shaped by four physical processes that govern exciton dynamics in the $Ir(ppy)_3$:CBP film: $Ir(ppy)_3$ exciton radiative decay, nonradiative decay, ET

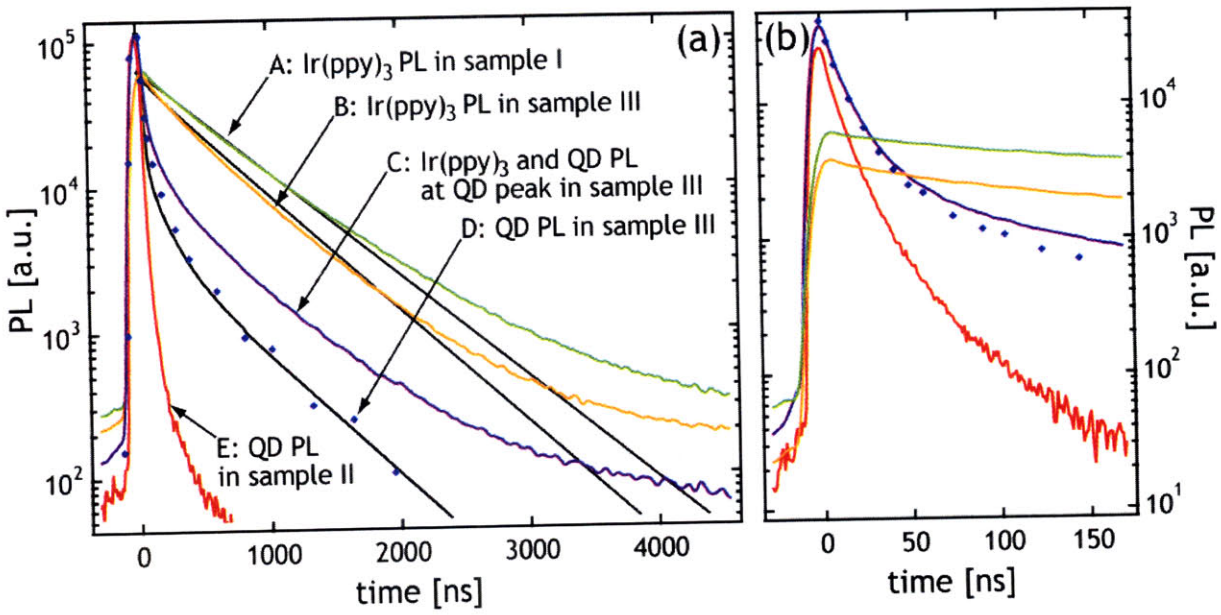

Figure 4-6: Time resolved PL measurements for samples I, II, and III, performed over (a) a 5000 ns time window and (b) a 500 ns time window (first 200 ns shown). The colored lines and markers represent the experimental measurements, and the black lines represent numerical fits using the proposed diffusion model. To obtain data sets A and B, the sample PL was integrated over the wavelength range of λ =511 nm to λ =568 nm, to yield in each case the time dependence of the $Ir(ppy)_3$ PL. Similarly, to obtain data sets C and E, a wavelength range of λ =600 nm to λ =656 nm was used. Data set C therefore reflects the intensity of combined $Ir(ppy)_3$/ QD PL near the QD PL peak. Data set E reflects the intensity of solely the QD PL. To obtain data set D, the intensity due to the $Ir(ppy)_3$ PL was subtracted from C to yield just the QD PL intensity in Sample III. Note that the black fit lines assume a single exponential time decay for the $Ir(ppy)_3$, and so are only expected to fit the $Ir(ppy)_3$ at early times (where the single exponential decay dominates).

to the QD film, and diffusion. The two decay mechanisms combine to determine the observed radiative lifetime of 610 ns and a PL quantum efficiency of $\sim$ 15% (as calculated from optimized electroluminescence efficiencies of 12% doped $Ir(ppy)_3$:CBP OLEDs [93]). The ET mechanism leads to the observed quenching of the $Ir(ppy)_3$ PL and the associated enhancement of the QD PL, and capturing the $Ir(ppy)_3$ excitons that are closest to the QD film. Finally, the diffusion mechanism induces a net flow of $Ir(ppy)_3$ excitons towards the QD film, due to the depletion by ET of $Ir(ppy)_3$ excitons near the QD interface.

To numerically model the combined processes we model the ET mechanism as an

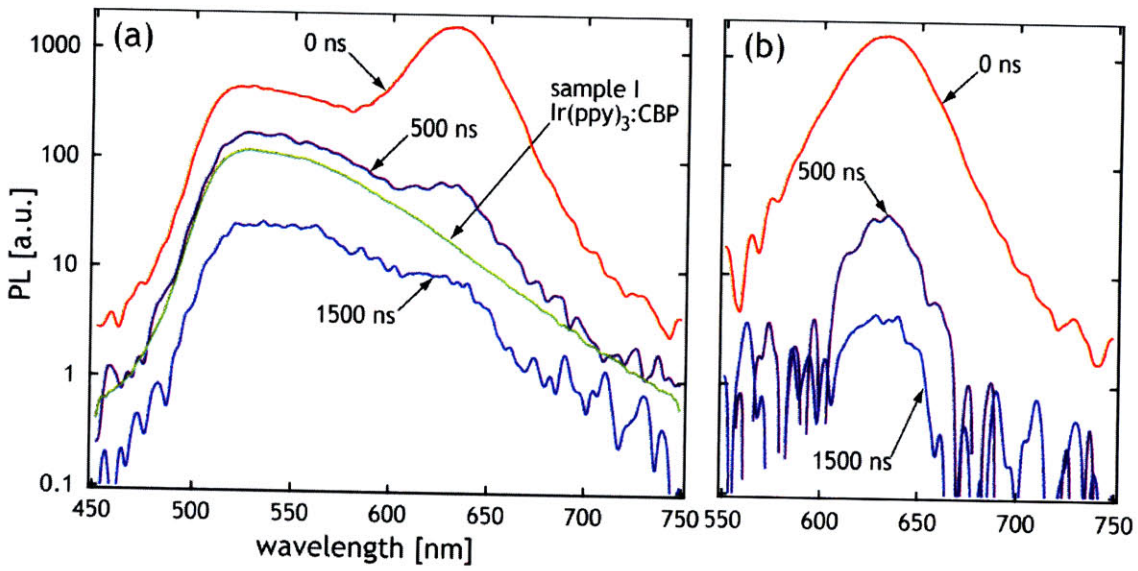

Figure 4-7: (a). PL spectra of sample III are shown at times t = 0 ns, t = 500 ns, t = 1500 ns after excitation. $Ir(ppy)_3$ integrated PL spectrum is shown for comparison (not to scale). (b) QD PL in sample III obtained by subtracting scaled $Ir(ppy)_3$ spectrum from the PL of sample III is shown at t = 0 ns, t = 500 ns, t = 1500 ns after excitation.

instant energy transfer of any $Ir(ppy)_3$ exciton that is within a distance, L_{ET}, from the QD film. In this model the dynamics of the ET process is controlled entirely by $Ir(ppy)_3$ exciton diffusion, which determines the rate at which excitons are supplied to the region within L_{ET} of the QD film.

A reasonable value for L_{ET} is determined by considering the possible ET mechanisms. In the case of Dexter transfer [46], the exciton capture region consists of a single $Ir(ppy)_3$ layer adjacent to QDs, since the transfer rate falls off exponentially with distance, reducing to negligible ET contributions from all the more distant molecular layers. Since the $Ir(ppy)_3$ molecule is on the order of 1 nm in extent, then we estimate that L_{ET} =1 nm for Dexter energy transfer. In the case of Förster transfer, the capture region can be larger. For Förster transfer, the rate of ET between a donor (D) and an acceptor (A), is given by [77],

$$K_{D\rightarrow A} = \frac{1}{\tau}\left(\frac{R_F}{R}\right)^6 \tag{4.5}$$

where R is the distance between the donor and the acceptor, τ is the donor lifetime,

and, R_F is a Förster radius,

$$R_F^6 = \frac{9}{8\pi}\frac{c^4}{n^4}\eta_D \int \frac{F_D(\omega)\sigma_A(\omega)}{\omega^4} d\omega \tag{4.6}$$

where c is the speed of light in vacuum, n is the index of refraction of the medium, κ is an orientational factor, η_D is the donor PL quantum efficiency, F_D is the donor emission spectrum (normalized to integral over frequency to unity), and σ_A is the acceptor absorption cross section.

We calculate $R_F = 4.1$ nm from Equation 4.6 by inserting the donor $Ir(ppy)_3$ PL and acceptor QD absorption spectra shown in Figure 4-3, setting n =1.7 and $\kappa^2 = 2/3$ (which averages the result over randomly oriented donor and acceptor dipoles), and using $\eta_D = 0.15$ (as estimated above). (Note: We use n =1.7 characteristic of organic thin films to obtain an upper bound on R_F. Locally the refractive index could be higher due to the higher QD index, of $n \sim 2.1$, which would lead to a lower R_F value.) This R_F value is roughly equal to the center-to-center distance between a QD and an adjacent $Ir(ppy)_3$ molecule, i.e. 3.5 nm (half the QD diameter) + 0.5 nm (half the extent of the $Ir(ppy)_3$ molecule) = 4.0 nm. We, therefore, expect that the $Ir(ppy)_3$-to-QD Förster ET is dominated by nearest neighbor transfers. However, it is worth noting that the total rate of energy transfer from a single organic molecule to a QD layer should be integrated over all of the dots in the QD layer. This calculation yields a total transfer rate that scales as R^{-4} [78]. For a hexagonally close packed QD monolayer, the total rate is given by,

$$K_{D\rightarrow AL} = \frac{1}{\tau}\frac{R_F^6}{2a^2R^4} = \frac{1}{\tau}\frac{D_F^4}{R^4} \tag{4.7}$$

where a is the radius of the QD. Using the values for a and R_F, we obtain D_F =3.7 nm. Given that as noted above the transfer distance between nearest neighbors is just 4.0 nm, we conclude, as expected from the R_F calculation, that transfer is dominated by the layer of donors in immediate contact with the QD layer, and thus we set L_{ET} =1 nm. (We note that reabsorption, Förster, and Dexter are the most commonly proposed ET mechanisms and are, hence, the mechanisms focused on in this paper.

The following analysis, however, is unchanged even for other ET mechanisms, as long as L_{ET} remains of the order of 1 nm.)

We model the emission, diffusion, and ET processes in $Ir(ppy)_3$ though a differential equation governing the time, t, and space, x, dependence of the exciton population, $n(x,t)$, in the $Ir(ppy)_3$ film:

$$\frac{d}{dt}n(x) = -\frac{1}{\tau}\left(-n(x) + L_D^2\frac{d^2}{dx^2}n(x)\right),\ 0 \leq x < L - L_{ET} \tag{4.8}$$

where L is the total thickness of the $Ir(ppy)_3$ film and $x = L$ corresponds to the $Ir(ppy)_3$/QD interface. For the film region comprising $x \geq L - L_{ET}$, we assume that any non-zero value of n is instantly lost due to ET to QD film. We further assume that initially, at $t = 0^-$, the film is uniformly excited and a moment later, at $t = 0^+$, for $x \geq L - L_{ET}$, all of the exciton concentration is lost to ET. (Because the film absorbs less than 20% of the incident excitation light, the error incurred in assuming uniform excitation is small.) Subsequently, the system evolves following Equation 4.8 with diffusion current through the $x = L - L_{ET}$ plane comprising the $Ir(ppy)_3$ excitons lost to ET due to diffusion. We perform a discrete time numerical calculation of two functions of this system: the number of emitted photons per time step, $n_{PL}(t)$, and the number of energy transferred excitons per time step, $n_{ET}(t)$. Setting L =40 nm, L_{ET} = 1.0 nm and τ =610 ns we find that for a 21% $Ir(ppy)_3$ quenching fraction, we obtain L_D = 8.1 nm. In Figure 4-6 we plot the associated fits (black lines). The $n_{PL}(t)$ function provides the fit to the $Ir(ppy)_3$ PL in Sample III. To fit the QD PL in Sample III, we scale the $n_{ET}(t)$ function by 0.6 relative to the $Ir(ppy)_3$ PL curve (to reflect the reduced PL efficiency of QDs as compared to $Ir(ppy)_3$ and the spectral collection window) and we add to it the QD PL observed in Sample II, which provides the PL due to direct excitation of the QD film. For comparison, a single exponential decay with τ =610 ns is plotted besides $Ir(ppy)_3$ PL of Sample I (data set A).

The model generated PL time dependence is consistent with both the $Ir(ppy)_3$ and QD time dependent PL intensity from Sample III. For the $Ir(ppy)_3$ PL (data set B), the deviations mainly occur at longer times ($t > 2000$ ns) where the single

exponential character of the intrinsic $Ir(ppy)_3$ PL is no longer valid. For the QD PL (data set D), the fit agrees to within the experimental error at all times. The fit suggests that the QD PL is initially due to both PL of QDs excited by incident light and PL of QDs excited by ET from $Ir(ppy)_3$. At later times ($t > 150$ ns) the QD PL dynamics are entirely due to the $Ir(ppy)_3$ exciton diffusion process. We also note that the value of L_D =8.1 nm obtained from the fit is comparable to exciton L_D values measured in other molecular organic thin film systems [94, 95].

By considering the scaling factor required to fit the QD PL in Sample III (data set D) we can calculate the PL efficiency of the QD film. Due to the measurement windows utilized in generating the intensity profiles in Figure 4-6, the $Ir(ppy)_3$ PL curve (comprising the signal between λ =511 nm and λ =568 nm) reflects 0.59 of the total $Ir(ppy)_3$ spectral intensity, while the QD PL curve (comprising the signal between λ =600 nm and λ =656 nm) reflects 0.86 of the total QD spectral intensity. Consequently, transferring $Ir(ppy)_3$ excitons to the QD layer should yield a corresponding increase in the QD PL curve equal to 0.86/0.59 = 1.46 times the loss in $Ir(ppy)_3$ photons for equal quantum efficiencies. Since we fit our QD PL data by scaling the $n_{ET}(t)$ curve down by 0.6 relative to the $Ir(ppy)_3$ fit, this implies that the quantum efficiency, η_{QD}, of the QD film is 0.6/1.46 = 0.41 times the $Ir(ppy)_3$ quantum efficiency, yielding η_{QD} =0.41*0.15 = 0.06, which is consistent with typical thin film QD PL efficiencies.

Finally, we note that the model employed here is only weakly dependent on L_{ET}, with the main effect being that as L_{ET} increases, L_D decreases because a larger fraction of the $Ir(ppy)_3$ photons are instantly quenched and therefore less diffusion is required to obtain the desired 21% total quenching. In the rather extreme case where L_{ET} =5 nm, the data can still be roughly fit by setting L_D =4.0 nm, yielding a corresponding calculation of η_{QD} =0.12. Indeed, we find that this model produces a similar time dependence to the $Ir(ppy)_3$ PL quenching and QD PL enhancement for a wide range of L_{ET} values. Consequently, on the basis of only the experiments shown here, it is not possible to conclusively identify the dominant ET mechanism (e.g. Dexter or Förster).

4.6 Energy Transfer from Fluorescent Organic Donors to QDs

The experiment described above conclusively confirms that QDs can accept triplet excitons from a phosphorescent organic donor. However, an overwhelming majority of charge transporting organics are fluorescent materials. Since one of the proposed mechanisms of QD-LED operation requires QDs to accept excitons generated in charge transporting layers, it is essential to investigate this possibility. It is evident from the overlap between red QD absorption and Alq_3 and TPD PL spectra (Figure 3-4 of Chapter 3) that red QDs could potentially accept excitons from either of the organic materials. Here we perform time-resolved PL measurements to confirm the possibility of energy transfer from Alq_3 to CdSe/ZnS core-shell QDs.

For this experiment we fabricate three samples: sample I is a 40 nm Alq_3 film on glass; sample II is CdSe/ZnS core-shell QDs emitting at λ =604 nm on top of 40 nm of TAZ (we found it difficult to print this particular batch of QDs onto glass, hence we use a wide band gap organic underlayer of TAZ that does not absorb the excitation light with λ =395 nm, but rather provides a low energy surface for QDs to rest on); finally, sample III is a monolayer of QDs printed onto a 40 nm Alq_3 film.

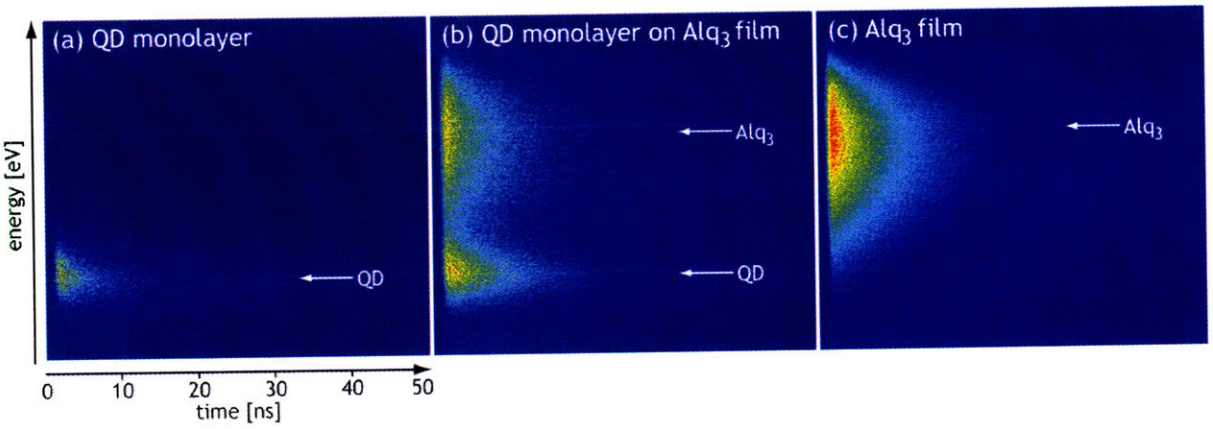

Figure 4-8: Streak camera images show the Alq_3 PL quenching and QD PL intensity increase in a hybrid Alq_3/QD structure.

We used the same optical setup as was employed in the experiment above (also shown in Figure 2-11) to collect time-resolved PL spectra of our three samples. It

is evident from the streak camera pictures in Figure 4-8 that the brightness of QD emission increases and the brightness of the Alq_3 emission decreases in the presence of each other (Sample III Figure 4-8(b)). For a more quantitative analysis we need to investigate the PL spectra in both time and wavelength domains.

Figure 4-9(a) shows the time-integrated PL spectra of Samples I, II and III. There is a clear $\sim 190\%$ increase in QD PL intensity and a concomitant $\sim 70\%$ Alq_3 PL intensity decrease, indicating a potential energy transfer from Alq_3 to QDs. Analogous to the previous experiment with a phosphorescent donor, the QD PL increase due to reabsorption of donor emission is negligible due to very low ($< 1.5\%$) absorption of a QD monolayer. Note, that the number of excitons lost by Alq_3 seems to exceed the number of excitons gained by QDs, which implies an additional quenching mechanism of Alq_3 PL in the presence of QDs, which we will not discuss here.

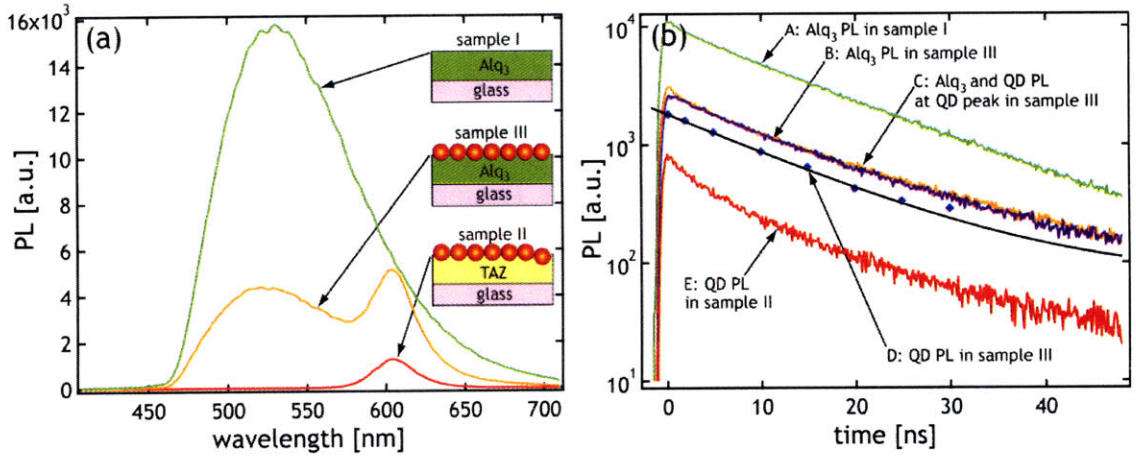

Figure 4-9: (a) Time-integrated PL spectra of samples I, II, III. All measurements were obtained at the same excitation source power of $\lambda = 395$ nm light. The PL spectrum of sample III can be constructed from a linear superposition of the PL spectra of samples I and II. (b) Time resolved PL measurements for samples I, II, and III, performed over a 50 ns time window. The colored lines and markers represent the experimental measurements. To obtain data sets A and B, the sample PL was integrated over the wavelength range of $\lambda = 509$ nm to $\lambda = 551$ nm, to yield in each case the time dependence of the Alq_3 PL. Similarly, to obtain data sets C and E, a wavelength range of $\lambda = 583$ nm to $\lambda = 626$ nm was used. Data set C therefore reflects the intensity of the combined Alq_3/ QD PL near the QD PL peak. Data set E reflects the intensity coming solely from the QD PL. To obtain data set D, the intensity due to the Alq_3 PL was subtracted from C to yield just the QD PL intensity in Sample III.

As we mentioned earlier in this Chapter, it is difficult to extract information about ET when the PL relaxation time of a donor is lower than that of an acceptor. From the PL relaxation curve for Alq_3 in sample I (data set A) and the PL relaxation curve for QDs in sample II (data set E) shown in Figure 4-9(b) we find the PL relaxation times of both QDs and Alq_3 are ~10-12 ns. Therefore, it is difficult to detect changes in the PL relaxation times of these materials in the presence of ET. While Alq_3 PL is quenched in sample III, the difference in the PL relaxation time is on the order of the experimental error (data set B). However, the PL decay taken at the QD emission wavelength (data set C) matches the Alq_3 PL decay almost exactly, confirming the ET nature of Alq_3 PL quenching. To avoid errors associated with the Alq_3 PL contribution to data set C, we subtract the Alq_3 component (akin to Figure 4-7(b)) to obtain the solely QD PL decay curve in sample III (data set D), which also closely matches the Alq_3 PL decay profile.

It is evident from the QD PL intensity increase in Figure 4-9(a) that the presence of neighboring Alq_3 enhances the QD PL. The ET to QDs is the most likely mechanism of the Alq_3 PL quenching. Consequently, exciton generation in Alq_3 and ET to QDs can benefit the performance of QD-LEDs. The analogous argument can be made with respect to QDs and TPD. However the short TPD PL relaxation time of ~1 ns complicates the data analysis.

4.7 Summary

Here we clearly demonstrated that colloidal CdSe/ZnS core-shell QDs routinely used in QD-LED design can accept triplet excitons from an organic phosphorescent donor $Ir(ppy)_3$, which is manifested in an increase in the PL intensity and an increase in PL lifetime for a CdSe/ZnS QD thin. The observed ET dynamics are self-consistently explained by a simple numerical model that combines exciton diffusion in the $Ir(ppy)_3$ film with short-range ET from $Ir(ppy)_3$ to the QD layer. The demonstrated transfer of triplet excitons to luminescent QDs could benefit the development of QD optoelectronic technologies, such as QD-LEDs.

We have also demonstrated the possibility of singlet exciton energy transfer from Alq_3 to QDs, which implies that the exciton generation in organic charge transporting layers and subsequent exciton transfer to the emissive QD monolayer is an important mechanism to consider for QD-LED design and operation.

Chapter 5

Mechanism of QD-LED Operation: Experimental Study

Previous chapters have discussed different aspects of the QD-LED operation such as charge injection into different QD types, energy transfer (ET) between the different QD types, and ET between the organics and QDs. This chapter is dedicated to gaining an understanding of the fundamentals of carrier transport and exciton generation in QD-LEDs through experimental investigation of various QD-LED structures.

5.1 Energy Transfer vs. Charge Injection

To date, QD-LED emission across the visible and near-IR spectrum [17, 54, 96] has been demonstrated. However, we still find that the external quantum efficiency differs for QD-LEDs of different color. The best published green, red, and orange QD-LEDs exhibit peak efficiencies in the range of 1-2% [17, 30, 31, 32], while the efficiency of blue QD-LEDs is on the order of 0.3% for QDs of similar starting QD solution photoluminescence (PL) efficiencies [17, 33]. Finding the origins of QD electroluminescence in QD-LEDs through understanding the differences in performance of various QD-LED types is essential to the systematic design of more efficient QD-LEDs.

Figure 5-1 illustrates the mechanisms involved in QD-LED operation. When positive bias is applied to the anode (potential at the anode $\phi_a = V > 0$) and the cathode

is grounded (potential at the cathode $\phi_c = 0$), electrons are injected from a metallic cathode (e.g. Mg/Ag alloy) into an organic hole transporting layer (e.g. TPD, CBP) and holes are injected from a transparent conductive oxide anode (e.g. ITO) into an organic electron transporting layer (e.g. Alq_3). The injected carriers then travel through the organics towards the QD film. These carriers can then form excitons on (I) or near (II) QD sites leading to the QD electroluminescence (EL). Two mechanisms have been proposed to explain the QD EL in QD-LEDs [17, 54, 74]. In mechanism I in Figure 5-1, which we will refer to as the "direct charge injection", carriers transported through the organic charge transport layers are directly injected into QDs, where they can form excitons that can radiatively recombine. In mechanism II in Figure 5-1, which we will refer to as the "exciton energy transfer", excitons are formed on the organic molecules surrounding the QD film. Excitons then can resonantly transfer to QDs, where they recombine radiatively. In this chapter we assess the relative contributions of the two mechanisms to QD-LED EL.

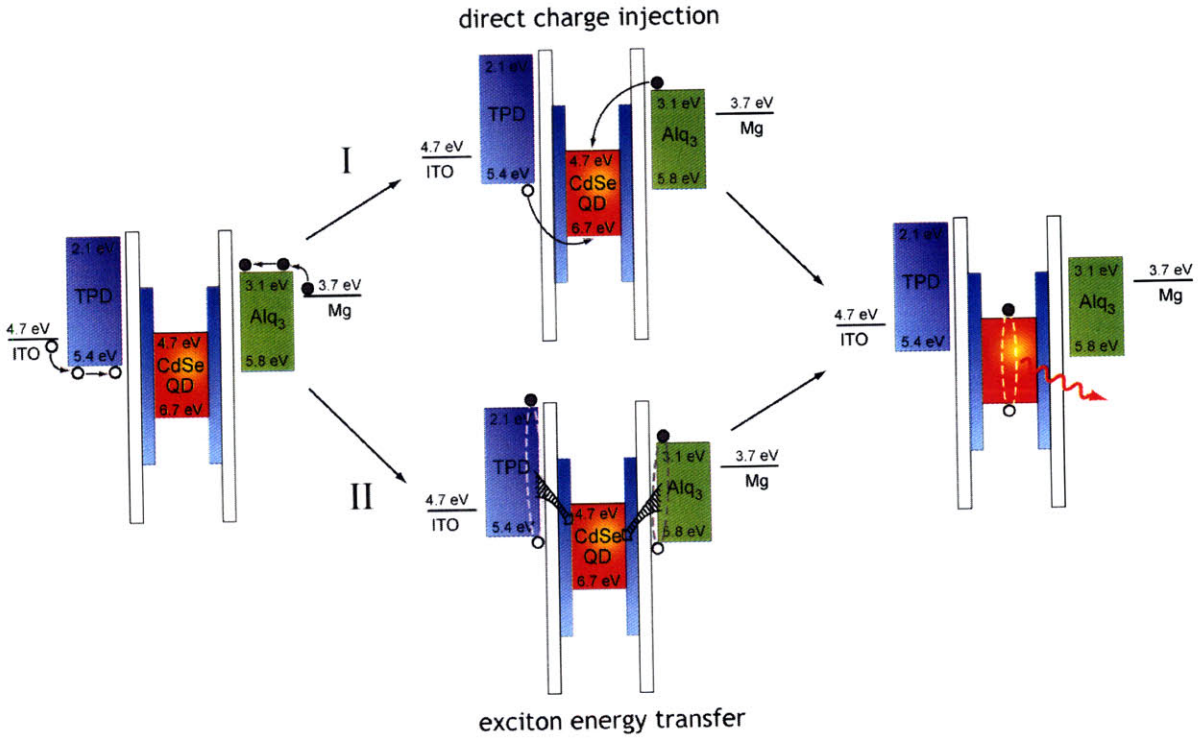

Figure 5-1: Schematic diagram illustrates the two proposed mechanisms of QD-LED operation. Mechanism I is referred to as "direct charge injection", and mechanism II is referred to as an "exciton energy transfer".

In order to investigate the relative positions of the exciton generation and recombination regions, we fabricate a set of devices shown in Figure 5-2, in which we vary the position of the emissive QD monolayer within the QD-LED structure. Device 1 is a control OLED [8, 9], device 2 represents a standard QD-LED structure with a QD monolayer deposited at the interface between the hole and electron transporting layers, in devices 3 and 4 QD monolayers are embedded into the hole transporting layer (HTL) 10 nm and 20 nm, respectively, away from the interface. In devices 5 and 6 QD monolayers are embedded into the electron transporting layer (ETL) 10 nm and 20 nm, respectively, away from the interface.

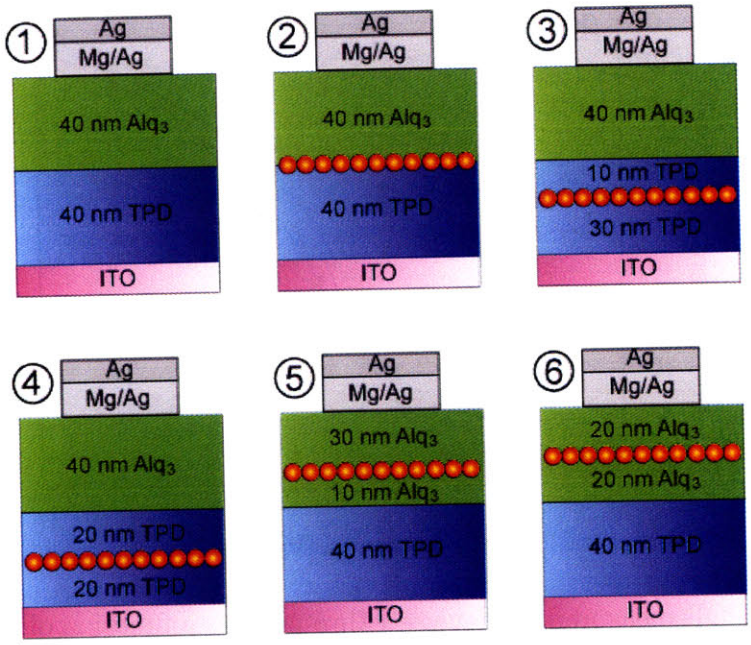

Figure 5-2: Schematic diagrams of device structures 2 through 6 with QD monolayer deposited at different positions within the device stack. Device 1 is a control OLED, containing no QDs.

5.2 Experimental Observations

Figure 5-3(a) plots the EQE of the devices 1 through 6. Device 1 exhibits a peak EQE of 0.8% consistent with previous reports [8, 9]. (Note: Throughout this Chapter, the EQE, by definition, is the number of emitted photons per number of injected electrons multiplied by 100 %.) Device 2 shows a 1.5% peak EQE, which is on the

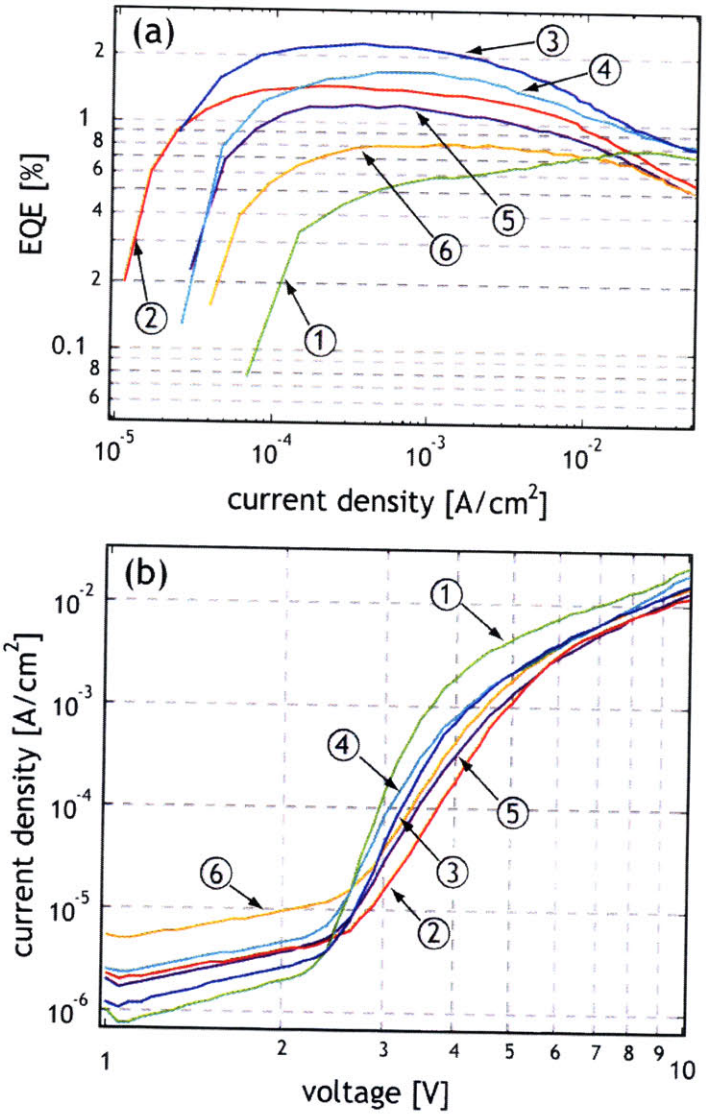

Figure 5-3: (a) EQE measured for devices 1 through 6 as a function of current through each device. (b) Current-voltage characteristics for devices 1 through 6.

same order of magnitude as in previous reports [30]. Devices 3 and 4 that have QD monolayer embedded into a hole transporting layer show higher peak EQE values of 2.3% and 1.7%, respectively, while devices 5 and 6 have peak EQE values of 1.1% and 0.8%. From these results it is evident that embedding a QD monolayer into a HTL improves the device efficiency by $\sim 50\%$, while embedding QDs into an ETL leads to a decreased device efficiency as compared to the standard device 2 structure.

Normalized EL spectra for devices 1 through 6 are shown in Figure 5-4. The EL spectrum of the device 1 OLED is solely due to Alq_3 emission, which is consistent

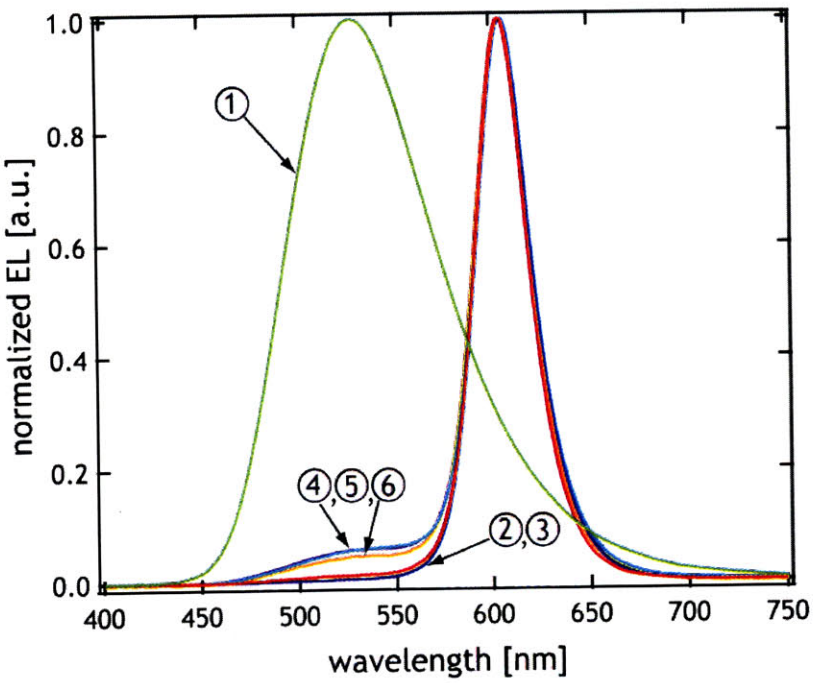

Figure 5-4: Normalized EL spectra for devices 1 through 6 are shown at 4 V of applied bias.

with previous reports [8, 9]. EL spectrum for the device 2 archetypical QD-LED is solely due to narrow QD emission, which is also consistent with the previous studies [30]. However, we note that the rest of the devices 3 through 6 have EL spectra dominated by QD emission despite the variable position of the QD monolayer in different structures. The EL spectrum of the most efficient device 3 does not exhibit any organic emission contribution, and the EL spectra of devices 4, 5 and 6 show only minor Alq_3 components.

Figure 5-5 plots the energy band diagrams for devices 1 through 6. HOMO levels of organic materials are obtained from electron photoemission measurements, and optical absorption spectroscopy is used to determine the relative position of the LUMO levels [97]. The energy band structure of QDs is derived numerically by starting with the bulk semiconductor energy band structure and confining it to the size of the QDs while assuming that carriers in QDs retain the effective mass of bulk semiconductors [13]. It is apparent from Figure 5-5 that QDs provide an energy trap for the mobile electrons in the structure, and are not likely to trap holes, due to the high $\sim$1 eV energy barrier for the hole transport from the HOMO levels of TPD and Alq_3 into

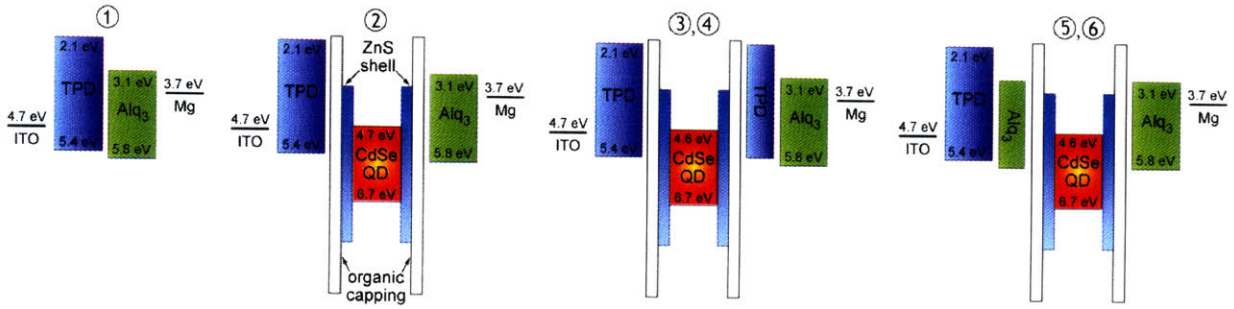

Figure 5-5: Suggested energy band diagrams for devices 1 through 6.

QDs (see Figure 5-5).

QD charging, due to the accumulation of electrons, can lead to QD luminescence quenching via the non-radiative Auger recombination mechanism [80]. Auger recombination requires a presence of an exciton and an unpaired carrier (electron or hole) at a QD site, which can arise when the concentration of one charge carrier type is significantly higher than the concentration of the other carrier type at a QD. During the Auger recombination, the energy released from the exciton recombination promotes the unpaired carrier to a higher energy level, from which it can thermally relax to its ground state [98]. Auger recombination occurs on a 100 ps time scale [80], much faster than the radiative recombination lifetime of QDs, which is on the order of 10 ns [45, 75], resulting in the rapid quenching of QD luminescence. Embedding the QDs into a HTL can decrease the electron concentration at QD sites, and consequently, decrease the likelihood of Auger recombination events, consistent with the observed increase in QD luminescence efficiency for devices 3 and 4.

5.3 Contribution of the Exciton Energy Transfer to QD-LED Electroluminescence

In Chapter 4 we have demonstrated that thin films of colloidal QDs can efficiently accept excitons from organic thin film donors, which was manifested as an increase of the QD luminescence intensity in time-resolved PL experiments [92]. The exciton energy transfer from organic thin films to QDs can also be responsible for a QD EL

in QD-LEDs, akin to its contribution to EL of OLED structures. For example, in the device 1 OLED structure, excitons are formed at the TPD/Alq_3 interface. Due to the higher potential barrier for the electron injection from Alq_3 into TPD, as compared to the potential barrier for the hole injection from TPD into Alq_3, the majority of excitons are formed on Alq_3 molecules. Furthermore, all excitons formed on TPD molecules can efficiently transfer their energy via the Förster mechanism [77] to Alq_3 molecules due to the spectral overlap of the Alq_3 absorption and TPD emission, resulting in an EL spectrum that consists entirely of Alq_3 luminescence (Figure 5-4).

As we have shown in Chapters 3 and 4 the absorption spectra of orange and red QDs overlap with the Alq_3 and TPD PL spectra, which indicates the possibility of Förster energy transfer (ET) from these materials to QDs. In Chapter 4 we have also demonstrated the increase of QD PL intensity in the presence of neighboring Alq_3 film. Due to the large absorption cross-section of each QD, we find the Förster radius R_F to be on the order of 7.5 nm for the energy transfer from a single Alq_3 or TPD molecule to a single QD. The exciton energy transfer rate from a single molecule to a plane of QD acceptors is then obtained by integrating over a QD monolayer [78]:

$$K_{D\to A} = \frac{R_F^6}{\tau}\int_{r=0}^{r=\infty}\frac{2\pi\rho_A r dr}{(r^2+D^2)^3} = \frac{R_F^6}{2a^2D^4\tau} = \frac{1}{\tau}\left(\frac{D_F}{D}\right)^4 \tag{5.1}$$

where a is the QD radius, τ is the donor PL relaxation time, D is the distance from a donor to a plane of QD acceptors, and D_F is the Förster distance for the energy transfer from a single donor to a plane of acceptors. For the energy transfer from the TPD or Alq_3 molecules to a monolayer of QDs ($a = 2.5$ nm), we find a Förster distance of $D_F \sim 11$ nm.

This implies that we should observe a substantial energy transfer to QDs of the Alq_3 or TPD excitons formed a distance D_F away from the QD layer. This is in agreement with the QD-LED EL spectra displayed in Figure 5-4: For the devices 2 and 3, that have QDs deposited at the TPD/Alq_3 interface or embedded 10 nm into the TPD HTL, we observe no Alq_3 or TPD contribution to the EL spectra, which implies a complete energy transfer of the Alq_3 or TPD excitons to the QDs. In

devices 4 and 6, 20 nm spacing between the QD monolayer and TPD/Alq_3 interfaces is arguably large compared to the Förster distance of 11 nm for the resonant energy transfer to be observed, but we nevertheless only observe a small Alq_3 contribution in the EL spectra of devices 4 and 6. This can be explained by taking into account the exciton diffusion length, which is on the order of 8 nm in organic thin films [92, 94, 95]. In devices 4 and 6, the excitons formed at the TPD/Alq_3 interface have to diffuse, prior to the energy transfer to QDs, and can recombine on Alq_3 molecules contributing to the Alq_3 spectral signature.

If we assume that the exciton energy transfer is the dominant mechanism in QD-LED operation, the observed increase in the QD-LED efficiency upon embedding the QDs into a hole transporting layer (as in devices 3 and 4) can be accounted for by the diminished charge accumulation at the QD sites. Since the electron transport from Alq_3 to QDs in this case is inhibited by the intervening TPD layer, and a hole accumulation at QDs is unlikely due to the energy level alignment, the probability of an exciton transfer to a charged QD is low, which leads to a low occurrence of the Auger quenching process, and a desired increased EQE.

To form excitons on the organic charge transporting layers of QD-LEDs, holes have to be able to travel through the TPD layer to the TPD/Alq_3 interface, but the proposed band diagrams of Figure 5-5 show that the hole transport should be impeded in devices 2, 3, and 4 by the presence of the QD monolayer that forms a potential barrier to the hole transport. We note however, that the one-dimensional energy diagrams sketched in Figure 5-5, fail to take account of the three-dimensional shape of the QDs. AFM images of QD monolayers in QD-LEDs show that the 5 nm diameter QDs form hexagonally close packed monolayers on top of TPD surface after the microcontact printing [15] (e.g. Figures 2-7 and 3-3), producing nm-scale openings between the QD sites. Deposited organic films fill these openings allowing for the holes and electrons to pass through the device, bypassing QDs, and reaching the Alq_3/TPD interface where the excitons are formed.

In efficient OLEDs, where Auger recombination is negligible and leakage currents are small, higher current densities result in higher exciton formation rates. In less

power efficient OLED structures, charge accumulation (at charge trap sites or heterointerface potential steps) results in internal electric fields, driving charge in the opposite direction to the applied bias voltage, leading to lower space charge-limited currents [62, 99] at a given externally applied voltage, and consequently, to lower exciton formation rates. Similarly, the charge transport in QD-LEDs is also governed by the properties of organic charge transporting layers, so that space charge limited conduction [62, 99] is the dominating conduction mechanism. As QDs trap electrons efficiently, we expect electron accumulation at QD sites, which contributes to space charge build-up and results in lower currents through the device at a given external bias, lower exciton formation rates, and higher Auger loss rates at the QD sites, which is manifested in lower QD-LED EQE. The performance of devices 2, 5 and 6 is consistent with this analysis, as they demonstrate lower current densities at a given bias voltage (Figure 5-3(b)) and lower EQEs (Figure 5-3(a)) as compared to devices 3 and 4.

It is assumed in the analysis above that the leakage currents through the devices are small, which is supported by the OLED EQE value consistent with previous reports [8, 9]. High leakage currents resulting from short circuit pathways through the device, typically caused by morphological defects, impede the device efficiency, as they do not contribute to the device EL. In order to compare the exciton generation in different LED structures, it is essential to fabricate the devices in a parallel process conserving the design parameters so that the internal morphology is consistent from one device to another.

5.4 Contribution of the Direct Charge Injection to QD-LED Electroluminescence

While the experiment described above provides evidence for the exciton energy transfer contribution to the QD-LED operation, the observed trends also appear consistent with the direct charge injection model for the QD-LED operation. The increase in the

QD-LED EQE upon embedding the QDs into a HTL, as in devices 3 and 4, may imply better electron and hole balance. In these structures electrons travel through a thin HTL before reaching the QDs, which slows down the electron arrival to the QD sites, lowering the number of electron-exciton complexes at QDs, reducing the occurrence of Auger recombination events and therefore increasing the overall QD luminescence efficiency. Conversely, embedding QDs into an ETL, as in devices 5 and 6, leads to an increase in the electron concentration at QD sites leading to higher probability of formation of the electron-exciton complexes, and consequently, a decreased QD-LED efficiency. In order to test the charge balance hypothesis and to investigate electron transport in QD-LEDs, we fabricated QD-LED structures shown in Figure 5-6, in which we insert a TPD electron blocking layer (EBL) inside Alq_3 ETL and we vary the thickness of TPD from 0 nm to 16 nm inside the Alq_3 ETL. The presence of the barrier to the electron transport may result in a reduced electron concentration at QD traps, leading to more balanced electron and hole concentrations at the QD sites and consequently reduced formation of undesirable electron-exciton complexes.

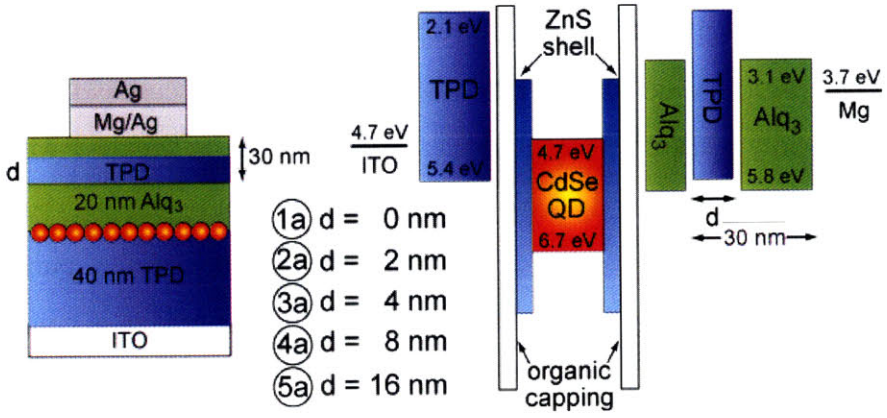

Figure 5-6: Schematic device structure for devices 1a through 5a. Thickness of the TPD electron blocking barrier, d, is varied for the devices, while the total thickness of the electron transporting layer is kept equal to 50 nm, and the TPD blocking layer is separated by 20 nm of Alq_3 from the QD monolayer. d = 0 nm for device 1a, d = 2 nm for device 2a, d = 4 nm for device 3a, d = 8 nm for device 4a, d = 16 nm for device 5a.

All the devices of Figure 5-6 are fabricated on glass substrates, and have an ITO anode with a PEDOT:PSS hole injecting layer, with a 40 nm TPD layer for hole transport, on top of which an emissive colloidal QD monolayer is deposited via contact

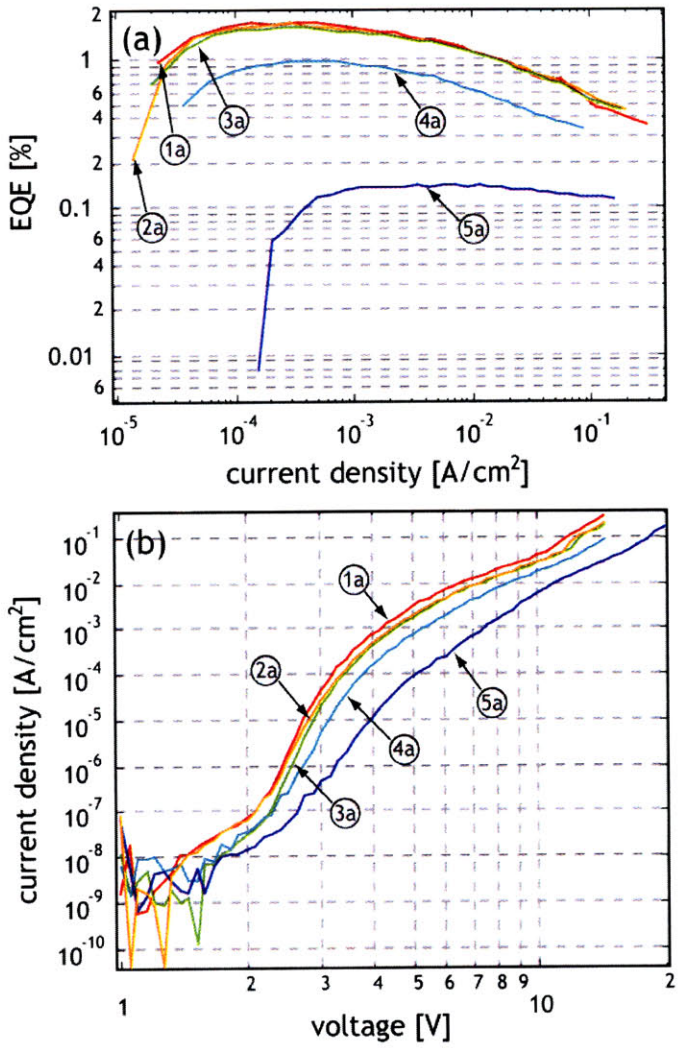

Figure 5-7: (a) EQE of devices 1a (red), 2a (orange), 3a (green), 4a (cyan), and 5a (blue) as a function of the current density through each device. (b) Current-voltage characteristics for devices 1a (red), 2a (orange), 3a (green), 4a (cyan), and 5a (blue).

printing [16]. The 50 nm electron transporting layer consists of Alq_3 for device 1a; for the remaining devices, the electron transporting layer is built of a 20 nm thick Alq_3 film on top of the QD monolayer followed by the TPD EBL of varying thickness (2, 4, 8 and 16 nm) and an Alq_3 layer with its thickness chosen to result in a total 50 nm thick electron transporting layer (28, 26, 22 and 14 nm,). Mg:Ag cathodes protected with Ag overlayers are deposited on top of the structures.

Figure 5-7(a) shows EQEs for devices 1a through 5a. Devices 1a, 2a and 3a have EQEs of 1.8, 1.7 and 1.6% respectively. The EQE of device 4a is significantly lower $\sim 1\%$, and finally device 5a is the least efficient with its EQE of $\sim 0.14\%$.

The IV-characteristics (Figure 5-7(b)) for devices 1a through 5a show that device 1a is the least resistive and device 5a is the most resistive. The resistance of the devices gradually increases with increasing thickness of the electron blocking TPD layer, which is in agreement with the device structures and band diagrams of Figure 5-6 that illustrate an increasingly impeded electron transport with the increasing thickness of the inserted TPD layer. However, the decrease of EQE with increasing thickness of inserted TPD layer is unexpected, as the inserted TPD layer should improve the balance of electron and hole densities at QD sites, reducing the Auger process and increasing EQE. This surprising finding implies that the charge balance at QD sites, and consequently, the direct charge injection into QDs does not contribute significantly to the QD-LED efficiency. In contrast, the exciton energy transfer plays a more significant role in the QD-LED operation.

5.4.1 Effects of the QD Charging on QD-LED efficiency

We also performed repeated EQE measurements on each of the devices of Figure 5-6, using 4 measurement cycles with a 30 sec interval between the cycles (Figure 5-8(a) plots). For devices 1a, 2a, 3a, we find a nearly 50% decrease in EQE from the first to the second measurement, with an additional $\sim 20\%$ decrease in EQE on the third measurement cycle, and $\sim 10\%$ decrease on the fourth cycle. A smaller decrease in EQE is observed for the sequence of measurements on device 4a ($\sim 40\%$ decrease on the second measurement, $\sim 10\%$ on the third, and $\sim 5\%$ on the fourth cycle); while for device 5a there is no noticeable change of EQE with consecutive measurement cycles. We also notice that EQE of the originally most efficient device 1a decreases the most in the second, third and fourth cycles, which makes it less efficient in those cycles than the devices 2a and 3a.

We repeated the test cycling of our devices on the following day and found EQEs nearly the same as for the fresh devices (Figure 5-8(b)), prior to cycling. The observed decrease in EQE of the cycled devices, and subsequent recovery after a one day wait period, can therefore be attributed to the charging of the QD monolayer with excess electrons during operation, and a slow release of charge that was trapped on QDs as

the devices rested for one day. (Note: We perform all of the QD-LED testing in the N_2 glovebox, and a small number of oxygen and particularly water molecules may accumulate in the glovebox environment. A minor permanent decrease in QD-LED EQE can be attributed to the potential morphological modifications in the organic films due to the aggressive testing conditions and the presence of oxygen and water molecules in the surrounding environment. In addition the presence of oxygen and moisture may cause the oxidation of Mg/Ag contacts, which decreases the active area of the device pads.)

The charging of the QDs in the QD-LED structure contributes to the decrease in EQE, and from the above cycling experiment it is apparent that structures 2a through 5a reduce the QD charging as compared to device 1a, with the most pronounced decrease in charging observed for devices 4a and 5a. However, while in these structures we can controllably eliminate electron accumulation at the QD sites, we do not observe an increase in QD-LED efficiency upon inserting thicker TPD EBL into the Alq_3 layer. Instead, the QD-LED peak efficiency is the lowest for devices 4a and 5a.

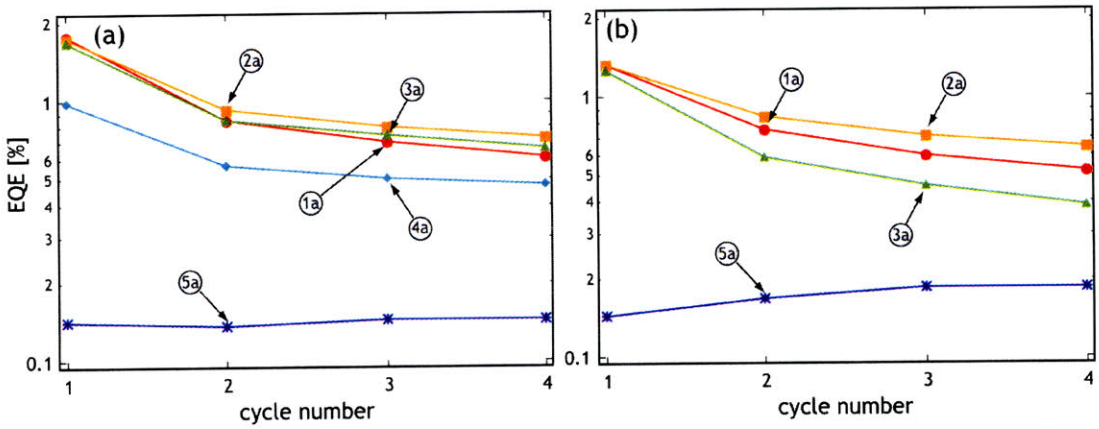

Figure 5-8: (a) Peak EQE for devices 1a through 5a, taken in four consecutive cycle measurements separated by ~30 seconds. In every measurement cycle the bias voltage is scanned from 1 V to 15 V (devices 1a through 4a) or from 1 V to 20 V (device 5a). (b) Peak EQE for devices 1a, 2a, 3a and 5a measured in an experiment identical to the one in (a) performed on a next day.

To explain the observed data, we note that the EQEs of these devices are not solely governed by the QD charging but also by exciton generation. Charge accumulation in Alq_3 at the TPD EBL interface located closer to the cathode results in a decreased

current through the device, and consequently, a decreased exciton formation. Thin TPD EBL of devices 2a and 3a does not lead to a significant charge accumulation at the Alq_3/TPD interface and consequently does not have a major impact on the peak EQE. The thick TPD EBL of devices 4a and particularly 5a significantly impedes electron transport through these devices (which is in agreement with the observed IV-characteristics of Figure 5-7(b) that show higher resistance for these devices) reducing exciton formation and consequently lowering EQE.

Another important factor contributing to QD-LED EQE is the distribution of internal electric fields within a structure. It has been previously demonstrated that in the structures that incorporate single QDs into hole transporting organic thin films the field induced exciton dissociation is the primary mechanism for QD luminescence quenching [100]. In those structures QD charging is not expected to significantly contribute to QD luminescence quenching, since QDs are well separated from each other, providing low resistance pathways for carrier transport. Additionally, the current in those devices is dominated by the holes that are not trapped efficiently by QDs. In our study a close-packed QD monolayer provides an electron trap, and the proximity of the electron transporting layer results in a high probability of the electron capture by QDs. While incorporating the TPD EBL may cause a change in the distribution of internal electric fields in QD-LED structures, we do not expect the field across the QD monolayer to change by the several orders of magnitude needed to significantly impact the exciton dissociation rate. Consequently the QD charging with electrons is expected to have a more dramatic effect on the QD luminescence efficiency in our devices.

5.4.2 Exciton Formation in QD-LEDs

To investigate the exciton formation mechanism in devices 2a through 5a we perform EL measurements at different applied bias conditions (Figure 5-9). The EL for devices 2a through 4a was measured at bias voltages between 3 V and 15 V, and for device 5a the EL was measured at bias voltages between 6 V and 20 V, since this device has a significantly higher resistance and a higher turn-on voltage. Figure 5-9 shows

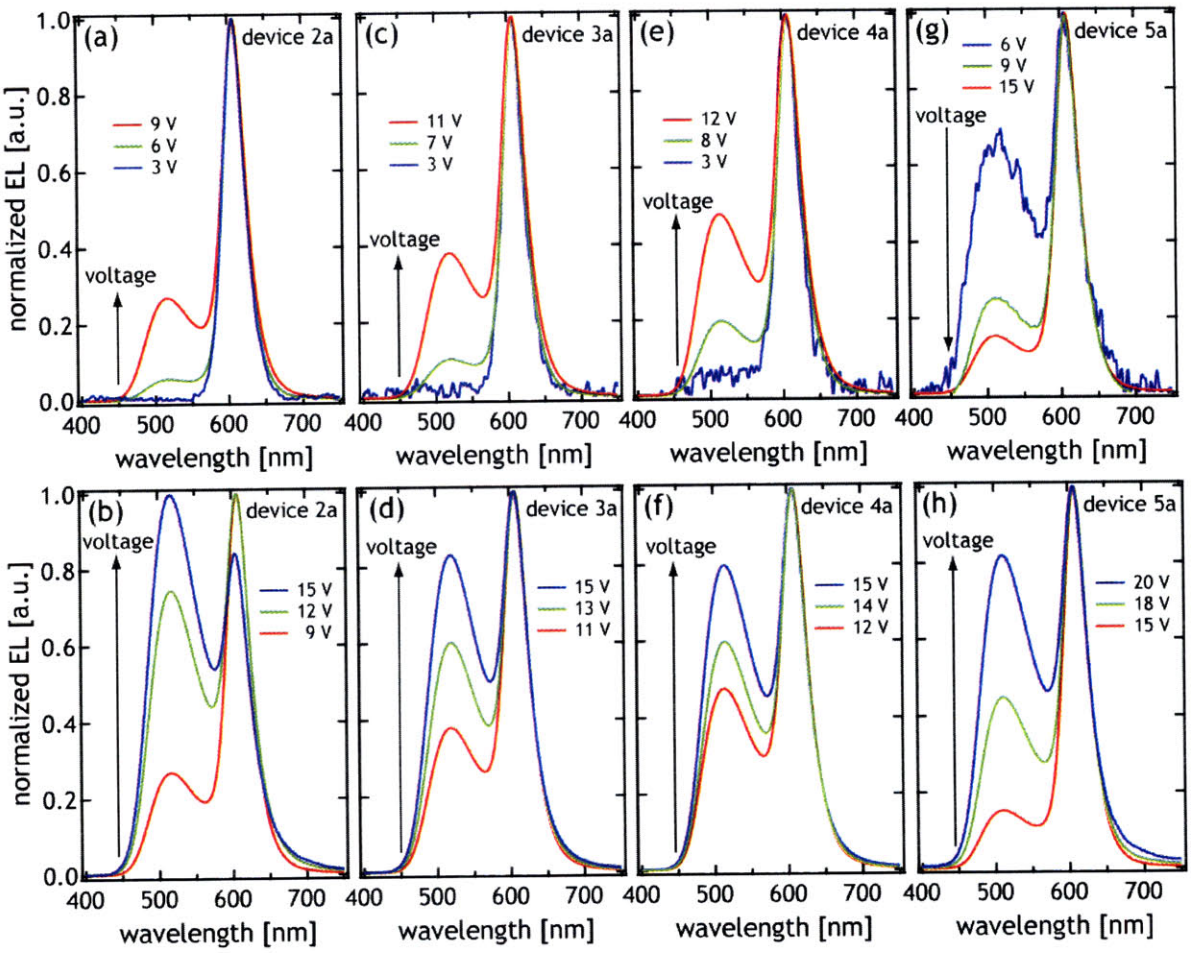

Figure 5-9: (a), (c), (e), and (g) Normalized EL spectra for devices 2a, 3a, 4a, and 5a taken at different bias voltages. EL intensity increases with increasing applied bias. (b), (d), (f), and (h). Normalized EL spectra for devices 2a, 3a, 4a, and 5a taken at different bias voltages. In these plots EL intensity decreases with increasing applied bias. The arrow shows the direction of the increasing bias voltage.

normalized EL spectra for each of the devices divided into two groups. The first set of EL spectra (Figure 5-9 (a), (c), (e), (g)) corresponds to the voltages, at which the EL intensity increases with the increasing applied bias voltage, and the second set (Figure 5-9 (b), (d), (f), (h)) corresponds to the voltages, at which the EL intensity decreases with the increasing applied bias. All the devices reach a maximum brightness at similar driving current densities $J \sim (3 \pm 1)$ mA/cm^2 that correspond to 9 V for the device 2a, 11 V for the device 3a, 12 V for the device 4a, and 15 V for the device 5a. The decrease of the EL intensity with higher applied currents (voltages) is atypical of OLEDs, and in these QD-LED structures can be caused by the charge accumulation at QD sites and at the TPD (EBL)/Alq_3 interface.

We also notice that the contribution of the Alq_3 emission to the device EL spectra increases consistently with increasing applied bias for the devices 2a, 3a and 4a. For the device 5a EL spectra, we first observe the decrease in the Alq_3 component at bias voltages between 6 V and 13 V, followed by an increase at bias voltages above 13 V, akin to that of the devices 2a through 4a. The evolution of the EL spectra appears consistent with the energy transfer model and can be explained by the position of the exciton formation region within the devices. In devices 2a, 3a, and 4a, where the TPD EBL is sufficiently thin for electrons to transport through, the majority of excitons form in the Alq_3 layer next to a QD monolayer, from where they resonantly transfer to the QDs. At higher currents through the device, the concentration of electrons at QD sites significantly increases, leading to the Auger-facilitated quenching of the QD emission. In addition, the exciton generation region becomes wider occupying a larger volume of Alq_3, and consequently, some excitons form further than a distance D_F away from the QD monolayer, which increases the probability of their radiative recombination on Alq_3 molecules [101]. In device 5a, where the TPD EBL is thick, at lower bias voltages a majority of electrons are slowed down by the barrier, and do not reach the Alq_3/QD interface. Consequently, the exciton formation region is shifted towards the Alq_3/TPD (EBL) interface, which is more than $2D_F$ away from the QD monolayer, leading to a significant radiative recombination of the excitons on Alq_3 molecules. At higher bias voltages, the electrons have a higher probability of reaching

the Alq_3/QD interface, thus contributing to exciton generation near QD sites, and hence, resulting in a more efficient energy transfer and a higher QD emission intensity. At very high bias voltages >13 V we observe the same trend as for devices 2a, 3a and 4a, where the exciton formation region at higher bias voltages occupies the bulk of the Alq_3 layer adjacent to QDs.

The spectral purity of the QD-LED emission is very sensitive to the device structure and can differ with respect to different fabrication methods. Factors such as the closeness of the QD-to-QD packing in the QD monolayer, or number of QD monolayers in a QD-LED structure have a significant impact on the QD-LED EL spectra. The morphology of a monolayer depends on both the QD size distribution and on the average QD size, i.e. smaller QDs tend to provide denser films. In archetypical QD-LED structures, akin to the device 1a in Figure 5-6, organic components of the EL spectra tend to increase with increasing bias voltage [101]. However this effect may not be apparent at low voltages (<10-15 V) in devices with a high QD packing density or multiple QD layers. In order to investigate exciton generation regions in QD-LEDs in our work, we only compare devices fabricated in parallel that have identical design parameters, such as the QD film morphology.

5.5 Summary

Our experiments suggest that charging of the QDs with electrons significantly contributes to a decrease in the QD-LED efficiency. One method to improve the performance of these devices is to embed the luminescent QD monolayer into a hole transporting layer $\leq$10 nm away from the exciton-generating interface. We also suggest that resonant energy transfer makes a significant contribution to the device performance, and exciton formation within the Förster distance away from the QD monolayer can be beneficial for increasing the device efficiency. Having a precise control over the position of the exciton formation region enabled us to monitor energy transfer processes within the device structure, which is crucial for applications where the contribution to the EL spectrum by each emitter type is important. While exci-

ton formation through direct charge injection could potentially lead to more efficient devices (since this process eliminates exciton losses associated with an incomplete energy transfer), it demands a precise electron and hole concentration balance, and a similar barrier for electron/hole injection into the QDs. In the case of a charge imbalance, or if one carrier is trapped by QDs more efficiently than the other, the EQE of the device would be reduced by QD charging and consequent Auger recombination.

Designing devices that rely on the precise charge balance and exciton formation on QDs can be difficult and requires a hole transporting material with a lower HOMO level than the QD valence band and a bandgap larger than that of QDs. Designing devices that mostly rely on the exciton generation within the organic layers and their resonant transfer to QDs does not call for the design and synthesis of new organic materials, while gives an opportunity to use efficient donors (for example phosphorescent materials) for the exciton generation and a subsequent transfer to the QDs.

Chapter 6

Mechanism of QD-LED Operation: Physical Model

In our experimental effort described in detail in Chapter 5 we investigate the contribution of two main mechanisms to the QD-LED operation, the first, based on the direct charge injection into QDs followed by exciton formation and recombination on QD sites, and the second, relying on the exciton formation in organic films in the vicinity of QDs and a subsequent exciton energy transfer to QDs. We find that maximizing the exciton energy transfer from organic donors to QDs as a primary device operating mechanism may result in more efficient QD-LEDs, as it eliminates QD charging, and thus Auger recombination, which is one of the main processes contributing to QD luminescence quenching. Our experiments show that embedding QDs into a hole transporting layer <10 nm away from the interface between a hole and an electron transporting materials results in a 50% QD-LED efficiency increase, which we attribute to both decreasing QD charging and improving exciton generation at the interface between the hole and electron transporting materials.

This Chapter is dedicated to a physical model for the carrier and exciton transport in QD-LEDs that allows us to calculate numerically carrier and exciton concentration profiles, and local electric fields, for a variety of QD-LED device structures.

6.1 Theoretical Background

6.1.1 Carrier Transport

As we discussed in Chapter 1, organic semiconductors are characterized by carrier mobilities lower than those of crystalline inorganic semiconductors such as silicon (Si) or gallium nitride (GaN). In contrast to crystalline semiconductors, in amorphous organic thin films, carriers are localized at any given moment in time, and carrier transport is dominated by molecule-to-molecule hopping rather than by an in-band travel process [102]. Since the molecules composing organic charge transporting films are electrically neutral in equilibrium, the concentration of free charges in organic semiconductors is low ($\sim 10^6$ cm^{-3}) [46] compared to the intrinsic concentration in Si (10^{10} cm^{-3}), and therefore the current through the device at a given externally applied bias voltage is dominated by the injected carriers. As carriers move slowly through the organic devices and can potentially be trapped on organic molecules with relatively lower LUMO (or higher HOMO), the field across the device depends on the net charge present inside it. According to Poissons law in one dimension [62]:

$$\frac{dE}{dx} = \frac{4\pi}{\varepsilon} e(p - n) \tag{6.1}$$

where E is the magnitude of the electric field, x is the position, ε is the dielectric constant of the organic film, e is the electron charge, n and p are electron and hole concentrations, respectively.

If we only consider our devices after the "turn-on" and, hence, neglect the effects of charge trapping, then, in the simplest approximation, we can describe carrier transport through an organic device with the field-driven (drift) and concentration gradient-driven (diffusion) fluxes. The total carrier flux is a sum of the drift and diffusion carrier fluxes [103]:

$$\begin{aligned} J_n &= nE\mu_n B_c + D_n \tfrac{dn}{dx} B_c \\ J_p &= pE\mu_p B_v + D_p \tfrac{dp}{dx} B_v \end{aligned} \tag{6.2}$$

where J_n and J_p are electron and hole fluxes, respectively, μ_n and μ_p are electron and hole mobilities, D_n and D_p are electron and hole diffusion constants, and B_c and B_v are scaling factors used to describe carrier transport between materials with different HOMO and LUMO levels. For simplicity we can use Einstein relation to approximate the carrier diffusion constants [103]:

$$D_{n,p} = \frac{\mu_{n,p} k_B T}{e} \tag{6.3}$$

In order to describe the carrier transport in an optoelectronic device such as an OLED, we have to take into account the differences in energies between the HOMO and LUMO bands for different materials comprising the device. We use the Boltzmann distribution coefficients to represent the probabilities for carriers to be transported from one material to another material with a different energy of the corresponding band. Boltzmann coefficients here represent a portion of the carriers that have higher energies at a given temperature with the average carrier energy corresponding to that of the band. This approximation is likely an underestimate of the number of carriers transporting charge from a material with lower LUMO (higher HOMO) into a material with higher LUMO (lower HOMO) as material interfaces may be interdiffused, hence reducing the effective barrier height by creating a potential staircase:

$$\begin{aligned} B_c &= \begin{cases} e^{-\frac{\Delta E_c}{k_B T}}, & \Delta E_c > 0 \\ 1, & \Delta E_c \leq 0 \end{cases} \\ B_v &= \begin{cases} e^{\frac{\Delta E_c}{k_B T}}, & \Delta E_c < 0 \\ 1, & \Delta E_c \geq 0 \end{cases} \end{aligned} \tag{6.4}$$

Here E_c and E_v are the energy values for the conduction (LUMO) and valence (HOMO) bands, k_B is the Boltzmann constant and T is the temperature in K. This definition implies that for the number of electrons hopping from molecules with a lower LUMO band onto molecules with a higher LUMO band is scaled according to the Boltzmann distribution B_c. Number of electrons hopping from molecules with a

higher LUMO band to molecules with a lower LUMO band is not subject to scaling, i.e. there are no energy barriers for electron transport into that material. By analogy, the concentration of holes hopping from molecules with a higher HOMO band onto molecules with a lower HOMO band is scaled by the Boltzmann factor B_v. When there is no energy barrier for the hole transport onto a molecule the scaling factor is 1.

Finally to determine the carrier concentrations in a device we use continuity equations that include a recombination term, since in an active opto-electronic device electrons and holes can form pairs and eventually recombine. We assume that in LEDs there is no significant charge generation and we do not include the generation terms into the following continuity equations. Note that in photovoltaic devices, generation terms have to be taken into account (see Appendix C for details).

$$\begin{aligned} \frac{dn}{dt} &= \frac{dJ_n}{dx} - npR \\ \frac{dp}{dt} &= \frac{dJ_p}{dx} - npR \end{aligned} \tag{6.5}$$

Here t is time and R is the recombination rate.

Together with Equations 6.1 and 6.2 for the electric field and carrier fluxes in the device, Equation 6.5 provides a simple description of the behavior of an active optoelectronic device.

While analytical solutions exist for simple single-carrier single-film systems [62, 99], in order to model complex devices, such as hybrid organic-QD LEDs, we need to employ numerical simulation methods [104]. QD-LEDs consist of multiple layers of different organic and QD materials deposited between an anode and a cathode. Thus it is valuable to model the carrier concentration and electric field profiles along the anode-cathode direction. We approximate all device design parameters to be uniform across the plane perpendicular to the anode-cathode direction, which essentially yields a one-dimensional model. We break our devices into $\Delta x = 1$ nm layers that correspond to an approximate size of a single organic molecule or a colloidal QD. We assign various parameters such as carrier concentrations, mobilities, diffusion constants and recombination rates in every 1 nm layer, as well as Boltzmann scaling

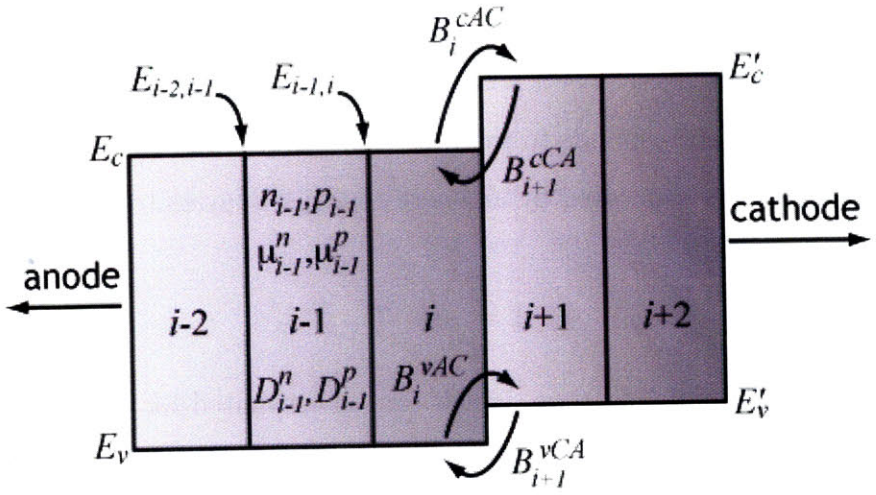

Figure 6-1: Illustration of model parameters with respect to the molecular layers.

factors for carrier transport in different directions (towards the cathode or towards the anode), and we define electric fields between the layers in order to keep track of the direction of the drift current (Figure 6-1).

Equations 6.1 and 6.5 provide a complete description for the nearest neighbor carrier transport in a drift and diffusion model. For a more realistic description of QD-LEDs we do not limit our model to the nearest neighbor interactions, as in addition, we may observe tunneling and long-range carrier hopping. For the thin energy barriers, tunneling dominates over the in-band hopping, since the fraction of tunneling carriers in this case may be higher than the fraction of carriers defined by a Boltzmann transport coefficient. To describe the tunneling through a thin continuous energy barrier, such as the tunneling of electrons (holes) through an organic material with a higher LUMO (lower HOMO) band, we use the WKB approximation, which defines the tunneling probability as [105]:

$$P \sim e^{-2\alpha d} \tag{6.6}$$

where d is the total tunneling distance, and the coefficient α is given by the following expression:

$$\alpha = \frac{\sqrt{\pm 2 m_{n,p}(V_0 - E_{c,v})}}{\hbar} \tag{6.7}$$

where $m_{n,p}$ is an electron or a hole mass, V_0 is the height of a potential barrier, and $E_{c,v}$ is the energy of an electron or a hole. Here the + sign corresponds to the electron tunneling and − sign corresponds to the hole tunneling. The tunneling rate from the j^{th} layer to the i^{th} layer separated by an energy barrier d layers (or nm) thick is then:

$$\Gamma = \frac{1}{\tau_t} e^{-2\alpha d} \tag{6.8}$$

τ_t is a characteristic tunneling time, which can be estimated for both field and concentration driven tunneling. Based on the drift flux contribution to the continuity equation, we can estimate the field-driven tunneling time using the carrier mobility and electric field:

$$\frac{1}{\tau_f} \sim \frac{\mu_{n,p} E}{\Delta x} \tag{6.9}$$

Analogously, based on the diffusion flux contribution to the continuity equation, we estimate the concentration-driven tunneling time using the diffusion constant:

$$\frac{1}{\tau_D} \sim \frac{D_{n,p}}{\Delta x^2} \tag{6.10}$$

While the WKB approximation provides a satisfactory formalism for calculation of the tunneling probability through the thin continuous energy barriers, such as organic thin films, it is not necessarily the best approximation for the hole tunneling through a monolayer of colloidal QDs. In a typical QD-LED the QD conduction band (for red CdSe QDs, $E_c \sim 4.7$ eV below the vacuum level) lies lower than the LUMO levels of any of the organic charge transport materials (typically 2-3.5 eV below the vacuum level), providing a deep trap level for electrons. In contrast, the QD valence band (for red CdSe QDs, $E_c \sim 6.8$ eV below the vacuum level) lying lower than the HOMO levels of the organic materials (typically 5-6.5 eV below the vacuum level) provides a significant barrier for the hole transport. Tunneling rates calculated by the WKB approximation provide an underestimate for the number of transported carriers, since an energy barrier of $\sim$ 1-2 eV results in a negligible penetration of holes beyond the QD layer. This contradicts the previous experimental observations

that show significant emission from organic electron transport layers in QD-LEDs at high applied bias voltages, which implies exciton formation in layers separated from the anode by a hole-blocking QD layer [101].

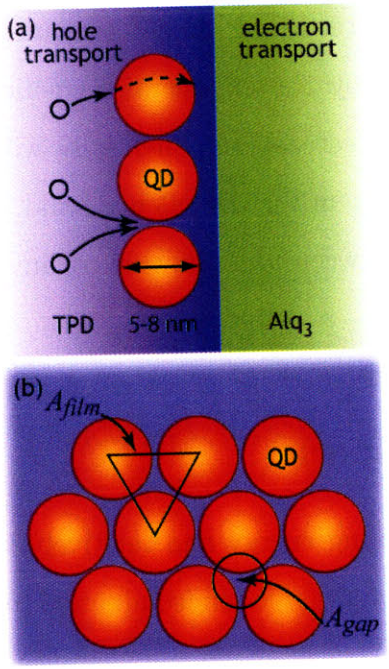

Figure 6-2: (a) Schematic diagrams illustrating two potential scenarios of hole transport through a QD monolayer. (b) This picture shows the area of a close-packed QD monolayer and the area of a gap between QDs.

The morphology of a QD monolayer plays a key role in hole transport in QD-LEDs. Unlike a thin organic film, a QD monolayer is not continuous, but rather is a hexagonally close-packed (hcp) layer with gaps between the spherical QDs (Figure 6-2). These gaps are most likely filled with organic molecules from the neighboring organic charge transporting films. Since the HOMO band of the organic molecules in the gaps between QDs is significantly higher than the valence band of QDs, the holes are likely to hop through these low resistance channels. Then the probability for the hole to be transported through the gaps in the QD layer is proportional to the relative area not covered by the QDs, $P \sim A_{gap}/A$, where A is the total area, which for a hcp film is $\sim \sqrt{3}a^2$; here a is the QD radius, and A_{gap} is the fraction of the total area not occupied by QDs, $A_{gap} = A - A_{QD} = (\sqrt{3} - \pi/2)a^2$ (see the schematic shown in Figure 6-2). Then the hole transport rate through a QD monolayer is given

by:

$$\Gamma = \frac{1}{\tau_t}\left[1 - \frac{\pi}{2\sqrt{3}}\right] e^{\frac{(d-\Delta x)}{\Delta x}} B_v \tag{6.11}$$

where τ_t is the characteristic tunneling time determined by Equations 6.9 and 6.10. We multiply the expression by the exponential coefficient, since by analogy with tunneling, the hopping rate decreases exponentially with distance. We also include a Boltzmann transport coefficient for the valence band, since for some of our devices the QD layer is deposited between two different organic films with different HOMO levels.

6.1.2 Exciton Transport

Due to the high exciton binding energy and relatively long exciton lifetime ranging from 1 ps - 10 ns for fluorescent organic semiconductors to 10s of μs for phosphorescent materials [106], excitons can travel significant distances in an active optoelectronic device before recombining [94, 95]. Exciton transport between nearest neighbors can be treated within the diffusion framework using the exciton lifetime and exciton diffusion length to determine the exciton diffusivity.

In addition to exciton diffusion, we take into account the energy transfer between different types of organic materials and QDs. In a majority of OLEDs, different organic charge transporting materials have different band gaps. Consequently, the emission spectrum of a wider band gap material may overlap with the absorption spectra of the other, narrower band gap, materials. For example, as we briefly discussed in Chapter 1, in a TPD/Alq_3 OLED, the TPD molecules near the material interfaces act as the exciton donors, while Alq_3 molecules act as the exciton acceptors [8, 9]. We note that the organic materials used in QD-LED fabrication generally have higher band-gap values than that of the red CdSe/ZnS QDs used in the experimental study of Chapter 5. This implies that there can only be energy transfer from the organic molecules to the red QDs, and not from the QDs to the organics (Note: the energy transfer from QDs to organic materials should be included when modeling

blue or green QD-LEDs). Within the assumption of thin film geometry characteristic of OLEDs and QD-LEDs we can use the Equation 5.1 to describe the donor-to-film energy transfer between different organic materials. Taking all the energy transfer and exciton diffusion processes into account, we formulate the continuity equations for exciton concentrations in organic materials and QDs:

$$\begin{aligned}
\frac{d\xi^{OA}}{dt} &= -\frac{\xi^{OA}}{\tau^{OA}} - \frac{L_D^2}{\tau^{OA}} B_g \frac{d^2\xi^{OA}}{dx^2} - k^{plane}_{org-QD}\xi^{OA} + \sum_{OD} k^{plane}_{org-org}(x)\xi^{OD} + G^{OA} - k^{OA}_{xd} \\
\frac{d\xi^{OD}}{dt} &= -\frac{\xi^{OD}}{\tau^{OD}} - \frac{L_D^2}{\tau^{OD}} B_g \frac{d^2\xi^{OD}}{dx^2} - k^{plane}_{org-QD}\xi^{OD} - \left[\sum_{OA} k^{plane}_{org-org}(x)\right] \xi^{OD} + G^{OD} - k^{OD}_{xd} \\
\frac{d\xi^{QD}}{dt} &= -\frac{\xi^{QD}}{\tau^{QD}} - \frac{L_D^2}{\tau^{QD}} B_g \frac{d^2\xi^{QD}}{dx^2} + \sum_{organic} k^{plane}_{org-QD}(x)\xi^{OA+OD} + G^{QD} - k^{QD}_{xd}
\end{aligned} \tag{6.12}$$

Here ξ^{OA}, ξ^{OD} and ξ^{QD} are exciton concentrations in "organic acceptors" (organic molecules that accept excitons from the molecules of the other organic material), "organic donors" (organic molecules that donate their excitons to the "organic acceptors") and QD films, respectively; τ^{OA}, τ^{OD} and τ^{QD} are exciton relaxation times for the organic materials and QDs; L_D is the exciton diffusion length defined as the characteristic distance that an exciton can diffuse until it recombines; G^{OA}, G^{OD} and G^{QD} are the exciton generation rates in organic materials and QDs. Exciton generation rates can be obtained from the charge transport model, knowing the carrier concentrations n and p and recombination rate R; in a simplest approximation $G \approx Rnp$. The quantities k^{plane}_{org-QD}, $k^{plane}_{org-org}$ are the energy transfer rates between organic molecules and QDs and between "organic donors" and "organic acceptors". k^{OA}_{xd}, k^{OD}_{xd} and k^{QD}_{xd} are the exciton dissociation rates in organic materials and QDs, while the B_g coefficients account for the proportion of excitons that can diffuse from one material into another material with a different value of band gap (HOMO-LUMO gap). We approximate these coefficients with Boltzmann factors, as they represent exponential tails of the exciton population centered at the energy equal to the band

gap. (Note that akin to the B_c and B_v coefficients for carrier transport from one material into another, the B_g coefficients have different values dependent on the direction of transport, since the diffusion into different neighbors may be accompanied by different energy barriers.)

$$B_g = \begin{cases} e^{-\frac{\Delta E_g}{k_B T}}, & \Delta E_g > 0 \\ 1, & \Delta E_g \leq 0 \end{cases} \tag{6.13}$$

where E_g is the width of a band gap (HOMO-LUMO gap).

In our work, we consider the field-induced (Onsager) exciton dissociation [107] as the predominant mechanism of the exciton dissociation in QD-LEDs. We model the exciton dissociation process as an escape of one or both carriers into the neighboring molecules or QDs. In this case the exciton dissociation rate can be described by [108]:

$$k_{xd} \sim \frac{1}{\tau_{hop}^n(E)} B_c(E) + \frac{1}{\tau_{hop}^p(E)} B_v(E) \tag{6.14}$$

where $\tau_{hop}^n(E)$ and $\tau_{hop}^p(E)$ are field-dependent hopping times for electrons and holes described by Equation 6.9; $B_c(E)$ and $B_v(E)$ are the Boltzmann factors that describe the potential barriers for the transport of field-driven electrons and holes into the neighboring layers:

$$\begin{aligned} B_c &= \begin{cases} e^{-\frac{\Delta E_c + E_b - eE\Delta x}{k_B T}}, & \Delta E_c + E_b - eE\Delta x > 0 \\ 1, & \Delta E_c + E_b - eE\Delta x \leq 0 \end{cases} \\ B_v &= \begin{cases} e^{\frac{\Delta E_c - E_b + eE\Delta x}{k_B T}}, & \Delta E_c - E_b + eE\Delta x < 0 \\ 1, & \Delta E_c - E_b + eE\Delta x \geq 0 \end{cases} \end{aligned} \tag{6.15}$$

where E_b is the exciton binding energy and Δx is the distance between the neighboring molecules.

6.2 QD-LED Design and Parameters of the Model

In the experimental part of this work described in Chapter 5 we studied the operation of QD-LEDs that employed TPD for the hole transport and Alq_3 for the electron

transport [109]. Parameters of these materials are shown in the Table 6.1.

material	μ_n, cm^2/Vs	μ_p, cm^2/Vs	E_c, eV	E_c, eV
TPD	1.88×10^{-7}, [110]	1.25×10^{-3}, [110]	2.1	5.4
Alq_3	10^{-5}, [111]	-	3.1	5.8

Table 6.1: Electronic parameters of commonly used organic materials TPD and Alq_3

In our model we make an approximation for the Alq_3 hole mobility to be on the order of 10^{-7} cm^2/Vs, i.e. comparable to the electron mobility in TPD. Being crystalline inorganic semiconductors, CdSe QD cores can potentially have higher mobilities than organic films, but since colloidal QDs are surrounded by insulating organic ligands that provide their solubility in organic solvents, we approximate the average carrier mobilities in the QD layer to be comparable to those of the worst organic conductors, i.e. μ_n, $\mu_p \sim 10^{-7}$ cm^2/Vs [112]. $E_c \approx 4.7$ eV and $E_v \approx 6.7$ eV provide estimates for the energy values of the QD conduction and valence bands [13]. We use Equation 6.3 to approximate the carrier diffusion constants in organic materials and QDs.

We use the data from our previous experiments [109] to estimate the boundary conditions for the electron and hole concentrations at the cathode and the anode. Considering only drift current, we can find approximate injected carrier concentrations in a typical QD-LED:

$$\begin{aligned} n &= \frac{J}{eE\mu_n} \approx 2.5 \times 10^{16}\ cm^{-3} \\ p &= \frac{J}{eE\mu_p} \approx 2 \times 10^{14}\ cm^{-3} \end{aligned} \tag{6.16}$$

here we use $J \sim 0.04$ A/cm^2 as the current density in a QD-LED at 10 V of applied bias. In our model though for simplicity we used a hole injection concentration of 10^{14} cm^{-3} and an electron injection concentration of 1.25×10^{16} cm^{-3}. Higher electron injection accounts for the difference in the majority carrier mobilities in Alq_3 ($\mu_n \sim 10^{-5}$ cm^2/Vs) and TPD ($\mu_p \sim 1.25 \times 10^{-3}$ cm^2/Vs) maintaining spatially continuous current from the anode to the cathode and device neutrality.

The carrier recombination rate R is the only variable parameter of our model, and in the calculations presented in this Chapter R was chosen to be $\sim 10^{-14}$ cm^3/s as it

resulted in satisfactory agreement with the experimental data. We acknowledge that the carrier recombination rate varies depending on the material, but in order to avoid the use of an excess number of parameters in the model, we keep the recombination rate constant across the entire device.

For the exciton transport model we choose exciton diffusion lengths of 1 nm and 8 nm for TPD and Alq_3, respectively, consistent with experimental studies [94, 95] and the exciton relaxation times in these materials ($\tau^{TPD} \approx 1$ ns and $\tau^{Alq_3} \approx 10$ ns). For QDs we choose an exciton diffusion length of 1 nm due to exciton confinement within a QD site; the exciton relaxation time is chosen to be $\tau^{QD} = 20$ ns, consistent with previous experimental observations [45, 92]. For the exciton dissociation rate calculations, we choose a lower limit value of the exciton binding energy $E_b \approx 0.1$ eV [13, 108].

In Chapter 5 we experimentally investigated carrier and exciton transport in QD-LED structures with the QD monolayer placed at different positions within the device stack [109]. In this Chapter we focus on the modeling of a typical QD-LED structure (device 2 in Figure 5-5) and QD-LEDs with higher values of EQE (devices 3 and 4 in Figure 5-5), in which the QD monolayer is embedded into a hole-transporting layer 10 nm and 20 nm away from the TPD/Alq_3 interface.

6.3 Modeling Results

Figures 6-3(a) through 6-3(c) display the carrier concentration profiles at applied bias voltages from 1V to 5 V obtained from our numerical simulations. Note that the bias voltage in our numerical simulations does not include the voltage drop at the injecting contacts arising from the differences in Fermi levels of the cathode and the anode. In order to compare the voltages used in our model to the experimentally applied voltages, one needs to take that difference into account.

We verify the consistency of our model by first calculating the carrier concentration profiles in an OLED consisting of a 41 nm TPD hole transporting layer and a 40 nm Alq_3 electron transporting layer as shown in Figure 5-5. We find that the

electrons accumulate in Alq_3 and the holes accumulate in TPD at the TPD/Alq_3 interface (Figure 6-3(a)) due to the interface energy barriers. As a result of the carrier accumulation, an electric field has a spike at the interface, which is shown in Figure 6-3(g). Consequently, there is a steeper potential drop across the interface, as seen in Figure 6-3(j). According to Figure 6-3(d), which plots the exciton generation rate proportional to the product of electron and hole concentrations, the bulk of exciton generation in an OLED takes place in the first several nanometers of Alq_3 film adjacent to the TPD/Alq_3 interface. The exciton generation rate profile appears consistent with the experimental observations of OLED electroluminescence spectra solely consisting of Alq_3 emission [8, 9].

Figure 6-3(b) shows the electron and hole concentration profiles in a typical QD-LED structure (device 2 in Figure 5-5). We find that electrons accumulate at QD sites, which is consistent with the QD electron-trapping properties. We also observe a hole accumulation in TPD at the TPD/QD interface due to the barrier for the hole injection from TPD into QDs or Alq_3, i.e. even if the holes were to travel through the spaces between the QDs, there still is an energy barrier for their transport into the Alq_3 layer. The carrier accumulation at the TPD/QD interface is manifested in a spike in the electric field between the TPD layer and QDs, as shown in Figure 6-3(h), and a steep potential drop across the interface shown in Figure 6-3(k). The exciton generation profile in Figure 6-3(e) shows relatively uniform exciton generation throughout the Alq_3 film and negligible exciton generation at QD sites resulting from charge imbalance. The observed QD charging with electrons leads to the high probability of Auger recombination events and thus impedes the QD-LED efficiency. The high electric field across the QDs results in higher rates of field-induced exciton dissociation, which also has a negative impact on the QD-LED efficiency. In contrast, electron concentration profiles in QD-LEDs, where QDs are embedded into the TPD hole transporting layer (Figure 6-3(c)), exhibit no electron accumulation at QD sites. The electrons accumulate in Alq_3 at the TPD/Alq_3 interface, and holes travel through the spaces between the QDs to the TPD/Alq_3 interface. As a result there is a spike in the electric field and a consequent potential drop at the TPD/Alq_3 interface rather

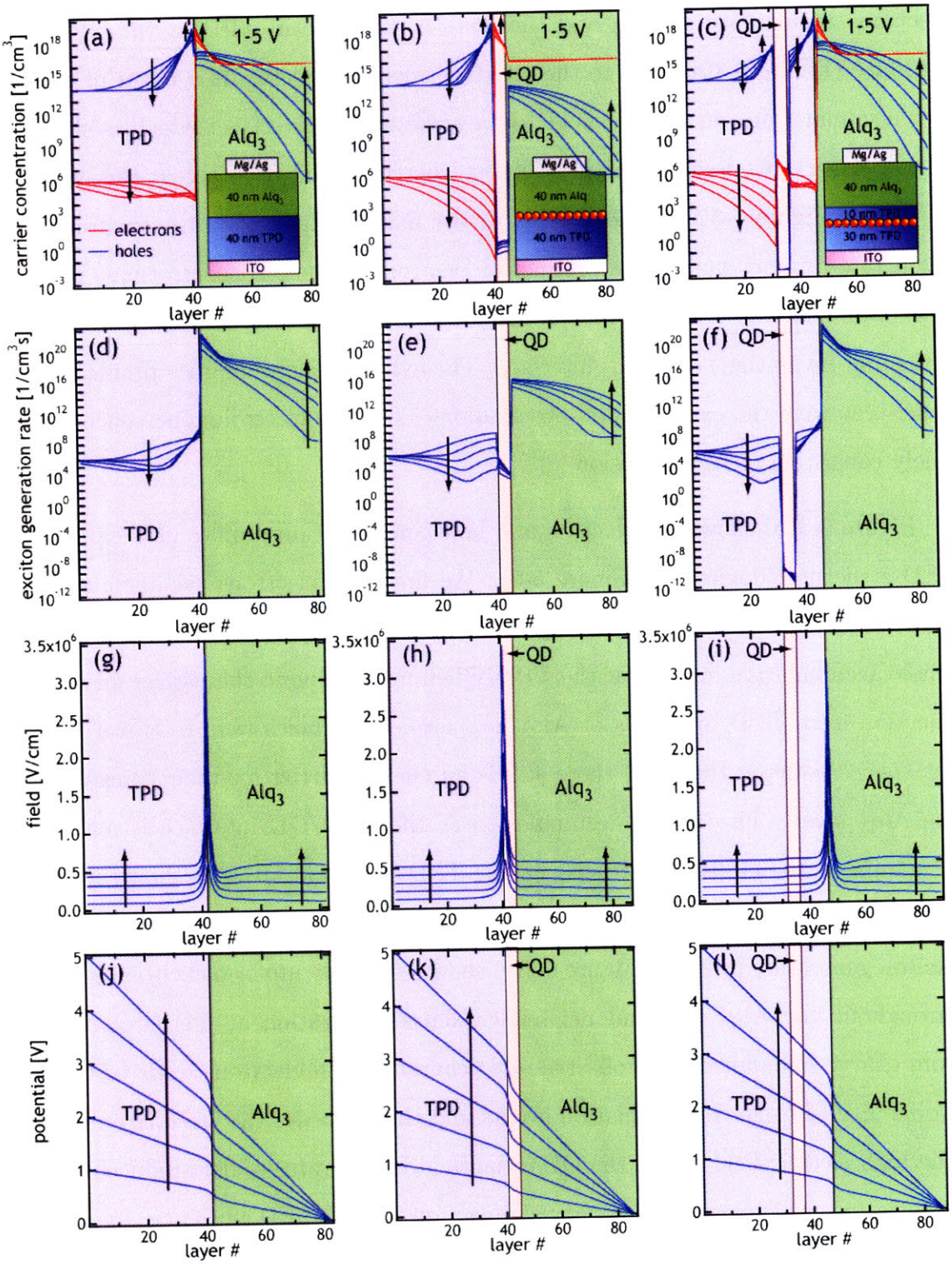

Figure 6-3: (a), (b) and (c) Carrier concentration profiles inside an OLED, a QD-LED and a QD-LED with a QD monolayer embedded into the TPD layer 10 nm away from the TPD/Alq_3 interface. (d), (e) and (f) Exciton generation rate profiles inside an OLED, a QD-LED and a QD-LED with a QD monolayer embedded into TPD. (g), (h), (i) Electric field distributions inside an OLED, a QD-LED and a QD-LED with a QD monolayer embedded into TPD. (j), (k), (l) Potential profiles across an OLED, a QD-LED and a QD-LED with a QD monolayer embedded into TPD. Multiple curves correspond to bias voltages between 1-5 V. Arrows indicate the direction of increasing bias voltage.

than at the TPD/QD interface (Figures 6-3(i) and 6-3(l)). In these structures the exciton generation rate at the TPD/Alq_3 interface is not obstructed by the presence of QDs (Figure 6-3(f)). The increased exciton generation rate in the device, the reduced electric field across the QDs, and the reduced QD charging with electrons provide a plausible explanation for the experimental observation of an increased EQE of these devices as compared to conventional QD-LEDs [109].

Figures 6-3(e) and 6-3(f) show high exciton generation rates in Alq_3 and comparatively negligible exciton generation rates in QDs, while our previous experiments demonstrate QD-LED spectra dominated by narrow colloidal QD emission. In order to compare the results of our model to the experimental EL measurements we use Equation 6.12 to calculate exciton concentration profiles in an OLED and QD-LEDs using the exciton generation rates (Figures 6-3(d) through 6-3(f)) obtained from the carrier transport model.

Figure 6-4(a) displays exciton concentration profiles in an OLED at bias voltages 1-5 V. The bulk of the exciton population is concentrated in the Alq_3 film resulting from the higher exciton generation rate (Figure 6-3(d)) and energy transfer of occasional excitons formed on TPD molecules. Based on the exciton concentration profile in Figure 6-4(a) we can calculate normalized EL spectra for an OLED using the exciton population normalized by the spectral area and photoluminescence quantum efficiency in different materials as scaling factors for the relative spectral contributions of these materials. The calculated OLED EL spectra solely consist of Alq_3 emission (Figure 6-4(d)), which is consistent with experimental observations [8, 9].

Exciton concentration profiles in Figures 6-4(b) and 6-4(c) and the corresponding calculated EL spectra in Figures 6-4(e) and 6-4(f) emphasize the importance of energy transfer from organics to QDs in a typical QD-LED (device 2 in Figure 5-5.) Exciton concentration profiles and EL spectra in Figures 6-4(b) and 6-4(e) are calculated based on the exciton generation rate profile in a typical QD-LED (Figure 6-3(e)) using Equation 6.12 and setting the energy transfer rate from organics to QDs to zero ($k_{org-QD}^{plane} = 0$). In the absence of the exciton energy transfer from the organics to QDs, the majority of excitons reside in the Alq_3 film. This results in calculated

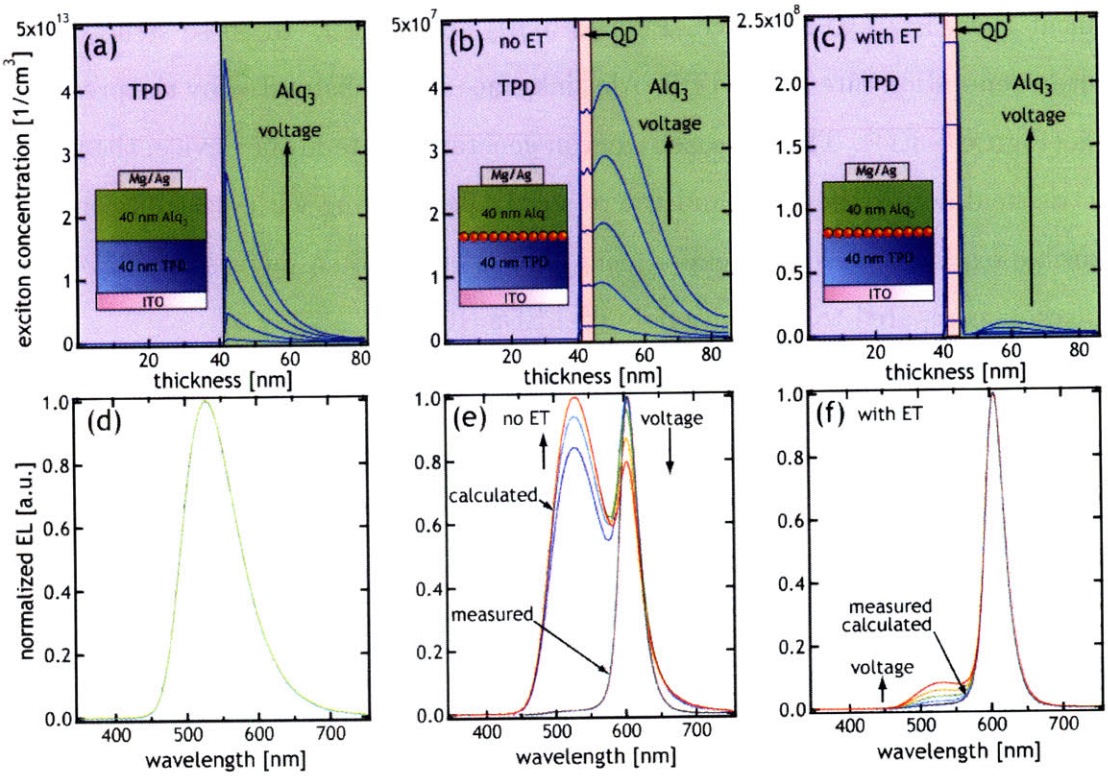

Figure 6-4: (a) Exciton concentration profiles calculated for an OLED at bias voltages 1-5 V. (b) and (c) Exciton concentration profiles calculated for a typical QD-LED without (b) and with (c) energy transfer from organics to QDs included. (d) Normalized EL spectra calculated for an OLED based on the exciton concentration profile in (a) (Note that the OLED spectra look identical at bias voltages 1-5 V). (e) and (f) Normalized EL spectra calculated for a QD-LED based on the exciton concentration profiles in (b) and (c), respectively. Arrows indicate the direction of increasing bias voltage. Dashed lines correspond to the experimentally measured spectra.

QD-LED EL spectra dominated by Alq_3 emission (Figure 6-4(e)), inconsistent with the experimental EL spectra dominated by the narrow QD emission. In contrast, exciton concentration profile in Figure 6-4(c) calculated for a typical QD-LED in the presence of energy transfer from the organics to QDs has a spike at the QD site, while the exciton concentration in organics is negligible. The corresponding calculated EL spectra in Figure 6-4(f) are dominated by the QD emission and exhibit only a minor Alq_3 emission contribution, which increases at higher applied bias voltages consistent with experimental observations [3, 101]. An Alq_3 contribution in experimental QD-LED EL spectra is not typically observed at low voltages <10-15 V. This quantitative inconsistency originates from the lack of geometrical factors in our calculation that

would take into account the QD size and shape. In the exciton transport model we treat QDs as a single continuous 1 nm thick layer, while realistically QDs occupy a larger volume. Additionally the energy transfer rates to QDs are dependent on the relative positions of small organic donors with respect to comparatively large colloidal QDs [92].

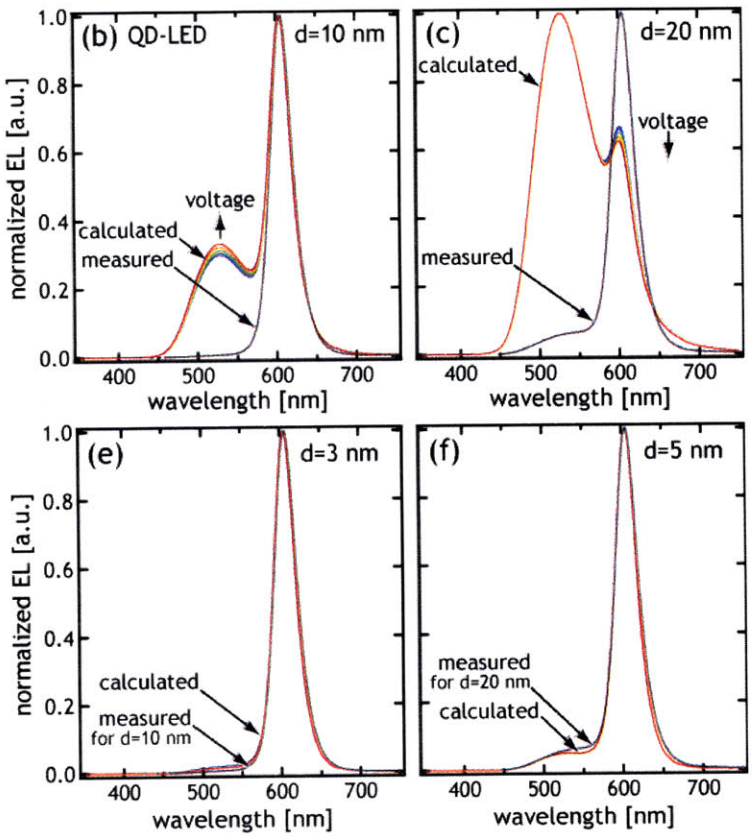

Figure 6-5: EL spectra calculated for QD-LEDs with QD monolayer embedded into TPD HTL 10 nm (a), 20 nm (b), 3 nm (c) and 5 nm (d) away from the TPD/Alq_3 interface. Dashed lines correspond to the experimentally measured spectra. Multiple overlapping lines correspond to the bias voltages 1-5 V.

While the energy transfer from organics to QDs is sufficient to explain the QD-dominated EL spectra of a typical QD-LED, including energy transfer into the exciton transport model does not yield calculated EL spectra of QD-LEDs with QD monolayer embedded into the TPD hole transporting layer 10 nm and 20 nm away from the TPD/Alq_3 interface to match the experimentally measured spectra for these devices. The calculated EL spectra of the QD-LED with the QD monolayer embedded into the TPD layer 10 nm away from the TPD/Alq_3 interface show a significant Alq_3

contribution in addition to the QD peak (Figure 6-5(a)). The experimental EL spectra of this device do not contain any Alq_3 signal at low bias voltages. The calculated EL spectra for the QD-LED with the QD monolayer embedded into the TPD film 20 nm away from the TPD/Alq_3 interface are dominated by the Alq_3 emission (Figure 6-5(b)), while the experimental EL spectra for this QD-LED exhibit only a minor Alq_3 contribution and are dominated by the QD emission.

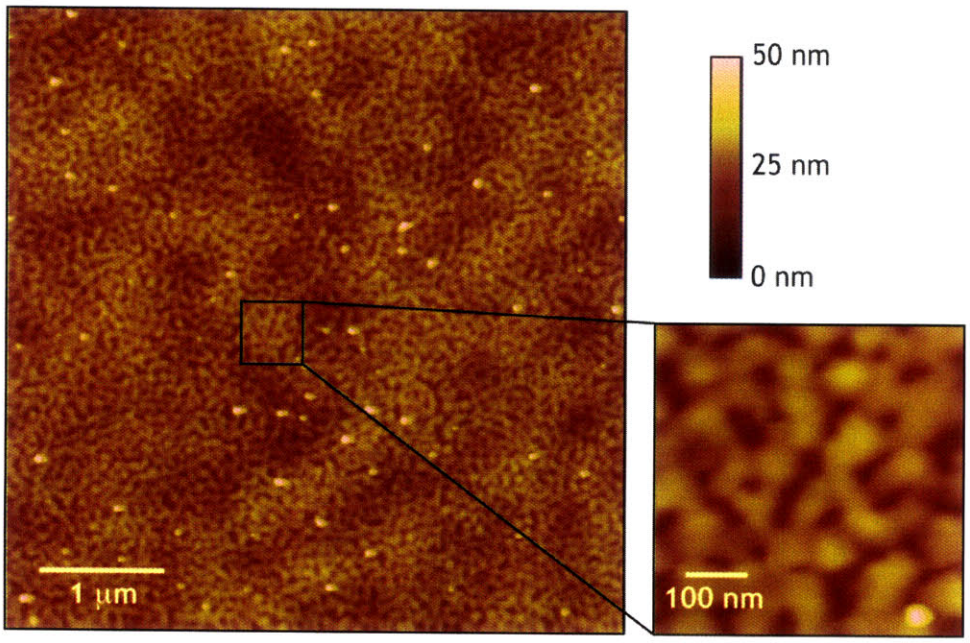

Figure 6-6: AFM image shows 10 nm Alq_3 film evaporated onto a monolayer of colloidal QDs.

In our simulation we neglected the morphology of the QD monolayer and a thin TPD layer deposited on top of it. According to our AFM images (Figure 6-6), aromatic organic molecules are chemically repelled by the aliphatic ligands surrounding QDs leading to high surface roughness and discontinuities of thin organic films deposited on top of QD monolayers [3, 101]. (Note: TPD layers >30 nm thick regain low roughness and continuity of the amorphous organic films.) As a result, in a real QD-LED, excitons formed in Alq_3, travel through thinner parts of the TPD film and the apparent EL spectrum does not correspond to a 10 nm (or 20 nm) spacing between QDs and the exciton generation region but rather to a shorter distance. Figure 6-5(c) plots the calculated EL spectra for a hypothetical QD-LED with the QD monolayer

embedded into TPD 3 nm away from the TPD/Alq_3 interface. These spectra, which are dominated by the QD emission at bias voltages from 1 V to 5 V, are close to the experimentally measured EL spectra of the QD-LED where QDs are embedded into TPD 10 nm away from the TPD/Alq_3 interface. The rough morphology of a thin TPD layer on top of a QD monolayer effectively reduces the spacing between QDs and the exciton generation region from 10 nm to $\leq$3nm. The calculated spectra of the QD-LED with the QD monolayer embedded into TPD 5 nm away from the interface (Figure 6-5(d)) are similar to the experimental EL spectra of the QD-LED with 20 nm spacing. The TPD film morphology on top of a QD monolayer in this case again results in the effective decrease of the distance between the QDs and the exciton generation region.

6.4 Summary

A physical model based on carrier drift, diffusion and recombination allows us to numerically calculate the carrier concentration and electric field profiles in hybrid organic-QD LEDs. Furthermore, the results of the carrier transport model are used in the calculation of exciton concentration profiles and EL spectra based on exciton generation, diffusion, dissociation, and exciton energy transfer. We find that the bulk of the exciton generation in QD-LEDs takes place in Alq_3 at the TPD/Alq_3 or QD/Alq_3 boundary. Insertion of a QD monolayer at the TPD/Alq_3 interface impedes the exciton formation by trapping electrons and reducing the electron concentration in Alq_3. High electron accumulation in QDs initiates frequent Auger recombination events decreasing the QD-LED efficiency. Accumulation of holes in TPD and electrons in QDs at the TPD/QD interface results in an electric field spike across the interface, which enhances the probability of field-induced Onsager exciton dissociation, which impedes QD-LED performance. Our model confirms that embedding QDs into a hole transporting layer <10 nm away from the TPD/Alq_3 interface is beneficial for the QD-LED performance, as we previously observed experimentally. First, it eliminates QD charging with electrons thereby reducing the probability of

Auger recombination events; second, it separates the QD monolayer from the spike in the electric field associated with the charge accumulation at the TPD/Alq_3 interface reducing the potential of exciton dissociation; finally, it eliminates the obstruction of exciton generation in Alq_3 at the TPD/Alq_3 interface by the electron-trapping QD monolayer. Exciton concentration profiles obtained from our calculations are in qualitative agreement with the experimental QD-LED EL spectra. The quantitative differences between calculated and experimental EL spectra can be explained by the morphological nonuniformity of QD monolayers and thin TPD films deposited on top of them. The morphology can be taken into account in our model by introducing geometric factors into energy transfer rates, which would effectively reduce the spacing between QD monolayers and exciton generation regions.

The key components of our physical model that yield a realistic prediction of QD-LED operation are:

- Taking account of the discrete structure of the colloidal QD monolayer in the carrier transport equations.
- Introducing exciton energy transfer from the organics to QDs.
- Using AFM images to account for the non-uniform nature of thin aromatic organic films on top of QD monolayers.

Chapter 7

Material Choices for High-Performance QD-LEDs

The work described in this Chapter builds upon findings of all the previous Chapters as we use our understanding of the processes contributing to QD-LED operation to design devices with superior performance and colors tunable across the entire visible spectrum. Here we introduce a single device structure that can be used for different QD-LED colors, which simplifies fabrication of multi-color flat panel displays, making this technology commercially viable [113].

Designing of a QD-LED can be broken into 3 steps: (1) choice of colloidal QDs; (2) choice of organic charge transporting layers; (3) choice of deposition techniques. In the following sections we will discuss our approach to solving the issues associated with each step.

7.1 Step I: Colloidal QDs

While the EQEs for QD-LEDs reported in the literature do not exceed 2%, ultimately the EQEs of these devices are limited by the photoluminescence efficiency (or quantum yield) of QDs in a thin film, which can be as high as 10% [114]. Consequently, independent of the device design it is very important to use the QD materials with the highest available quantum yield (QY) values. Most of the previously reported

work employed QDs with CdSe cores overcoated with wide bandgap material shells. These QDs have high PL QYs only in the yellow and red parts of the visible spectrum [3, 31, 32], and consequently, are not the most desirable materials for blue and green QD-LEDs. In this work we employ materials optimized to produce QDs with the highest available PL QY in each part of the visible spectrum (Figure 7-1).

For deep red emission we choose CdZnSe alloyed QD cores passivated with oleic acid, synthesized in a procedure similar to Zhong et al. [35, 115] with a PL peak at 647 nm in chloroform and a QY of 50%.

For orange emission we choose CdSe/ZnS core-shell QDs passivated with trioctylphosphine (TOP) and trioctylphosphine oxide (TOPO), prepared via well-established procedures [28, 29], with a PL peak at 600 nm in chloroform and a QY of 75%.

For green emission we use ZnSe/CdSe/ZnS core-double-shell QDs passivated with hexylphosphonic acid and TOPO synthesized via procedures similar to Ivanov et al. [53] and Steckel et al. [52] with a PL peak in chloroform at 540 nm and a QY of 65%.

For blue emission we choose ZnCdS alloyed QD cores passivated with oleylamine and oleic acid produced in a synthetic route similar to Zhong et al. [34, 115] with a PL peak at 460 nm in chloroform and a QY of 50%.

Finally, we use cyan emitters with a solution PL QY of 80% prepared in a novel synthetic procedure by overcoating ZnCdS alloyed cores emitting at 490 nm with a ZnS shell [115].

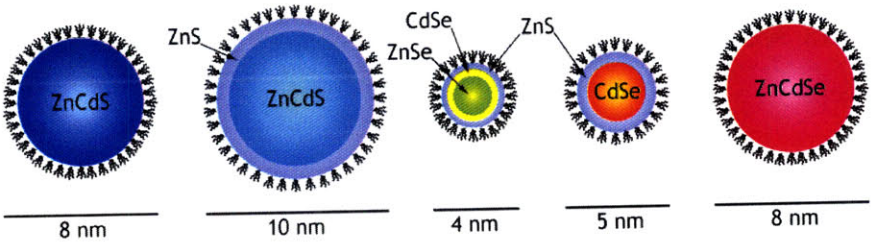

Figure 7-1: Types of colloidal QDs used in our study: ZnCdS cores emitting at λ =460 nm, ZnCdS/ZnS core-shell QDs emitting at λ =490 nm, ZnSe/CdSe/ZnS core-double-shell QDs emitting at λ =540 nm, CdSe/ZnS core-shell QDs emitting at λ =600 nm, ZnCdSe cores emitting at λ =650 nm. QDs are shown to scale with respect to each other. QD sizes were obtained from AFM images of the corresponding QD monolayers. The length of the organic ligands corresponds to the approximate length of the actual molecules.

7.2 Step II: Organic Charge Transport Layers

Figure 7-2 summarizes the four main processes that determine the efficiency of QD-LEDs, which we discussed in detail in previous Chapters. There are two main processes contributing to the QD EL [109]: (1) carriers can be directly injected into QDs where they form excitons, which recombine producing saturated QD emission (Figure 7-2(a)); (2) carriers can meet in organic layers and form excitons that can then transfer to QDs non-radiatively [77] yielding QD emission (Figure 7-2(b)). Similarly, there are two main processes limiting QD-LED efficiency: (1) QD charging [109] and consequent non-radiative Auger recombination [80] (Figure 7-2(c)), during which an exciton recombines to donate its energy to an unpaired carrier, which then relaxes to the ground state via interactions with phonons; (2) field-induced Onsager exciton dissociation [100, 107] (Figure 7-2(d)).

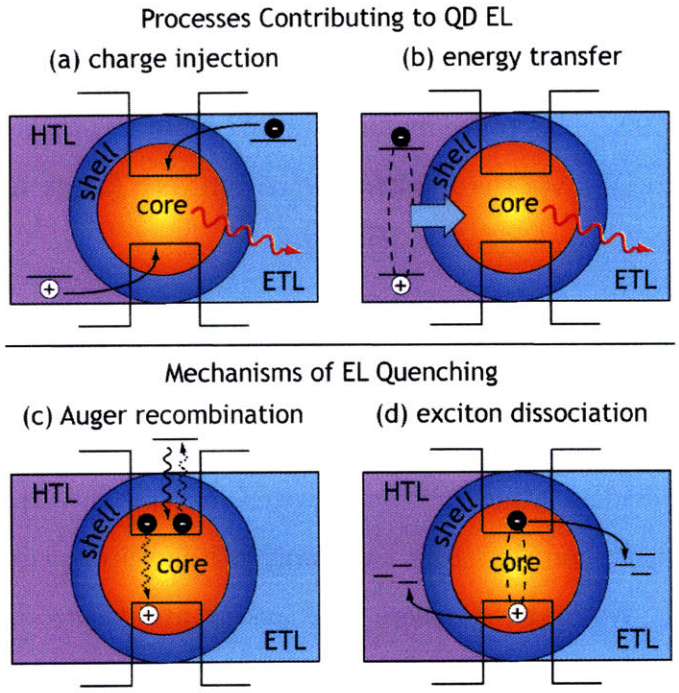

Figure 7-2: Top: schematic diagrams illustrate the main processes contributing to QD-LED EL: (a) charge injection and (b) energy transfer from organic thin films. Bottom: processes responsible for QD EL quenching: (c) Auger recombination and (d) field-induced exciton dissociation. Courtesy of Dr. Jonathan Halpert.

As of today, despite the advances in design and synthesis of organic charge trans-

porting materials, the HOMO level of available hole-transporting materials is positioned between 5.0-6.1 eV below the vacuum level [79], consequently there is a significant energy barrier for the hole injection into a valence band of QDs positioned >6.5 eV below the vacuum level [13]. The LUMO bands of organic electron transporting materials are usually found between 2.7-3.1 eV below the vacuum level [79], and consequently, there is no potential barrier for electron injection into the QD conduction bands found between 4.0-4.8 eV below the vacuum level [13] (see Figure 7-3). The only obstacle for the electron injection (and is also a barrier for the hole injection) into QDs is the insulating barrier consisting of organic ligands passivating the QD surface. The ligand layer is usually <0.5 nm thick, hence carriers can tunnel through it. This dramatic difference in barriers for hole and electron injection into QDs results in carrier imbalance at QD sites and the formation of electron-exciton pairs that recombine via the Auger mechanism (Figure 7-2(c)). Since the organic hole transporting materials with a low HOMO level are not readily available, we can improve the QD-LED performance by improving the energy transfer from the organic films to the QDs [109]. This route requires finding materials that: (1) can efficiently transfer excitons to QDs via the Förster mechanism [77]; (2) do not accept excitons formed on QD sites (or transferred to QD sites).

Figure 7-4(a) shows the absorption spectra of all the QD types (from red to blue) used in our study, as well as the PL spectra of TPD and Alq_3, which we previously used in QD-LED fabrication in Chapters 3 and 5, for hole and electron transport respectively. It is evident from the spectral overlap between Alq_3 emission and red and orange QD absorption that Alq_3 can transfer its excitons efficiently to red and orange QDs [109]. We find that there is a lack or an absence of overlap between the green, cyan and blue QD absorption and Alq_3 emission, and consequently these QDs cannot act as efficient acceptors of Alq_3 excitons. In addition, Alq_3 can accept excitons from blue QDs, acting as an exciton sink rather than a source (e.g., Figure 3-2). In previously reported work, including our own experiments described in Chapter 3, it was common to use hole blocking layers [17, 33, 52] (HBLs), such as TAZ or extremely thick (up to 7 monolayers) QD films [32] to prevent exciton formation

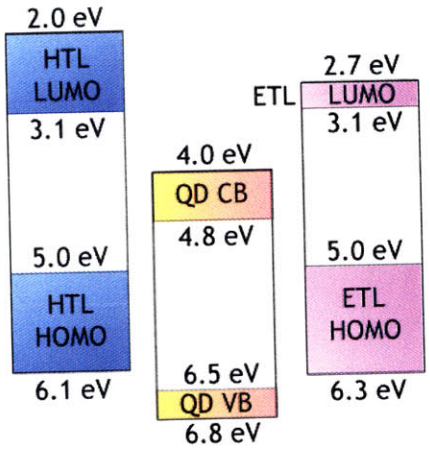

Figure 7-3: Schematic diagrams summarizes the positions of the energy bands of organic carrier transporting materials and colloidal QDs. Each colored block on the diagram represents a range of energies found for a particular band within a class of materials. Here HTL refers to the hole transporting layer and ETL refers to the electron transporting layer.

on Alq_3 molecules in green and blue QD-LEDs, which was manifested as a large Alq_3 emission contribution to the QD-LED EL [101]. Consequently, Alq_3 is not an optimal electron transport material for hybrid organic/QD LEDs. If we now examine the spectral overlap of TPD emission with QD absorption, we find that TPD could potentially transfer its excitons to all of the QD types with the energy transfer to blue QDs being the least efficient process. However, due to its low glass transition temperature 65 C° [79], TPD is prone to rapid crystallization upon exposure to oxygen and moisture, which results in a poor film morphology that degenerates the device performance.

To improve the transfer of excitons formed in QD-LED ETL to QDs, we replace Alq_3 with 2,2',2"-(1,3,5-benzenetriyl)-tris(1-phenyl-1-H-benzimidazole) (TPBi) [31] (Figure 7-4(b)). It is apparent from the spectral overlap between TPBi PL and QD absorption spectra (7-4(a)) that TPBi can potentially transfer its excitons to all the QD types (Figure 7-4(b)). In addition, due to its wide band gap (Figure 7-4(c)) TPBi cannot accept excitons formed on blue QD sites. Hence, we do not need to use HBLs or thick QD films to achieve narrow QD-LED EL spectra dominated by QD emission. Additionally, we can now take advantage of excitons formed in TPBi

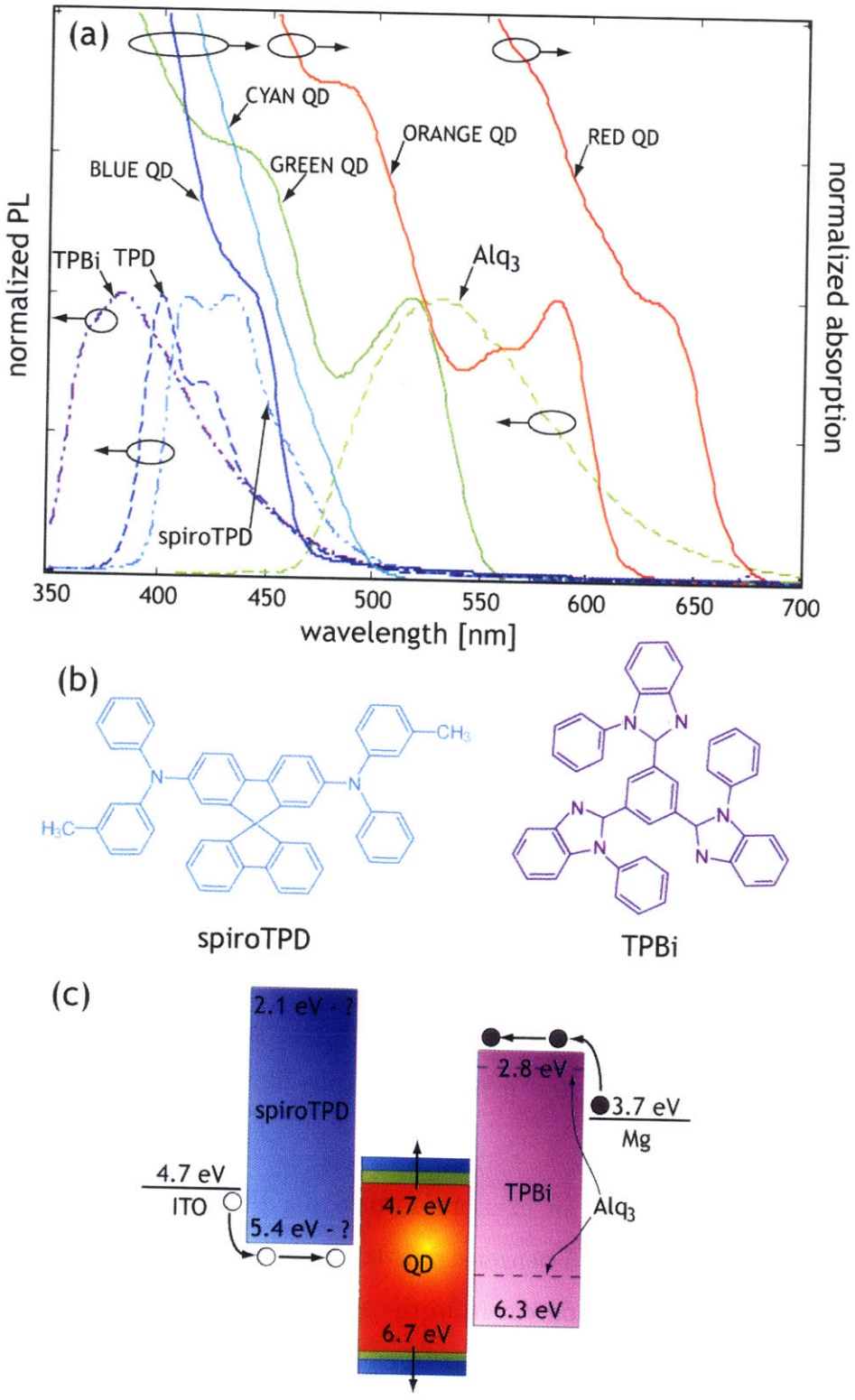

Figure 7-4: (a) The absorption spectra of red, orange, green, cyan and blue QDs in chloroform solutions are shown together with thin film TPD, Alq_3, spiroTPD and TPBi PL. (b) SpiroTPD and TPBi structural formulas. (c) Suggested energy band diagram for our QD-LEDs.

ETL. TPBi also has a higher glass transition temperature of 122 C° than the glass transition of Alq_3 (85 C°), and consequently TPBi is less likely to crystallize during the device operation, which improves the QD-LED shelf life. To improve the stability of the devices, we replace TPD with spiro-N, N'-diphenyl-N, N'-bis(3-methylphenyl)-(1, 1'-biphenyl)-4, 4'-diamine (spiroTPD), as its larger (non-flat) molecules (Figure 7-4(b)) are less likely to realign into poly-crystalline structure, and hence the film morphology is less likely to change during the device operation (this is indicated by spiroTPD high glass transition temperature of 103 C°). The overlap of the spiroTPD PL spectrum with the absorption spectra of all the QD types makes it a suitable exciton donor during QD-LED operation (Figure 7-4(a)).

7.3 Step III: Deposition Techniques

The final important step in QD-LED fabrication is the choice of deposition techniques for organic thin films and QDs. Thermal evaporation is the preferred method of the deposition of organic thin films as it allows us to deposit essentially any low molecular weight organics including those that do not dissolve in organic solvents, and hence, are incompatible with solution processing methods such as spin-casting. Thermal evaporation also yields superior film purity and thickness control as the specimens are kept under high vacuum conditions, and the growth rates are monitored in real time. Additionally, this deposition method avoids the exposure of the device to potentially harmful effects of organic solvents.

In Chapters 2 and 3 we already discussed the challenges associated with simultaneous deposition of different QD types in a single reliable step. In those chapters we found that contact printing can be used to deposit different QD types onto CBP and TPD HTLs. Here we choose a contact printing technique to deposit close-packed monolayers of different QDs onto evaporated spiroTPD HTL without exposing the structure to solvents. AFM images in Figure 7-5 demonstrate the compatibility of all the QD types with the spiroTPD surface as well as with the surface of parylene-C coated PDMS stamps used for contact printing.

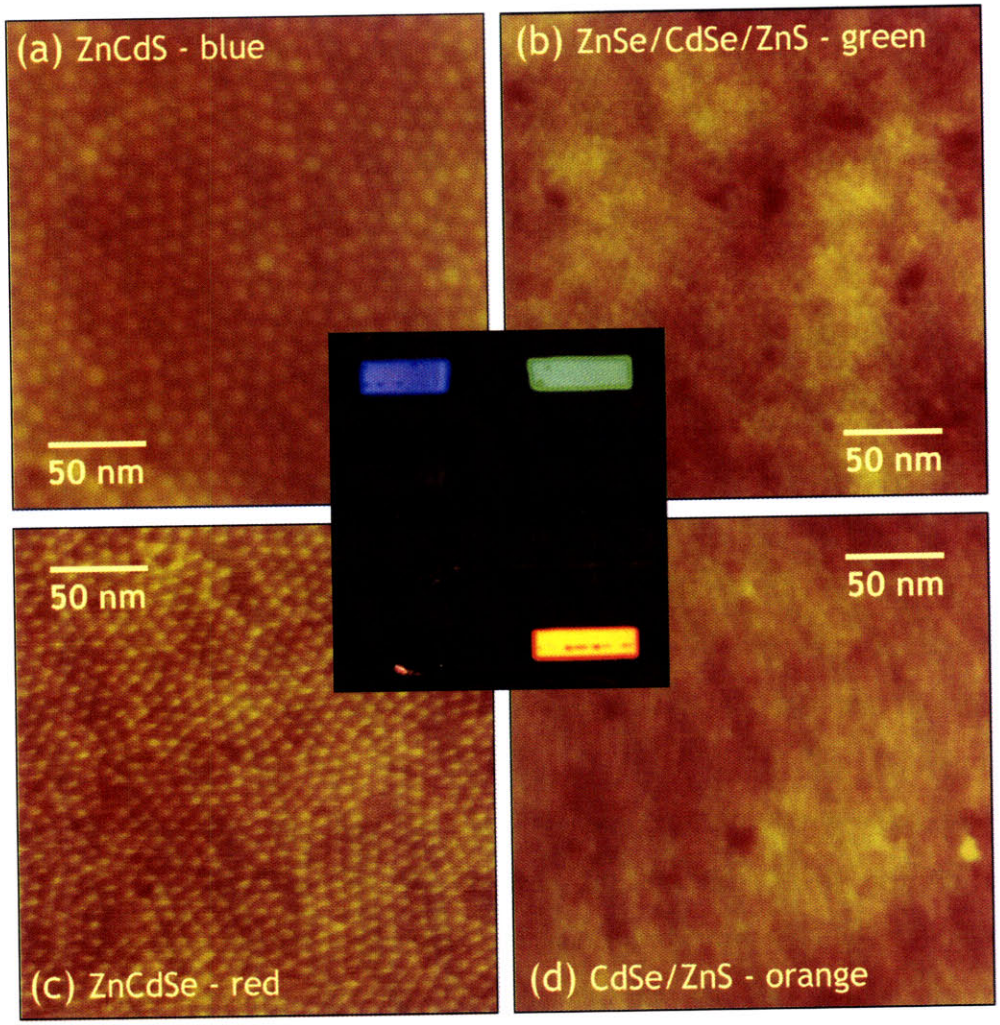

Figure 7-5: Atomic force microscope height images show close packed monolayers of different QD types on top of a 40 nm spiroTPD film: (a) CdZnS alloyed cores passivated with oleylamine and hexylphosphonic acid; (b) ZnSe/CdSe/ZnS core double-shell QDs passivated with oleic acid and TOP; (c) CdSe/ZnS core-shell QDs passivated with TOPO/TOP; (d) ZnCdSe alloyed cores passivated with oleic acid. Inset shows simultaneous emission from orange, green and blue QD-LEDs fabricated on the same substrate.

In Figure 7-5 close-packed monolayers of different QD types are deposited onto a 40 nm thick spiroTPD layer evaporated onto a layer of hole injecting polymer poly(3, 4-ethylenedioxythiophene):poly(styrenesulfonate) (PEDOT:PSS) on top of the indium-tin oxide (ITO) coated glass (this surface exactly replicates the bottom part of our QD-LED structure). Structures identical to those shown in Figure 7-5 are then completed by evaporation of a 40 nm TPBi film and a 100 nm Mg:Ag cathode with a 20 nm protective Ag overlayer.

7.4 QD-LED Performance

Figure 7-6(b) shows normalized EL spectra of the red, orange, green, cyan and blue QD-LEDs fabricated using 40 nm thick spiroTPD HTL and TPBi ETL and the printed close-packed monolayers of QD types described above. While red, orange, green and cyan QD-LEDs exhibit narrow EL spectra solely due to QD emission, blue QD-LEDs show an additional organic contribution, presumably due to an incomplete transfer of excitons formed on spiroTPD molecules.

It is not apparent from the spiroTPD PL spectrum, that this material can produce a significant contribution to a QD-LED EL spectrum, as it only exhibits a minor shoulder at ~480 nm. However, this peak, which most likely corresponds to the emission of one of the spiroTPD aggregate complexes, becomes amplified in an electrically driven structure. Figure 7-7 shows the PL and EL spectra of an OLED that consists of 40 nm thick spiroTPD and TPBi films between an ITO/PEDOT:PSS anode and a Mg:Ag/Ag cathode. We find that the PL spectrum of this OLED, obtained using an excitation from a 337 nm Nitrogen laser, consists of a linear combination of spiroTPD and TPBi PL spectra. In contrast, EL spectrum of this OLED (taken at 7 V of applied bias) shows a negligible TPBi contribution. The proportional contribution of the molecular and aggregated spiroTPD emission peaks is changed dramatically as compared to the spiroTPD PL spectrum. We note, that according to the suggested band diagram in Figure 7-4(c), in a spiroTPD/TPBi OLED most of the exciton formation takes place in the spiroTPD HTL, since the ~0.7 eV barrier for the electron injection

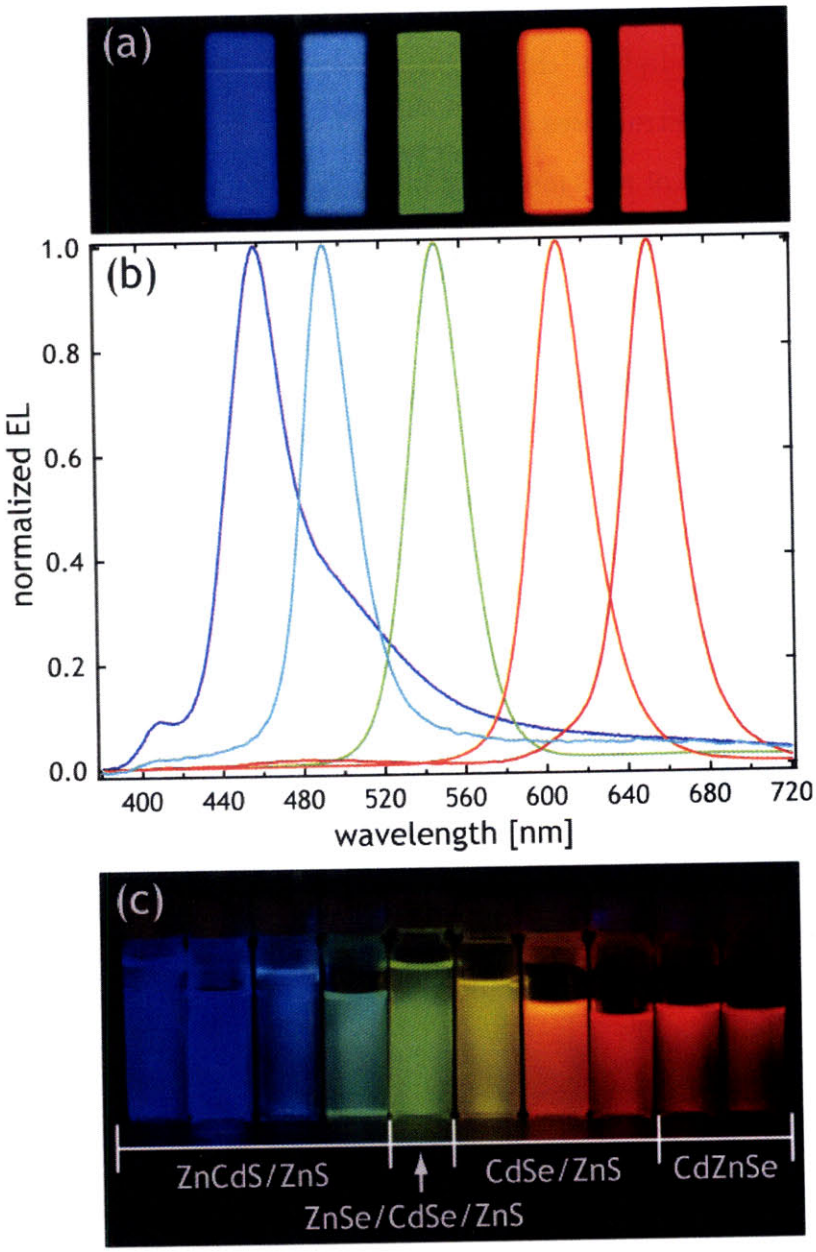

Figure 7-6: (a) Photographs of QD-LED pixels at an applied bias voltage of 6 V for blue and cyan, 4 V for green and orange, and 5 V for red. (b) Electroluminescence spectra of QD-LEDs at applied bias voltages of 10 V for blue, 5 V for cyan, green, orange and red. (c) Photograph of the chloroform solutions of different QD types used in this study. PL is excited by a UV lamp.

into spiroTPD is lower than the ~1 eV barrier for the hole injection into TPBi. In addition, excitons formed in TPBi can be transferred via a Förster mechanism to the spiroTPD molecules, as the spiroTPD band gap lies within the TPBi emission spectrum. Since excitons in an electrically driven spiroTPD/TPBi OLED form at the materials interface, and a chemical incompatibility between slightly polar TPBi and non-polar spiroTPD may promote spiroTPD aggregation at the interface, the EL spectra are dominated by the emission of spiroTPD aggreates. In contrast, during optical excitation excitons form throughout the structure, and hence, properties associated with the material interfaces are overwhelmed by the intrinsic properties of the bulk films.

Because the low energy aggregated spiroTPD excitons generated in the electrically driven structures cannot be transferred to blue QDs, the EL spectra of blue QD-LEDs exhibit a lower energy shoulder. The amplification of the 460 nm spiroTPD aggregate peak in electrically driven structures makes this material non-ideal for QD-LEDs with target emission wavelengths <500 nm.

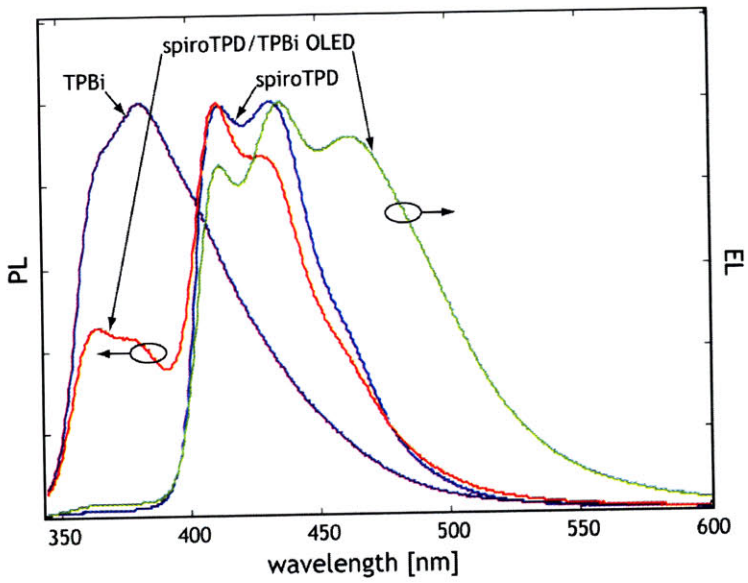

Figure 7-7: PL spectra for 80 nm TPBi and spiroTPD films are shown together with PL and EL spectra of a ITO/PEDOT:PSS/spiroTPD(40 nm)/TPBi(40 nm)/Mg:Ag/Ag OLED.

Photographs of QD-LED pixels are shown above the corresponding EL spectra (Figure 7-6(a)). Despite the minor organic emission contribution, QD-LED pixels

based on ZnCdS and ZnCdS/ZnS QDs appear blue and cyan to the eye. The photograph in Figure 7-6(c) shows solutions of the QDs used in the current study as well as other QD types that can potentially be used in QD-LED fabrication. The materials are indicative of the highest PL QY reported for QDs within a certain spectral range.

The EQEs of our QD-LEDs are displayed in Figure 7-8(a). Since EQE is defined as a number of the emitted photons per number of the injected electrons, it is the only measure of the efficiency, with which a particular QD-LED converts injected current into the output light. The peak EQE values are 1% for red, 2.7% for orange, 2.6% for green, 0.2% for cyan and 0.4% for blue QD-LEDs. Corresponding peak values of power efficiency (Figure 7-8(b)) are 0.25 lm/W for red, 2.4 lm/W for orange, 5 lm/W for green, 0.1 lm/W for cyan, 0.2 lm/W for blue QD-LEDs. The EQE and power efficiency values for orange, green and blue QD-LEDs represent record values reported so far for QD-LEDs. It is not surprising that despite almost equal EQE values, the power efficiency of green QD-LEDs is >2 times higher than that of orange QD-LEDs as in this case the overlap between the QD-LED EL spectrum and the standard luminosity function, which reflects the sensitivity of a human eye (Figure 2-12), is much higher.

While the EQE of our green QD-LEDs is >4 times higher than previously reported values, we observe only a slight increase in the blue QD-LED EQE. This result is consistent with our previous observations, where we find that the QD EL in QD-LEDs is primarily due to the excitons that have been non-radiatively transferred to QDs from organic materials [109]. In previous QD-LED designs, green QD-LEDs could only operate via direct charge injection and energy transfer from TPD (or polymer TPD derivatives) HTL [17, 32, 52]. Exciton formation in organic HTL is inhibited by electron accumulation in neighboring sites and exciton formation in Alq_3 ETL was purposely eliminated by a HBL to any avoid Alq_3 contribution to the QD-LED spectrum. Consequently the EQEs of these devices did not exceed 0.5-0.6% [17, 32, 52]. In our design we eliminate the HBL and allow exciton formation in both the spiroTPD HTL and the TPBi ETL, that can both transfer its exciton energy to green QDs. The operation of blue QD-LEDs is still limited by charge injection,

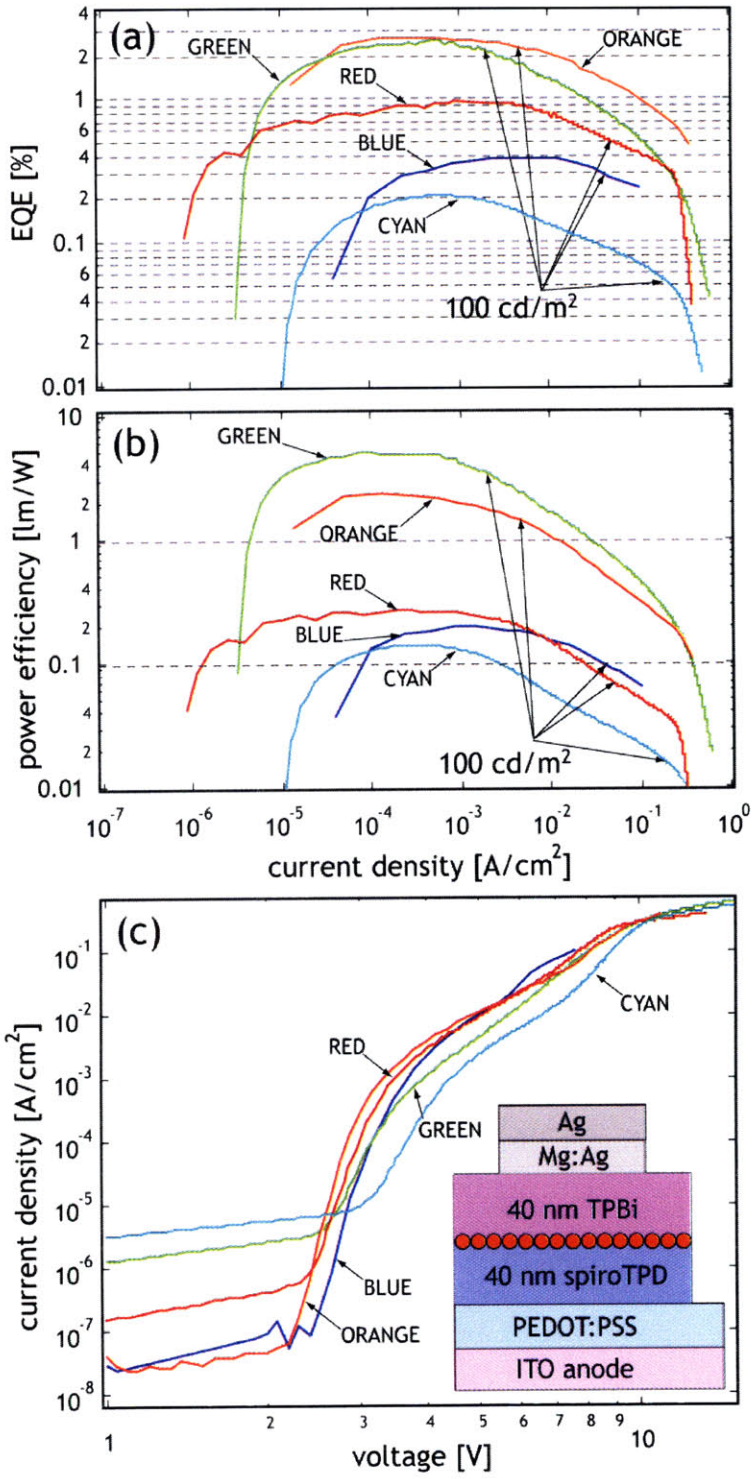

Figure 7-8: (a) The EQE and (b) power efficiency in lm/W for red, orange, green, cyan and blue QD-LEDs are plotted vs. current density. (c) Current-voltage characteristics of the different color QD-LEDs. The inset shows the schematic cross section of the device structure used in this study.

which is manifested in the low EQE value of 0.4%. The charge injection into cyan ZnCdS/ZnS core-shell QDs is further inhibited by a thick wide band gap ZnS shell, and consequently the EQE of cyan QD-LEDs is 2 times lower than that of blue QD-LEDs, despite the increased solution PL QY of the overcoated QDs.

7.5 Summary

We demonstrate that through the novel synthetic procedures for colloidal QDs and optimized organic charge transport layers, the EQE of hybrid organic/QD LEDs can be pushed towards the fundamental efficiency limit associated with QD luminescence efficiency in a thin film. While we can routinely obtain EQEs between 1-3% for QD-LEDs emitting in the green and red parts of the visible spectrum, achieving a high EQE in blue QD-LEDs remains a challenge. The final step towards achieving efficient full color red-green-blue QD-LED displays is the design and synthesis of wide band gap hole and electron transporting materials for improved exciton energy transfer and direct charge injection into blue QDs.

We also emphasize the importance of electronic characterization of the organic materials considered for hole and electron transport layers in QD-LEDs. Since material interfaces play a significant role in electrically driven structures, measuring the EL spectra of organic materials provides us with information more relevant to QD-LEDs than the information obtained from PL measurements.

Chapter 8

Conclusions and Future Directions

LEDs based on organic charge transport layers and emissive colloidal QD monolayers are a natural extension of OLEDs and potentially a next step towards the development of thin, bright and efficient flat panel displays and general lighting sources. QD-LEDs exhibit narrow electroluminescence (EL) spectra characteristic of colloidal QDs, leading to saturated color pixels. Unlike doped OLEDs, QD-LED pixels of different emission colors can be fabricated on the same substrate in one simple solvent-free contact printing step. Multiple color QDs can be mixed in solution and then deposited as a single emissive layer inside a QD-LED structure, leading to essentially unlimited tunability of QD-LED colors. The main challenge on the way to QD-LED commercial adoption is the efficiency of these devices, which, to date, is 3-10 times lower than that of OLEDs. Understanding the fundamental processes governing the QD-LED operation is a key step to improving the efficiency of these devices through intelligent design.

8.1 Guidelines for Hybrid Organic/QD LED Design

This thesis was dedicated to the development of the experimental guidelines and theoretical insights for the design of QD-LEDs. Below are the steps that I found

essential for improving the performance of these devices:

- **Choice of colloidal QDs.** It is crucial to use materials with the highest possible solution (and, hence thin film) photoluminescence (PL) quantum yield, as the external quantum efficiency (EQE) of QD-LEDs is ultimately limited by this number.

- **Choice of organic materials: band gap.** In Chapter 5 we found that exciton formation on organic materials and subsequent energy transfer to QDs is the dominating mechanism of QD EL in QD-LEDs. Maximizing the energy transfer dramatically improves the EQE values of QD-LEDs. Consequently, it is essential to use organic charge transporting materials with emission spectra that overlap with the absorption spectra of all the QD types and colors from blue to deep red. The band gap of organics should be sufficiently high so that they cannot accept QD excitons.

- **Choice of organic materials: HOMO and LUMO levels.** For improved hole injection into QDs we need to find hole-transporting layers (HTLs) with the lowest possible HOMO level, since the valence band of QDs is generally positioned below -6.6 eV. Unlike hole injection, electron injection into QDs is not obstructed by energy barriers. Hence QDs tend to charge efficiently with electrons, which then results in a high probability of formation of exciton-electron complexes that recombine via non-radiative Auger mechanism. Consequently, electron transporting materials with low LUMO levels < -4.5 eV can potentially improve the charge balance at QD sites.

- **Material characterization.** Organic materials are often characterized by their optical properties in solution. However, optical and electronic properties differ drastically in a thin film, as molecules of the material are brought in immediate contact with each other. For example, polar organic materials exhibit different solvato-chromic shifts upon dissolution in different organic solvents. Hence, prior to device fabrication, it is essential to measure the thin film absorption and PL spectra of organic charge transporting layers. In Chapter 7, we

found that the material behavior can also differ between optical and electrical excitation, as optical excitation probes bulk properties of the thin film while electrical excitation probes the properties of materials interfaces (i.e. exciton generation regions).

- **QD charging.** While direct charge injection can potentially yield superior QD-LED efficiencies, as it avoids exciton loss during the energy transfer step, it requires accurate carrier concentration balance at the QD sites due to a high probability of Auger recombination events. Since QDs charge with electrons more efficiently than with holes, it is beneficial to isolate QDs from ETL by embedding them into the HTL less than a Förster distance away from the HTL/ETL interface, i.e. the exciton formation region.

- **Morphology of hybrid interfaces.** In QD/organic optoelectronics the morphology of different device layers governs the device performance. Rough films, resulting from chemical incompatibility of the materials, yield electrically shorted devices. Change in morphology of an organic thin film is usually a sign of crystallization, which yields fundamental changes of material properties, such as conductivity. The morphology of the QD layer determines the color purity of the QD-LED EL, i.e. hexagonally close-packed defect-free QD films result in narrow QD-LED EL spectra dominated by QD emission, while poorly packed and incomplete QD layers allow for an organics emission contribution to the QD-LED EL. The morphology of different QD layers can be characterized by atomic force microscopy (AFM) or scanning electron microscopy (SEM).

- **Device Modeling.** In Chapter 6 we developed a numerical model that produces carrier concentration, exciton concentration, and electric field profiles in hybrid organic/QD devices. Using a simple numerical model may shorten the device design "trial-and-error" process by providing the possible EL spectra and carrier accumulation regions for the hybrid structures of interest.

While, the experimental design guidelines proposed above apply most directly to QD-LEDs, our numerical model described in Chapter 6 can be used for the develop-

ment of any hybrid organic/QD opto-electronic devices, such as solar cells, photodetectors, and chemical sensors.

8.2 Possible Future Directions for Hybrid Organic/QD Optoelectronics

Despite a more than ten year old history, the field of hybrid organic/QD electronics has not reached its maturity. This is indicated by the rapid and significant improvements in the efficiency of the QD-LEDs and photovoltaic (PV) devices, which increased by two orders of magnitude over the last decade. External quantum efficiency (EQE) values of up to 2.7% and power efficiencies of up to 5 lm/W have been achieved for QD-LEDs [32, 113]; EQE values of up to 60% and power conversion efficiencies of up to 2.8% have been observed in hybrid PV devices [40, 116]. Despite this rapid progress, the efficiencies of hybrid QD-LEDs and PV devices have not reached the fundamental limits set by the material properties. For example, the solution quantum yield (QY) of high quality luminescent QDs is approaching 90%, which implies that the internal quantum efficiency of QD-LEDs may be as high as the QY. However, currently the QY of colloidal QDs in thin film is 10-20 times lower than that of the same QDs in solution. It is reasonable to expect that this drastic difference between the solution and thin film QY of colloidal QDs will be reduced or completely eliminated by the synthesis of more robust organic ligands and wide band gap shells coating the QD cores. These chemical modifications would reduce the exciton dissociation due to carrier loss to the deep trap states formed by dangling bonds on the QD surface. In addition thicker shells may prevent energy transfer between the QDs within a thin film, which will reduce the exciton loss due to energy transfer from bright (neutral) to dark (charged) QDs. Device design plays a dramatic role in QD-LED performance. The record QD-LED efficiencies are 3-10 times lower than the QD QY in thin film, which means that significant improvements to currently used QD-LED structures and, potentially, novel QD-LED structures can be introduced to

close the existing efficiency gap.

An overwhelming majority of the QD-LED and QD-PV device design research focuses on the employment of novel organic materials for carrier transport [31, 32, 33, 40, 68, 74, 116]. A variety of small molecule organic materials as well as polymers have been employed as carrier transporting films in QD-LEDs and hybrid PVs. Novel types of colloidal semiconductor nanoparticles have been synthesized to suit a particular purpose in PV devices or QD-LEDs. A variety of semiconductor materials, as well as shapes and sizes of nanoparticles have been tested in hybrid optoelectronic devices (e.g. nanorods, tetrapods and hyperbranched nanocrystals have been employed in hybrid PV devices [2, 40, 116], while core-multishell structures [17, 52] and several semiconductor alloys [17, 115] have been used for highly luminescent QD-LEDs). Less research has been dedicated to novel fabrication methods, such as film deposition and packaging techniques. Despite that, a controlled deposition of QD monolayers [30], multilayers [31, 32] and organic-nanoparticle blends [2, 40, 74] has been demonstrated, and the contact printing method allows us to deposit high resolution patterns of QD films [16]. Finally, significantly less effort has been dedicated towards studying the fundamental physical properties of organic/QD interfaces as well as the properties of QDs as electronic components [104, 109, 117]. Mechanisms for the operation of hybrid optoelectronic devices are often discussed briefly in the device design literature [17, 31, 68, 74]. However there is little research dedicated specifically to understanding the physical processes in hybrid optoelectronic devices, particularly QD-LEDs.

Below, I propose several research projects aiming to improve the efficiencies of QD-LEDs an hybrid PV devices through studying the fundamental physical processes in hybrid material systems:

- **Computer-based device design tools.** Optical and electronic properties of organic materials and QDs have been studied independently from each other over the past twenty years [13, 47]. Despite that, we only now start to apply this knowledge to the design of hybrid optoelectronic devices. Still, the approach to device design remains rather empirical and inefficient (i.e., based on trial and error). To expedite the design process, it is essential to create databases of the

available materials and their properties, such as positions of their energy bands, carrier mobilities, glass transition temperature, PL efficiency, absorption cross section etc. We can then create search algorithms that would find materials systems optimized to be efficient at a particular function, e.g. charge separation for solar cells or exciton generation for LEDs. We can also take into account less obvious properties such as the possibility of energy transfer in the materials systems. The resulting materials systems or suggested devices structures obtained by the search engine can then be analyzed using a physical model, for example the model described in this thesis. Based on the carrier and exciton concentrations and electric field profiles in the hypothetical devices, we can then pick the structures that promise the highest available efficiency (most photons per injected carrier in an LED, or most extracted carriers per absorbed photon and the highest open circuit voltage for PV devices). We can then study these materials systems with respect to their interface properties, such as chemical and structural compatibility, environmental stability.

- **Relative energy band positions in hybrid devices.** We can perform optical measurements to find band offsets between the organic materials and QDs. For instance, we can optically excite QDs in contact with an organic material, and based on the change in the QD PL relaxation time and QD PL intensity we can determine whether QDs act as exciton donors or acceptors with this material, and whether this material contributes to the QD exciton confinement or dissociation. If we find that the QD conduction band is lower than the conduction band of our organic material, we can then use induced IR absorption measurement to find the exact difference in energy. In induced IR absorption experiments QDs can be first excited with a visible light pulse to create an exciton, which is then followed by an excitation with an IR pulse of variable energy. An additional absorption peak that may arise corresponds to the conduction band offset between QDs and the organic material. Measuring energy band offsets between the different materials within an active optoelectronic structure is

fundamentally different from finding the energy band structure of every material constituting the structure, since electronic and mechanical constraints that different materials impose onto each other may alter the positions of energy levels of each of the materials. For example, recent studies suggest that the positions of QD conduction and valence bands can be shifted by up to 1 eV from their equilibrium positions when QDs are blended into a conductive polymer matrix [118].

- **Optical properties of charged QDs.** Scanning tunneling probe microscopy (STM) can be used to determine the position of conduction and valence bands of individual QDs in contact with a conductive surface such as a metal or a highly doped semiconductor [119]. Low temperature measurements can even provide us with the information about the fine structure of electron and hole energy levels in QDs. STM combined with a single QD optical spectroscopy could provide us with unique information about the optical properties of charged QDs, which are most likely present in hybrid optoelectronic devices.

  Similar ensemble measurements can be applied to QD films. Such measurements are enabled by the hybrid devices, which can be excited electronically, enabling carrier injection into QDs. The charged QDs can be concomitantly excited optically in order to measure their PL and absorption spectra.

- **The role of spin symmetry in hybrid devices.** The effects of the magnetic field on the performance of hybrid organic/QD devices have not been explored. Such experiments can provide us with insights into the importance of the spin-symmetry in these devices, i.e. whether different spin states of QDs interact differently with organic materials with respect to carrier and exciton transport.

- **Using surface plasmons in hybrid devices.** Interactions between colloidal QDs and metal films have not received much attention. It was shown that the PL intensity of epitaxial QDs can be amplified through energy transfer from surface plasmons of metallic films [120]. Similarly, we could use surface plasmons for long distance energy transfer between the different components of

a hybrid organic/QD device [121]. For example, one can imagine a LED, in which excitons are generated efficiently in phosphorescent organic films. This exciton energy can then be transferred through a surface plasmon to QDs that are otherwise isolated from the rest of the structure, and are not susceptible to charging. One can also imagine a PV device, where excitons generated in QDs are then transferred through a surface plasmon to an exciton-dissociating interface.

- **Parallel design and synthesis of novel organic materials and QDs.** The development of novel organic materials should be performed in parallel with the development of novel QDs. Currently organic materials are being developed specifically for OLED applications, and, in most cases, lack the properties desirable for successful interactions with the colloidal QDs. For example, the HOMO level of the majority of available organic hole transporting materials lies below the valence band of the majority of colloidal semiconductor QDs. This property, naturally, results in poor hole injection into QDs and leads to charge imbalance that impedes the performance of QD-LEDs. On the other hand, the QD conduction band lies below the LUMO level of the majority of organic electron transporting materials. Consequently, in hybrid PV devices, photogenerated electrons cannot be extracted from QDs, which results in the loss of a significant portion of the photocurrent. In addition, excitons generated on QDs populated with electrons recombine rapidly via an Auger mechanism rather than dissociating and contributing to the photocurrent. Chemical compatibility between the organics and QDs should also be taken into account, as chemically strained surfaces would most likely be unstable when exposed to atmospheric oxygen and water.

- **Environmental stability and life-time of hybrid devices.** Significant effort should be dedicated to studying the environmental stability of the hybrid organic/QD structures. The fragility of organic materials constitutes a major obstacle on the way to industrial development and potential commercialization

of optoelectronic devices containing organic thin films. Currently, there has been only a few, mostly anecdotal, observations of hybrid optoelectronic device lifetimes [32]. Until this point, we primarily relied on the data available for organic optoelectronic devices. While this data is somewhat relevant to the bulk properties of organic films, the stability of hybrid interfaces has not been thoroughly characterized.

Here I discussed only the most obvious directions in hybrid organic/QD optoelectronic devices research. I expect the field to change dramatically within next several years, as we take advantage of novel chemical procedures and physical concepts that have been developed for both organics and QDs, and that are yet to be applied in active optoelectronic devices.

Hybrid interfaces provide us with an inexhaustible wealth of challenges and research opportunities. The basic physics approach to studying these novel hybrid materials systems may yield discoveries of properties that are fundamentally different from those of neat materials and hold keys to understanding issues associated with energy production, efficient utilization, and storage.

Appendix A

QD-LED Fabrication Step-by-Step

The process flow described in this Appendix is an example of a standard QD-LED fabrication process. All the QD-LEDs discussed in this thesis were fabricated in a process identical or similar to this one. The detailed description provided here is supposed to facilitate further development as well as reproducibility of QD-LEDs.

A.1 Preparation of QD Solutions

In this section we outline the steps associated with QD solution preparation. Since colloidal QDs are synthesized in a hot bath of organic molecules, which then serve as their ligands, simply dissolving QDs, extracted from growth solution, in organic solvents is not sufficient for QD use in active optoelectronic devices. Dilutions of QD growth solutions contain excess organic ligands, which impede the carrier transport through optoelectronic devices, as well as yield poor QD layer morphology. Below we describe the procedures that eliminate excess ligands from QD solutions. These procedures produce QD solutions that yield high quality close-packed QD films and efficient QD-LEDs.

A.1.1 Purifying TOPO/TOP Coated QDs

Typically CdSe/ZnS core-shell QDs emitting in the yellow or red parts of the visible spectrum, are coated with TOPO and TOP. Below is the procedure ("crash-out") for cleaning these types of QDs.

1. Start with QDs in hexane solution
2. For 4 ml of QD solution, add 1 ml of butanol and 2 ml of methanol. You may need to add more methanol. Stop immediately after solution becomes cloudy. Cloudiness corresponds to QDs precipitating out of solution.
3. Centrifuge for 4 min at 4000 rpm. You should find QDs precipitated on the bottom of the centrifuge tube. The supernatant should be clear or almost clear. The more transparent the supernatant is the cleaner are the QDs.
4. Pour out the supernatant carefully into the hazardous waste bottle. Dry the QDs under air or nitrogen flow for ~30 sec.
5. Redissolve QDs in 2-4 ml of hexane. If QDs dissolve easily you may perform steps 2 through 4 up to two more times (recommended for electronics quality QDs).
6. After final drying step, redissolve QDs in 2-4 ml of any non-polar solvent of your choice (e.g., hexane, chloroform, chlorobenzene, toluene etc.)
7. Sonicate the resulting solution at room temperature for $\sim$ 1 min or until it is translucent.
8. Filter QDs through a 0.2 μl PTFE filter.

A.1.2 Purifying Oleic Acid Coated QDs

Typically ZnCdSe and ZnCdS alloyed QDs emitting in the red (ZnCdSe) or blue (ZnCdS) parts of the visible spectrum, are coated with oleic acid. Below is the procedure ("crash-out") for cleaning these types of QDs, which also may work for

ZnSe/CdSe/ZnS core-double-shell QDs emitting in the green part of the visible spectrum or PbSe and PbS QDs emitting in the infra red. Note: the crash-out of the alloyed QDs should be performed in a nitrogen or argon glovebox. Alloyed QDs are prone to degradation in air and will loose their luminescent properties if exposed to oxygen and light at the same time. After the purification alloyed QDs should be stored in a glovebox in a dark container (you may simply wrap the vial in aluminum foil).

1. Start with QDs in hexane solution
2. For 4 ml of QD solution, add $\sim$ 4-8 ml of acetone. Stop immediately after solution becomes cloudy. You may need to use a lot of acetone to reach the precipitation point.
3. Centrifuge for 4 min at 4000 rpm. You should find QDs precipitated on the bottom of the centrifuge tube. The supernatant should be clear or almost clear.
4. Pour out the supernatant carefully into the hazardous waste bottle. Dry the QDs for $\sim$30 sec.
5. Redissolve QDs in 2-4 ml of hexane.
6. For 4 ml of QD solution, add 1 ml of butanol and 2 ml of methanol. You may need to add more methanol. Stop immediately after solution becomes cloudy.
7. Centrifuge for 4 min at 4000 rpm. You should find QDs precipitated on the bottom of the centrifuge tube. The supernatant should be clear or almost clear.
8. Pour out the supernatant carefully into the hazardous waste bottle. Dry the QDs for $\sim$30 sec.
9. After final drying step, redissolve QDs in 2-4 ml of any non-polar solvent of your choice (e.g., hexane, chloroform, chlorobenzene, toluene etc.)
10. Sonicate the resulting solution at room temperature for $\sim$ 1 min or until it is translucent.

11. Filter QDs through a 0.2 μl PTFE filter.

The "crash-out" procedures described above are most likely to be sufficient for most of the standard QDs used in QD-LEDs and hybrid PVs. However, the novel QD types often have a combination of multiple ligand types coating their surface (TOPO, TOP, oleic acid, hexylphosphonic acid, oleylamine etc.). In the case of combination ligands you might need to combine the procedures described above with the procedures from the relevant synthetic chemistry literature.

A.2 Preparation of Substrates

1. Solvent cleaning of ITO coated glass substrates

    - Sonicate for 5 min in de-ionized (DI) water with detergent
    - Spray with DI water
    - Sonicate for 5 min in DI water
    - Spray with DI water
    - Sonicate for 2 min in acetone I
    - Sonicate for 2 min in acetone II
    - Immerse for 2 min into boiling isopropanol I
    - Immerse for 2 min into boiling isopropanol II
    - Dry each substrate under Nitrogen (N_2) or dry air flow

2. Expose clean substrates to Oxygen plasma for 5 min. This step removes any residual organics that were not dissolved in the solvent cleaning step as well as creates a hydrophilic surface, crucial for the next step.

3. Spin-cast an aqueous solution of resistive PEDOT:PSS (Baytron CH 8000) onto the substrates. Spin for 60 sec at speed of 4000 rpm with a 1000 rpm/sec ramp. The PEDOT:PSS smoothes out occasionally rough ITO surface, and

thus eliminates electrical shorting. In addition, it facilitates the hole injection from the ITO anode.

4. Bake PEDOT:PSS coated substrates for 7-8 min at 120°C in a N_2 glovebox to eliminate residual water from the film.

A.3 Deposition of the Organic Films and QD monolayers

1. Deposit a hole transporting layer (HTL - e.g., TPD, spiroTPD etc.) of desired thickness (often 40 nm) in a thermal evaporator. For better film quality, deposit at a starting evaporator pressure $< 5 \times 10^{-7}$ torr and rate < 0.15 nm/sec.

2. Print a monolayer of colloidal QDs onto HTL in a N_2 glovebox. Prior to device fabrication, the solution has to be calibrated to produce a desired number of QD layers (usually 1 monolayer) upon spin-casting onto parylene-C coated PDMS (60 sec at 3000 rpm with a 10000 rpm/sec ramp) and consecutive printing onto a HTL. This can be achieved by preparing multiple dilutions of stock QD solution. These solutions are then spun-cast onto parylene-C coated PDMS and printed onto a HTL identical to the one used in the target QD-LED. AFM images of the resulting films provide information about the thickness and morphology of each of the films. Consequently, they can be used to choose the solution with an appropriate QD concentration.

3. Deposit an electron transporting layer (ETL - e.g., Alq_3, TPBi etc.) of a desired thickness (often 40 nm) in a thermal evaporator. For better film quality, deposit at a starting evaporator pressure $< 5 \times 10^{-7}$ torr and at a rate < 0.15 nm/sec.

4. Deposit metallic cathode in a thermal evaporator. For a Mg:Ag alloy use the rate of 0.3 nm/sec for magnesium and 0.03 nm/sec for Ag when thickness monitor is set to Mg parameters. This produces a Mg:Ag alloy with an element ratio

of ~100:1. In this thesis, I used 100 nm thick Mg:Ag cathodes with 20 nm Ag protective layers deposited on top (at a rate of $\sim$ 0.15 nm/sec).

Devices should not be exposed to ambient conditions after step 4. QD-LEDs then can be tested in N_2 glovebox. For testing in ambient conditions QD-LEDs should be packaged in a N_2 glovebox, for example, using glass coverslips attached to the substrates with UV-curing epoxy.

Appendix B

Calculation of the Color Rendering Index

The color rendering index (CRI) is a quantitative measure of the ability of a light source to reproduce colors of illuminated objects accurately in comparison to sunlight (black body radiator at 5500 K).

In order to find the CRI, we use 8 test sample functions (TSCs) (Figure B-1(b)), that represent subtle colors: TSC_1 - light greyish red, TSC_2 - dark greyish yellow, TSC_3 - strong yellow green, TSC_4 - moderate yellowish green, TSC_5 - light bluish green, TSC_6 - light blue, TSC_7 - light violet, and TSC_8 - light reddish purple.

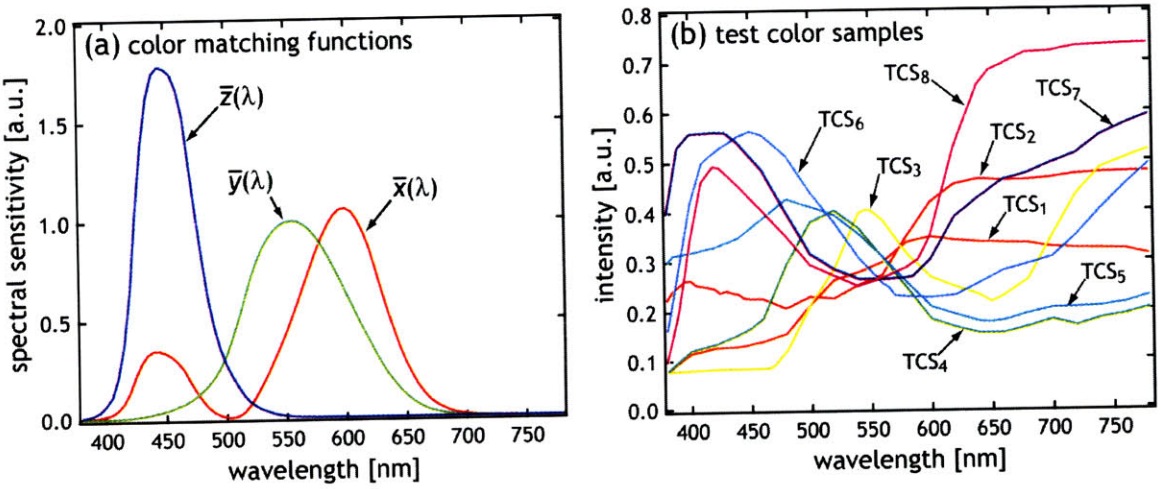

Figure B-1: (a) Spectral responsivity functions. (b) Test sample functions.

The CRI calculation then follows the steps listed below:

1. Find the CIE color coordinates for reflected sunlight in uv-color space

   - To find the spectra of sunlight reflected from TCS-colored objects we simply multiply the spectrum of sunlight $S(\lambda)$ by the TSCs:

   $$S_i(\lambda) = S(\lambda)TSC_i(\lambda) \tag{B.1}$$

   - Calculate the eye response functions for the sunlight using spectral responsivity functions in Figure B-1(a):

   $$\begin{aligned} X_i^S &= \int_{380}^{780} \bar{x}(\lambda)S_i(\lambda)d\lambda \\ Y_i^S &= \int_{380}^{780} \bar{y}(\lambda)S_i(\lambda)d\lambda \\ Z_i^S &= \int_{380}^{780} \bar{z}(\lambda)S_i(\lambda)d\lambda \end{aligned} \tag{B.2}$$

   - Find the CIE coordinates of reflected sunlight in xy-color space:

   $$\begin{aligned} x_i^S &= \frac{X_i^S}{X_i^S+Y_i^S+Z_i^S} \\ y_i^S &= \frac{Y_i^S}{X_i^S+Y_i^S+Z_i^S} \end{aligned} \tag{B.3}$$

   - Convert the CIE coordinates into uv-color space [122]:

   $$\begin{aligned} u_i^S &= \frac{4x_i^S}{-2x_i^S+12y_i^S+3} \\ v_i^S &= \frac{6y_i^S}{-2x_i^S+12y_i^S+3} \\ w_i^S &= 1 - u_i^S - v_i^S \end{aligned} \tag{B.4}$$

2. Find the CIE color coordinates of the light source of interest in uv-color space. Follow the steps presented above, replacing the sunlight spectrum $S(\lambda)$ with the spectrum $F(\lambda)$ of the light source of interest.

3. Find the difference between the color coordinates of your light source and sun-

light:

$$\begin{aligned} \Delta u_i &= u_i - u_i^S \\ \Delta v_i &= v_i - v_i^S \\ \Delta w_i &= w_i - w_i^S \end{aligned} \tag{B.5}$$

4. Calculate the CRI of your light source:

$$CRI = \frac{100}{8} \sum_{1}^{8} R_i, \tag{B.6}$$

where R_i can be found from the following equation:

$$R_i = 1 - 4.6\sqrt{\Delta u_i^2 + \Delta v_i^2 + \Delta w_i^2} \tag{B.7}$$

Naturally the CRI of sunlight is 100.

Appendix C

Structure of Carrier and Exciton Transport Models

As we are interested in modeling complex hybrid organic/QD devices, optimizing the numerical model is essential for decreasing the computational time. To reduce the computational load, we first break our model into charge transport and exciton transport parts. The solution to the carrier transport model is then taken as an input for the exciton transport model. Note, that for modeling photovoltaic devices, the exciton transport model should be applied first, and the solutions should be used as an input for the charge transport model. As photo-action is the process opposite to electroluminescence, it is natural that the charge and exciton models should be applied to these problems in the opposite order.

C.1 Charge Transport Model

The charge transport part is dedicated to a self-consistent solution of the continuity equations 6.2 and 6.5 that can be rewritten in a discrete form for each layer i of the device:

$$\begin{aligned} \frac{dn_i}{dt} &= \frac{\Delta J_{n,i}}{\Delta x} - n_i p_i R_i \\ \frac{dp_i}{dt} &= \frac{\Delta J_{p,i}}{\Delta x} - n_i p_i R_i \end{aligned} \tag{C.1}$$

here n_i and p_i are electron and hole concentrations in layer i of the device. $J_{n,i}$ and $J_{p,i}$ are electron and hole fluxes through layer i, R_i is the recombination rate in layer i, and $\Delta x = 1$ nm is the thickness of each layer. Note, that the equations above are most applicable for hybrid LEDs. In the case of photovoltaic devices these equations should include a carrier generation rate proportional to the exciton dissociation rate obtained from the exciton transport model. In the case of negligible carrier recombination in photovoltaic devices the equations C.1 take the following form:

$$\begin{aligned} \frac{dn_i}{dt} &= \frac{\Delta J_{n,i}}{\Delta x} - n_i p_i R_i + G_i^n \approx \frac{\Delta J_{n,i}}{\Delta x} + G_i^n \\ \frac{dp_i}{dt} &= \frac{\Delta J_{p,i}}{\Delta x} - n_i p_i R_i + G_i^p \approx \frac{\Delta J_{p,i}}{\Delta x} + G_i^p \end{aligned} \tag{C.2}$$

Independent of the device structure or purpose, in the most simple case the local carrier fluxes are defined by:

$$\begin{aligned} J_{n,i} &= n_i E_i \mu_{n,i} B_c + D_{n,i} \frac{\Delta n_i}{\Delta x} B_{c,i} \\ J_{p,i} &= p_i E_i \mu_{p,i} B_v + D_{p,i} \frac{\Delta p_i}{\Delta x} B_{v,i} \end{aligned} \tag{C.3}$$

Plugging Equations C.3 into Equations C.1 results in a set of equations that can be written in a matrix form:

$$\begin{aligned} \frac{d\vec{n}}{dt} &= S_n \vec{n} - \vec{n}\vec{p}\vec{R} \\ \frac{d\vec{p}}{dt} &= S_p \vec{p} - \vec{n}\vec{p}\vec{R} \end{aligned} \tag{C.4}$$

Here $\vec{n} = (n_1, ..., n_N)$ and $\vec{p} = (p_1, ..., p_N)$, $\vec{R} = (R_1, ..., R_N)$, S_n and S_p are electron and hole transport matrices. Carrier transport matrices are mostly tri-diagonal since we only take into account nearest neighbor interactions with the exception of the tunneling through thin energy barriers (e.g., hole tunneling through a QD monolayer).

The boundary conditions for these equations are such that the hole concentration at the anode p_1 and the electron concentration at the cathode n_N stay constant. Initial conditions then are $\vec{p}_0 = (p_1, p_i, ..., p_i)$ and $\vec{n}_0 = (n_i, ..., n_i, n_N)$, where the intrinsic carrier concentrations are $p_i = n_i = 10^6$ cm^{-3}.

Local electric fields in our model obey Poisson's equation:

$$\frac{E_{i,i+1} - E_{i-1,i}}{\Delta x} = \frac{4\pi}{\varepsilon_i} e(p_i - n_i) \tag{C.5}$$

Then the electric field between layers i and $i+1$ is defined by the following expression:

$$E_{i,i+1} = 4\pi \Delta x e \sum_{k=1}^{k=i} \frac{(p_k - n_k)}{\varepsilon_k} \tag{C.6}$$

Since in our experiments we usually apply a voltage to our devices and then we measure the current, we then set the boundary conditions for the electric field such that the potential at the anode is $\phi_{0,1} = V$ and the cathode is grounded: $\phi_{N,N+1} = 0$, where the anode is the 0^{th} layer and the cathode is the $(N+1)^{th}$ layer. These boundary conditions translate into the condition for the electric field:

$$E_{0,1} = \frac{1}{d}\left[V - \Delta x \sum_{i=2}^{N+1} E_{i-1,i}\right] \tag{C.7}$$

Here $E_{0,1}$ is the electric field between anode and the 1^{st} device layer, and $d = N\Delta x$ is the total device thickness. To simplify the notation in the future we will refer to $E_{i-1,i}$ as E_i and $E_{i,i+1}$ as E_{i+1}.

Since we have a system of non-linear differential equations for both electrons and holes in a matrix form, we choose MATLab as a programming interface for our model due to its efficiency in operations with matrices.

Equations C.3 are a primitive representation for the equations for carrier fluxes. In our model, we define fluxes across the interfaces analogous to local electric fields. In order to avoid lengthy definitions of multiple cases for different carrier concentration relationships in neighboring layers and different signs of electric fields at the borders of each layer, we use simple algorithms to create carrier transport matrices.

First we break the transport matrices into drift and diffusion parts (this follows directly from the definition of flux): $S_{n,p} = S_{n,p}^{drift} + S_{n,p}^{diff}$. In both the drift and diffusion matrices, elements $S_{n/p,ij}$ represent the dependence of the carrier concentration in layer i on the carrier concentration in the neighboring layer j.

C.1.1 Carrier Drift Matrices

The flux direction at each of the borders of any layer is determined by the signs of the local electric field at the borders of the layer. Conventionally a positive electric field implies electron flux from the cathode to the anode and hole flux from the anode to the cathode.

Understanding of the basic operation of the model code is facilitated by the example in Figure C-1.

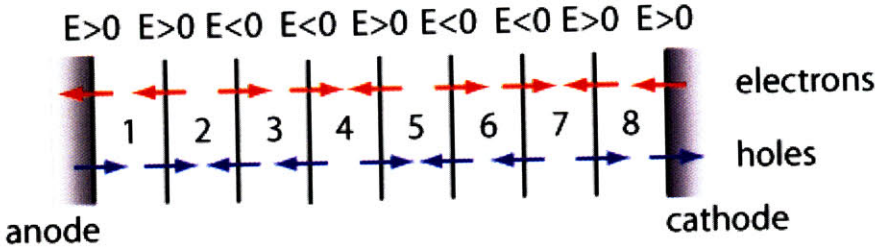

Figure C-1: Schematic diagram showing the 8-layer device with electron and hole fluxes marked with red and blue arrows, respectively.

Electron and hole drift matrices for the electric field profile shown in Figure C-1 have the following structures:

$$S_n^{drift} = \begin{bmatrix} 0 & S_n^{CA}(2) & 0 & 0 & 0 & 0 & 0 & 0 \\ 0 & -S_n^{CA}(2) - S_n^{AC}(2) & 0 & 0 & 0 & 0 & 0 & 0 \\ 0 & S_n^{AC}(2) & -S_n^{AC}(3) & 0 & 0 & 0 & 0 & 0 \\ 0 & 0 & S_n^{AC}(3) & 0 & S_n^{CA}(5) & 0 & 0 & 0 \\ 0 & 0 & 0 & 0 & -S_n^{CA}(5) - S_n^{AC}(5) & 0 & 0 & 0 \\ 0 & 0 & 0 & 0 & S_n^{AC}(5) & -S_n^{AC}(6) & 0 & 0 \\ 0 & 0 & 0 & 0 & 0 & S_n^{AC}(6) & 0 & S_n^{CA}(8) \\ 0 & 0 & 0 & 0 & 0 & 0 & 0 & -S_n^{CA}(8) \end{bmatrix} \quad \text{(C.8)}$$

$$S_p^{drift} = \begin{bmatrix} -S_p^{AC}(1) & 0 & 0 & 0 & 0 & 0 & 0 & 0 \\ S_p^{AC}(1) & 0 & S_p^{CA}(3) & 0 & 0 & 0 & 0 & 0 \\ 0 & 0 & -S_p^{CA}(3) & S_p^{CA}(4) & 0 & 0 & 0 & 0 \\ 0 & 0 & 0 & -S_p^{CA}(4) - S_p^{AC}(4) & 0 & 0 & 0 & 0 \\ 0 & 0 & 0 & S_p^{AC}(4) & 0 & S_p^{CA}(6) & 0 & 0 \\ 0 & 0 & 0 & 0 & 0 & -S_p^{CA}(6) & S_p^{CA}(7) & 0 \\ 0 & 0 & 0 & 0 & 0 & 0 & -S_p^{CA}(7) - S_p^{AC}(7) & 0) \\ 0 & 0 & 0 & 0 & 0 & 0 & S_p^{AC}(7) & 0 \end{bmatrix} \quad \text{(C.9)}$$

In these matrices the diagonal elements are always negative as they represent carrier escape from the layer. Labels "CA" = "from cathode to anode" and "AC" = "from anode to cathode" indicate the direction of a carrier flux, as Boltzmann factors contributing to the matrix elements can be different for the carrier transport from a layer into each of its neighbors.

Off-diagonal elements for the electron drift matrix are constructed similarly to the following:

$$S_{n,32} = S_n^{AC}(2) = \frac{1}{\Delta x}|E_3|\mu_{n,2}B_{c,2}^{AC} \quad \text{(C.10)}$$

Here E_3 is the electric field that drives electrons from layer 2 to layer 3 ($E_{2,3} = E_3$), we use the mobilities and the Boltzmann factors of layer 2 since the electrons start their transport from this layer (Figure C-1), i.e. the electron flux between layers 2 and 3 is in the direction from the anode to the cathode.

By analogy, off-diagonal elements for the hole drift matrix are constructed in the following way:

$$S_{p,32} = S_p^{CA}(3) = \frac{1}{\Delta x}|E_3|\mu_{p,3}B_{v,3}^{CA} \quad \text{(C.11)}$$

Here we use the mobilities and the Boltzmann factors of layer 3 since the holes start their transport from this layer (Figure C-1). Here the hole flux between layers

2 and 3 is in the direction from the cathode to the anode.

A diagonal matrix element $S_{n/p,ii}$ is 0 when there is carrier in-flux from both neighbors into the layer i. When there is carrier flux out of the layer into the neighbors, the matrix elements are negative and equal with the "-" sign to the matrix elements determining the flux into the neighbors from the layer (compare Equations C.12 and C.9 with carrier fluxes in Figure C-1).

To find these matrices in the code of our model we first find all the layers, into which there is carrier flux from left and/or right neighbors (i.e. for electrons $E_i < 0$ and/or $E_{i+1} > 0$ and the opposite for holes). We then find the indexes of these layers and the corresponding parameters that construct the matrix elements (mobilities, Boltzmann factors).

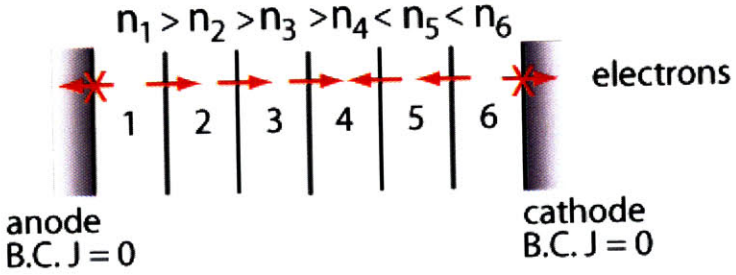

Figure C-2: Schematic diagram showing a 6-layer device with electron fluxes marked with red arrows.

C.1.2 Carrier Diffusion Matrices

Unlike the case of the carrier drift matrices, where the sign of the electric field determines the directions of the electron and hole fluxes (note that the same sign of the electric field results in the hole and electron fluxes in opposite directions), for the carrier diffusion matrices, the concentration gradients determine the directions of flux for both carrier types, and therefore the hole and electron diffusion matrices are built in an identical manner. In addition, since the fluxes are determined by the concentration differences between the neighboring layers (see Equation 6.2), the diffusion matrices are always tri-diagonal (with all non-zero elements in all three diagonals) and hermitian ($S_{ij}^{diff} = S_{ji}^{diff}$).

Analogous to the previous section, here we again employ a simple example in Figure C-2 to illustrate the basic structure of the diffusion matrices. We only consider electron fluxes, since the identical arguments can be made with respect to hole fluxes.

The electron diffusion matrix for the device state shown in Figure C-2 has the following form:

$$\begin{bmatrix} -S_n^{AC}(1) & S_n^{AC}(1) & 0 & 0 & 0 & 0 \\ S_n^{AC}(1) & -S_n^{AC}(1) - S_n^{AC}(2) & S_n^{AC}(2) & 0 & 0 & 0 \\ 0 & S_n^{AC}(2) & -S_n^{AC}(2) - S_n^{AC}(3) & S_n^{AC}(3) & 0 & 0 \\ 0 & 0 & S_n^{AC}(3) & -S_n^{AC}(3) - S_n^{CA}(5) & S_n^{CA}(5) & 0 \\ 0 & 0 & 0 & S_n^{CA}(5) & -S_n^{CA}(5) - S_n^{CA}(6) & S_n^{CA}(6) \\ 0 & 0 & 0 & 0 & S_n^{CA}(6) & -S_n^{CA}(6) \end{bmatrix} \tag{C.12}$$

The off-diagonal matrix elements here are constructed as follows (see Equation 6.2):

$$S_{n,34} = S_n^{AC}(3) = \frac{1}{\Delta x^2} D_{n,3} B_{c,3}^{AC} = S_{n,43} \tag{C.13}$$

Here the diffusion constant $D_{n,3}$ and the Boltzmann factor $B_{c,3}^{AC}$ indicate that the diffusive flux is from layer 3 into layer 4. Naturally all the off-diagonal elements are positive as they connect the concentration change in a given layer to concentrations in neighboring layers, and high concentrations in neighboring layers both reduce the flux out of a given layer or induce the flux into the given layer.

The diagonal elements are simply the negative sums of the neighboring elements:

$$S_{ii}^{diff} = -S_{i,i-1}^{diff} - S_{i,i+1}^{diff} \tag{C.14}$$

This directly follows from the difference representation of a second order differential. All the diagonal elements are negative since a high concentration in a given layer promotes the flux out of that layer as well as reduces the flux into the layer.

The code automatically finds the layers which will have flux out of them and into

their neighbors and builds the corresponding matrix elements (Equation C.13). The Hermitian property of the matrix and Equation C.14 are then used to build the rest of the matrix elements.

C.1.3 Tunneling

Finally, in the absence of tunneling, the carrier transport matrices are: $S_{n,p} = S_{n,p}^{drift} + S_{n,p}^{diff}$.

If our device has thin energy barriers so that electrons or holes can tunnel through, we need to include additional matrix elements that describe tunneling (Equation 6.8 for carrier tunneling through organic barriers and Equation 6.11 for hole tunneling through the QD barrier).

For carrier (for example electrons) tunneling through a thin organic barrier from layer i into layer j, we need to introduce corrections to the matrix elements $S_{n,ji}$ and $S_{n,ii}$ (note, that due to flux conservation $S_{n,ii} = -S_{n,ji}$):

$$\Delta S_{n,ji} = \left(\frac{1}{\tau_{ji}^{f}} + \frac{1}{\tau_{ji}^{D}} \right) e^{-2\alpha|i-j-1|\Delta x} \tag{C.15}$$

Here the field assisted and gradient assisted hopping times τ_{ji}^{f} and τ_{ji}^{D} can be found from Equations 6.9 and 6.10.

C.1.4 Numerical Solution Process

1. Start with initial conditions for electron and hole concentration vectors.

2. Calculate the local electric fields using Equations C.6 and C.7

3. Calculate the carrier transport matrices

   Note, that the boundary conditions for the transport matrices are different for different modes of device operation. For example, hybrid LEDs have injecting contacts. Consequently it is convenient to set the electron concentration constant at the cathode and set the hole concentration constant at the anode, since there is a bath of carriers at each injecting contact. This assumption is

implemented in the carrier transport matrices by setting $S_{p,11} = S_{p,12} = 0$ and $S_{n,NN} = S_{n,N(N-1)} = 0$ (For our devices we assume that layer 1 is adjacent to the anode and the last layer N is adjacent to the cathode.) Different boundary conditions should be considered for photovoltaic devices, since in these devices the drift and diffusion currents do not necessarily counteract each other at the injecting contacts, and hence the boundary conditions need to be considered separately for the drift and diffusion matrices.

4. Calculate the change in the carrier concentrations using the transport matrices and recombination rates

5. Repeat steps 2 through 4 until the concentrations in the layers and the local electric fields reach the steady state

C.2 Exciton Transport Model

The exciton transport model is focused on finding the steady state solution to Equation 6.12 written in a matrix form based on the initial conditions posed by the results of our carrier transport model.

C.2.1 Exciton Transport Matrix

The core of the exciton transport matrix is identical to the carrier diffusion matrices as the excitons move through the device driven by the exciton concentration gradients (Here the diffusion constants $D = \frac{L_D^2}{\tau}$, where L_D is the diffusion length and τ is the exciton relaxation time). However, we need to include three important exciton processes: (1) exciton generation; (2) exciton relaxation; (3) Förster energy transfer; (4) Onsager field-induced exciton dissociation.

1. **Exciton Generation**

   For hybrid LEDs the exciton generation rates are obtained from the charge transport model as $\vec{G} = \vec{R}\vec{n}_{SS}\vec{p}_{SS}$, where $\vec{n}_{SS}$ and $\vec{p}_{SS}$ are steady state electron

and hole concentration vectors. For photovoltaic devices the exciton generation rate should be calculated based on the illumination density and the material absorption coefficients.

The generation rates are included as a separate constant vector in the exciton transport equation:

$$\frac{d\vec{\xi}}{dt} = M\vec{\xi} + \vec{G} \tag{C.16}$$

where $\vec{\xi}$ is the vector of exciton concentrations in the device layers, and M is the transport matrix.

2. **Exciton Relaxation**

Exciton relaxation is included by adding the relaxation rates to the diagonal elements of the transport matrix:

$$M^1_{ii} = M^0_{ii} - \frac{1}{\tau_i} \tag{C.17}$$

where M^0 is the exciton diffusion matrix and M^1 is exciton transport matrix corrected for exciton relaxation.

3. **Förster Energy Transfer**

This part of the matrix has to be "custom-built" for every device, depending on the different donors and acceptors present in the structure. However, the basic structure of these energy transfer matrices remains the same. Consequently, here we demonstrate how the energy transfer matrix is set up in the case of transfer from a thin film of donors placed between layers i and j to a thin film of acceptors placed between layers k and l, where $k \geq j$.

In the most general case, we consider energy transfer from each donor to each acceptor, so that the off-diagonal terms $F_{\nu,\mu}$ ($i \leq \mu \leq j$ and $k \leq \nu \leq l$), that indicate excitons transfered to the acceptor in layer ν from a donor in layer μ, have the following form:

$$F_{\nu\mu} = k_{\nu,\mu}^{ET} = \frac{1}{\tau_\mu}\left(\frac{D_F}{(\nu-\mu)\Delta x}\right)^4 \tag{C.18}$$

The diagonal terms $F_{\mu\mu}$ $(i \leq \mu \leq j)$ indicate excitons lost by the donor in layer μ due to the energy transfer to all the acceptors between layers k and l:

$$F_{\mu\mu} = -\sum_{\nu=k}^{\nu=l} k_{\nu,\mu}^{ET} \tag{C.19}$$

We then simply add the energy transfer matrix F to the exciton transport matrix:

$$M^2 = M^1 + F \tag{C.20}$$

where M^2 indicates the energy transfer-corrected exciton transport matrix.

4. **Exciton Dissociation**

   Analogous to exciton relaxation, exciton dissociation is included by adding the dissociation rates to the diagonal elements of the transport matrix:

$$M_{ii}^3 = M_{ii}^2 - k_i^{xd} \tag{C.21}$$

   Exciton dissociation rates are calculated based on the electric field profiles obtained from the charge transport model using Equations 6.9 and 6.14.

C.2.2 Numerical Solution Process

1. Start with the initial condition for the exciton concentration vector, i.e. $\vec{\xi}(0) = \vec{0}$
2. Calculate the exciton transport matrix
3. Calculate the change in concentration using the transport matrix and the generation rate
4. Repeat steps 2 and 3 until the exciton concentrations in the layers reach the steady state.

Appendix D

Contributions Associated with This Thesis

D.1 Publications

1. P. O. Anikeeva, C. F. Madigan, J. E. Halpert, M. G. Bawendi, V. Bulović. Electronic and Excitonic Processes in Hybrid Organic-Quantum Dot LEDs. *Phys. Rev. B*, 78:085434, 2008.

2. L. Kim, P. O. Anikeeva, S. A. Coe-Sullivan, J. S. Steckel, M. G. Bawendi, V. Bulović. Contact Printing of Quantum Dot Light Emitting Devices. *Nano Lett.*, 8:4513, 2008.

3. P. O. Anikeeva, J. E. Halpert, M. G. Bawendi , V. Bulović. Electroluminescence from a Mixed Red-Green-Blue Colloidal Quantum Dot Monolayer. *Nano Lett.*, 7:2196, 2007.

4. P. O. Anikeeva, C. F. Madigan, S. A. Coe-Sullivan, J. S. Steckel, M. G. Bawendi, V. Bulović. Photoluminescence of CdSe/ZnS core/shell quantum dots enhanced by energy transfer from a phosphorescent donor. *Chem. Phys. Lett.*, 424:120, 2006.

5. J. S. Steckel, P. Snee, S. A. Coe-Sullivan, J. P. Zimmer, J. E. Halpert, P. O.

Anikeeva, L. Kim, V. Bulović, M. G. Bawendi. Color-Saturated Green-Emitting QD-LEDs. *Angew. Chem. Int. Ed.*, 45:5796, 2006.

6. S. A. Ivanov, J. Nanda, A. Piryatinski, M. Achermann, L. P. Balet, I. V. Bezel, P. O. Anikeeva, S. Tretiak, V. I. Klimov. Light Amplification Using Inverted Core/Shell Nanocrystals: Towards Lasing in Single-Exciton Regime. *J. Phys. Chem. B*, 108:10625, 2004.

D.2 Patents

1. J. Chen, V. Bulović, P. O. Anikeeva, M. G. Bawendi. Light Emitting Device Including Semiconductor Nanocrystals. U. S. Patent No. 20080074050, 2008.

2. S. A. Coe-Sullivan, V. Bulović, J. S. Steckel, M. G. Bawendi, P. O. Anikeeva, J. E. Halpert. White Light Emitting Devices. Wipo Patent No. WO/2007/095173 (Application PCT/US2007/003677).

3. J. E. Halpert, P. O. Anikeeva, M. G. Bawendi, V. Bulović. Blue Light Emitting Semiconductor Nanocrystals and Devices. Wipo Patent No. WO/2008/021962 (Application PCT/US2007/075593).

4. J. A. Hollingsworth, V. I. Klimov, P. O. Anikeeva. Semiconductor nanocrystals quantum dots and metallic nanocrystals as UV blockers and colorants for sunscreen and/or sunless tanning compositions. U. S. Patent No. 20050265935, 2005.

Bibliography

[1] C. B. Murray, D. J. Norris, and M. G. Bawendi. Synthesis and characterization of nearly monodisperse CdE (E = S, Se, Te) semiconductor nanocrystallites. *J. Amer. Chem. Soc.*, 115:8706–8715, 1993.

[2] W. U. Huynh, J. J. Dittmer, and A. P. Alivisatos. Hybrid nanorod-polymer solar cells. *Science*, 295:2425–2427, 2002.

[3] S. Coe, W. K. Woo, M. G. Bawendi, and V. Bulović. Electroluminescence from single monolayers of nanocrystals in molecular organic devices. *Nature*, 420:800–803, 2002.

[4] R. Friedel and P. Israel. *Edison's electric light: biography of an invention.* Rutgers University Press, New Jersey, 1987.

[5] T. Edison. Fluorescent electric lamp. U. S. Patent No. 865367, 1907.

[6] N. Zheludev. The life and times of the LED - a 100-year history. *Nat. Photon.*, 1:189–192, 2007.

[7] S. Nakamura, G. Fasol, and S. Pearton. *The blue laser diode: the complete story.* Springer, 2000.

[8] C. W. Tang and S. A. Vanslyke. Organic electroluminescent diodes. *Appl. Phys. Lett.*, 51:913–915, 1987.

[9] C. W. Tang, S. A. Vanslyke, and C. H. Chen. Electroluminescence of doped organic fhin films. *J. Appl. Phys.*, 65:3610–3616, 1989.

[10] B. W. D'Andrade, R. J. Holmes, and S. R. Forrest. Efficient organic electrophosphorescence white-light emitting device with a triple doped emissive layer. *Adv. Mater.*, 16:624–628, 2004.

[11] H. Kanno, R. J. Holmes, Y. Sun, S. Kena-Cohen, and S. R. Forrest. White stacked electrophosphorescent organic light-emitting devices employing MoO_3 as a charge-generation layer. *Adv. Mater.*, 18:339–342, 2006.

[12] S. M. Kelly. Flat panel displays. In *Advanced Organic Materials*. Royal Society of Chemistry, 2000.

[13] Al. L. Efros and M. Rosen. The electronic structure of semiconductor nanocrystals. *Annu. Rev. Mater. Sci.*, 30:475–521, 2000.

[14] M. C. Schlamp, X. Peng, and A. P. Alivisatos. Improved efficiencies in light-emitting diodes made with cdse(cds) core/shell type nanocrystals and a semiconducting polymer. *J. Appl. Phys.*, 82:5837–5843, 1997.

[15] L. Kim. Deposition of colloidal quantum dots by microcontact printing for LED display technology. Master's thesis, Massachusetts Institute of Technology, 2006.

[16] L. Kim, P. O. Anikeeva, S. A. Coe-Sullivan, J. S. Steckel, M. G. Bawendi, and V. Bulović. Contact printing of quantum dot light emitting devices. *Nano Lett.*, 8:4513–4517, 2008.

[17] P. O. Anikeeva, J. E. Halpert, M. G. Bawendi, and V. Bulović. Electroluminescence from mixed red-green-blue colloidal quantum dot monolayer. *Nano Lett.*, 7:2196–2200, 2007.

[18] Y. Sato and H. Kanai. Stability of organic electroluminescent diodes. *Mol. Cryst. Liq. Cryst.*, 252:435–442, 1994.

[19] P. E. Burrows, V. Bulović, S. R. Forrest, L.S. Sapochak, D. M. McCarthy, and M. E. Thompson. Reliability and degradation of organic light-emitting devices. *Appl. Phys. Lett.*, 65:2922–2924, 1994.

[20] A. H. Mueller, M. A. Petruska, M. Achermann, D.J. Werder, E. A. Akhadov, D. D. Koleske, M. A. Hoffbauer, and V. I. Klimov. Multicolor light-emitting diodes based on semiconductor nanocrystals encapsulated in GaN charge injection layers. *Nano Letters*, 5:1039–1044, 2005.

[21] J. M. Caruge, J. E. Halpert, V. Bulović, and M.G. Bawendi. NiO as an inorganic hole transport layer in quantum-dot light-emitting devices. *Nano Letters*, 6:2991–2994, 2006.

[22] J. M. Caruge, J. E. Halpert, V. Wood, V. Bulović, and M.G. Bawendi. Colloidal quantum-dot light-emitting diodes with metal-oxide charge transport layers. *Nat. Photon.*, 2:247–250, 2008.

[23] A. P. Alivisatos. Semiconductor clusters, nanocrystals, and quantum dots. *Science*, 271:933–937, 1996.

[24] N. N. Ledentsov, V. M. Ustinov, V. A. Shchukin, P. S. Kop'ev, Zh. I. Alferov, and D. Bimberg. Quantum dot heterostructures: frabrication, properties, lasers (review). *Semiconductors*, 32:343–365, 1998.

[25] D. Schikora, S. Schwedhelm, D. J. As, K. Lischka, D. Litvinov, A. Rosenauer, D. Gerthsen, M. Strassburg, and A. Hoffmann anf D. Bimberg. Investigations of the stranski-krastanow growth of CdSe quantum dots. *Appl. Phys. Lett.*, 76:418–422, 2000.

[26] D. R. Larson, Warren. R. Zipfel, R. M. Williams, S. W. Clark, M. P. Bruchez, F. W. Wise, and W. W. Webb. Water-soluable quantum dots for multiphoton fluorescence imaging *in vivo*. *Science*, 300:1434–1436, 2003.

[27] V. I. Klimov, D. W. McBranch, C. A. Leatherdale, and M. G. Bawendi. Electron and hole relaxation pathways in semiconductor quantum dots. *Phys. Rev. B*, 60:13740–13749, 1999.

[28] M. A. Hines and P. Guyot-Sionnest. Synthesis and characterization of strongly luminescing ZnS-capped CdSe nanocrystals. *J. Phys. Chem.*, 100:468–471, 1996.

[29] B. O. Dabbousi, J. Rodriguez-Viejo, F. V. Mikulec, J. R. Heine, H. Mattoussi, R. Ober, K. F. Jensen, and M. G. Bawendi. (CdSe)ZnS core-shell quantum dots: Synthesis and characterization of a size series of highly luminescent nanocrystallites. *J. Phys. Chem. A*, 101:9463–9475, 1997.

[30] S. Coe-Sullivan, J. S. Steckel, W. K. Woo, M. G. Bawendi, V., and Bulović. Large-area ordered quantum-dot monolayers via phase separation during spin-casting. *Adv. Funct. Mater.*, 15:1117–1124, 2005.

[31] J. Zhao, J. A. Bardecker, A. Munro, M. S. Liu, Y. Niu, I.-K. Ding, J. Luo, B. Chen, A. K.-Y. Jen, and D. S. Ginger. Efficient CdSe/CdS quantum dot light-emitting diodes using a thermally polymerazed hole transport layer. *Nano Lett.*, 6:463–467, 2006.

[32] Q. Sun, Y. A. Wang, L. S. Li, D. Wang, T. Zhu, J. Xu, C. Yang, and Y. Li. Bright, multicoloured light-emitting diodes based on quantum dots. *Nat. Photon.*, 1:717–722, 2007.

[33] J. S. Steckel, J. P. Zimmer, S. Coe-Sullivan, N. E. Stott, V. Bulović, and M. G. Bawendi. Blue luminescence from (CdS)ZnS core-shell nanocrystals. *Angew. Chem. Int. Ed.*, 43:2154–2158, 2004.

[34] X. Zhong, Y. Feng, W. Knoll, and M. Han. Alloyed $Zn_xCd_{1-x}S$ nanocrystals with highly narrow luminescence spectral width. *J. Amer. Chem. Soc.*, 125:13559–13563, 2003.

[35] X. Zhong, M. Han, Z. Dong, T. J. White, and W. Knoll. Composition tunable $Zn_xCd_{1-x}Se$ nanocrystals with highly luminescence and stability. *J. Amer. Chem. Soc.*, 125:8589–8594, 2003.

[36] R. W. Balluffi, S. M. Allen, and W. C. Carter. *Kinetics of Materials.* Wiley-Interscience, 2005.

[37] L. Manna, D. J. Milliron, A. Meisel, E. C. Scher, and A. P. Alivisatos. Controlled growth of tetrapod-branched inorganic nanocrystals. *Nat. Mater.*, 2:382–385, 2003.

[38] A. G. Kanaras, C. Sönnichsen, H. Liu, and A. P. Alivisatos. Controlled synthesis of hyper-branched inorganic nanocrystals with rich three-dimentional structures. *Nano Lett.*, 5:2168–2172, 2005.

[39] D. J. Milliron, S. M. Hughes, Y. Cui, L. Manna, J. Li, L.-W. Wang, and A. P. Alivisatos. Colloidal nanocrystal heterostructures with linear and branched topology. *Nature*, 430:190–195, 2004.

[40] B. Sun, E. Marx, and N. C. Greenham. Photovoltaic devices using blends of branched CdSe nanoparticles and conjugated polymers. *Nano. Lett.*, 3:961–963, 2003.

[41] C. R. Pidgeon and R. N. Brown. Interband magneto-absorption and faraday rotation in InSb. *Phys. Rev.*, 146:575–583, 1966.

[42] J. M. Luttinger and W. Kohn. Theory of donor states in silicon. *Phys. Rev.*, 97:869–883, 1955.

[43] A. I. Ekimov, F. Hache, M. C. Schanne-Klein, D. Ricard, C. Flytzanis, I. A. Kudryavtsev, T. V. Yazeva, A. V. Rodina, and A. L. Efros. Absorption and intensity-dependent photoluminescence measurements on cdse quantum dots: assignment of the first electronic transitions. *J. Opt. Soc. Am. B*, 10:100–107, 1993.

[44] M. G. Bawendi, W. L. Wilson, L. Rothberg, P. J. Carroll, T. M. Jedju, M. L. Steigerwald, and L. E. Brus. Electronic structure and photoexcited-carrier dynamics in nanometer-size cdse clusters. *Phys. Rev. Lett*, 65:1623–1626, 1990.

[45] M. Nirmal, D. J. Norris, M. Kuno, M. G. Bawendi, Al. L. Efros, and M. Rosen. Observation of the "dark exciton" in CdSe quantum dots. *Phys. Rev. Lett*, 75:3728–3731, 1995.

[46] M. Pope and C. E. Swenberg. *Electronic processes in organic crystals.* New York: Oxford University Press, 1982.

[47] S. R. Forrest. The path to ubiquitous and low-cost organic electronic appliances on plastic. *Nature*, 428:911–918, 2004.

[48] C. D. Dimitrakopoulos, S. Purushothaman, J. Kymissis, A. Callegari, and J. M. Shaw. Low-voltage organic transistors on plastic comprising high-dielectric constant gate insulators. *Science*, 283:822–824, 1999.

[49] C. F. Madigan. *Theory and simulation of amorphous organic electronic devices.* PhD thesis, Massachusetts Institute of Technology, 2006.

[50] W. Helfrich and W. G. Schneider. Recombination radiation in anthracene crystals. *Phys. Rev. Lett*, 14:229–231, 1965.

[51] V. L. Colvin, M. C. Schlamp, and A. P. Alivisatos. Light emitting diodes made from cadmium selenide nanocrystals and a semiconducting polymer. *Nature*, 370:354–357, 1994.

[52] J. S. Steckel, P. Snee, S. Coe-Sullivan, J. P. Zimmer, J. E. Halpert, P. O. Anikeeva, L. Kim, V. Bulović, and M. G. Bawendi. Color-saturated green-emitting QD-LEDs. *Angew. Chem. Int. Ed.*, 45:5796–5799, 2006.

[53] S. A. Ivanov, J. Nanda, A. Piryatinski, M. Achermann, L. P. Balet, I. V. Bezel, P. O. Anikeeva, S. Tretiak, and V. I. Klimov. Light amplification using inverted core/shell nanocrystals: Towards lasing in the single-exciton regime. *J. Phys. Chem. B*, 108:10625–10630, 2004.

[54] S. A. Coe-Sullivan. *Hybrid Organic/Quantum Dot Thin Film Structures and Devices.* PhD thesis, Massachusetts Institute of Technology, 2005.

[55] J. Chen, V. Leblanc, S. H. Kang, P. J. Benning, D. Schut, M. A. Baldo, M. A. Schmidt, and V. Bulović. High definition digital fabrcation of active organic devices by molecular jet printing. *Adv. Funct. Mater.*, 17:2722–2727, 2007.

[56] A. Kumar and G. M. Whitesides. Features of gold having micrometer to centimeter dimensions can be formed through a combination of stamping with an elastomeric stamp and an alkanethiol "ink" followed by chemical etching. *Appl. Phys. Lett.*, 63:2002–2004, 1993.

[57] V. Santhanam and R. P. Andres. Microcontact printing of uniform nanoparticle arrays. *Nano Lett.*, 4:41–44, 2004.

[58] S. N. Magonov and M.-H. Whangbo. *Surface analysis with STM and AFM.* VCH, 1996.

[59] P. J. Goodhew. *Electron microscopy and analysis.* Taylor & Francis, 2001.

[60] P. W. Atkins and R. S. Friedman. *Molecular quantum mechanics.* Oxford University Press, 1997.

[61] B. E. A. Saleh and M. C. Teich. *Fundamentals of photonics.* John Wiley and Sons, 1991.

[62] A. Rose. Space-charge-limited currents in solids. *Phys. Rev.*, 97:1538–1544, 1955.

[63] Y. Shimizu, K. Sakano, Y. Noguchi, and T. Moriguchi. Light emitting device having a nitride compound semiconductor and a phosphor containing a garnet fluorescent material. U. S. Patent No. 5998925, December 1999.

[64] E. F. Schubert and J. K. Kim. Solid-state light sources getting smart. *Science*, 308:1274–1278, 2005.

[65] H. Matsubara, T. Takebe, and K. Motoki. Substrate-fluorescent LED. U. S. Patent No. 6509651, January 2003.

[66] A. Duggal, J. J. Shiang, C. M. Heller, and D. F. Foust. Organic light-emitting devices for illumination quality white light. *Appl. Phys. Lett.*, 80:3470–3472, 2002.

[67] M. Gao, B. Richter, and S. Kirstein. White-light electroluminescence from self-assempled Q-CdSe/PPV multilayer structures. *Adv. Mater.*, 9:802–805, 1997.

[68] Y. Li, A. Rizzo, M. Mazzeo, L. Carbone, L. Manna, R. Cingolani, and G. Gigli. White organic light-emitting devices with CdSe/ZnS quantum dots as a red emitter. *J. Appl. Phys.*, 97:113501 1–4, 2005.

[69] J. H. Park, J. Y. Kim, B. D. Chin, Y. C. Kim, J. K. Kim, and O. O. Park. White emission from polymer/quantum dot ternary nanocomposites by incomplete energy transfer. *Nanotechnology*, 15:1217–1220, 2004.

[70] J. Lee, V. C. Sundar, J. R. Heine, M. G. Bawendi, and K. F. Jensen. Full color emission from II-VI semiconductor quantum dot-polymer composites. *Adv. Mater.*, 12:1102–1105, 2000.

[71] M. J. Bowers, J. R. McBride, and S. J. Rosenthal. White-light emission from magic-sized cadmium selenide nanocrystals. *J. Amer. Chem. Soc.*, 127:15378–15379, 2005.

[72] H. S. Chen, S. J. J. Wang, C. J. Lo, and J. Y. Chi. White-light emission from organics-capped znse quantum dots and application in white-light-emitting diodes. *Appl. Phys. Lett.*, 86:131905 1–3, 2005.

[73] P. O. Anikeeva, J. E. Halpert, M.G. Bawendi, and V. Bulović. Efficient white-light quantum dot leds. In *Basic Research Needs for Solid-State Lighting*, 2006.

[74] Y. Li, A. Rizzo, R. Cingolani, and G. Gigli. Bright white-light-emitting device from ternanry nanocrystal composites. *Adv. Mater.*, 18:2545–2548, 2006.

[75] C. R. Kagan, C. B. Murray, M. Nirmal, and M. G. Bawendi. Electronic energy transfer in CdSe quantum dot solids. *Phys. Rev. Lett*, 76:1517–1520, 1996.

[76] S. A. Crooker, J. A. Hollingsworth, S. Tretiak, and V. I. Klimov. Spectrally resolved dynamics of energy transfer in quantum-dot assemblies: towards engineered energy flows in artificial materials. *Phys. Rev. Lett*, 89:186802 1–4, 2002.

[77] Th. Förster. Zwischenmolekulare energiewanderung and fluoreszenz. *Annalen der Physik*, 6:55–75, 1948.

[78] H. Kuhn. Classical aspects of energy transfer in molecular systems. *J. Chem. Phys.*, 53:101–108, 1970.

[79] Luminescence technology corp., 2008.

[80] V. I. Klimov, A. A. Mikhailovsky, D. W. McBranch, C. A. Leatherdale, and M. G. Bawendi. Quantization of multiparticle auger rates in semiconductor quantum dots. *Science*, 287:1011–1013, 2000.

[81] M. R. Krames, J. Bhat, D. Collins, N. F. Gardner, W. Götz, C. H. Lowery, M. Ludowise, P. S. Martin, G. Mueler, R. Mueller-Mach, S. Rudaz, D. A. Steigerwald, S. A. Stockman, and J. J. Wierer. High-power III-nitride emitters for solid state lighting. *Phys. Stat. Sol. A*, 192:237–245, 2002.

[82] M. Nirmal, B. O. Dabbousi, M. G. Bawendi, J. J. Macklin, J. K. Trautman, T. D. Harris, and L. E. Brus. Fluorescence intermittency in single cadmium selenide nanocrystals. *Nature*, 383:802–804, 1996.

[83] M. A. Baldo, D. F. O'Brien, M. E. Thompson, and S. R. Forrest. Excitonic singlet-triplet ratio in a semiconducting organic thin film. *Phys. Rev. B*, 60:14422–14428, 1999.

[84] C. Adachi, M. A. Baldo, M. E. Thompson, and S. R. Forrest. Nearly 100% internal phosphorescence efficiency in an organic light emitting device. *J. Appl. Phys.*, 90:5048–5051, 2001.

[85] M. A. Baldo, M. E. Thompson, and S. R. Forrest. High-efficiency fluorescent organic light-emitting devices using a phosphorescent sensitizer. *Nature*, 403:750–753, 2000.

[86] A. R. Clapp, I. L. Medintz, J. M. Mauro, B. R. Fischer, M. G. Bawendi, and H. Mattoussi. Fluorescence resonance energy transfer between quantum dot

donors and dye-labeled protein acceptors. *J. Am. Chem. Soc.*, 126:301–310, 2004.

[87] I. L. Medintz, A. R. Clapp, H. Mattoussi, E. R. Goldman, B. Fisher, and J. M. Mauro. Self-assembled nanoscale biosensors based on quantum dot FRET donors. *Nat. Mater.*, 2:630–638, 2003.

[88] A. R. Clapp, I. L. Medintz, G. P. Anderson, and H. Mattoussi. Can luminescent quantum dots be efficient energy acceptors with organic dye donors. *J. Am. Chem. Soc.*, 127:1242–1250, 2005.

[89] M. Anni, L. Manna, R. Cingolani, D. Valerini, A. Creti, and M. Lomascolo. Förster energy transfer from blue-emitting polymers to colloidal CdSe/ZnS core shell quantum dots. *Appl. Phys. Lett.*, 85:4169–4171, 2004.

[90] M. Achermann, M. A. Petruska, S. Kos, D. L. Smith, D. D. Koleske, and V. I. Klimov. Energy-transfer pumping of semiconductor nanocrystals using an epitaxial quantum well. *Nature*, 429:642–646, 2004.

[91] D. J. Norris. Electronic structure in semiconductor nanocrystals. In *Semiconductor and Metal Nanocrystals: Synthesis and Electronic and Optical Properties*. Marcel Dekker Ltd, 2003.

[92] P. O. Anikeeva, C. F. Madigan, S. A. Coe-Sullivan, J. S. Steckel, M. G. Bawendi, and V. Bulović. Photoluminescence of cdse/zns core/shell quantum dots enhanced by energy transfer from a phosphorescent donor. *Chem. Phys. Lett.*, 424:120–125, 2006.

[93] M. A. Baldo, S. Lamansky, P. E. Burrows, M. E. Thompson, and S. R. Forrest. Very high-efficiency green organic light-emiting devices based on electrophosphorescence. *Appl. Phys. Lett.*, 75:4–6, 1999.

[94] N. Matsusue, S. Ikame, Y. Suzuki, and H. Naito. Charge-carrier transport and triplet exciton diffusion in a blue electrophosphorescent emitting layer. *Appl. Phys. Lett.*, 97:123512, 2005.

[95] E. B. Namdas, A. Ruseckas, I. D. W. Samuel, S.-C. Lo, and P. L. Burn. Triplet exciton diffusion in fac-tris(2-phenylpyridine) iridium (III)-cored electroluminescent dendrimers. *Appl. Phys. Lett.*, 86:091104, 2005.

[96] J. S. Steckel, S. Coe-Sullivan, V. Bulović, and M. G. Bawendi. 1.3 μm to 1.55 μm tunable electroluminescence from PbSe quantum dots embedded within an organic device. *Adv. Mater.*, 15:1862–1866, 2003.

[97] H. Ishii, K. Sugiyama, and K. Seki. Interfacial electronic structures of organic/metal interfaces studied by UV photoemission. *Proc. SPIE*, 3148:228, 1997.

[98] P. T. Landsberg. *Recombination in semiconductors.* Cambridge University Press, 2003.

[99] M. A. Lampert. Simplified theory of space-charge-limited currents in an insulator with traps. *Phys. Rev.*, 103:1648–1656, 1956.

[100] H. Huang, A. Dorn, G. Nair, V. Bulović, and M. G. Bawendi. Bias-induced photoluminescence quenching of single colloidal quantum dots embedded in organic semiconductors. *Nano Lett.*, 7:3781, 2007.

[101] S. Coe-Sullivan, W. K. Woo, J. S. Steckel, M. G. Bawendi, V., and Bulović. Tuning the performance of hybrid organic/inorganic quantum dot light-emitting devices. *Organic Electronics*, 4:123–130, 2003.

[102] H. Bässler. Localized states and electronic transport in single component organic solids with diagnal disorder. *Phys. Stat. Sol.*, 107:9–54, 1981.

[103] R. F. Pierret. *Semiconductor Fundamentals Second Edition.* Addison-Wesley Publishing Group, 1988.

[104] P. O. Anikeeva, C. F. Madigan, M. G. Bawendi, and V. Bulović. Modeling of carrier and exciton transport in organic and quantum dot leds. *In preparation*, 2008.

[105] C. Cohen-Tannoudji, D. Diu, and F. Laloe. *Quantum mechanics.* New York: Wiley, 1977.

[106] D. B. Papkovski. New oxygen sensors and their applications to biosensing. *Sens. Actuators B*, 29:213–218, 1995.

[107] L. Onsager. Initial recombination of ions. *Phys. Rev.*, 15:554–557, 1938.

[108] M. Scheidler, U. Lemmer, R. Kersting, S. Karg, W. Reiss, B. Cleve, R. F. Mahrt, H. Kurz, H. Bässler, E. O. Göbel, and P. Thomas. Monte carlo study of picosecond exciton relaxation and dissociation in poly(phenylenevinylene). *Phys. Rev. B*, 54:5536–5543, 1996.

[109] P. O. Anikeeva, C. F. Madigan, J. E. Halpert, M. G. Bawendi, and V. Bulović. Electronic and excitonic processes in light-emitting devices based on organic materials and colloidal quantum dots. *Phys. Rev. B*, 78:085434 1–8, 2008.

[110] S. Gambino, P. Cusumano, and C. Cali. Measurement of drift mobilities in amrphous organic films using the time of flight method. *Proc. SPIE*, 5464:280–291, 2004.

[111] B. Chen and S. Liu. Measurement of electron/hole mobility in organic/polymeric thin films using modified time-of-flight apparatus. *Synth. Met.*, 91:169–171, 1997.

[112] C. A. Leatherdale, C. R. Kagan, N. Y. Morgan, S. A. Empedocles, M. A. Castner, and M. G. Bawendi. Photoconductivity in cdse quantum dot solids. *Phys. Rev. B*, 62:2669–2680, 2000.

[113] P. O. Anikeeva, J. E. Halpert, M. G. Bawendi, and V. Bulović. Optimized materials for high performance qd-leds with electroluminescence tunable over entire visible spectrum. *In preparation*, 2008.

[114] V. I. Klimov, A. A. Mikhailovsky, S. Xu, A. Malko, J. A. Hollingsworth, C. A. Leatherdale, H.-J. Eisler, and M. G. Bawendi. Optical gain and stimulated emission in nanocrystal quantum dots. *Science*, 290:314–317, 2000.

[115] J. E. Halpert. *Design and synthesis of nanocrystal heterostructures for optoelectronic applications.* PhD thesis, Massachusetts Institute of Technology, 2008.

[116] B. Sun and N. C. Greenham. Improved efficiency of photovoltaics based on CdSe nanorods and poly(3-hexylthiopene) nanofibers. *Phys. Chem. Chem. Phys.*, 8:3557–3560, 2006.

[117] S. A. Coe-Sullivan, J. S. Steckel, L. Kim, M. G. Bawendi, and V. Bulović. Contact printing of quantum dot light-emitting devices. *Proc. SPIE*, 5739:108, 2005.

[118] I. H. Campbell and B. K. Crone. Efficient, visible organic light-emitting diodes utilizing a single polymer layer doped with quantum dots. *Appl. Phys. Lett.*, 92:043303 1–3, 2008.

[119] M. Olson-Hummon et al. Trap state charging in ZnCdSe quantum dots. *In preparation*, 2008.

[120] J. S. Biteen, L. A. Sweatlock, H. Mertens, N. S. Lewis, A. Polman, and H. A. Atwater. Plasmon-enhanced photoluminescence of silicon quantum dots: simulation and experiment. *J. Phys. Chem. C*, 111:13372–13377, 2007.

[121] D. Pacifici, H. J. Lezec, and H. A. Atwater. All-optical modulation by plasmonic excitation of CdSe quantum dots. *Nat. Photon.*, 1:402–406, 2007.

[122] D. MacAdam. Projective transformations of I.C.I color specifications. *J. Opt. Soc. Am.*, 27:294–299, 1937.